STUDY OF THE $\Delta(1232)$ USING DOUBLE POLARIZATION ASYMMETRIES

By

Angela Biselli

A Thesis Submitted to the Graduate

Faculty of Rensselaer Polytechnic Institute

in Partial Fulfillment of the

Requirements for the Degree of

DOCTOR OF PHILOSOPHY

Major Subject: Physics

Approved by the
Examining Committee:

____
Paul Stoler, Thesis Adviser

____
Gary Adams, Member

____
Volker Burkert, Member

____
James Napolitano, Member

____
Wayne Roberge, Member

____
Mauro Taiuti, Member

Rensselaer Polytechnic Institute
Troy, New York

March 2002
(For Graduation May 2002)

STUDY OF THE $\Delta(1232)$ USING DOUBLE POLARIZATION ASYMMETRIES

By

Angela Biselli

An Abstract of a Thesis Submitted to the Graduate

Faculty of Rensselaer Polytechnic Institute

in Partial Fulfillment of the

Requirements for the Degree of

DOCTOR OF PHILOSOPHY

Major Subject: Physics

The original of the complete thesis is on file
in the Rensselaer Polytechnic Institute Library

Examining Committee:

Paul Stoler, Thesis Adviser
Gary Adams, Member
Volker Burkert, Member
James Napolitano, Member
Wayne Roberge, Member
Mauro Taiuti, Member

Rensselaer Polytechnic Institute
Troy, New York

March 2002
(For Graduation May 2002)

CONTENTS

LIST OF TABLES

LIST OF FIGURES

ACKNOWLEDGMENT

I would like to thank the Spectrum 7 theatre for showing arty movies, the Cedar Point Amusement Park for having built Millennium Force, the tallest rollercoaster in the US, Mother Nature for having created the Rocky mountains and powder snow conditions and the NY Yankees for playing great World Series.

Incidentally, I would like to also thank Paul Stoler for being a great advisor and friend, and Joachim for helping, supervising, supporting and sharing his life with me.

ABSTRACT

An extensive experimental program to measure the spin structure of the nucleons is underway in Hall B at Jefferson Lab using a polarized electron beam incident on a polarized target. Spin degrees of freedom offer the possibility to test, in an independent way, existing models of resonance electro-production.

The present analysis selects the $\Delta^+(1232)$ in the exclusive channel $\vec{p}(\vec{e}, e'p)\pi^0$ from data of the EG1 run period, taken in the Fall of 1998, to extract single and double asymmetries in a Q^2 range from 0.5 to 1.5 GeV^2/c^2. Results of the asymmetries are presented as a function of the center of mass decay angles of the π^0, θ^* and ϕ^*, as well as a function of momentum transfer Q^2. A comparison with the Effective Lagrangian Model by R. Davidson and N. Mukhopadhyay, the unitary isobar model MAID and the dynamic model by Sato and Lee was performed. The data were found to be generally in good agreement with the models and a χ^2 comparison preferred the Sato-Lee model, which is tailored for the $\Delta(1232)$ photo- and electro-production. The present results are the first measurement of asymmetries for the exclusive reaction $\vec{p}(\vec{e}, e'p)\pi^0$ and will provide new constraints for the models.

CHAPTER 1
SINGLE PION ELECTRO-PRODUCTION

In the past few years many electro-production experiments have been performed in order to probe the structure of the nucleon. On one hand inclusive experiments allow one to measure, for example, the nucleon structure functions. On the other hand, exclusive channels give the possibility to study nucleon resonances in detail. A resonance that has inspired many experiments is the $\Delta(1232)$. It is the most accessible because it does not overlap with any other resonance, and it decays strongly only via single pion emission. One of the most interesting features of the $\Delta(1232)$ resonance is the ratio E_{1+}/M_{1+}, which is predicted to be very small in the Constituent Quark Model (CQM), and equal to 1 in the limit $Q^2 \to \infty$. These two very different limits presuppose a transition at a certain Q^2 which has been sought by many experiments. However all the existing analyses found this ratio very small, implying that the transition has to occur at $Q^2 > 4$ GeV$^2/c^2$.

Previously, nearly all of our knowledge about the properties of the Δ have come from the reactions $\gamma+N \to N+\pi$, $\gamma_v+N \to N+\pi$ and $\pi+N \to N+\pi$. All the single pion production experiments that have been performed so far, are with unpolarized beam and target. This kind of measurement does not access all the amplitudes of the reaction. There are 36 response functions that characterize $e + N \to e + N + \pi$ corresponding to the different combinations of photon and proton spins, but only four of these describe unpolarized scattering. Polarized targets and polarized beams allow one to explore the reaction completely and offer a new independent way to measure quantities previously determined with unpolarized experiments. The peculiarity of this kind of measurement is the possibility to extract asymmetries instead of cross-sections. Asymmetries, which are the differences between cross sections of opposite polarizations divided by the total cross section, have advantages, such as not requiring an absolute normalization.

In the range of energies of few GeV, neither CQM or perturbative Quantum Chromodynamics (pQCD) are good descriptions for electro-production processes.

The existing theories are instead effective field models, whose fundamental degrees of freedom are the hadrons and not the quarks. In this kind of description the vertex $\gamma_v + P \rightarrow \Delta$ is unknown and the models use unpolarized data to fit ad-hoc parameters. Although only unpolarized data are used to constrain the free parameters, the models are able to predict also the polarized part of the cross-section, therefore polarized experiments offer the possibility to test them independently.

In this chapter the formalism, the characteristics of the models as well as the properties of the $\Delta(1232)$ resonance will be described in more detail.

1.1 Formalism

To lowest order of the fine structure constant the reaction $e + N \rightarrow e + N + \pi$ occurs via one virtual photon exchange. In particular, as shown in Figure 1.1, the initial electron, characterized by the 4-vector $e = (\epsilon_i, \vec{k_i})$ emits a virtual photon $\gamma_v = (\omega, \vec{q})$ which interacts with the target $P = (E_i, P_i) = (M, 0)$ and produces a pion $\pi = (\omega_\pi, \vec{k})$ and a final state nucleon $P' = (E_f, P_f) = (E, \vec{P})$. The virtual photon 4-vector is determined by the kinematics of the ingoing and outgoing electron $e' = (\epsilon_f, \vec{k_f})$ through the relations $\omega = \epsilon_f - \epsilon_i$ and $\vec{q} = \vec{k_f} - \vec{k_i}$.

The mass of the virtual photon $q^2 = \omega^2 - |\vec{q}|^2 = -Q^2$, known also as momentum

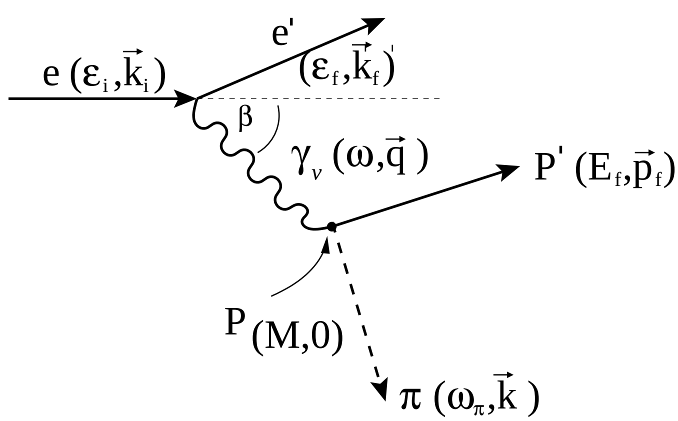

Figure 1.1: Schematic diagram of π nucleon electro-production.

transfer, the invariant mass $W = |e + P - e'|$ and θ^* and ϕ^*, the angles of the pion in the c.m. frame of the $P'\pi$ system, completely describe the electro-production process. It will be shown later in this section that the cross-section can be factorized into ϕ^* terms ($\sin\phi^*$ etc) and response functions which depend only on Q^2, W and θ^*. The well known ϕ^* dependence is a consequence of the one photon exchange approximation[1].

The differential cross section for electro-production can be written as

$$\begin{aligned} d\sigma =& \frac{\epsilon_i}{k_i}\frac{m_e}{\epsilon_i}\frac{M}{E_i}\frac{m_e}{\epsilon_f}\frac{d^3k_f}{(2\pi)^3}\frac{1}{2\omega_\pi}\frac{d^3k}{(2\pi)^3}\frac{M}{E_f}\frac{d^3P_f}{(2\pi)^3} \\ & (2\pi)^{(4)}\delta^4(P_i+q-k-P_f) \\ & |<P_f,k|J^\mu|P_i>q^{-2}<k_f|j_\mu|k_i>|^2 \end{aligned} \tag{1.1}$$

where j_μ and J^μ denote the electromagnetic currents of electron and hadrons, respectively. The hadronic current $J^\mu = (\rho, \vec{J})$ can be expressed in the general form

$$\begin{aligned} \vec{J} =& \frac{4\pi W}{M}[i\tilde{\vec{\sigma}}F_1 + (\vec{\sigma}\cdot\hat{\vec{k}})(\vec{\sigma}\times\hat{\vec{q}})F_2 + i\tilde{\vec{k}}(\vec{\sigma}\cdot\hat{\vec{q}})F_3 \\ & + i\tilde{\vec{k}}(\vec{\sigma}\cdot\hat{\vec{k}})F_4 + i\hat{\vec{q}}(\vec{\sigma}\cdot\hat{\vec{q}})F_5 + i\hat{\vec{q}}(\vec{\sigma}\cdot\hat{\vec{k}})F_6] \\ \rho =& \frac{4\pi W}{M}[i(\vec{\sigma}\cdot\hat{\vec{k}})F_7 + i(\vec{\sigma}\cdot\hat{\vec{q}})F_8] = \frac{\vec{q}\cdot\vec{J}}{\omega} \end{aligned} \tag{1.2}$$

where all the vectors are expressed in the center of mass frame and $\vec{\sigma}$ are the Pauli spin matrices. The vectors $\tilde{\vec{k}}$ and $\tilde{\vec{\sigma}}$ are the projections along the direction orthogonal to $\vec{q}$, $\tilde{\vec{k}} = \vec{k} - (\vec{k}\cdot\hat{\vec{q}})\hat{\vec{q}}$ and $\tilde{\vec{\sigma}} = \vec{\sigma} - (\vec{\sigma}\cdot\hat{\vec{q}})\hat{\vec{q}}$. The functions F_i are the so-called CGLN amplitudes [1].

The square of the transition matrix

$$|T_{fi}|^2 \equiv |<P_f,k|J^\mu|P_i>q^{-2}<k_f|j_\mu|k_i>|^2 \tag{1.3}$$

can be written as the product of two tensors $\eta_{\mu\nu}$ and $W_{\mu\nu}$

$$|T_{fi}|^2 = \sum \eta_{\mu\nu}W^{\mu\nu} \tag{1.4}$$

[1]It exists an alternative formalism to the one with response functions which makes use of the so called helicity amplitudes. This formalism is presented in Appendix A for completeness.

The lepton tensor, $\eta_{\mu\nu}$ can be expressed as

$$\begin{aligned}\eta_{\mu\nu} =& \sum_{s_f}(\bar{u}(k_f,s_f)e\gamma_\mu u(k_i,s_i))(\bar{u}(k_f,s_f)e\gamma_\nu u(k_i,s_i))^* \\ =& \frac{e^2}{2m_e^2}(2K_\mu K_\nu + \frac{1}{2}q^2 g_{\mu\nu} - \frac{1}{2}q_\mu q_\nu + ih\epsilon_{\mu\nu\alpha\beta}q^\alpha K^\beta)\end{aligned} \tag{1.5}$$

where K is defined as $K \equiv \frac{1}{2}(k_i + k_f)$, h is the helicity of the ingoing electron, $g_{\mu\nu}$ is the symmetric metric tensor and $\epsilon_{\mu\nu\alpha\beta}$ is the completely antisymmetric tensor. The hadronic tensor $W_{\mu\nu}$ is defined as

$$W_{\mu\nu} = (\frac{M}{4\pi W})^2 < \chi_f|J_\mu|\chi_i >< \chi_f|J_\nu|\chi_i >^* \tag{1.6}$$

where $J_\mu = (\rho, \vec{J})$ is the current operator defined in equation 1.2, and $|\chi_{i,f} >$ are the Pauli spinors of the nucleon in the initial and final state.

Using the previous equations the five-fold differential cross section can be expressed in terms of a flux of virtual photons Γ and the differential cross section for pion production by a virtual photon $d\sigma/d\Omega^*$ taking the following form:

$$\frac{d\sigma}{dE' d\Omega_e d\Omega^*} = \Gamma \frac{d\sigma}{d\Omega^*} \tag{1.7}$$

with

$$\Gamma = \frac{\alpha}{2\pi^2}\frac{\epsilon_f}{\epsilon_i}\frac{k_\gamma^{lab}}{Q^2}\frac{1}{1-\epsilon} \tag{1.8}$$

Here

$$\epsilon = (1 + 2\frac{|\vec{q}|^2}{Q^2}\tan^2\frac{\theta_e}{2})^{-1} \tag{1.9}$$

represents the degree of transverse polarization of the virtual photon, and

$$k_\gamma^{lab} = \frac{W^2 - M^2}{2M} \tag{1.10}$$

denotes the 'photon equivalent energy' necessary for a real photon to excite a hadronic system with c.m. energy W.

One can express $d\sigma/d\Omega^*$ in terms of response functions ${}^{c,s}R_i^{\beta\alpha}$[2] as

$$\begin{aligned} \frac{d\sigma}{d\Omega^*} = \frac{|\vec{k}|}{k_\gamma^{cm}} P_\alpha P_\beta (R_T^{\beta\alpha} + \epsilon_L R_L^{\beta\alpha} \\ + \sqrt{2\epsilon_L(1+\epsilon)}({}^cR_{TL}^{\beta\alpha}\cos\phi^* + {}^sR_{TL}^{\beta\alpha}\sin\phi^*) \\ + \epsilon({}^cR_{TT}^{\beta\alpha}\cos 2\phi^* + {}^sR_{TT}^{\beta\alpha}\sin 2\phi^*) \\ + h\sqrt{2\epsilon_L(1-\epsilon)}({}^cR_{TL'}^{\beta\alpha}\cos\phi^* + {}^sR_{TL'}^{\beta\alpha}\sin\phi^*) \\ + h\sqrt{1-\epsilon^2}R_{TT'}^{\beta\alpha}) \end{aligned} \tag{1.11}$$

where

$$k_\gamma^{cm} = \frac{M}{W} k_\gamma^{lab} \tag{1.12}$$

is the 'real photon equivalent energy' in the c.m. frame and

$$\epsilon_L = \frac{Q^2}{\omega^2}\epsilon \tag{1.13}$$

is the longitudinal polarization(frame dependent). $P_\alpha = (1, \vec{P})$ and $P_\beta = (1, \vec{P\prime})$ are four-vectors which specify the polarization of the target $\vec{P} = (P_x, P_y, P_z)$ and of the recoil $\vec{P\prime} = (P'_{x'}, P'_{y'}, P'_{z'})$, respectively. The reference frames for these vectors are described in Figure 1.2. The target polarization frame has $\hat{z}$ in the direction $\hat{q}$ of the virtual photon, $\hat{y}$ is perpendicular to the reaction plane ($\hat{y} = \hat{q} \times \hat{k}/\sin\theta^*$), and $\hat{x}$ is given by $\hat{x} = \hat{y} \times \hat{z}$. The recoil polarization frame has $\hat{z}'$ defined along the outgoing pion momentum $\vec{k}$, the $\hat{y}'$ axis coincides with $\hat{y}$ and $\hat{x}'$ is given by $\hat{x}' = \hat{y}' \times \hat{z}'$.

From equation 1.11 it can be seen that there are $4 \times 4 \times 9$ response functions. However some of them are identically zero and others are related to each other. These equalities, which can be found in [2], reduce the total number of independent response functions to 36. These functions depend on the scattering angle θ^* and can be written as a function of real or imaginary parts of the 6 complex CGLN amplitudes introduced in equation 1.2 as shown in Appendix B.

The previous expression for the cross section 1.11 is the most general one since it contains the electron, target and recoil polarizations. The object of this analysis

[2]The letters "c" and "s" indicate if the response function is multiplied to $\cos\phi^*$ or $\sin\phi^*$, respectively.

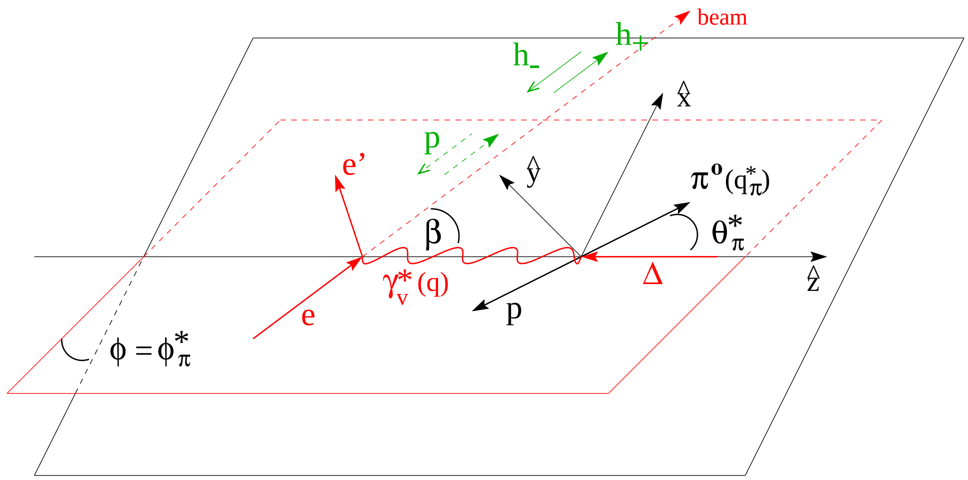

Figure 1.2: Decay plane: $\hat{z} = \frac{\vec{q}}{|\vec{q}|}$, $\hat{y} = \hat{z} \times \frac{\vec{q}^*_\pi}{|\vec{q}^*_\pi|}$, $\hat{x} = \hat{y} \times \hat{z}$.

is the measurement with both polarized beam and target, and unpolarized recoil proton. This means that in equation 1.11 $P^\beta = (1, 0, 0, 0)$. The cross section then becomes

$$\begin{aligned}\frac{d\sigma}{d\Omega^*} = \frac{|\vec{k}|}{k_\gamma^{cm}}\Big\{ &\big[R_T^0 + \epsilon_L R_L^0 + \sqrt{2\epsilon_L(1+\epsilon)}R_{TL}^0 \cos\phi^* + \epsilon R_{TT}^0 \cos 2\phi^*\big] + \\ &+ h\big[\sqrt{2\epsilon_L(1-\epsilon)}R_{TL'}^0 \sin\phi^*\big] + \\ &+ P_x\big[\sqrt{2\epsilon_L(1+\epsilon)}R_{TL}^x \sin\phi^* + \epsilon R_{TT}^x \sin 2\phi^*\big] + \\ &+ P_y\big[R_{TL}^y + \epsilon_L R_L^y + \sqrt{2\epsilon_L(1+\epsilon)}R_{TL}^y \cos\phi^* + \epsilon R_{TT}^y \cos 2\phi^*\big] + \\ &+ P_z\big[\sqrt{2\epsilon_L(1+\epsilon)}R_{TL}^z \sin\phi^* + \epsilon R_{TT}^z \sin 2\phi^*\big] + \\ &+ hP_x\big[\sqrt{2\epsilon_L(1-\epsilon)}R_{TL'}^x \cos\phi^* + \sqrt{1-\epsilon^2}R_{TT'}^x\big] + \\ &+ hP_y\big[\sqrt{2\epsilon_L(1-\epsilon)}R_{TL'}^y \sin\phi^*\big] + \\ &+ hP_x\big[\sqrt{2\epsilon_L(1-\epsilon)}R_{TL'}^z \cos\phi^* + \sqrt{1-\epsilon^2}R_{TT'}^z\big]\Big\}\end{aligned} \tag{1.14}$$

The first 4 terms of equation 1.14 are the unpolarized cross section. The first term is known as transverse, the second one as the longitudinal, the third as the transverse-longitudinal interference and the fourth one as the transverse-transverse interference structure function.

In EG1 the polarization of the target was along the beam axis, and therefore in the reference frame defined above the components are

$$\vec{P} = P(\sin\theta_\gamma \cos\phi^*, -\sin\theta_\gamma \sin\phi^*, \cos\theta_\gamma) \tag{1.15}$$

Substituting these components equation 1.14 can be written in the form

$$\frac{d\sigma}{d\Omega^*} = \frac{|\vec{k}|}{k_\gamma^{cm}}\left\{\frac{d\sigma_0}{d\Omega^*} + h\frac{d\sigma_e}{d\Omega^*} + P\frac{d\sigma_t}{d\Omega^*} - hP\frac{d\sigma_{et}}{d\Omega^*}\right\} \tag{1.16}$$

where

$$\begin{aligned}
\frac{d\sigma_0}{d\Omega^*} =& R_T^0 + \epsilon_L R_L^0 + \sqrt{2\epsilon_L(1+\epsilon)}R_{TL}^0 \cos\phi^* + \epsilon R_{TT}^0 \cos 2\phi^* \\
\frac{d\sigma_e}{d\Omega^*} =& \sqrt{2\epsilon_L(1-\epsilon)}R_{TL'}^0 \sin\phi^* \\
\frac{d\sigma_t}{d\Omega^*} =& \sin\theta_\gamma \cos\phi^*[\sqrt{2\epsilon_L(1+\epsilon)}R_{TL}^x \sin\phi^* + \epsilon R_{TT}^x \sin 2\phi^*] + \\
& -\sin\theta_\gamma \sin\phi^*[R_{TL}^y + \epsilon_L R_L^y + \sqrt{2\epsilon_L(1+\epsilon)}R_{TL}^y \cos\phi^* + \\
& +\epsilon R_{TT}^y \cos 2\phi^*] + \cos\theta_\gamma[\sqrt{2\epsilon_L(1+\epsilon)}R_{TL}^z \sin\phi^* + \epsilon R_{TT}^z \sin 2\phi^*] \\
\frac{d\sigma_{et}}{d\Omega^*} =& -\sin\theta_\gamma \cos\phi^*[\sqrt{2\epsilon_L(1-\epsilon)}R_{TL'}^x \cos\phi^* + \sqrt{1-\epsilon^2}R_{TT'}^x] + \\
& +\sin\theta_\gamma \sin\phi^*[\sqrt{2\epsilon_L(1-\epsilon)}R_{TL'}^y \sin\phi^*] + \\
& -\cos\theta_\gamma[\sqrt{2\epsilon_L(1-\epsilon)}R_{TL'}^z \cos\phi^* + \sqrt{1-\epsilon^2}R_{TT'}^z]
\end{aligned} \tag{1.17}$$

Equations 1.16 and 1.17 show the four contributions to the total cross section that arise in case of polarized beam and target and unpolarized recoil nucleon. The first term is the unpolarized cross section whereas the terms $\frac{d\sigma_e}{d\Omega^*}$ $\frac{d\sigma_t}{d\Omega^*}$ and $\frac{d\sigma_{et}}{d\Omega^*}$ arise when beam, target, and both beam and target are polarized. The asymmetries, which are quantities meant to exploit every single contribution, are then defined as a ratio of one of the polarized terms and the unpolarized cross section

$$\begin{aligned}
A_e \equiv& \frac{\sigma_e}{\sigma_0} \\
A_t \equiv& \frac{\sigma_t}{\sigma_0} \\
A_{et} \equiv& \frac{\sigma_{et}}{\sigma_0}
\end{aligned} \tag{1.18}$$

where $\sigma_e \equiv \frac{d\sigma_e}{d\Omega^*}$, $\sigma_t \equiv \frac{d\sigma_t}{d\Omega^*}$ and $\sigma_{et} \equiv \frac{d\sigma_{et}}{d\Omega^*}$ for simplicity.

Thanks to the fact that ϕ^* dependency appears explicitly in the cross section, one can see that the symmetry with respect ϕ^* of the terms A_e, A_t and A_{et} is well defined

$$\begin{aligned} A_e(\phi^*) &= -\,A_e(-\phi^*) \\ A_t(\phi^*) &= -\,A_t(-\phi^*) \\ A_{et}(\phi^*) &= A_{et}(-\phi^*) \end{aligned} \tag{1.19}$$

1.2 Multipoles

The cross section for electro-production can also be written as a combination of Legendre Polynomials and their 1st and 2nd derivatives. The coefficients of this expansion are the multipoles: $E_{l\pm}$,$M_{l\pm}$ and $S_{l\pm}$ [2]. The multipoles characterize the excitation mechanism (electric (E), magnetic (M) and coulomb or scalar(S) type of photon) and the angular momentum of the final state πN. $l\pm$ refers to a state with a πN relative angular momentum l and total angular momentum $J = l \pm \frac{1}{2}$.

When a particular reaction with definite angular momentum and parity is considered, the number of multipoles that contribute are limited due to parity and angular momentum conservation. In the case of the $\Delta(1232)$ excitation for example, which has $J^P = \frac{3}{2}^+$, the only possible multipoles contributing are E_{1+}, M_{1+} and S_{1+}. The reason is the following: for conservation of the total angular momentum we have $J_\Delta = \frac{3}{2} = l \pm \frac{1}{2}$ and therefore the possible values for l are $l = 1, 2$. Parity conservation gives $P_\Delta = 1 = P_N \times P_\pi \times (-1)^l = (+1) \times (-1) \times (-1)^l$, which is only true for $l = 1$. The transition amplitude of the excitation of the $\Delta(1232)$ can also be expressed as a function of magnetic dipole $M1$, electric quadrupole $E2$ and the coulomb quadrupole $C2$. In this case the multipoles MJ_γ, EJ_γ and CJ_γ again indicate the type of photon (M, E, C) and the total angular momentum of the photon $\vec{J_\gamma}$[3]. Conservation of angular momentum and parity arguments again imply that only $M1$, $E2$ and $C2$ contribute for the $\Delta(1232)$ resonance production. From momentum conservation $J_\Delta = \frac{3}{2} = J_\gamma \pm \frac{1}{2}$ and therefore $J_\gamma = 1, 2$ and conservation

[3]Note that $\vec{J_\gamma} = \vec{S_\gamma} + \vec{L_\gamma}$ where $\vec{S_\gamma} = 1$ is the spin of the photon and $\vec{L_\gamma}$ is the orbital angular momentum relative to the initial nucleon.

of parity gives

$$P_\Delta = (+1) = P_N \times P_\gamma = \begin{cases} (-1)^{J_\gamma+1} & \text{if M } \rightarrow \mathrm{J}_\gamma = 1 \\ (-1)^{J_\gamma} & \text{if C, E } \rightarrow \mathrm{J}_\gamma = 2 \end{cases}$$

which is true only for $M1$, $E2$, $C2$.

It is worth to point out that the multipoles $E2$, $M1$, $C2$ and E_{1+}, M_{1+}, S_{1+} are not the same, but there is a connection between them. E_{1+}, M_{1+}, S_{1+} are complex numbers, defined at every value of W and they become purely imaginary at the resonance pole $W = W_R$. $E2$, $M1$, $C2$ are defined only at the resonance and they are real numbers. The relationship between the two is [3]

$$\begin{aligned} M1 &= \mathrm{ImM_{1+}(W_R)A_\Delta} \\ E2 &= \mathrm{ImE_{1+}(W_R)A_\Delta} \\ C2 &= \mathrm{ImS_{1+}(W_R)A_\Delta} \\ A_\Delta &= \sqrt{\frac{8\mathrm{M_\Delta q}\pi\Gamma}{3\mathrm{MK_C}}} \end{aligned} \tag{1.20}$$

In the non-relativistic Constituent Quark Model (CQM) the Δ^+ is obtained with a quark spin-flip in the nucleon, same orbital momentum $L_\Delta = 0$, and therefore only $M1$ is non zero because an operator with $L_\gamma > 0$ cannot connect two states with angular momentum equal to zero ($L_{nucleon} = L_\Delta = 0$). The hyperfine interaction introduces a small $L_\Delta = 2$ component, so E2, C2 are non zero as well, but the dominance of the $L_\Delta = 0$ component still gives a very small ratio E_{1+}/M_{1+}.

The relationship between the cross section and the multipoles can be found using the expansion in multipoles of the CGLN amplitudes [1]

$$
\begin{aligned}
F_1 &= \sum_{l=0}^{\infty}[lM_{l+} + E_{l+}]P'_{l+1}(x) + [(l+1)M_{l-} + E_{l-}]P'_{l-1}(x) \\
F_2 &= \sum_{l=1}^{\infty}[(l+1)M_{l+} + lM_{l-}]P'_{l}(x) \\
F_3 &= \sum_{l=1}^{\infty}[E_{l+} - M_{l+}]P''_{l+1}(x) + [M_{l-} + E_{l-}]P''_{l-1}(x) \\
F_4 &= \sum_{l=2}^{\infty}[M_{l+} - E_{l+} - M_{l-} - E_{l-}]P''_{l}(x) \\
F_5 &= \sum_{l=0}^{\infty}[(l+1)L_{l+}P'_{l+1}(x) - lL_{l-}P'_{l-1}(x)] \\
F_6 &= \sum_{l=1}^{\infty}[lL_{l-} - (l+1)L_{l+}]P'_{l}(x)
\end{aligned}
\tag{1.21}
$$

where the longitudinal amplitudes $L_{l\pm}$ are related to the scalar amplitudes $S_{l\pm}$ by

$$\omega S_{l\pm} = |\vec{q}|L_{l\pm} \tag{1.22}$$

1.3 The Δ(1232) resonance

The formalism described in the previous section is valid for electro-production in general and therefore at any value of the invariant mass W. The object of this analysis is to study the Δ(1232) resonance and therefore the asymmetries in the W range around 1.232 GeV/c^2. The Δ(1232) resonance which is the lowest nucleon excitation, has always had a privileged position in experimental physics for several reasons. First it is the most accessible resonance because it does not strongly overlap with any other states, and second it decays strongly only via single pion emission.

The Δ(1232) has spin $J = \frac{3}{2}$, and isospin $I = \frac{3}{2}$. In the CQM, it belongs to the decuplet (flavor symmetric) of the $3 \otimes 3 \otimes 3$ decomposition in SU(3) and in particular Δ^+ and Δ^0 are the proton and neutron quark spin flip excitations. The CQM manages to explain the many features of the baryon and meson spectra by simply postulating 3 flavors of quarks u, d, s with charge 2/3, -1/3, -1/3 respectively, approximately satisfying SU(3) symmetry. Although SU(3) is already broken because of different quark masses, the CQM actually is based on a higher symmetry, SU(6), where quark flavors are considered also with their spins. For baryons we have the super multiplets $6 \otimes 6 \otimes 6 = 56_S \oplus 70_{MS} \oplus 70_{MA} \oplus 20_A$ where S (symmetric), MS (mixed symmetric), MA (mixed antisymmetric), A (antisymmetric) denote the symmetry of the (flavor)×(spin) wave function. The proton, neutron, and the $\Delta(1232)$, all belong to the 56_S multiplet. Many corrections and improvements have been made to the CQM [4] in order to predict the right energy splitting within the same multiplet. For example the Isgur-Karl model [5, 6] adds a quark-quark hyperfine interaction that causes splitting between the nucleon and $\Delta(1232)$ mass. This hyperfine interaction introduces also an orbital angular momentum $L = 2$ component. However, even taking into account relativistic effects this model becomes inadequate at higher Q^2. At very high Q^2, when the strong coupling constant α_s becomes small, one can apply perturbative Quantum Chromodynamics (pQCD). QCD is the theoretical framework of the strong interaction at any Q^2, however QCD becomes very difficult to apply in the non-perturbative domain (low Q^2). Instead one can use in this transition region between CQM and pQCD *effective field theories*. However, these models are not a fundamental theory, since the basic degrees of freedom are the hadrons, which are themselves composites.

The intermediate energy region is of great interest because the two limits (high and low Q^2) often give very divergent predictions and therefore a transition is expected. An example is the ratio of the multipoles E_{1+}/M_{1+} for the electroproduction of the $\Delta(1232)$: $\gamma_v + N \to \Delta \to N + \pi$ where γ_v is the exchanged virtual photon. In the CQM this ratio is predicted to be very small, while, in the limit $Q^2 \to \infty$, the ratio $E_{1+}/M_{1+} \to 1$, because of the helicity conserving properties of QCD [7]. Many experiments have been performed in order to measure this ratio. The current results [8, 9] show that the ratio remains small up to $Q^2 = 4$ GeV$^2/c^2$, implying that if this transition to the QCD predicted value occurs, it does so at a higher value of Q^2.

The characteristics of the $\Delta(1232)$ in terms of multipoles were described in section 1.2. In the next subsection a few considerations regarding the asymmetries in the $\Delta(1232)$ region will be presented.

1.3.1 Asymmetries in the Δ(1232) region

In section 1.1 and 1.2 it was shown that the cross section can be written in terms of CGLN functions, which can be expanded in multipoles. In the $\Delta(1232)$ region the expansion can be truncated at $l = 1$ and it can also be assumed that the multipole M_{1+} is dominant. These two assumptions simplify the form and the interpretation of the asymmetries. As an example consider the asymmetry A_e which has at the numerator σ_e. As seen in equation 1.17, σ_e is proportional to just one response function, $R^0_{TL'}$. This response function in terms of the CGLN amplitudes is

$$\begin{aligned} R^0_{TL'} = &-\sin\theta^* \mathrm{Im}\{F_2^* F_5 + F_3^* F_5 + F_1^* F_6 + F_4^* F_6 \\ &+ \cos\theta^* (F_4^* F_5 + F_3^* F_6)\} \end{aligned} \tag{1.23}$$

The simplified expressions under the above assumptions for the CGLN amplitudes are:

$$\begin{aligned} F_1 =& 3\cos\theta^* M_{1+} \quad F_2 = 2M_{1+} \quad F_3 = -3M_{1+} \\ F_4 =& 0 \quad F_5 = 6\cos\theta^* L_{1+} + L_{0+} \quad F_6 = L_{1-} - 2L_{1+} \end{aligned} \tag{1.24}$$

Replacing equations 1.24 in equation 1.23 one obtains

$$R^0_{TL'} = \sin\theta^* \mathrm{Im}\{-M^*_{1+}(6\cos\theta^* L_{1+} - L_{0+})\} \tag{1.25}$$

which shows that the term σ_e is non-zero only because of the interference of the $\Delta(1232)$ with the non-resonant background multipoles. For a pure M_{1+} resonance $R^0_{TL'}$ is zero. For this reason the asymmetry A_e is expected to be very small compared to the others.

The other asymmetries, A_t and A_{et} do not have such a simple interpretation. They depend on many response functions. However one can notice that they contain terms such as R^0_{TT} and $R^0_{TT'}$, which in turn depend on $|M_{1+}|^2$ and are therefore not small.

1.4 Models

At intermediate energies ($E < 4$ GeV) it is not yet possible to use pQCD. A possible phenomenological approach is to use effective field theories which can also help to separate the interesting physics from the background. Three models were considered for this work: the Effective Lagrangian model by R. Davidson and N. Mukhopadhyay, the Mainz unitary isobar model (MAID2000 and MAID98) and the dynamical model by T. Sato and H. Lee. These models will be briefly described in the following subsections.

1.4.1 Effective Lagrangian model

The Effective Lagrangian theory is an effective field theory developed by the theory group at RPI [10, 11, 12]. It is a model for electro-production that takes as the fundamental degrees of freedom the hadrons, i.e. the baryons and mesons, rather than the fundamental quarks and gluons. This is in recognition that we have not yet been able to solve the fundamental QCD structure of hadrons well enough to test against the data we propose to measure. The Feynman diagrams that are included in the Effective Lagrangian model are the contact term, the non resonant background and the production of the resonances themselves (see Figure 1.3). The last two terms are not completely known, and to describe them seven free parameters are introduced. The effective Lagrangian approach of Davidson and Mukhopadhyay fits the existing unpolarized data from the pion production threshold up to $W = 1.3$ GeV/c^2. Once the seven parameters are determined, other variables, like the asymmetries, can be predicted.

1.4.2 MAID2000 and MAID98

The MAID model is a unitary isobar model developed in Mainz which describes the cross section up to the third resonance region($P_{33}(1232)$, $P_{11}(1440)$, $D_{13}(1520)$, $S_{11}(1535)$, $F_{15}(1680)$ and $D_{33}(1700)$) [13]. Similarly to the Effective Lagrangian model, MAID is a phenomenological fit to previous photo- and electro-production data. The resonances are assumed to have Breit-Wigner forms, while the background is described using the Born terms and the t-channel vector-meson exchange (see

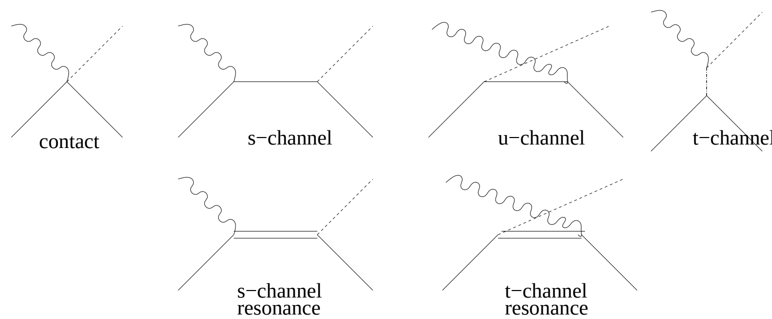

Figure 1.3: Feynman diagrams for the terms included in the Effective Lagrangian model.

first four diagrams in Figure 1.3). The πNN coupling in the Born terms is of mixed pseudo-scalar and pseudo-vector form. The final amplitude is unitarized. The Born terms are well known in the sense that the various couplings can be extracted by non-electro-production experiments and then tested against the results of analysis of photo- or electro-production data. The resonant contributions are determined by a direct fit of the existing photo- and electro-production data. One of the parameters extracted from data is the multipole $M_{1+}(Q^2)$, while E_{1+} and S_{1+} are just assumed to have the same Q^2 dependence as M_{1+} due to little experimental information available. This means that the ratio E_{1+}/M_{1+} is kept constant in the region of validity of the model.

There are two solutions of MAID: MAID98 and MAID2000 (or MAID2001), which differ in the way the unitarization is carried out. For MAID2000 a K-matrix approach is used. The two solutions turn out to be very similar for the $\Delta(1232)$ region.

1.4.3 Sato-Lee Model

The Sato-Lee model is a dynamical approach, which solve scattering equations with interactions defined by an effective Hamiltonian [14, 15, 16]. This model considers specifically the $\Delta(1232)$ production, as compared to the MAID models which describe more resonances.

The Hamiltonian after a unitary transformation is written as a sum of five

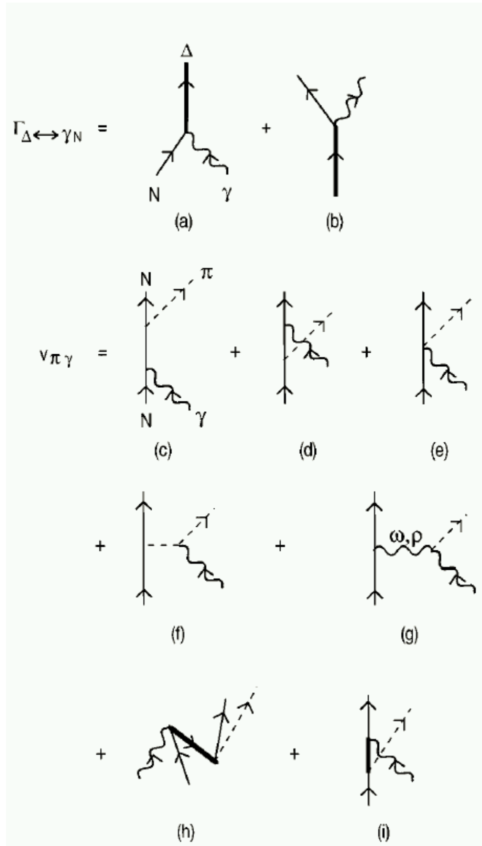

Figure 1.4: Graphical representation of the interactions $\Gamma_{\gamma N\leftrightarrow\Delta}$ and $v_{\gamma\pi}$.

terms:

$$\mathcal{H}_{eff} = \mathcal{H}_0 + v_{\pi N} + v_{\gamma\pi} + \Gamma_{\pi N\leftrightarrow\Delta} + \Gamma_{\gamma N\leftrightarrow\Delta} \tag{1.26}$$

where $\mathcal{H}_0$ is the free Hamiltonian, $v_{\pi N}$ is a non resonant πN potential, $v_{\gamma\pi}$ describes a non resonant $\pi N \leftrightarrow \gamma N$ transition and $\Gamma_{\pi N\leftrightarrow\Delta}$ and $\Gamma_{\gamma N\leftrightarrow\Delta}$ describe the $\Delta(1232)$ excitation for the $\pi N \leftrightarrow \Delta$ and $\gamma N \leftrightarrow \Delta$ transitions, respectively. Figures 1.4(a) and (b) are a graphical representation of the effective interaction $\Gamma_{\gamma N\leftrightarrow\Delta}$, while (c) through (i) show the non resonant background contributions, which include the Born terms (c) and (d), the contact term (e), the pion (f) and vector meson exchange (g), the anti-Δ component of the Δ propagation (h) and the Δ-exchange term (i). Figures 1.5(a) and (b) are a graphical representation of the effective interaction $\Gamma_{\pi N\leftrightarrow\Delta}$, while (c) through (g) represent the non resonant πN potential, $v_{\pi N}$. From this Hamiltonian a set of coupled equations for πN and γN reactions and then a pion

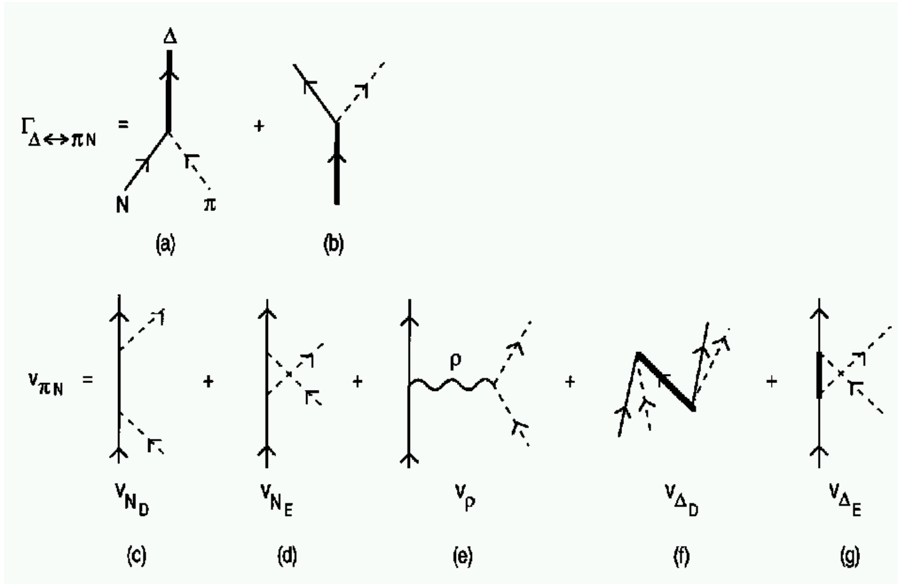

Figure 1.5: Graphical representation of the interactions $\Gamma_{\pi N \leftrightarrow \Delta}$ and $v_{\pi N}$.

photo-production amplitude $T_{\gamma\pi} =< \pi N|\vec{\epsilon} \cdot \vec{J}|\gamma N >$ are derived ($\vec{J}$ is the current operator and $\vec{\epsilon}$ is the photon polarization). This amplitude can be decomposed into two parts

$$T_{\gamma\pi} = t_{\gamma\pi} + \overline{\Gamma}_{\pi N \leftrightarrow \Delta} G_\Delta(E) \overline{\Gamma}_{\gamma N \leftrightarrow \Delta} \tag{1.27}$$

where $t_{\gamma\pi}$ is the non resonant transition amplitude and $\overline{\Gamma}_{\pi N \leftrightarrow \Delta} G_\Delta(E) \overline{\Gamma}_{\gamma N \leftrightarrow \Delta}$ is the amplitude which involves the Δ production. In the second part $G_\Delta(E)$ is the Δ propagator and $\overline{\Gamma}_{\pi N \leftrightarrow \Delta}$ and $\overline{\Gamma}_{\gamma N \leftrightarrow \Delta}$ are the *dressed* vertices, i.e. vertices which contains all the higher order processes. Without describing these terms in details (a detailed description can be found in [14, 15]), one can intuitively understand that this kind of approach takes into account explicitly 'all' the second orders diagrams for the Δ production. In this respect the model is very different from MAID and the Effective Lagrangian, where the Δ is described by just one diagram. The consequence is a difference in what is called "Δ" in the two models: for Sato-Lee Δ is just given by the *bare* diagram, for MAID is implicitly the sum of all the possible processes which result in a resonant amplitude in the data. From a practical point of view this fact does not have any consequences as long as one compares MAID results with the dressed Δ ones. However the model of Sato and Lee has some interesting developments. For example in an analysis of data done by Sato and Lee helicity amplitudes for the bare $\gamma N \to \Delta$ were extracted and they were found in agreement with the predictions of the constituent quark model [15].

CHAPTER 2
EXPERIMENTAL SET-UP

Experiment E-94-003, object of the present thesis, took place at Hall B of the Thomas Jefferson National Accelerator Facility (TJNAF). TJNAF is equipped with three experimental Halls which have detectors designed for complementary studies. While Hall A and Hall C have high resolution spectrometers ($\Delta p/p \sim 10^{-4}$), Hall B houses the CEBAF Large Acceptance Spectrometer (CLAS) with lower resolution ($\Delta p/p \sim 0.5 - 1\%$) but with the possibility of detecting many particles in the final state.

Experiment E-94-003 belongs, together with other four experiments, to the so called EG1 run which is characterized by having polarized electron beam and a dynamically polarized target inserted in CLAS. The first part of the EG1 run took place in the Fall of 1998. This thesis is based on data taken in this first period. The EG1 run was resumed and concluded in 2000-2001 adding a factor 10 of data to the one taken in 1998. In the following sections the experimental apparatus will be described.

2.1 The accelerator and the polarized electron beam

The Jefferson Laboratory's Continuous Electron Beam Accelerator Facility (CEBAF) is a pair of antiparallel superconducting radiofrequency (srf) linacs with a 45 MeV srf injector, capable of simultaneous delivery to three end stations of continuous wave (cw) beams of up to 200 μA with 75% polarization, geometric emittance less than 10^{-9} mrad, and relative momentum spread of 2.5×10^{-5}. The lowest operating energy is about 0.6 GeV, the present full energy nearly 6 GeV, and an upgrade to 12 GeV is planned [17]. The linacs are connected by recirculation beam lines with a total beam line length of over 4.5 km. Figure 2.1 shows a schematic view of the accelerator. The beams delivered to the three experimental halls can be at different energies, currents and with a specified orientation of the polarization allowing different experimental programs at the same time. The average current is $1-100\ nA$ for Hall-B and $1-150\ \mu A$ for Hall-A and Hall-C. The beam is

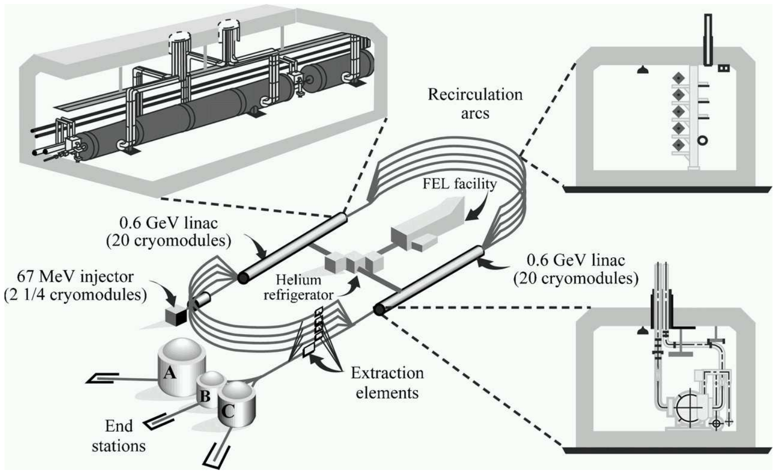

Figure 2.1: Schematic view of CEBAF site.

polarized using polarized laser light incident on a "strained" gallium arsenide photocathode [18]. Linearly polarized laser light is passed through the Pockels cell, an electro-optical crystal which converts the polarization from linear to circular. The voltage applied to the Pockels cell determines the helicity of the light and allows the rapid pseudo random switching of the electron beam polarization. The circularly polarized light is directed onto a GaAs photocathode, inducing electron transitions from the valence band to the conduction band. The frequency of light is chosen to preferentially pump specific electron spin transitions, resulting in a net polarization in the conduction band. A mono-layer of cesium and fluorine applied to the surface of the crystal produces a vacuum energy level outside the material which is less than the energy minimum of the conduction band. The electrons are released from the conduction band and accelerated by a 100kV cathode and injected into one of the linacs with an injection energy of approximately 45 MeV.

Beam was delivered to all 3 halls with a fixed helicity for a period of 500 ms, then with reversed helicity for the next 500 ms. After this "helicity pair" (of 1 second duration) the next helicity was chosen at random, again followed by the opposite helicity and so on. With this method possible systematic errors in the polarization are eliminated.

The polarization of the beam was measured with a Møller Polarimeter which is located upstream of the polarized target. The polarimeter is constructed from two foils which can be polarized parallel or antiparallel to the spin of the incoming beam. Two quadrupole magnets guide the scattered electrons to two scintillating fiber detectors located symmetrically on the two sides of the beamline. By measuring the asymmetry between aligned and anti-aligned incoming electrons it is possible to extract the beam polarization. The average polarization obtained during the EG1 run was 70%.

Because the polarization of the target can be destroyed by high currents, the current delivered to the experiment was 2 nA, lower than the one that is usually used in CLAS unpolarized experiments. For the same reason the beam was also rastered in a spiral pattern of $1 - 1.2$ cm over the surface of the target.

2.2 The CLAS detector

The CEBAF Large Acceptance Spectrometer (CLAS) is a nearly 4π detector in Hall-B [19]. The large azimuthal acceptance and the θ coverage up to 140° allows the detection of multi-particle final states and the study of resonances in a broad and continuous range of momentum transfer Q^2.

Figure 2.2(a) shows a schematic section along the beam line of CLAS in which the placement of the various detector parts is displayed. Figure 2.2(b) shows a section through the target position perpendicular to the beam line direction. As can be seen CLAS is divided in sectors by six superconducting coils which generate a toroidal magnetic field. Each of the six individually instrumented sectors contains three regions of drift chambers (DC), a Čerenkov detector (CC), scintillators (SC) and an electromagnetic calorimeter (EC). In addition, two sectors are equipped with a Large Angle Calorimeter (LAC) which extends the coverage up to 90° as compared to the forward calorimeters which cover angles from 10° to 45°.

In the following subsections each part of the detector components will be described in detail.

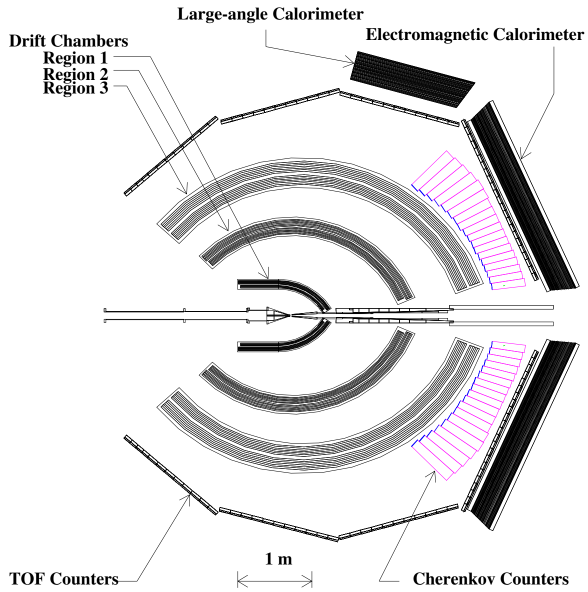

(a) Horizontal section along the beam line

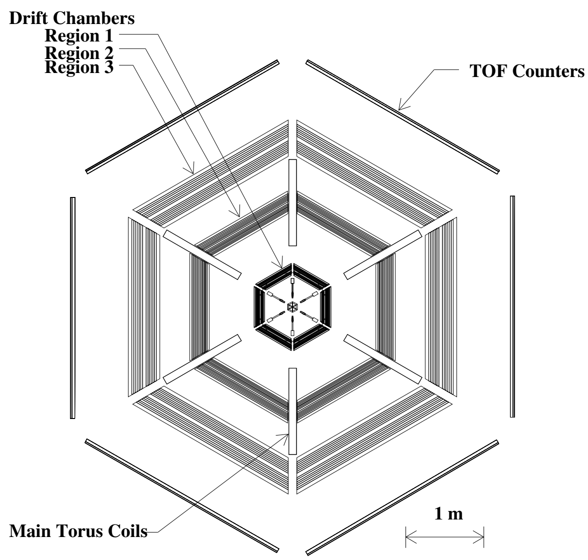

(b) Section through the target position normal to the beam line

Figure 2.2: A schematic diagram of the CLAS detector.

2.2.1 The torus magnet

The toroidal magnetic field is generated by six superconducting coils with a maximum current of 5×10^6 A (see Figure 2.3) [19]. The shape of the coils is such that the field is greater in the forward direction guaranteeing a good resolution in momentum for high energy particles which have low θ angles (see Figure 2.4). The

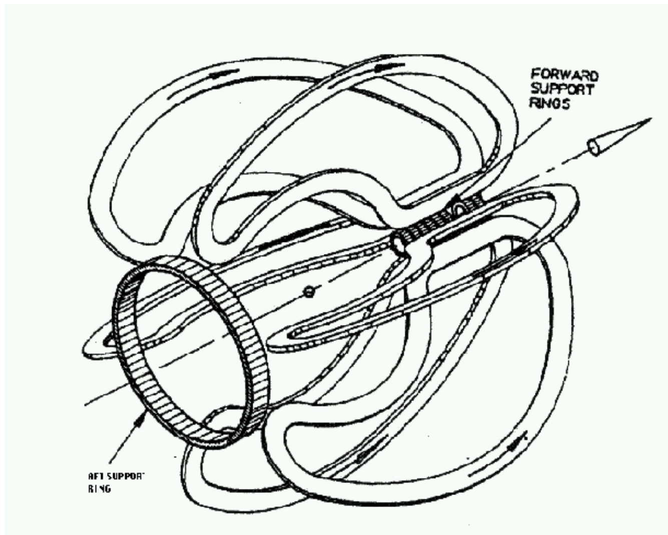

Figure 2.3: The torus magnet in CLAS.

intensity of the field goes from 0.4 T at $\theta = 90°$ to 2 T at $\theta = 15°$.

On one hand the non-uniformity of field makes the trajectory reconstruction more difficult, on the other hand a toroidal field is always transverse to the particle motion and therefore the determination of ϕ, which is preserved throughout the trajectory, is decoupled from the measurement of θ and the momentum. The toroidal field also has the advantage of providing a field free region along the beamline and therefore does not interfere with the solenoidal field in case of polarized target experiments.

2.2.2 The drift chambers

The measurement of particle trajectories is done by means of the drift chambers. This system is simply based on the fact that charged particles traveling through a gas ionize the atoms. If the gas is placed in an electric field the electrons and ions

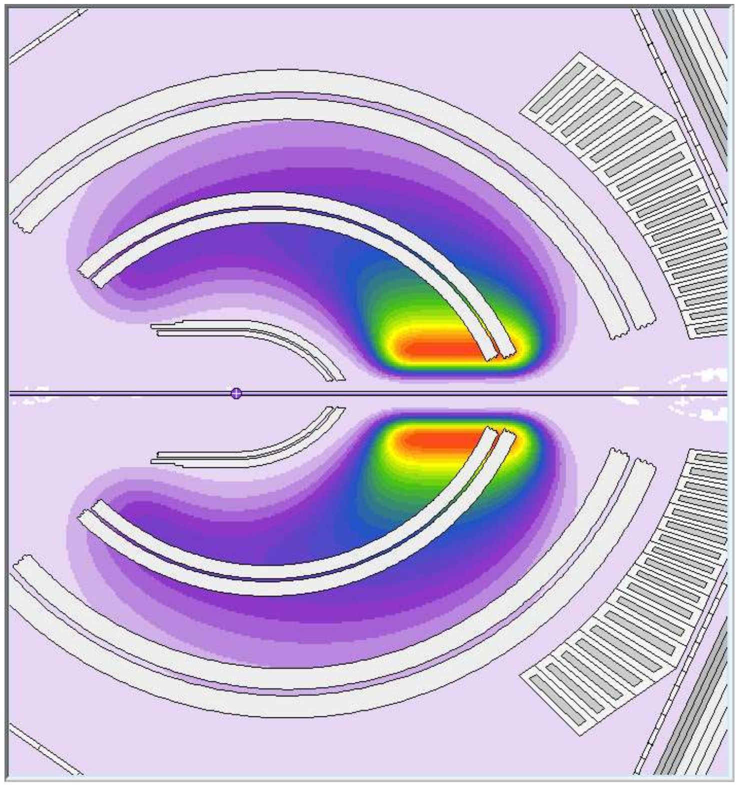

Figure 2.4: Magnetic field generated by the torus magnet.

drift in opposite directions and are collected by the anode and the cathode, respectively. The measurement of the anode current gives information on where the ionization occurred.

In CLAS there are 18 separate drift chambers, 3 for each sector placed at different radial distances (see Figure 2.2) [20]. The first region (R1) is surrounding the target in an area where the magnetic field is low. The second region (R2) is located between the torus coils in an area where the field is maximum. The third region (R3) is the largest and is placed outside the coils. Each region is divided into two *superlayers*, one with wires parallel to the direction of the magnetic field and one with wires tilted at a 6° stereo angle with respect to the previous ones. Each superlayer consists of six layers of *drift cells*, except for R1, which has only four due to space limitations. A drift cell is a hexagonal cylinder formed by six *field* wires and a *sense* wire in the middle. Figure 2.5 shows a section along the beam line of a part of region 3. A layer of guard wires surrounds the perimeter of each superlayer adjusted to reproduce the electric field configuration given by an infinite grid of hexagonal cells. The gas used is a 90%-10% mixture of Argon and CO_2 which allows for reasonably low multiple scattering and short collection times.

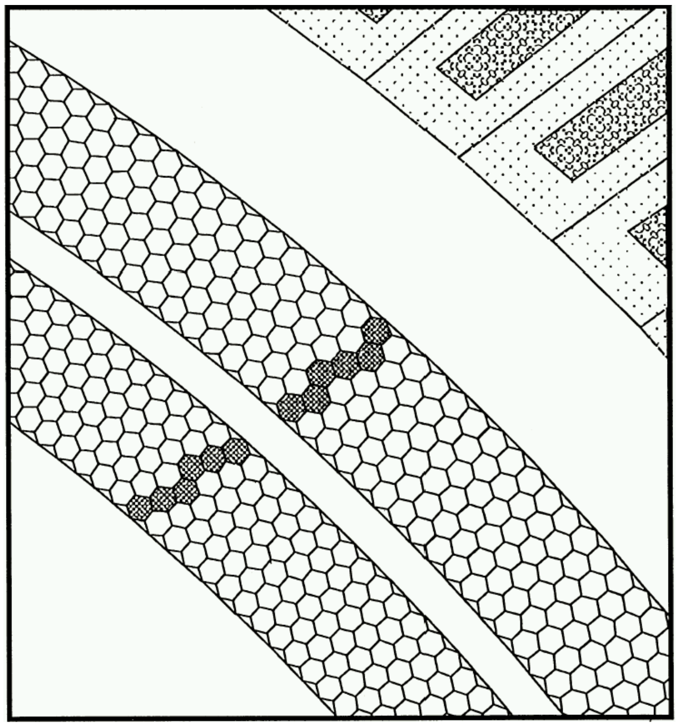

Figure 2.5: Representation of a portion of R3 showing the layout of its superlayer. The sense wire are at the center of each hexagon and the field wires are at the vertices. The darker cells correspond to a passing charged particle. In the upper corner a part of the Čerenkov detector appears.

2.2.3 The Čerenkov counters

The Čerenkov detector is used to discriminate electrons from pions and for the online trigger. A charged particle, traversing a medium with refractive index n exceeding the velocity of light in that medium, emits a characteristic electromagnetic radiation called Čerenkov radiation. The Čerenkov radiation is emitted because the charged particle polarizes the atoms along its track so that they become dipoles. The time variation of the dipole field leads to electromagnetic radiation. If $v < c/n$ the dipoles are arranged symmetrically around the particle's track, so that the dipole field integrated over all the dipoles vanishes. If $v > c/n$ the symmetry is broken and there is radiation. The Čerenkov counters, taking advantage of this effect, are filled with a medium such that the energy threshold for electron is much lower than the one for pions.

The CLAS Čerenkov counters [21] are filled with perfluorobutane C_4F_{10} which has a refraction index $n = 1.00153$. The threshold in energy to have radiation is then $E_t > \gamma m_0$ with $\gamma = 18.089$ and where m_0 is the mass of the particle. Therefore for electrons $E_t = 9.2$ MeV while for pions $E_t = 2.5$ GeV. The Čerenkov light is collected by a system of mirrors and focused toward photomultiplier tubes. Due to the toroidal configuration of the magnetic field, for which the particle trajectories lie on $\phi = const$ planes, the Čerenkov detectors are designed to focus light in the ϕ direction. Each sector is divided in 18 θ regions covering up to $\theta = 45°$. Each θ segment is divided in two modules symmetric with respect to the mid-sector plane. Each segment consists of an elliptical mirror, a hyperbolic mirror and a photomultiplier tube which is placed at the side of the sector in the region shadowed by the superconducting coils. Figure 2.6 schematically shows the optical arrangement of each segment.

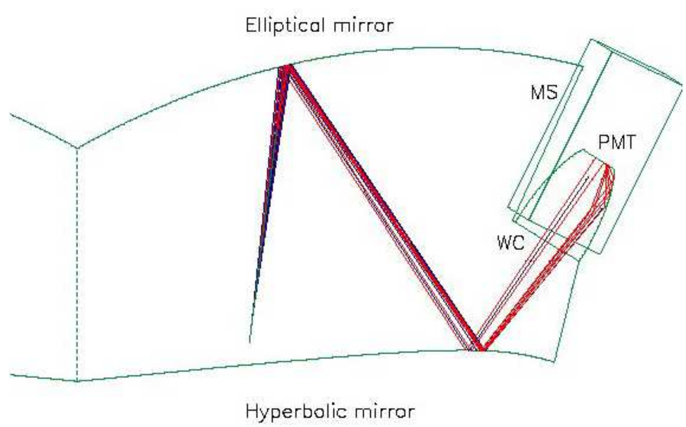

Figure 2.6: Optical arrangement of one segment of the Čerenkov Detector, showing the optical and light collection components.

2.2.4 The Time of Flight detector

The Time Of Flight (TOF) detector consists of a set of scintillators placed after the third region of the drift chambers and oriented approximately perpendicular to the track of the scattered particle [22]. Like the Čerenkov detector the non-active parts i.e. the photomultipliers, are placed in the regions obscured by the magnet coils.

There are 288 scintillator strips which overall cover up to $\theta = 140°$. Each strip is connected to 2 photomultiplier tubes, is 5 cm thick and has an angular coverage of 2°. The time and pulse height are measured for each photomultiplier. Figure 2.7 shows the scintillator arrangement for one sector.

The TOF is used to measure the time for a particle to travel from the target to the scintillators. This information together with the drift chamber measurements are crucial for the particle identification. The time resolution at small angles is 120 ps while at angles greater than 90° it is 250 ps. This resolution allows a good separation between kaons and pions up to energies of 2 GeV.

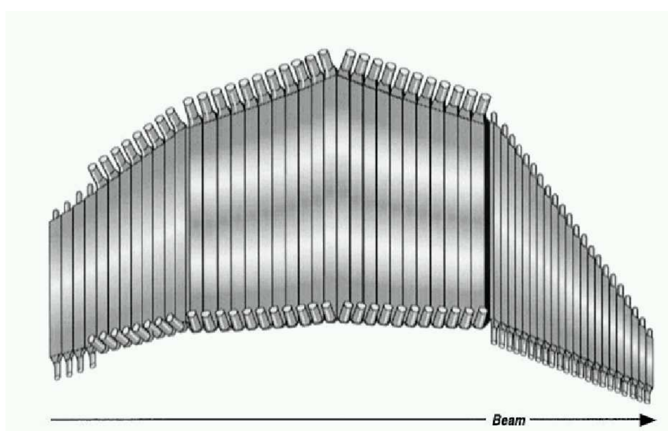

Figure 2.7: One sector of the Time-of-Flight counters.

2.2.5 The electromagnetic calorimeter

The electromagnetic calorimeter is used to identify particles through the measurement of the energy deposited in matter. The dominating interaction processes in the MeV energy range are photoelectric effect and Compton scattering for photons and excitation for charged particles. At high energies (GeV range) electrons lose their energy almost exclusively by bremsstrahlung and photons by electron-positron pair production. The sequence of these two processes results in an electromagnetic shower which can be detected by means of scintillators. Heavier particles such as pions lose their energy mainly by ionization which give signals distinctly different from the ones by electrons and photons.

CLAS is equipped with 6 modules of electromagnetic calorimeters which cover θ angles from $10°$ to $45°$, called Forward Angle Calorimeter (EC) [23], plus 2 modules in the first and second sector which cover from $50°$ to $75°$ called Large Angle Calorimeter (LAC). In this section only the forward detector will be described, however a full description of the LAC can be found in [24].

The forward calorimeter is designed for the detection and triggering of electrons with energies above 0.5 GeV, detection of photons at energies above 0.2 GeV allowing π^0 and η reconstruction from the measurement of their 2γ decays and the detection of neutrons which can be discriminated from photons using time-of-flight measurements.

The forward detector is made of alternating layers of scintillator strips and lead sheets with a total thickness of 16 radiation lengths. The EC is located after the TOF, and to respect the hexagonal structure of CLAS, consists of six volumes whose layers have the shape of an equilateral triangle. The area of each successive layer increases and the resulting volume is a truncated triangular pyramid with the projected vertex at the CLAS target point. This shape minimizes the shower leakage at the edges and minimizes the dispersion in arrival times of signals originating in different layers. There are 39 layers in the "sandwich" each one consisting of a 10 mm scintillator and a 2.2 mm lead sheet. Each scintillator layer is made of 36 strips parallel to one side of the triangle. The next scintillator layer has the strips parallel to another side and therefore is rotated by $120°$ with respect the previous one. Figure 2.8 shows the three orientations for three consecutive layers. The calorimeter is subdivided into an inner stack of 15 layers and an outer one of 24 layers to provide longitudinal sampling of showers. Overall the calorimeter has 8424 scintillator strips and 1296 photomultipliers. This construction results in approximately 0.27 of the energy of the scattered electron to be deposited in the scintillator.

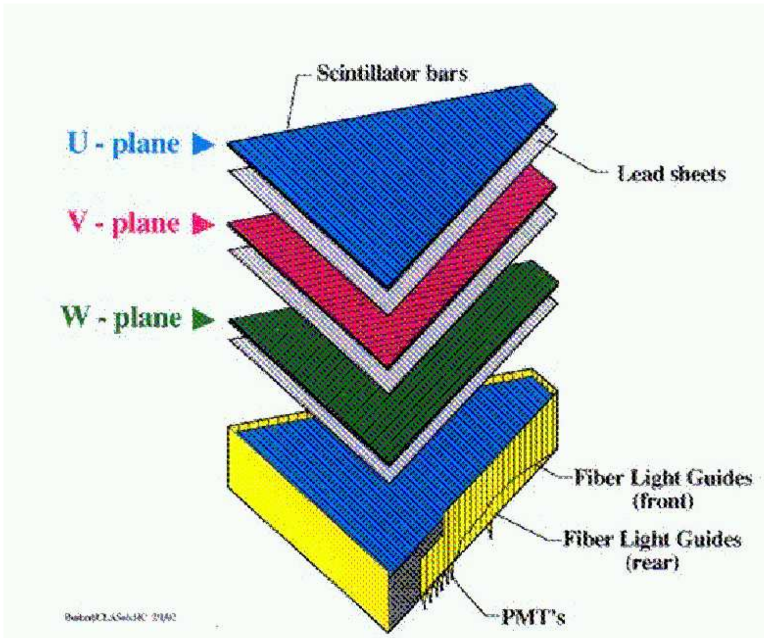

Figure 2.8: Exploded view of one of the six CLAS electromagnetic calorimeters modules.

2.3 The polarized target

The polarized target used for the experiment was a solid $^{15}NH_3$ target. The method used to polarize the target is Dynamic Nuclear Polarization (DNP) [25, 26, 27, 28]. With this method a proton polarization of about $80 - 90\%$ can be achieved. The actual polarization during the experiment was about 70% for positive polarization and about 60% for the opposite direction. The polarization of the target was monitored during data taking by using nuclear magnetic resonance (NMR).

The EG1 target was characterized mainly by the following components:

- Two superconducting Helmholtz coils housed inside a steel container which holds liquid helium at 4 K. This container is used to cool the coils to superconducting temperatures. The coils generate a strong uniform ($\frac{\Delta B}{B} = 10^{-4}$)

field of 5 T. The coils and the container limit the acceptance by allowing only the detection of particles with $\theta < 50°$ and $|\theta - 90°| < 17°$.

- A Helium-4 refrigerator system to keep the target material at the temperature of 1 K.
- A microwave system for the DNP.
- A target insert, which consists of an aluminum structure which holds four target cells. This structure is connected to a step motor which allows one to move the targets in or out of the beam.

The resulting complex structure, shown in Figure 2.9, was completely inserted inside the first drift chamber region.

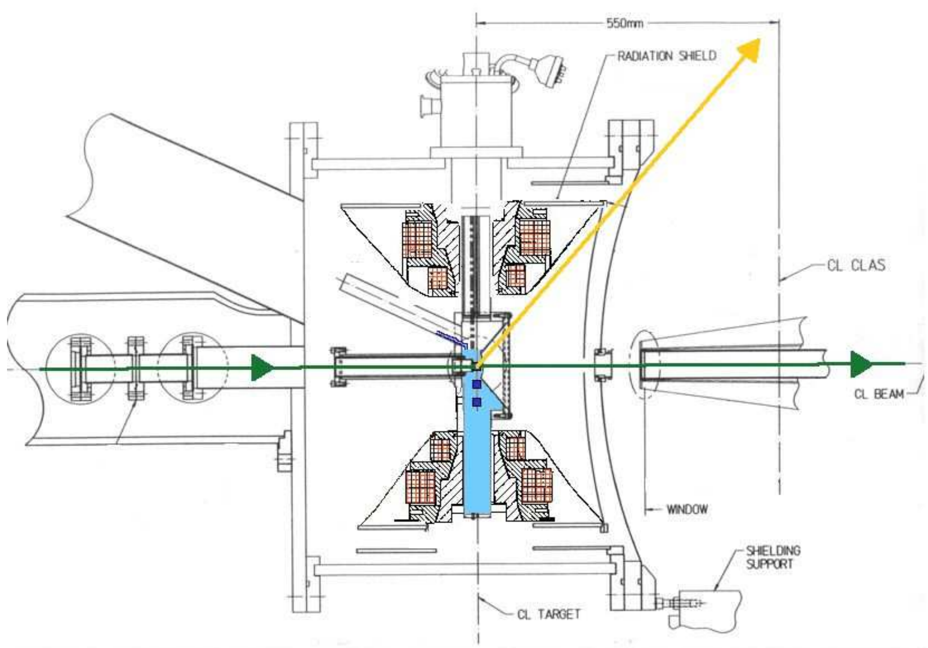

Figure 2.9: Polarized target.

The knowledge of the polarization is essential for the analysis. The value P_t was extracted from the data using the known asymmetry in the elastic region (see section 4.5). The measurement given by the NMR system was not used for several reasons. Firstly, the NMR has a non linear response in determining the polarization.

In addition systematic effects occur in subtracting the baseline from the signal of the NMR [41]. Finally the NMR coil has a non uniform sensitivity, in particular the signal is mainly determined by the polarization of the material close to the coil and it decreases like $1/r^6$ where r is the distance from the coil. This implies that possible depolarizations in the inner part of the target might not be detected, whereas the extraction from the data using the elastic asymmetry gives an accurate measurement of the target polarization as a whole.

In the following subsection the DNP and the target material will be described in more detail.

2.3.1 Dynamic Nuclear Polarization

The techniques used to polarize a system of nuclei or nucleons are based on the interaction of their magnetic moments with an external magnetic field in a low temperature environment.

The simplest technique would be to apply a constant magnetic field. In this condition a spin 1/2 particle gains a so called *thermal equilibrium polarization* which depends on the magnetic field intensity B and the temperature T as follows

$$P = \tanh(\frac{\mu B}{KT}) \tag{2.1}$$

where μ is the magnetic moment and K is the Boltzmann constant. However it is easy to calculate that a proton in a $B = 5\ T$ field and at $T = 0.01\ K$ will have a polarization $P = 47\%$, which is a fairly low value considering that $T = 0.01\ K$ is already a temperature hard to reach.

For this reason the more elaborate but more efficient method of Dynamic Nuclear Polarization (DNP) was developed. DNP is based on the interaction between nuclear species that have to be polarized and another species of spin more easily polarizable, contained in the material itself. In the case of $^{15}NH_3$ the species we want to polarize consists of the three free protons and the species easily polarizable consists of *paramagnetic centers.* A paramagnetic center is a localized region in the lattice with paramagnetic properties, such as free electrons, lattice vacancies or free radicals. These paramagnetic centers are produced by irradiating or doping the material and they are polarized by applying a strong solenoidal magnetic field of 5 T and keeping the material cryogenically at the low temperature of 1 K. If the paramagnetic centers are in adequate concentration and uniformly distributed in the material, a spin-spin interaction with the protons will occur. This interaction together with the fact that electrons interact with the lattice faster than protons are the crucial points for DNP, as will be explained in the next paragraph.

To explain the mechanism of DNP consider a system of protons and electrons, which have the same characteristics as the paramagnetic centers. The Hamiltonian in the case of a external magnetic field $\vec{B}$ applied to the system is

$$\mathcal{H} = \mathcal{H}_0 + \mathcal{H}_{Ze} + \mathcal{H}_{Zp} + \mathcal{H}_{dip} \tag{2.2}$$

where $\mathcal{H}_0$ is the free Hamiltonian for electrons and protons, $\mathcal{H}_{Ze}$ describes the interaction of the electrons and the magnetic field,

$$\mathcal{H}_{Ze} = -g_e \beta_e \vec{S} \cdot \vec{B} \tag{2.3}$$

$\mathcal{H}_{Zp}$ is the analogous one for the protons

$$\mathcal{H}_{Ze} = -g_p \beta_p \vec{I} \cdot \vec{B} \tag{2.4}$$

and $\mathcal{H}_{dip}$ is the dipole-dipole interaction between electrons and protons

$$\mathcal{H}_{dip} = \frac{1}{r^3}\left[\vec{\mu_e} \cdot \vec{\mu_p} - \frac{3(\vec{\mu_e} \cdot \vec{r})(\vec{\mu_p} \cdot \vec{r})}{r^2}\right] = \frac{1}{r^3} g_e g_p \beta_e \beta_p \left[\vec{I} \cdot \vec{S} - \frac{3(\vec{I} \cdot \vec{r})(\vec{S} \cdot \vec{r})}{r^2}\right] \tag{2.5}$$

where the following notation was used:

- $\vec{S}$ spin of the electron (dimensionless)
- $\vec{I}$ spin of the proton (dimensionless)
- $g_e = \frac{e\hbar}{2m_e}$ *Landé* factor for the electron
- β_e Bohr magneton
- $g_p = \frac{e\hbar}{2m_p}$ gyromagnetic factor for the proton

- β_p proton magneton
- $\vec{r}$ distance between electron and proton

The term $\mathcal{H}_{dip}$ can be seen as an interaction of the proton with the magnetic field generated by the electron $\mathcal{H}_{loc} = \frac{g_e|\beta e|}{r^3}$, which is typically of the order of $10^{-2}\ T$ and therefore small compared to the external field $\vec{B}$. For this reason the eigenstates of the previous Hamiltonian can be calculated considering first $\mathcal{H}_{Ze} + \mathcal{H}_{Zp}$ as a perturbation of $\mathcal{H}_0$ and then $\mathcal{H}_{dip}$ as a perturbation of $\mathcal{H}_0 + \mathcal{H}_{Ze} + \mathcal{H}_{Zp}$. The first perturbation creates the splitting of levels illustrated in Figure 2.10(a), which is known as Zeeman effect. The second perturbation causes a mixing of those levels as illustrated in Figure 2.10(b), where $\epsilon = \mathcal{H}_{loc}/\mathcal{H}_0$ describes the pure states mixtures.

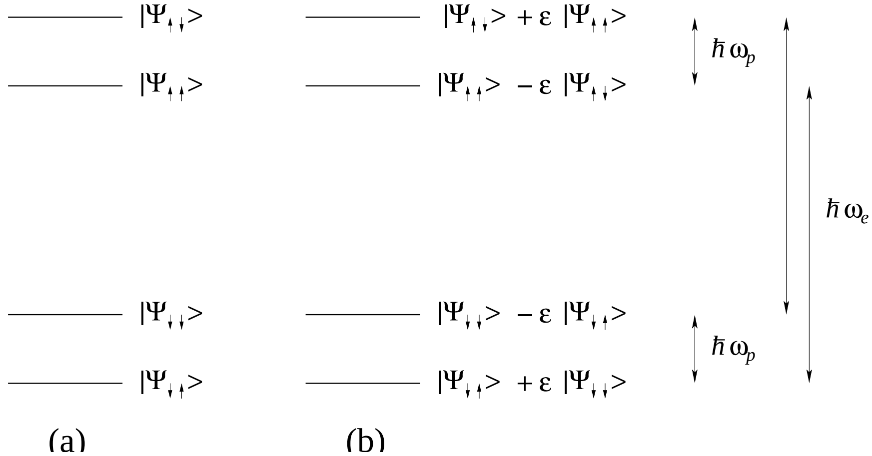

Figure 2.10: Levels for a system electron-proton in an external magnetic field *B*. The left and the right arrows represent the electron and the proton spin orientations, respectively. Figure(a) shows the splitting of the levels due to the terms $\mathcal{H}_{Ze} + \mathcal{H}_{Zp}$. Figure(b) illustrates the mixing of the levels occurring when the interaction $\mathcal{H}_{dip}$ between electron and proton is considered.

If a small and oscillating magnetic field is applied to the system

$$B_{int} = -g_e\beta_e B_1 S_x \cos\omega t - g_p\beta_p B_1 I_x \cos\omega t \tag{2.6}$$

where B_1 is the intensity of the field and ω its frequency, then for particular frequencies a transition between the levels can be induced. This perturbation is able to flip the spin of one particle and therefore the following transitions are possible (see Figure 2.11):

$\omega = \omega_e$	(a) $\leftrightarrow$ (c) and (b) $\leftrightarrow$ (d)
$\omega = \omega_p$	(a) $\leftrightarrow$ (b) and (c) $\leftrightarrow$ (d)
$\omega = \omega_e - \omega_p$	(b) $\leftrightarrow$ (c)
$\omega = \omega_e + \omega_p$	(a) $\leftrightarrow$ (d)

The last two transitions, which occur with less probability($\propto \epsilon^2$) are the most interesting, since they correspond to a flip of both, electron and proton spin: $|\downarrow\downarrow> \leftrightarrow |\uparrow\uparrow>$ or $|\downarrow\uparrow> \leftrightarrow |\uparrow\downarrow>$, neglecting the part proportional to ϵ. As an example let us consider the case $\omega = \omega_e - \omega_p$. After the transition (b) $\rightarrow$ (c), the electron will quickly decay to its fundamental state as compared to the proton which will stay on its excited level longer due to the small lattice interaction[4] and therefore the transition (c) $\rightarrow$ (a) will occur (see Figure 2.11). The net result is that level (a) will be more populated than the level (b). Since level (a) is characterized by having the electron with the original spin orientation but the proton with the spin flipped compared to the initial level (b), this process has the net result of polarizing the protons.

The numerical values of the frequencies ω_e and ω_p depend on the intensity of the magnetic field B applied to the system. In case of $B = 5\ T$, one has $\omega_e = 140\ GHz$ and $\omega_p = 213\ MHz$.

The DNP method leads to polarizations of 80-90% for the proton and 30-40% for the neutron.

2.3.2 Target Material

The target material used during the EG1 run was frozen ammonia $^{15}NH_3$ and $^{15}ND_3$. This material, compared to the traditionally used materials such as

[4] The relaxation time depends on the lattice interaction which depends on the magnetic moment. The bigger the magnetic moment, the bigger is the interaction and therefore the faster the decay. The typical relaxation time for an electron is of the order of 1 ms, whereas for a proton ranges from several minutes to hours. This effect is called *solid state effect*.

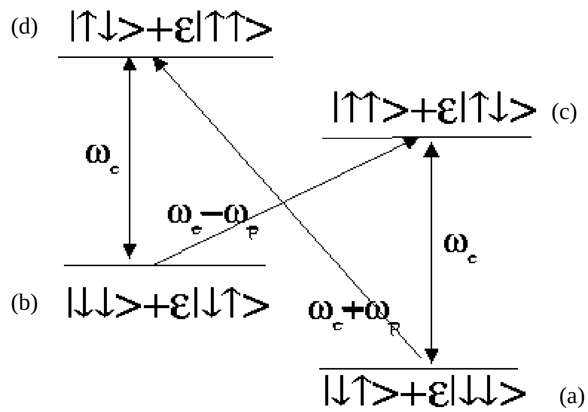

Figure 2.11: Schematic representation of the possible transitions in a electron-proton system in an external field. Due to the dipole interaction and therefore to the mixing of the levels, the transitions (b) $\leftrightarrow$ (c) and (a) $\leftrightarrow$ (d) can occur with probability ϵ^2. These transitions are the basis of the DNP.

hydrogenated and deuterated alcohols, has the following advantages:

- Bigger ratio of free to total nucleons (also called *dilution factor*)
- Better resistance to radiation
- In case of radiation damage there is the possibility to restore the original conditions by *annealing* the target.

In regards to the last two points, the ammonia can stand an accumulated dose of $10^{15} - 10^{16} electrons/cm^2$ before showing a decrease in polarization. The radiation damages the target since it can introduce an excess of paramagnetic centers. It is possible to remove these centers by a process called annealing. Annealing the target means to raise the temperature of the $^{15}NH_3$ target to 85K (95K for the $^{15}ND_3$) in order to recombine the excess of free radicals. The low currents used in Hall-B (on the order of few nA) reduce the need for this process. During the EG1 run the target was never annealed, the target material was simply replaced when needed during down time.

The target material was prepared by slowly freezing the gaseous ammonia at liquid-nitrogen temperatures. The material was then crushed into granules with diameters of 1-2 mm in order to increase the surface with the liquid helium bath and therefore reduce the heating within the material induced by the beam.

The paramagnetic centers were created by irradiating the material with a low energy electron beam at liquid Argon temperatures. The beam knocks out a proton in the material leaving a hole $^{15}NH_2^-$. The electron that was formerly attached to the ejected proton is then less tightly bound and can couple with the three free protons of the $^{15}NH_3$ molecules as described in the previous section.

The only disadvantage that this kind of target presents is that the ^{15}N in the ammonia contains an unpaired proton which may also be polarized. However, as will be discussed in section 5.6.4, this polarization can be estimated and corrected for.

2.4 Detector Performance

2.4.1 Drift Chambers

The drift chambers cover a range in θ from 8° to 140° and approximately 80% of 2π in ϕ [29]. The 90% - 10% Argon-CO_2 gas mixture results in a greater than 99% efficiency. This is limited by tracks passing close to the sense wires, which results in low pulse heights with long durations. The intrinsic resolution by this gas mixture is on the order of $\sim$ 100 μm, but in operating conditions a resolution of $\sim$ 500 μm is achieved, due to limited knowledge of the geometry and the time dependence of the calibration parameters. The resulting momentum resolution is $\sim$ 0.5% for low momentum tracks and $\sim$ 1.5% for high momentum tracks.

2.4.2 Čerenkov

The Čerenkov counter is filled with C_4F_{10} with an index of refraction of $n =$ 1.00153, giving a threshold of 9 MeV for electrons and $\sim$ 2.5 GeV for pions. Since the detector system is a part of the trigger regions of high efficiencies have to be selected in the final analysis. Studies using electrons elastically scattered from a hydrogen target show that the efficiency of the Čerenkov is greater than 99% in the regions selected by the fiducial cuts [21].

2.4.3 Electromagnetic calorimeter

The electromagnetic calorimeter, which covers a range in θ from 8° to 45° with additional coverage in two sectors of up to 80° is not only used for the detection of photons from the decay of π^0 and η, but aids also in the identification of electrons and neutrons [23]. It is also used as a part of the electron trigger. The energy resolution achieved is

$$\frac{\sigma(\mathrm{E})}{\mathrm{E}} = \frac{10\%}{\sqrt{\mathrm{E}}} \tag{2.7}$$

with the energy E given in GeV.

The position resolution is approximately $\delta r \sim 2\ cm$ using charged tracks, which were tracked to the position of the calorimeter using the drift chamber hits. For electrons of a few GeV the timing resolution is better than 200 ps and for electron-neutron data samples resolutions of $500 - 600\ ps$ have been obtained. The resolution in mass for $\pi^0 \rightarrow \gamma\gamma$ events is

$$\frac{\delta m}{m} \leq 15\% \tag{2.8}$$

2.4.4 Time of Flight system

The time of flight scintillator system [22] was used to aid in the particle identification of charged tracks and cover a θ range from 9° to 140°. The timing resolution in the forward direction is $\sim 120\ ps$ and provides good distinction between pions and kaons up to 2 GeV/c. Above $\theta = 90^\circ$ the resolution degrades to $\sim 250 - 300\ ps$ due to higher rate or background in these scintillator paddles.

2.4.5 Trigger and Data Acquisition

As mentioned earlier the electron trigger during the EG1 run consisted of simultaneous signals from the Čerenkov counter and the electromagnetic calorimeter. The thresholds were 150 mV for the calorimeter, corresponding to a energy deposit of 600 MeV and 38 mV for the Čerenkov counter, corresponding to a signal of less than one photoelectron. Approximately 60% of the events written with this pre-trigger condition contained one electron, the other 40% correspond to noise in the Čerenkov counter or hadrons interacting with the support structure of the detector and producing electromagnetic showers. These background events were easily removed in the offline analysis. The second stage of the trigger, called Level-1 and Level-2 were requiring at least one charged track in the drift chambers.

Once an event passed the trigger requirements the detector components were read out and passed to the Event Builder and the Event Recorder. Events were then recorded on a local disk and later transferred to the tape archive at Jefferson Lab. The readout of data was limited by the rate at which the data acquisition buffer was able to transfer data to the local disk. During the EG1 run the dead time, the time at which the data acquisition was unable to receive data, was on the order of $10-15\%$ with a data taking rate of $1500-2250$ kHz.

CHAPTER 3
DATA SELECTION

3.1 Run Selection

The experimental analysis described in this thesis utilized data with beam energy of 2.565 GeV and torus current of $I_t = 2250\ A$ (inbending) taken over a period of two months in 1998. In particular the groups of runs used for this analysis are listed in Table 3.1. As it can be seen from the table the positive target

Run	*Pol Target*	*Triggers*[10^6]
15058-15076	+	40.6
15091-15095	empty	5.0
15109-15111	^{12}C	10.8
15121-15156	-	82.3
15176-15206	+	59.4

Table 3.1: Event totals and target conditions for the $E = 2.565$ GeV and $I_t = 2250\ A$ from the EG1 run period.

polarization data were taken in two different periods. The average positive and negative target polarizations achieved were 38.6% and -55.3%, respectively. The beam polarization was $\sim 70\%$ over the whole period.

The selection of the runs has been made according to the "bad run flag" and some further quality checks. The "bad run flag" was based on the check of some basic monitoring histograms regarding various quantities related to the detector and the reconstructed variables. In addition comments on the log book were taken into account for judging runs.

The quality checks performed by the collaboration consist mostly in checks of the number of electrons under various conditions on a run-by-run basis for each sector[30]. Runs that show a different rate were rejected in order to avoid systematic effects in the asymmetries. The runs rejected according to these criteria were 15062, 15081, 15139, 15142, 15204, 15205, 15206 for a total of 7.3M and 6.2M triggers of positive and negative target polarization data, respectively.

3.2 Corrections

During the course of the analysis several problems arose for which ad hoc corrections were studied and applied to improve the quality of the data. In the two following subsections I will describe how the z-vertex position and the momentum were corrected in order to force the data to follow the expected behavior. Other problems related to the helicity pair selection and the identification of positive particles will be described in later sections.

3.2.1 Vertex Correction

The z-position of the vertex presents a dependency on the polar angle ϕ (see Figure 3.1 (a)). This dependency is due to the fact that the target is actually not exactly on the z-axis of the detector and this misalignment was not taken into account in the reconstruction of the charged tracks. In order to do an accurate cut on the vertex position equivalent for each sector, we need to remove this ϕ dependency.

The correction formula can be found **geometrically** and is given by

$$z_{corr} = z_{meas} + a\cot(\theta)\sin(\phi - \phi_0) \tag{3.1}$$

where a is the distance between the z-axis of the detector and the target axis and ϕ_0 is related to the angle of the plane containing the two axes with respect to the horizontal plane (see Figure 3.2).

The parameters a and ϕ_0 were fitted for different run conditions. The values found for the 2 GeV inbending data were $a = 0.33\ cm$ and $\phi_0 = -78°$ [31]. Figure 3.1(b) shows that the z-vertex after the correction does not have a ϕ dependency anymore.

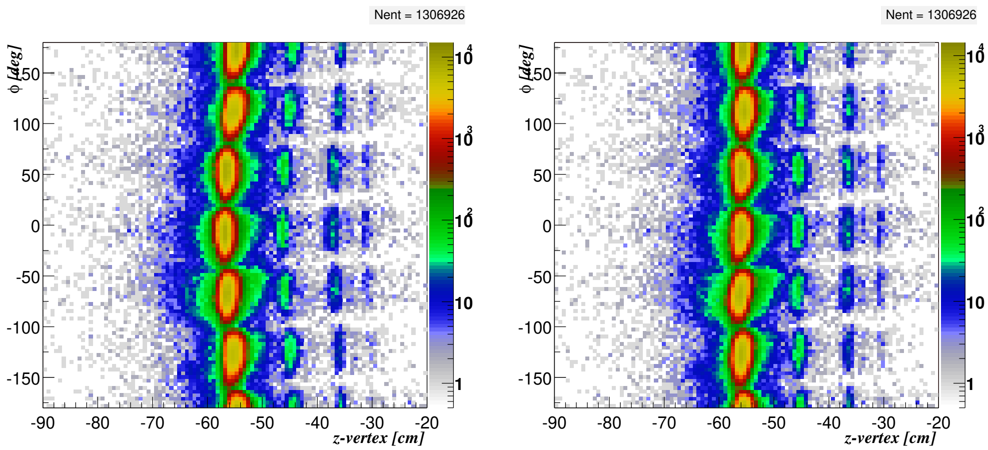

(a) original

(b) corrected

Figure 3.1: ϕ *vs* $z - vertex$ position for electrons before and after correction of inclusive events. The correction aligns the six peaks at approximately -57 cm, which is the target location. The ϕ dependency in the original distribution coming from a mismatch of the real target axis and the axis in the reconstruction code is removed. The peaks at approximately -45, -35 and -30 cm correspond to scattering off the cryostat windows.

3.2.2 Momentum Correction

The W spectrum of inclusive electron events calculated using the momentum given by the reconstruction program presents a slightly different location and width of the elastic peak for different sectors (see Figure 3.3 (a)). The invariant mass W is expected to be independent on the electron angle ϕ and this distortion is an indication of a non perfect momentum reconstruction. This problem is due to a slightly wrong description of the drift chamber position in the reconstruction code and a small shift of the torus magnetic field map. To improve the accuracy of the data, corrections to the momentum were studied and applied[30]. These corrections change the magnitude of the momentum as a function of ϕ and θ of the electron according to the formula

$$p_{corr} = p_{meas}(a + b\phi + c\phi^2)\frac{d\theta - f}{g\theta - h} \tag{3.2}$$

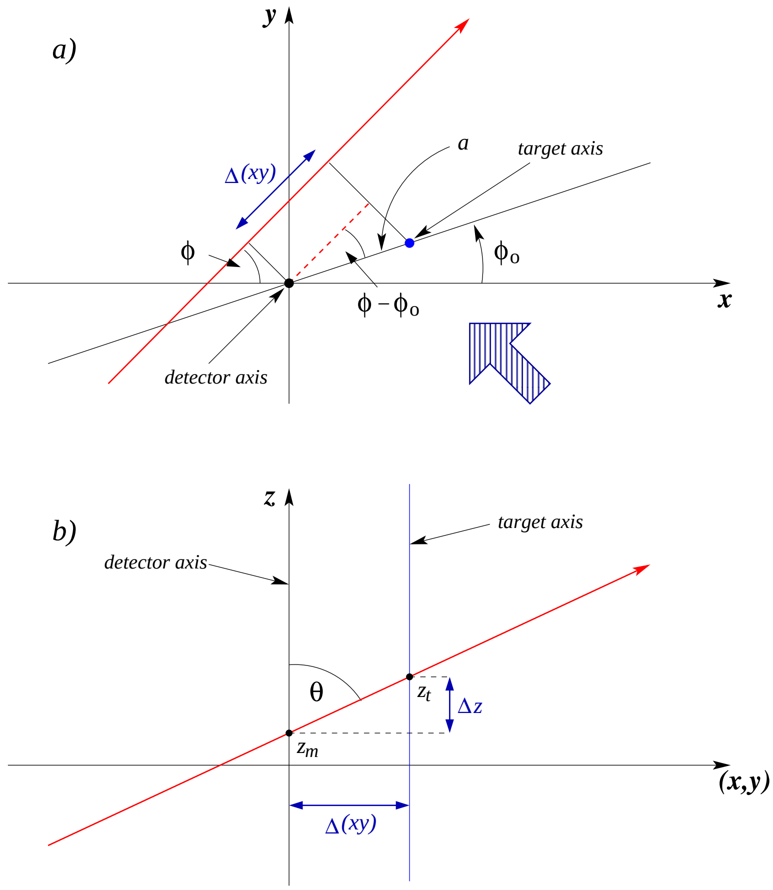

Figure 3.2: Explanation of the variables used to correct for the misalignment between detector and target z-axes. Figure (a) is a view of the (x, y) plane with the particle trajectory (red). The plane that contains the two different z-axes, which are separated by a distance a, is indicated by the black line. Figure (b) is the view with the trajectory parallel to the drawing plane (viewing direction is indicated by the blue arrow in figure (a)), containing the z-axis. The projections z_m and z_t of the trajectory onto the two z-axes are shown.

where the seven parameters $a - h$ were fitted to the data separately for each sector using as a constraint the correct position of the elastic peak.

Figure 3.3(b) shows that the correction aligns the peaks of the six sectors and improves the resolution. The achieved resolution was $\sigma = 15$ MeV.

A complete description of the momentum correction with all the formulas and the parameters used can be found in Appendix C.

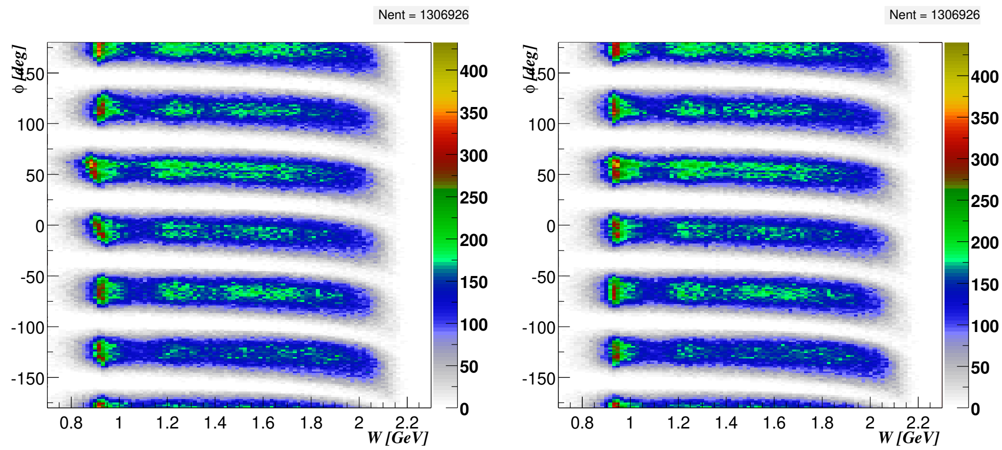

(a) original (b) corrected

Figure 3.3: ϕ *vs* W for electrons before and after correction of inclusive events. The correction aligns the six elastic peaks at $W = 0.938$ GeV$/c^2$ and improves the width of the elastic peak from ~ 23 MeV to ~ 16 MeV [30]. The skewing at high W is due to the target magnetic field. The lower the energy of the electron (high W) the stronger is the shift in ϕ.

3.2.3 Torus current correction

A shift of the order of $2-4$ MeV was observed in the elastic peak position for different runs. This problem is due to the fact that the reconstruction program does not use a nominal value of the torus current but instead reads the value from the run control map for each run. This map contains a torus current value read from the hardware which has the last two digits oscillating. This oscillation of the order of 0.1% is not real and therefore the calculation of the momentum is slightly wrong.

The error can be easily corrected by re-normalizing the momentum to the same current using the formula

$$p_{new} = p_{old}\frac{I_{nominal}}{I_{runcontrolmap}} \tag{3.3}$$

which is based on the fact that $p \propto B \propto I_{torus}$.

3.2.4 Sector misidentification

During the analysis it was discovered that approximately 10% of the positive hadrons in sector 2 were actually assigned a sector value equal to 1. This can be seen in Figure 3.4(a) where some events have $\phi > 60°$ even though they nominally are in sector 1. This problem was fixed reassigning a sector value of 2 to all the particles having originally sector=1 and ϕ in the region of sector 2. As can be seen the ϕ region of sector 2 actually depends on the momentum. To solve this problem, ϕ was translated into drift chamber coordinates ϕ_{DC} using the relationship discussed in section 3.7. Once ϕ_{DC} was found, sector 2 is defined by a momentum independent region $30° < \phi_{DC} < 90°$.

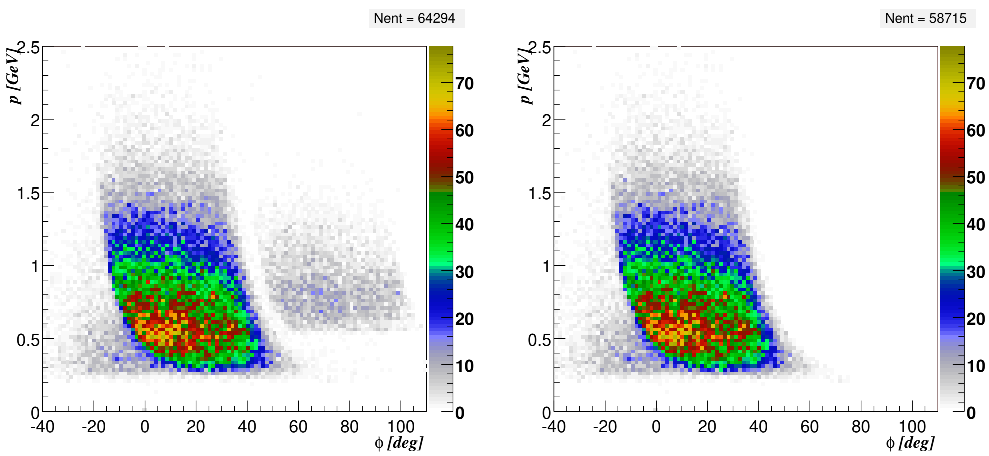

(a) original (b) corrected

Figure 3.4: p *vs* ϕ for protons with sector equal to 1 before and after correction . The events with $\phi > 60°$ in the original plot are completely removed in the corrected plot after reassigning the original sector value.

3.3 Electron Helicity Pairing

Pairing the helicity states is a crucial point in the study of asymmetries. A non perfect pairing can cause a false asymmetry which can have the same order of magnitude as the real one. In particular, the problem can arise in the case of the beam helicity states. Beam was delivered to the experimental hall with a fixed helicity for a period of 500 ms, then with reversed helicity for the next 500 ms. After this "helicity pair" (of 1 second duration) the next helicity was chosen at random, again followed by the opposite helicity and so on (see Figure 3.5). With this method possible systematic errors in the polarization from the hardware were eliminated. However, a few problems in the analysis were caused by this. The first problem is

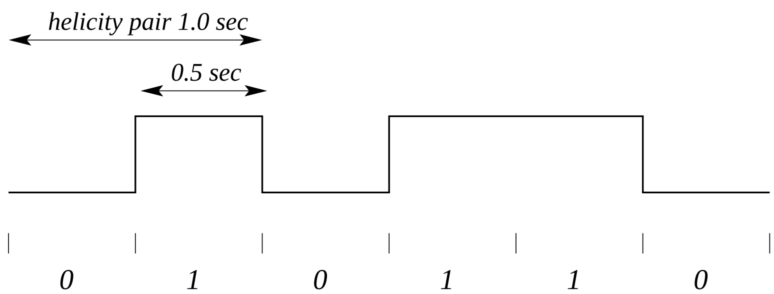

Figure 3.5: Helicity scheme. A helicity state has a duration of 0.5 sec and then is reversed. After this 'helicity pair', the next helicity state is chosen randomly. The random choice of every second helicity state minimizes the influence of long-term drifts and low-frequency noise (in the 1 Hz range).

related to the fact that sometimes the data acquisition may stop for a few seconds or that there is a dead time problem. This means that some helicity states may be incomplete or missing. In order to have a correct asymmetry we need to have complete pairs.

The second problem is that the beam intensity was different for the two helicity states. The beam asymmetry due to this fact was measured to be of the order of -0.3% [30]. To correct this it is necessary to know the Faraday cup charge for each helicity state which was read synchronously with the helicity flip and stored every 10 sec in a scaler.

A program, "HelP", was developed to solve these issues [32]. The program matches the helicity information written on an event-by-event basis with the values in the scaler in order to associate the right Faraday cup reading to the corresponding electron bucket. Secondly, it understands if some states are missing and rejects unpaired and incomplete helicity states.

The program writes a table containing the helicity state of a bunch of electrons and a flag to indicate if the pairing was successful. The latter was negative (-10, -50, etc) if the program was unable to pair helicity states and "1" or "2" for the first and second half of a good pair, respectively. Events were rejected at a later stage in the analysis if they belonged to a bunch of electrons with a negative flag. However, sometimes the "HelP" tables contained sequences like 1 2 1 2 1 1 1 1 2 -50, where the four "1"s do not have a meaning and there is clearly an unpaired state in the sequence. To fix this mistake of the program the flag was reassigned by scanning the helicity state sequence for patterns like 1001 or 0110 between negative flags. These patterns are an indication for a helicity pair, and tracking backward and forward the helicity flags "1" and "2" were reassigned until the negative flags were reached. During the reassignment it was checked that every pair was indeed two different helicity states and if the first state or the last state remained unpaired, it was rejected. This method is illustrated in Table 3.2.

flag	−10	1	2	1	2	1	2	1	2	1	2	1	1	1	1	2	−50
hel	−10	0	1	0	1	1	0	1	0	0	1	0	1	1	0	1	−50
					←	→											
corr	−10	1	2	1	2	1	2	1	2	1	2	1	2	1	2	-100	−50

Table 3.2: Helicity pairs correction. The line "flag" corresponds to the original flag assigned by HelP, "hel" is the helicity of the electron and "corr" is the corrected flag. The two arrows indicate the first point where it is possible to understand that a pair began. This is the point where the program begins to reassign the flag. In this example the last helicity state remain unpaired and therefore a negative flag is assigned.

3.4 Electron selection

The trigger for EG1 is a coincidence signal of the electromagnetic calorimeter and the Čerenkov Counter, so that every event has a candidate for an electron track. During the reconstruction not all the events have an electron identified and in such a case the event is rejected. The final 'cooked' data have therefore all events with at least an electron, however the identification can be still ambiguous due to poor reconstruction or contamination of other negative particles, for example a π^- activating the Čerenkov detector and the calorimeter. For this reason some basic cuts were applied to improve the electron selection. These cuts, mostly directly related to the detectors like Čerenkov counters or electromagnetic calorimeter, were made on the following quantities

- z-position of the vertex
- total energy of the calorimeter vs momentum
- total energy vs inner energy of the calorimeter
- number of photo-electrons in the Čerenkov counter

Due to the complicated tracking back in the magnetic field of the polarized target, the z-position at the vertex is known only with poor resolution. Looking at Figure 3.6 one can see other peaks than the one centered at the target position of $z = -57$ cm which correspond to scattering of the beam off the windows of the target. A loose cut -70 cm $< z <$ -50 cm was applied to remove these events. When an electron hits the calorimeter close to the edge, it might happen that the

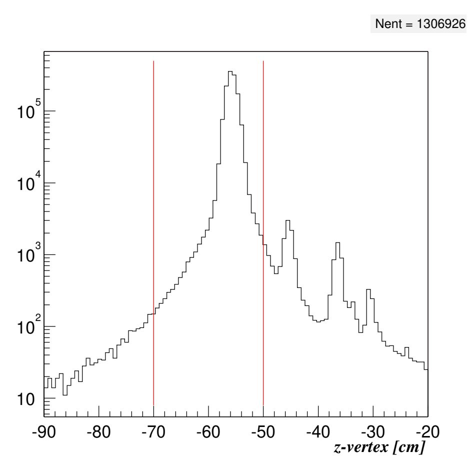

Figure 3.6: Vertex z-position of the electron. The lines, which indicate the applied cut, show that the peaks coming from the scattering off the cryostat windows are completely removed.

electromagnetic shower is not fully deposited in the detector. This means that the released energy is not fully reconstructed. To study this effect one can use the plot $E_{in} \quad vs \quad p$. Electrons interact in the calorimeter and release a total energy that is proportional to their momentum. The sampling fraction $\alpha = \frac{E_{tot}}{p}$ depends on the detector, and in the case of CLAS is $\alpha = 0.27$. Figure 3.7 shows, as expected, that most of events are around a line with slope 0.27, however some events deviate. The ones that are most distant correspond to electrons that hit the edges of the EC as described before. We can therefore remove these events applying a safe cut around the region where we expect them: $\alpha(-a + p - 3\sigma\sqrt{p}) < E_{tot} < \alpha(+a + p + 3\sigma\sqrt{p})$ where $\sigma = 0.1\sqrt{GeV}$ is the total width of the distribution and $a = 0.05$ GeV/c Now that we have confidence in the energy measurement we can apply the third

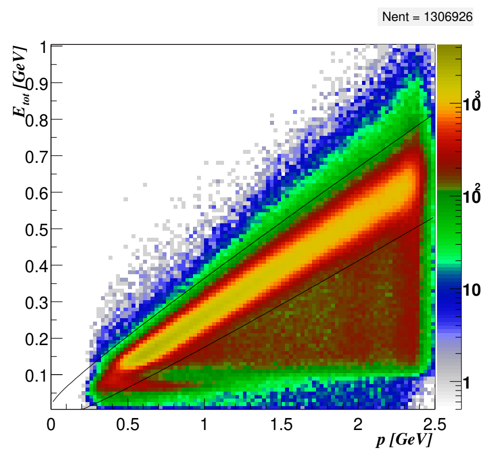

Figure 3.7: E_{tot} vs p for electrons. The energy released in the calorimeter, E_{tot}, by electrons is expected to be proportional to their momentum, p. The two lines indicate the cut applied to remove events which deviate by more than three sigma from the expected behavior. Events hitting the edges of the calorimeter will not deposit all their energy and are located below the dense region of the plot.

cut which is aimed to remove misidentified electrons. Figure 3.8(a) shows the total energy absorbed by the calorimeter vs the energy absorbed in the inner part. When electrons shower in the calorimeter, they release most of their energy already in the inner part of the calorimeter, whereas pions go through the calorimeter losing energy by multiple scattering. This loss is smaller in the inner part because the pions have a greater speed there. The spot indicated by the arrow in Figure 3.8(a) represents misidentified pions. The cut $E_{in} > 0.05$ was applied to remove these events.

In addition the same plot in logarithmic scale (Figure 3.8(b)) shows that there are actually events with $E_{in} > E_{tot}$. A cut, $E_{in} < E_{tot}$, was applied to removed these non physical events[5]. The last cut applied was on the number of

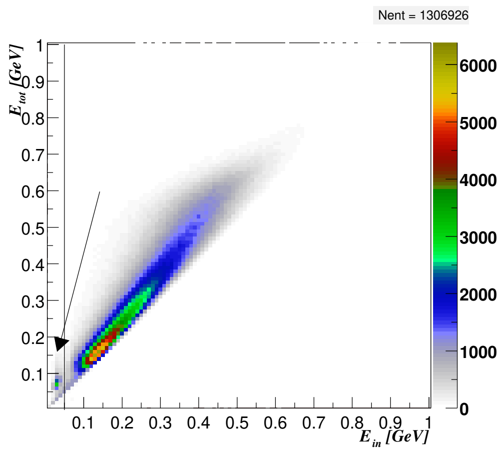

(a) Cut on misidentified pions

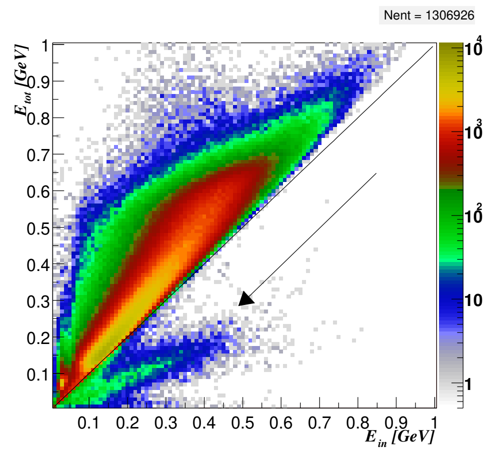

(b) Cut on non physical events

Figure 3.8: E_{tot} *vs* E_{in} for electrons. The intense region in the left plot are electrons which have $E_{tot} \sim E_{in}$, as expected. The line indicates the cut applied to remove events that have E_{in} much smaller than E_{tot}. These events, pointed at by the arrow, are misidentified pions. The right plot is the same as the left one, but with logarithmic scale. It shows the presence of events with the inner energy greater then the total energy (indicated by the arrow). These events are not physical and were removed by imposing $E_{in} < E_{tot}$.

photo-electrons in the Čerenkov counter. The Čerenkov threshold is much higher for pions (2.5 GeV) than for electrons (9 MeV), however it is still possible for a pion to create photoelectrons with enough energy to trigger the Čerenkov detector.

[5]The total energy deposited in the calorimeter can actually be determined in two different ways. In the first method the track reconstruction treats the calorimeter as one detector yielding the value E_{tot}. The second method considers the inner and the outer part of the calorimeter as independent and the total energy is given by the sum $E_{in}+E_{out}$. The two values E_{tot} and the sum $E_{in}+E_{out}$ can be different since it is possible that the signal in the outer part of the calorimeter does not exceed the threshold and therefore no track is associated with this value, while it is fitted when the inner part is also taken into account. In order to take into account this problem the cut was actually defined as $E_{in} < max(E_{tot}, E_{in}+E_{out})$.

Further sources of contamination are possible light leakage and electronic noise. In order to reduce these effects the cut $nphe > 0.5$ was applied (see Figure 3.9). Figure 3.10 shows the effect of all the four cuts on the various plots.

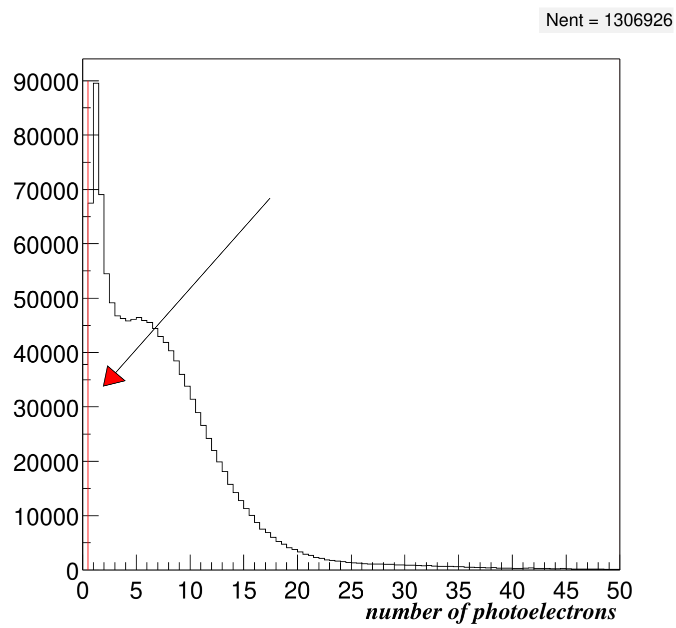

Figure 3.9: Number of photoelectrons detected in the Čerenkov Counter. The red line shows the cut applied to reduce events with photoelectrons created by pions, light leakage and electronic noise.

3.5 Particle ID

The analysis described in this note consists of the study of the exclusive reaction $e + p \rightarrow e' + p + \pi^0$, therefore the identification of the proton is one of the fundamental aspects. The particle ID is typically done by means of a cut in the β vs p distribution, in which the particles have distinct curves according to their mass differences. From the relation

$$\beta = \frac{p}{E} = \frac{1}{\sqrt{1 + \frac{m^2}{p^2}}} \tag{3.4}$$

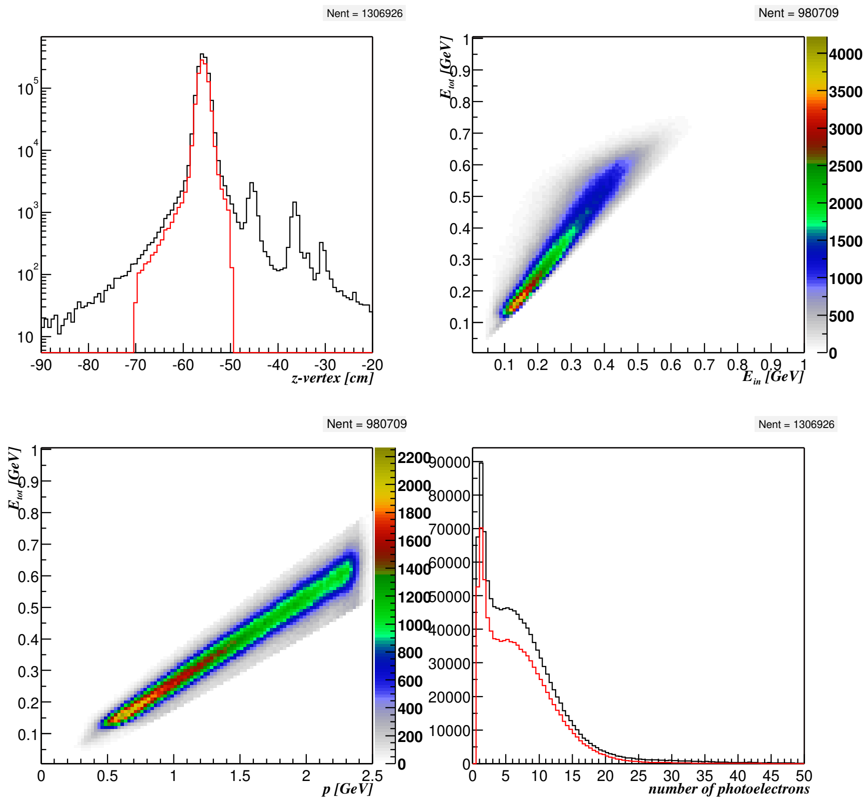

Figure 3.10: Electron cuts. Effect of the various electron cuts on vertex distribution (a), E_{in} vs p (b), E_{tot} vs E_{in} (c) and the number of photoelectrons (d). Note that the four cuts are applied at the same time and remove, approximately 25% of the original number of events.

it is obvious that pions will have $\beta \sim 1$, because their mass is negligible compared to their momentum. Heavier particles, like kaons and protons will have curves below the pions. This cut and the ID assignment is done in the reconstruction code, however the identification of the proton can be improved.

Figure 3.11(a) shows the plot β vs p obtained using the variables of the reconstruction program and Figure 3.11(b) shows how the ID is assigned for pion and the proton (the green and red regions respectively). The proton curve presents two small wings on either sides. These wings are due to the fact that the RF corrections sometimes fail to assign the scattered electron to the right bunch, thus skewing all timing measurements for those events. RF corrections are most useful to improve

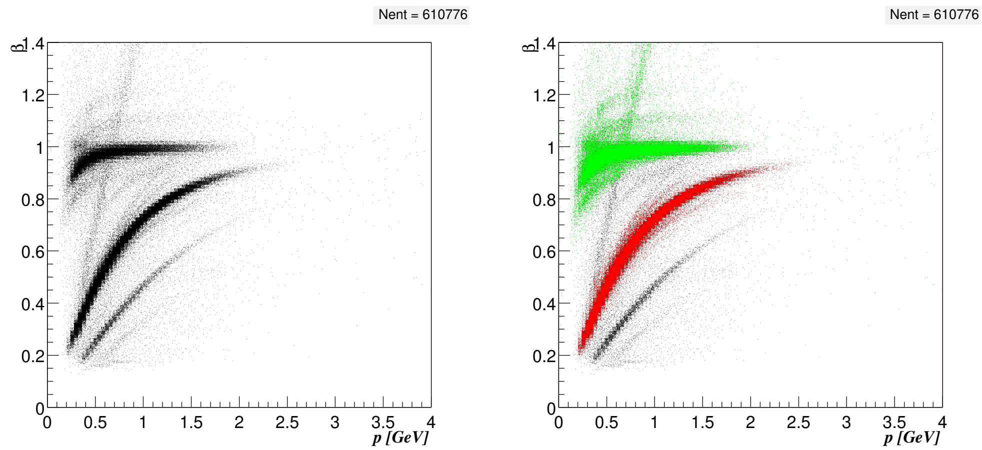

(a) (b)

Figure 3.11: β *vs* p for all positive charge particles. The left plot shows the original β from the reconstruction program versus the momentum. The plot presents several anomalous lines, for example the straight line from $\beta = 0.2$ up to a $\beta = 1.4$. The right plot shows how the program assigns the ID to pions (green) and protons (red). The curves below the proton correspond to scattering off heavier nuclei such as ^4He.

the resolution for the detection of kaons. However, they are not strictly necessary for protons, which are well separated from pions and which are barely contaminated by kaons which have a very low rate. For these reasons the β was recalculated without RF correction according to the formula

$$\beta = \frac{pathlength_{hadron}}{TOF_{hadron} - starttime} \tag{3.5}$$

where

$$starttime = TOF_{elec} - \frac{pathlength_{elec}}{c} \tag{3.6}$$

Thus, all hadron timing is relative to the calculated electron start time. The results are shown in figure 3.12. As can be seen, even after removing the RF correction, the plot presents anomalous structures, besides the two curves that identify pions and protons, such as for example the straight line that crosses the pion region. These regions are due to a bad TOF calibration and several bad scintillator paddles. In

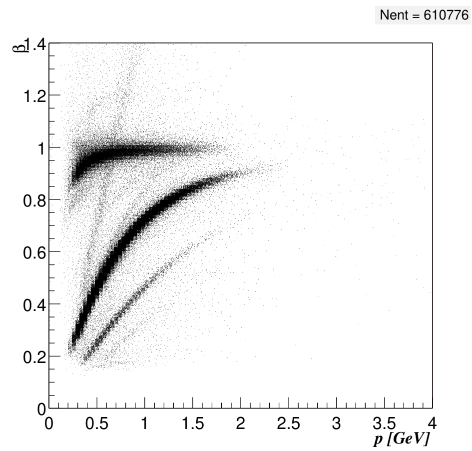

Figure 3.12: *β vs p* without RF correction. The two small wings on either sides of the proton curve are eliminated by removing the RF correction (compare with Figure 3.11(b)).

order to have a good particle ID these need to be either removed or corrected. The TOF calibration was studied for each paddle and for different run groups, and time corrections were calculated. Some of the paddles were found unrecoverable and therefore removed [33].

The β was recalculated using time corrections *timecorr* according to the formula

$$\beta = \frac{pathlength_{hadron}}{TOF_{hadron} - starttime - timecorr} \tag{3.7}$$

The final β vs p distribution after all corrections is shown in Figure 3.13. The cuts to select protons and pions are indicated and show that the two particles can be clearly separated throughout the whole momentum range.

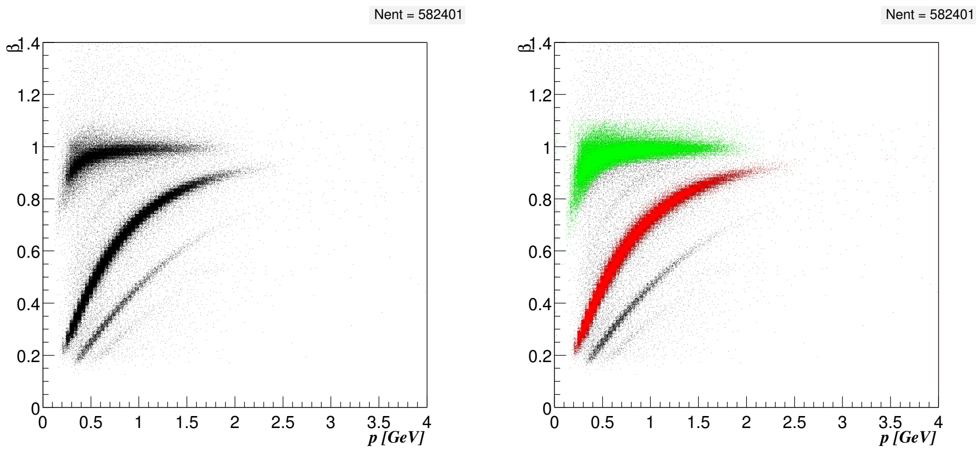

(a) (b)

Figure 3.13: β *vs* p after correction. The left plot show β recalculated with the time correction versus the momentum. All the anomalous lines are removed. The right plot shows how pion (green) and proton (red) were assigned. The cut is more conservative than the original one since now the two curves are well defined and separated.

3.6 Channel selection - Proton cuts

In the present analysis we are interested in the study of the $\Delta(1232)$ resonance, in particular in the decay channel $\Delta^+ \to \pi^0 p$. The first step in the analysis is the selection of events that contain a proton. For this we can use the particle ID procedure described in the previous section. The second step is to identify among all these exclusive events the ones coming from the Δ^+ decay. For this purpose the following quantities were studied

- M_X^2 missing mass
- W invariant mass

In addition possible background coming from the **elastic radiative tail** was studied as well and a cut to remove these events was performed.

3.6.1 *W* invariant mass and missing mass cuts

The $\Delta(1232)$ resonance has mass of 1.232 GeV/c^2 and can be seen experimentally by looking at the invariant mass W

$$W = |e + P - e'| \tag{3.8}$$

where $e = (\epsilon_i, \vec{k}_i)$ and $e' = (\epsilon_f, \vec{k}_f)$ are the initial and final 4-vector of the electron, respectively and $P = (E_i, \vec{P}_i) = (M, \vec{0})$ is the initial proton 4-vector. A cut 1.1 GeV/$c^2 < W <$ 1.3 GeV/c^2 was applied (see Figure 3.14(a)). This cut is fairly loose, but was chosen in order to have higher statistics. The square of missing mass

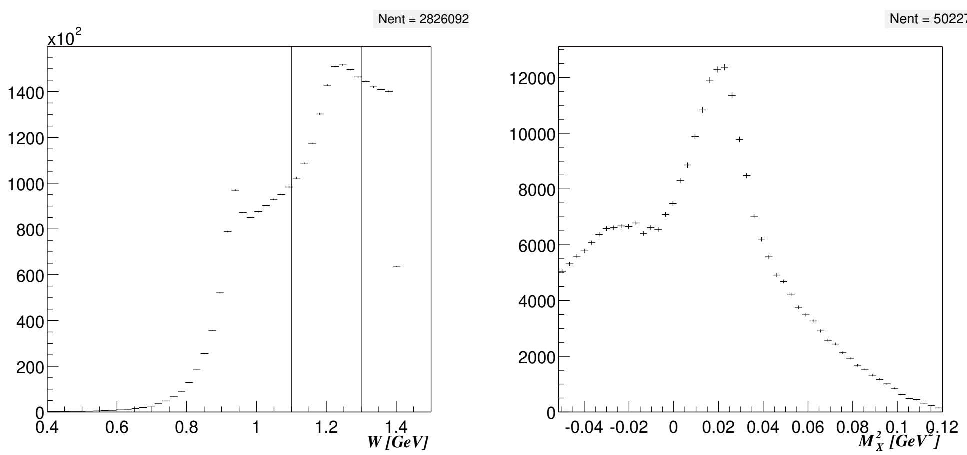

(a) W mass (b) M_X^2

Figure 3.14: The left plot shows the W exclusive spectrum. The two lines indicate the cut applied to identify the $\Delta(1232)$. The right plot shows the missing mass squared M_X^2, corresponding to this region. The peak is centered at the mass squared of the pion $M_X^2 = 0.018$ GeV$^2/c^4$. The shoulder on the left side is due to the quasi-elastic peak.

$$M_X^2 = |e + P - e' - P'|^2 \tag{3.9}$$

where $P' = (E_f, \vec{P}_f)$ is the final proton 4-vector, shows, as expected, a peak corresponding to the pions from the decay $\Delta^+ \rightarrow \pi^0 p$ (see Figure 3.14(b)). However it appears from the plot that there is a shoulder coming from the broad quasi-elastic peak of the nuclear background. In order to improve $\Delta \to \pi^0 p$ events the two dimensional plot W vs M_X^2 was studied (see Figure 3.15(a)).

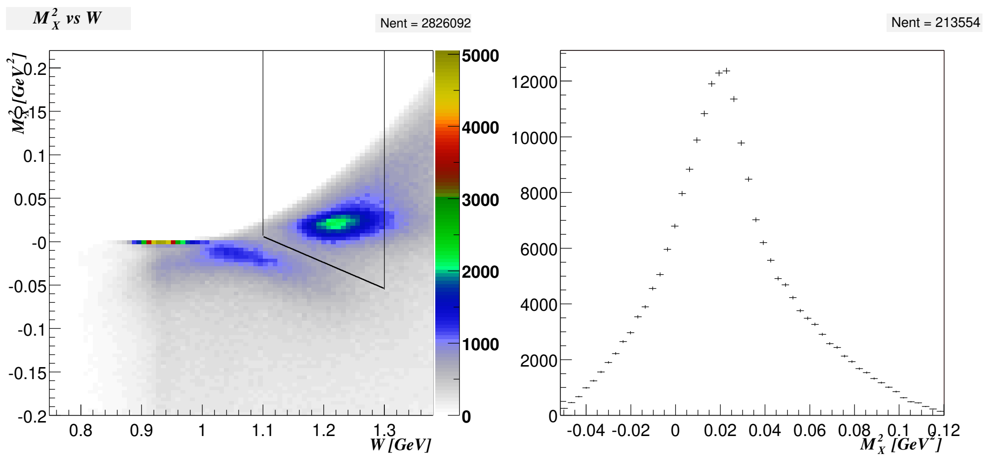

(a) M_X^2 *vs* W (b) M_X^2

Figure 3.15: The left plot shows the two-dimensional cut applied in order to remove the quasi elastic shoulder. The right plot shows the resulting M_X^2 spectrum after the cut. The shoulder at negative M_X^2 is completely removed.

In this plot the quasi-elastic peak and the $\Delta(1232)$ peak are well separated and a cut $M_X^2 > -0.3(W - 1.12)$ was applied to better select $\Delta(1232)$ events. After this cut the shoulder in the M_X^2 disappears as shown in Figure 3.15(b). The M_X^2 shown in these plots is actually the missing mass of the target NH_3 and therefore contains pions coming from both the scattering on the three free proton and the nucleons in ^{15}N. The peak coming from the scattering on the second is much broader due to the binding energy and the Fermi motion. Subtracting this background results in a much narrower peak[6]. Considering that for this analysis we are actually only interested in the events in this narrow peak, another cut -0.01 GeV$^2/c^4 < M_X^2 < 0.06$ GeV$^2/c^4$ was applied (see Figure 3.16).

[6]Details about how the background is subtracted will be given in section 4.3.

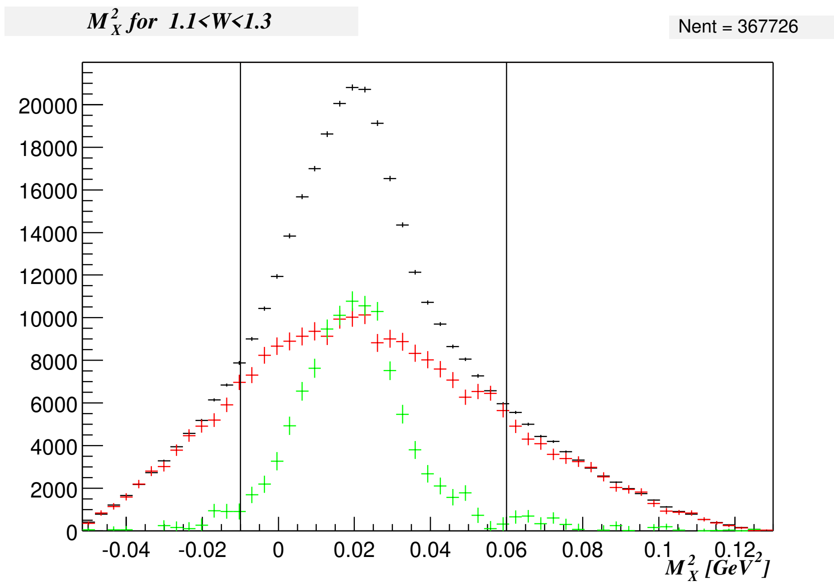

Figure 3.16: Missing mass squared spectra for $^{15}NH_3$ (black), ^{12}C (red) data and the resulting subtraction (green). The carbon data is normalized to the $^{15}NH_3$ using the corrected constant obtained with the inclusive method (see section 4.3). The plot shows that the actual peak coming from the free protons is narrower and therefore a narrower cut indicated by the two lines could be applied in the analysis.

3.6.2 Elastic radiative tail

A source of background when studying the $\Delta(1232)$ resonance is coming from elastic radiative events. These events are elastic events in which a photon is emitted by either the incident or the scattered electron (see Figure 3.17) and they can be at any invariant W mass depending only on the energy of the photon. In previous analyses a technique was found to identify and remove these events [34]. This technique is based on the calculation of the angle of the proton assuming an elastic reaction:

$$\theta_{calc} = \arctan\left(\frac{1}{(1+\frac{E_{beam}}{M_{prot}})\tan(\frac{\theta_{el}}{2})}\right) \tag{3.10}$$

A proton from elastic scattering where a photon is emitted after the scattering (see Figure 3.17) has an angle θ_{prot} which is approximately equal to the angle θ_{calc}. The reason for this can be seen from the equation above which depends only on

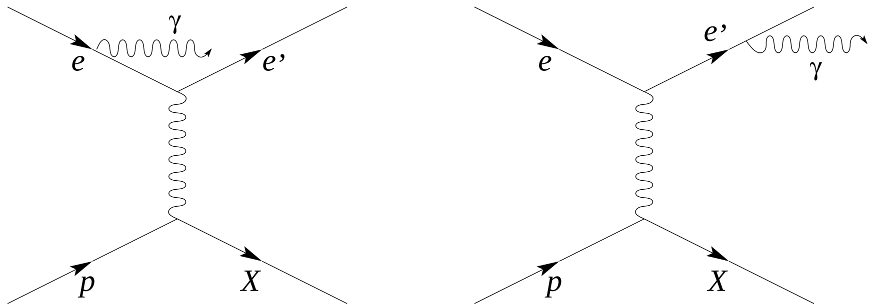

Figure 3.17: Feynman diagrams for elastic radiative processes.

the initial energy of the beam and the angle θ_{el}. The latter is almost unchanged in case of emission of a photon due to the fact that the photon is preferably radiated in the direction of the electron (peaking approximation [35]). Since in this case the invariant mass of the reaction W is greater than the mass of the proton, the plot $\theta_{calc} - \theta_{prot}$ vs W will show a narrow line around $\theta_{calc} - \theta_{prot} = 0$. This is clearly visible in the top histogram of Figure 3.18 which shows events collected in the E1 run period (unpolarized beam and H_2 target). The second curved line in this plot comes from elastic events with a photon being emitted before the scattering of the electron with the proton.

The same plot for EG1 data does not show these lines (Figure 3.18). The reasons for this behavior are twofold. Firstly the reaction target used in EG1 is NH_3 and therefore reactions occur not only on the 3 free but also the 8 bound protons in ^{15}N. The middle plot of Figure 3.18 shows data taken in the E2 run period on a ^{12}C target and the distribution is clearly smeared out due to the binding energy and the Fermi motion of the bound nucleons. Secondly, because of the geometry of the target magnet coils, elastic events with a forward electron have a θ_{prot} around 40° to 70°, which is exactly the region obscured by the target magnet coils. Protons emitted in this area are therefore not detected and lost for the analysis. This suppression can be 'simulated' by applying a cut on θ_{prot} in E1 data and the result in Figure 3.19 shows that this cut indeed removes the radiative tail almost completely.

In order to eliminate possible residual radiative tail events, $\theta_{calc} - \theta_{prot}$ was plotted against M_X^2 (see Figure 3.20). In this plot radiative events appear with $\theta_{calc} - \theta_{prot} = 0$ or slightly negative in the lower part of the graph. The advantage

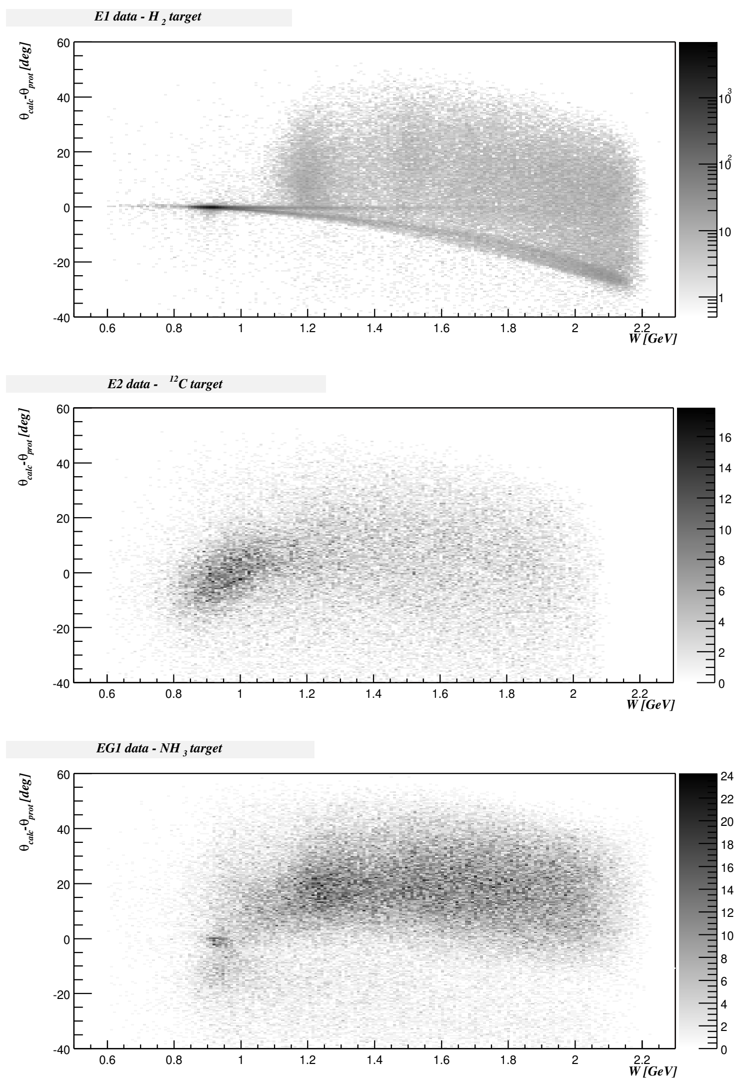

Figure 3.18: $\theta_{calc} - \theta_{prot}$ *vs* W. Comparison between E1 (top), E2 (middle) and EG1 data (bottom). The two lines appearing in the E1 data plot correspond to the two radiative tails in case of emission of the photon before (negative line) or after (line at $\theta_{calc} - \theta_{prot} = 0$) the scattering. E2 and EG1 data do not present these two lines for reasons fully explained in the text.

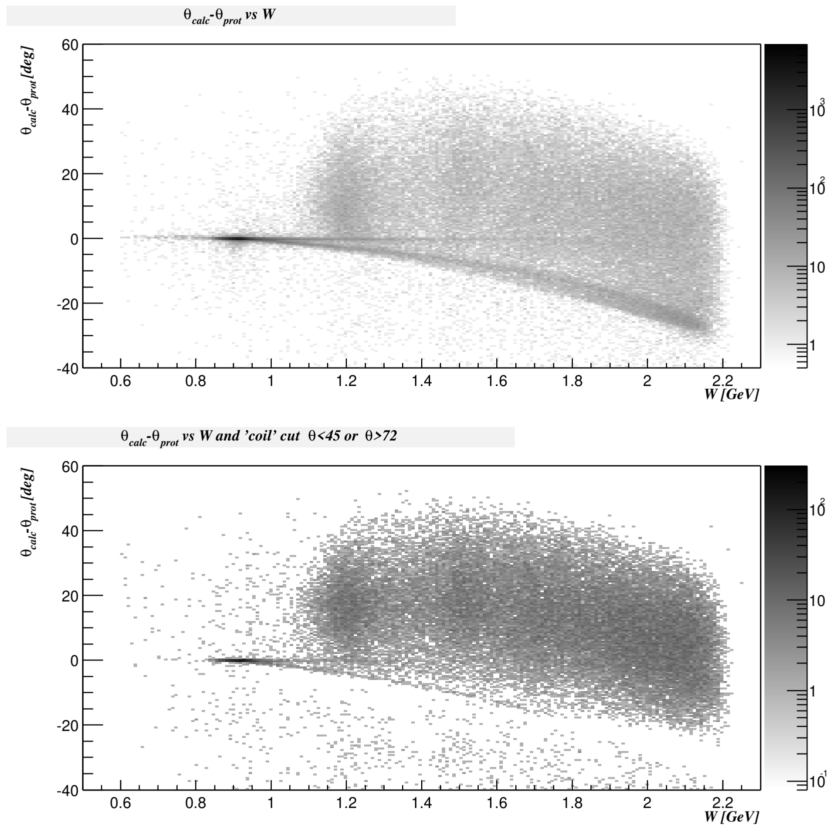

Figure 3.19: $\theta_{calc} - \theta_{prot}$ *vs* W. The top plot is normal E1 data while for the bottom a cut $45° < \theta_{prot} < 72°$ was applied to simulate the target magnet coils present in EG1 run. The comparison shows that this cut suppresses most of the elastic radiative tail events.

of this plot is that, as opposed to the plot $\theta_{calc} - \theta_{prot}$ vs W, $\Delta(1232)$ events are well separated from the radiative background. It is therefore possible to cut the background without losing good events. Figure 3.20 shows that there is indeed a small presence of radiative events and the box indicates the cut applied to remove them ($M_X^2 < 0.0125 \, \cap \, \theta_{calc} - \theta_{prot} < 2°$).

3.7 Fiducial cuts

A good electron and proton identification is still not sufficient for a correct analysis. The detector acceptance has holes and regions where the efficiency is not 100% which has to be taken into account in the analysis. The holes are mainly due

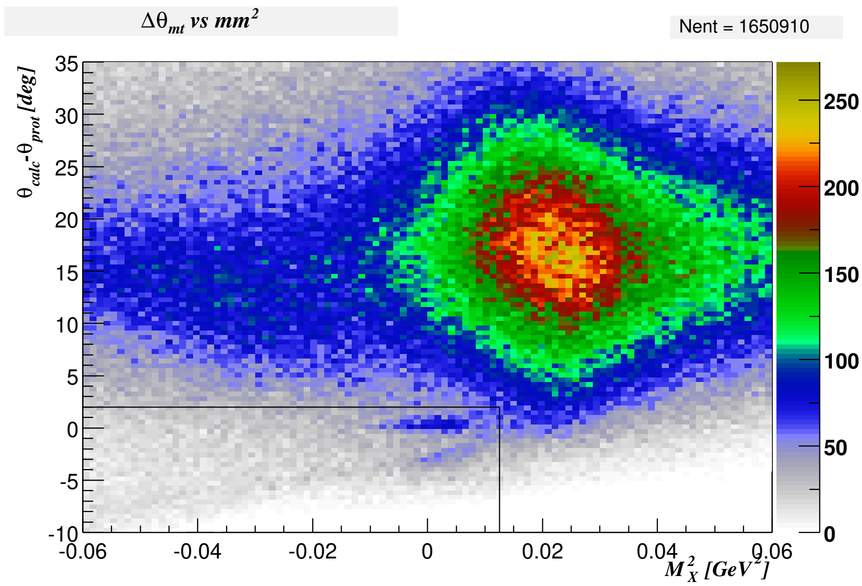

Figure 3.20: $\boldsymbol{\theta_{calc} - \theta_{prot}}$ ***vs*** $\boldsymbol{M_X^2}$**. The two spots around** $\boldsymbol{M_X^2 = 0}$ **and** $\boldsymbol{\theta_{calc} - \theta_{prot} = 0}$ **correspond to radiative tail events. In this plot they are well separated from the** $\boldsymbol{\Delta(1232)}$ **peak and therefore they can be removed by the box cut without losing good events.**

to the coils of the torus and the forward hole where non-interacting beam particles are exiting the detector. The usual approach in many particle physics analyses is to perform a simulation of the detector. However, in the case of CLAS a good description of the detector is a very difficult task and in the case of the EG1 run it is even more complicated by the geometry of the polarized target structure and the tracking in the target magnetic field. In addition there are some anomalies in the data that the existing simulation program is unable to properly reproduce. The biggest one of these anomalies is related to the Čerenkov counters which, at certain kinematics of the electron, collect only little Čerenkov light. This effect can be seen for example in the plot of the electron angles ϕ_{DC} vs θ_{DC} for a particular sector (see Figure 3.21) where two fringes and a depletion appear at low θ angles.

For these reasons it was decided to avoid a simulation and apply fiducial cuts which were established to select a safe region were the acceptance can be considered to be 100%. To select these regions the fact was used that the cross section is ϕ independent and therefore, by fixing θ and p, one expects to find a flat distribution in ϕ. Similar cuts were already studied for the unpolarized analysis (E1 run) in

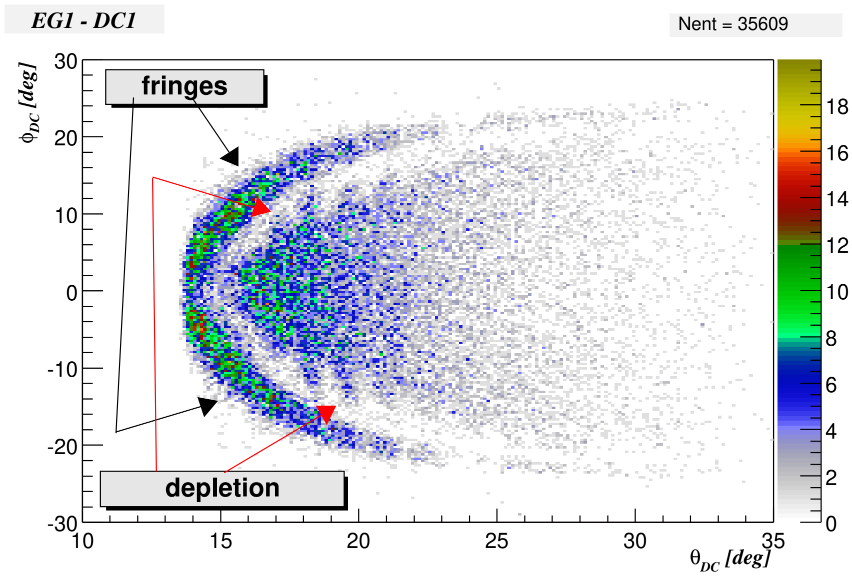

Figure 3.21: ϕ_{DC} *vs* θ_{DC} for sector 1 at the drift chamber for the momentum bin 1.8 GeV/c < p < 2 GeV/c. The arrows indicate the fringes and the depletion caused by the Čerenkov counters. Note that the depletion region extends into the central part of the distribution, causing striations which have to be removed as well.

which they are made on ϕ according to an empirical function of momentum p and azimuthal angle θ, that eliminates the fringes and the depletion[36]. However these cuts cannot be applied to the EG1 data because of the effects of the magnetic field of the polarized target. While in unpolarized target runs the only field present is the toroidal field in the region of the drift chambers which does not change ϕ of the particles, in the EG1 run period there is also the axial field of the target which causes a shift in ϕ. This means that the ϕ distributions at the vertex for E1 and EG1 data are different as can be seen in figure 3.22. The problem can be simplified using some considerations about trajectories of charged particles in a magnetic field. The trajectory of a particle in an axial field is such that the momentum of the particle **outside** the magnetic field points approximately back to the vertex position. In particular the projection on the x-y plane of the momentum points exactly to the vertex (for more details see Appendix D and Figure 3.23) and for θ there is a slight

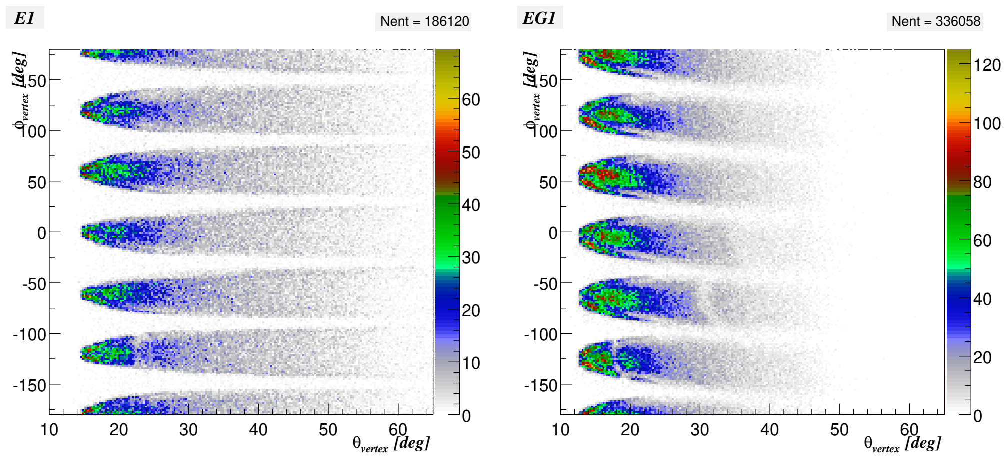

(a) E1 data (b) EG1 data

Figure 3.22: Comparison of the ϕ vs θ distributions at the vertex for E1 and EG1 data. Due to the target magnetic field, EG1 data present a distortion compared to E1. In the E1 run particles hit the coils (six horizontal depletions in the plot) if emitted at certain ϕ independent of θ. In EG1 a particle with a certain ϕ, depending on its energy and therefore θ is bent in a different way by the target magnetic field and therefore the six depletions do not appear to have a constant ϕ.

focusing effect that gives an overall change in θ less than 0.5° (see Figure 3.24)[7]. Considering the poor z resolution of the experiment, this last effect can be neglected for the present purposes. At the first drift chamber the target field is negligible, in other words DC1 is **outside** of the target field but not yet in the region of the strong torus field. It is easy to see that the configurations for E1, where a particle goes straight from the target to the first drift chamber, and for EG1, where particles at the first drift chamber point back to the vertex, are perfectly equivalent at the position of the first drift chamber. Therefore one can expect that the ϕ distributions of EG1 at DC1 will look like the E1 distribution at either vertex or DC1. This was proven to be true (see figure 3.25) and therefore it was possible to use the E1 basic form of the fiducial cuts with an adjustment of the parameters for the present run conditions.

[7] "Focusing effect" means that the magnetic field bends the trajectories toward the axis of the field. In other words θ decreases. The reason is explained at the end of Appendix D.

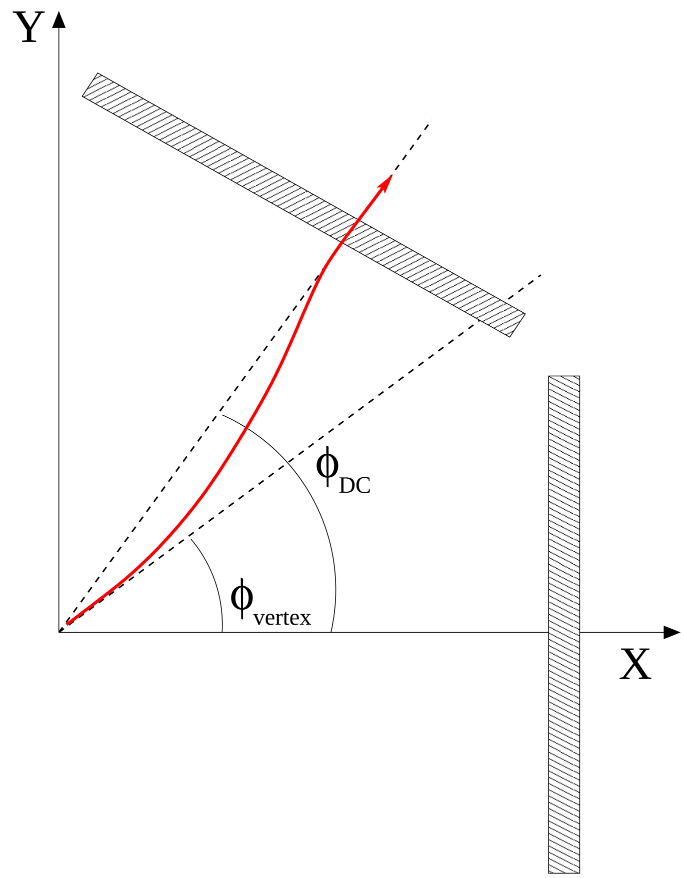

Figure 3.23: View of the X-Y plane of the trajectory of a particle in the target magnetic field. The particle at the vertex has an angle ϕ_{vertex}. The magnetic filed of the target deflects the particle and in the first drift chamber region (indicated by the shaded area) the particle has an angle ϕ_{DC} which correspond to the ϕ direction of the line that joins the vertex and the point where the drift chamber is hit.

The general form of the cut for the electron is:

$$30^\circ - \Delta\phi < \phi_{sec} < 30^\circ + \Delta\phi \tag{3.11}$$

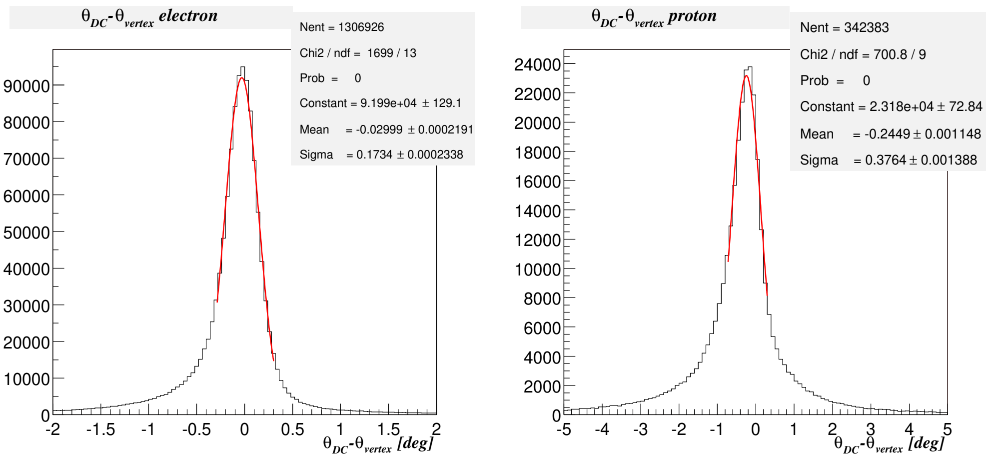

(a) electron

(b) proton

Figure 3.24: $\theta_{DC} - \theta_{vertex}$. The plots show that the focusing effect due to the target magnetic field is very small. Considering the poor resolution of the z-vertex position, this effect can be neglected. The slight asymmetry in the proton plot is due to the fact that protons have lower momentum than electrons and therefore they are more distorted by the magnetic field.

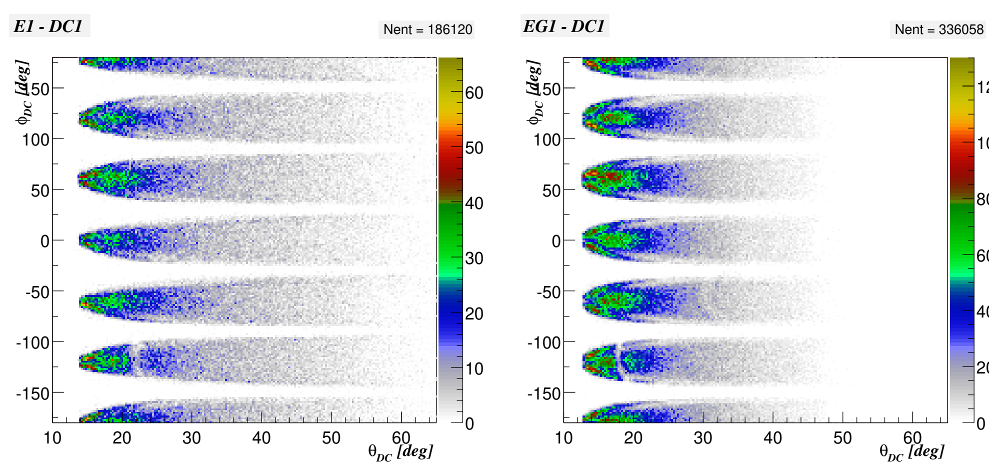

(a)

(b)

Figure 3.25: Comparison of the ϕ vs θ distributions at the first drift chamber for E1 and EG1 data. As expected they are very similar.

where $\Delta\phi$ is give by

$$\Delta\phi = A(\sin(\theta_{DC} - \theta_{cut}))^{expon} \tag{3.12}$$

$$expon = B(p_{scaled})^{C} \tag{3.13}$$

$$\theta_{cut} = D + \frac{E}{(p_{scaled})} \tag{3.14}$$

ϕ_{sec} is ϕ of the electron in the sector coordinates, i.e. between 0 and 60 degrees. The variable $p_{scaled} = p\frac{3375}{torcur}$ is the momentum scaled to the maximum torus current. In this way the torus current dependency of the cut is completely absorbed and the cuts are generally valid for all run conditions. The parameters A through E were found empirically. The parameter D corresponds to the minimum θ of the highest energy electrons. The parameter E is related to fact that the minimum θ increases when the momentum decreases. The parameters A and B control the 'opening' of the curve, in particular the bigger they are, the tighter is the cut.

The general form of the cut for positive particles is the same except for the momentum dependence of the θ_{cut}

$$\theta_{cut} = D' - E'(1. - p_{scaled}/5)^{F'} \tag{3.15}$$

which is extremely weak compared to the electron one. The reason for this weak dependence is that electrons bend towards the beam axis and their acceptance depends strongly on the starting θ angle and the momentum. Positive particles are instead bent away from the beam axis and even for very small angles they will be accepted as long as they have a θ greater than the minimum angle of $8°$[8]. In addition their momentum has to exceed a certain minimum value in order to make it through the entire detector. Parameters A' through F' were again found empirically. Figure 3.26 and 3.27 show the result of these cuts for different momentum bins. Note that the hole in θ from 43 to 75 degrees for the proton is due to the coils of the magnet around the target. Two sets of parameters were actually found for both electrons

[8] If the angle θ is less than $8°$ out-bending particles will not hit the drift chambers and therefore will not be detected. Inbending particles with $\theta > 8°$ however can still be lost in the forward hole depending on the momentum.

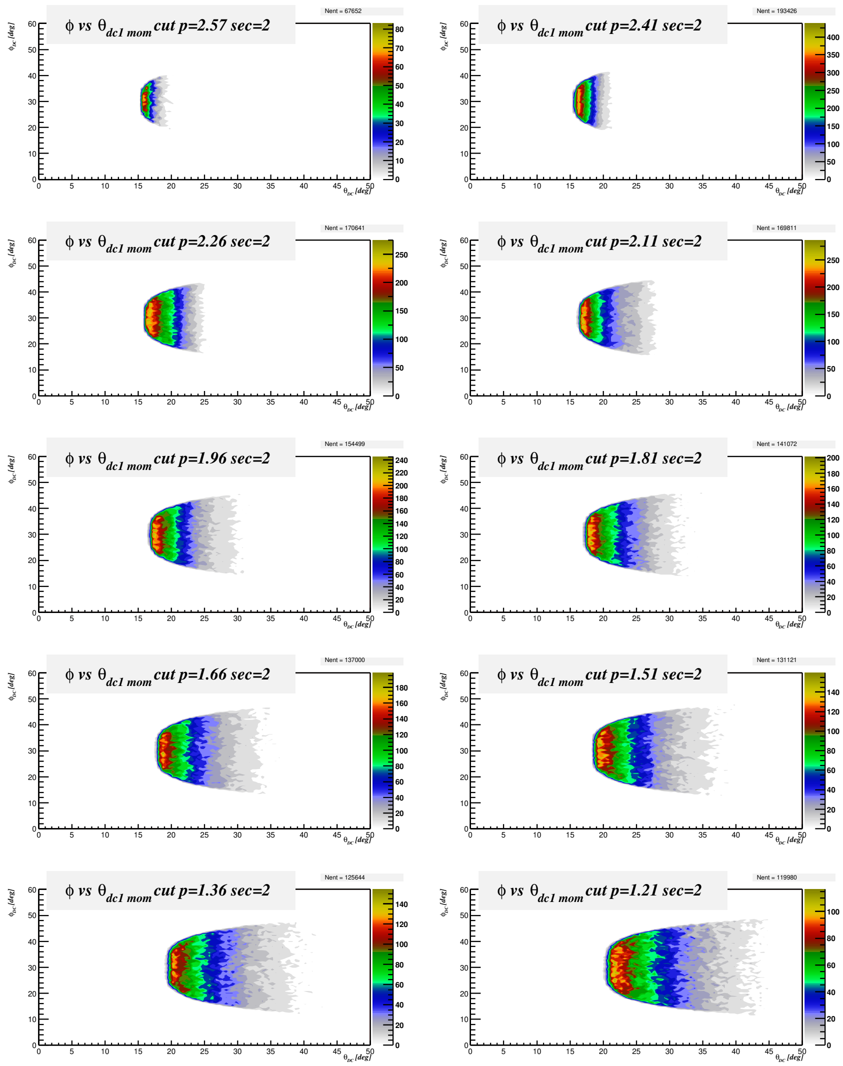

Figure 3.26: ϕ_{DC} vs θ_{DC} distributions for electrons after loose fiducial cuts for $sector = 2$. The various plots correspond to different momentum bins.

and protons. These two sets correspond to a tighter or looser version of the cuts. The choice of either one of the two versions depends on the kind of analysis one wants to do. To calculate a cross section it is safer to choose the tight cut in order to eliminate any possible effect at the edges of the detector. On the other hand loose cuts can be applied for asymmetries. Figures 3.28 and 3.29 show the comparison between tight and loose fiducial cut for electron and proton.

So far only fiducial cuts performed on the drift chamber variables were dis-

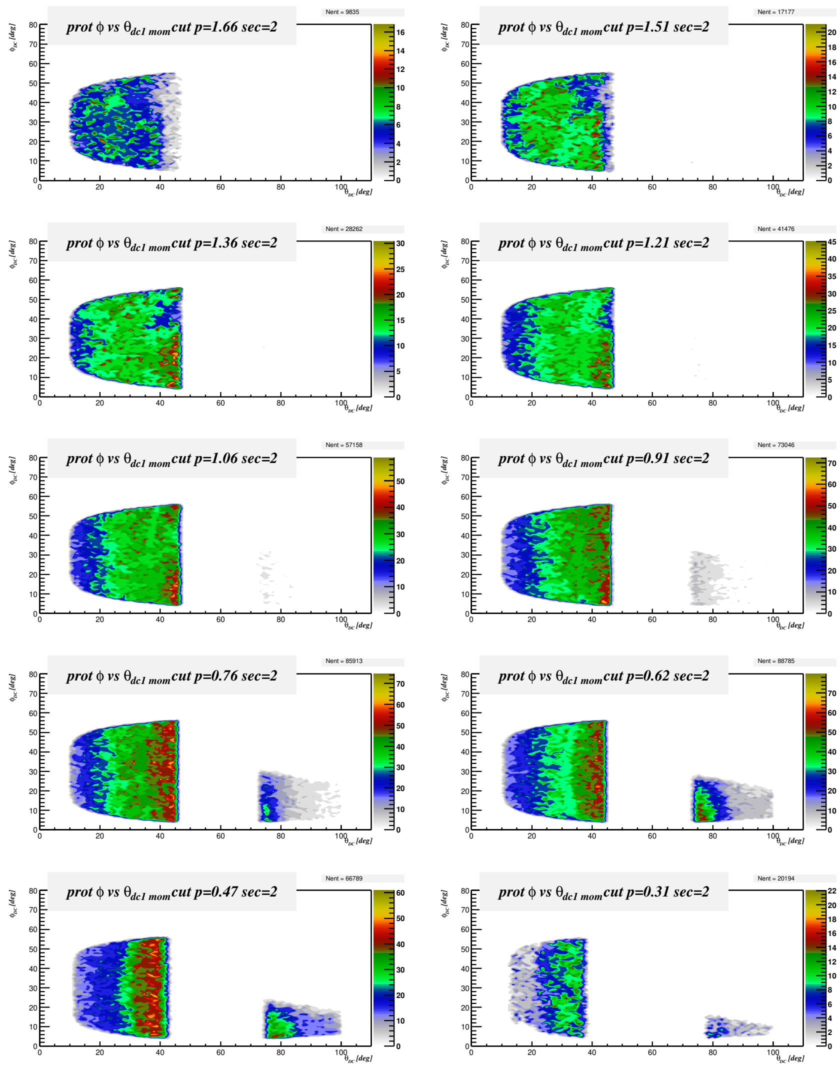

Figure 3.27: ϕ_{DC} vs θ_{DC} distributions for protons after loose fiducial cuts for *sector* = 2. The various plots correspond to different momentum bins. The gaps are caused by the target magnet coils.

cussed. With such cuts it is possible to correct for the acceptance only if the latter one is calculated analytically (see the section on acceptance correction). If on the other hand one uses Monte Carlo generated events for the correction, fiducial cuts using the vertex variables are needed. As mentioned before θ remains approximately unchanged and therefore one can simply replace θ_{vertex} with θ_{DC} in the previous formulas. On the other hand $\phi_{vertex} = \phi_{DC} + \Phi(p)$ where the shift $\Phi(p)$ depends on

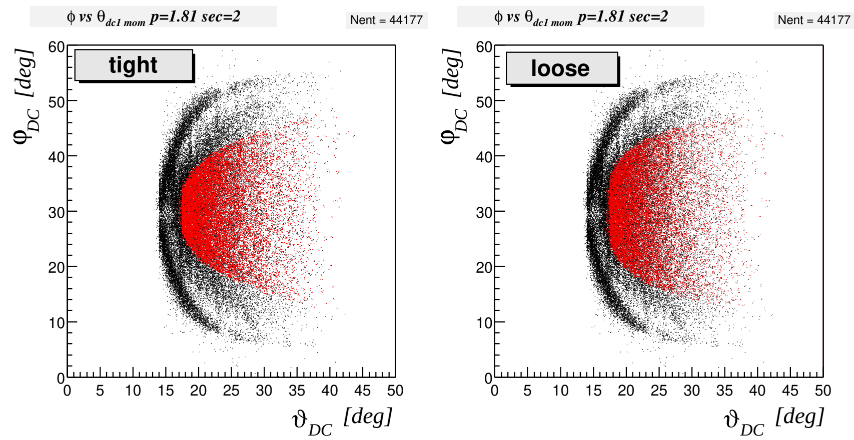

Figure 3.28: Comparison between tight and loose cuts for the electron. The black regions are all events, the red are events selected by the fiducial cuts.

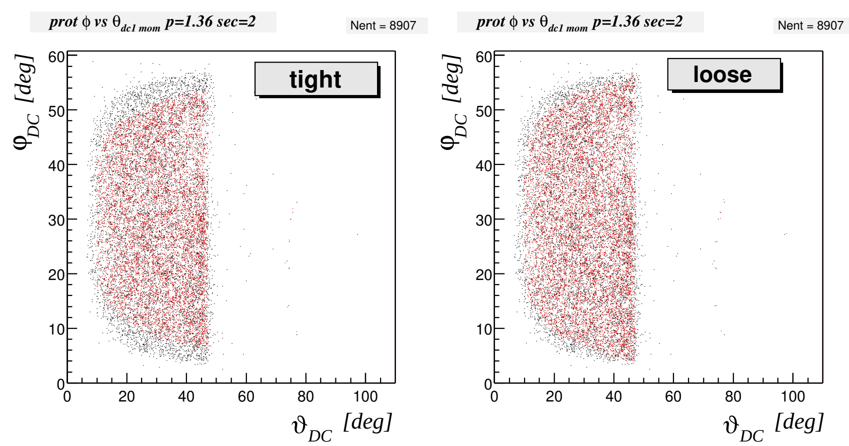

Figure 3.29: Comparison between tight and loose cuts for the proton. The black regions are all events, the red are events selected by the fiducial cuts.

the momentum (see Figure 3.30). This dependency was found fitting the profile of the histogram $\phi_{vertex} - \phi_{DC}$ vs p. with a three-parameter function:

$$\phi_{DC} - \phi_{vertex} = a + \frac{b}{p^c} \tag{3.16}$$

as can be seen in Figure 3.31. Substituting $\phi_{DC} = \phi_{vertex} + a + \frac{b}{p^c}$ in the previous formulas, the cuts are completely transformed into a function of the vertex variables

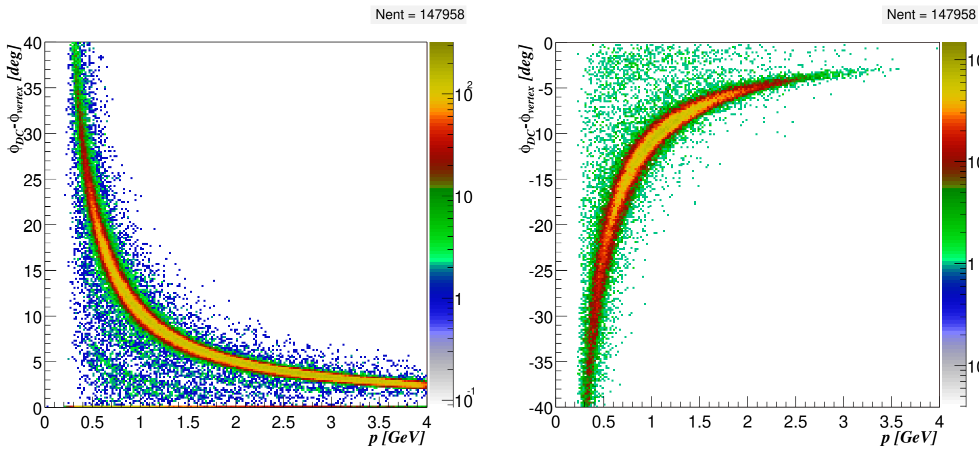

(a) electron (b) proton

Figure 3.30: $\phi_{DC} - \phi_{vertex}$ *vs* p for electrons and protons. The plots show a strong correlation between ϕ_{DC} and ϕ_{vertex} as a function of momentum. For this plot 4 GeV data were used.

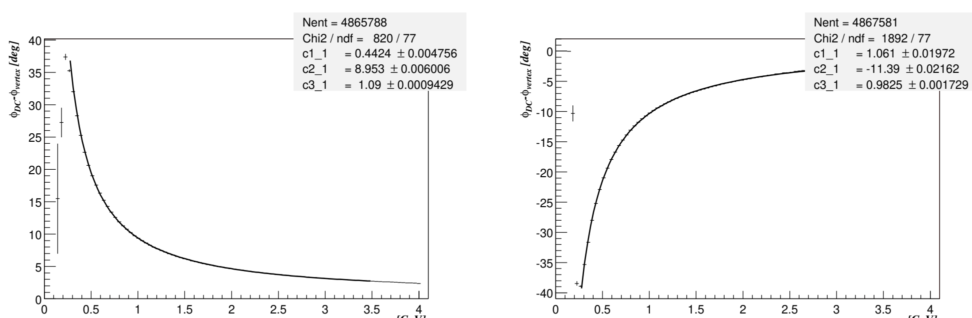

(a) electron (b) proton

Figure 3.31: Profile histogram of $\phi_{DC} - \phi_{vertex}$ *vs* p and fit for electrons and protons. 2 GeV and 4 GeV data have the same behavior in $\Phi(p) = \phi_{DC} - \phi_{vertex}$. The fit was therefore performed on 4 GeV data since the 2 GeV momentum range is a subset of the 4 GeV range.

only, as wanted. Figure 3.32 and Figure 3.33 show how the cuts work. After these

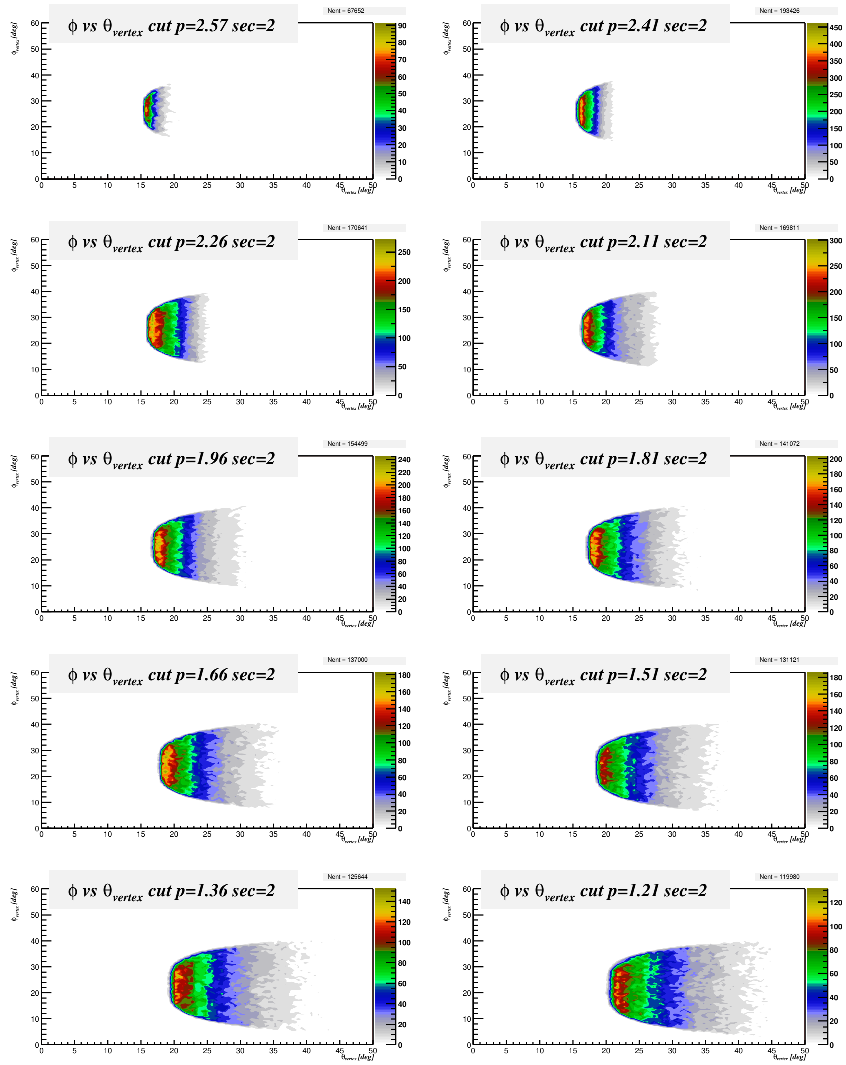

Figure 3.32: ϕ_{vertex} *vs* θ_{vertex} distributions for electrons after loose fiducial cuts for *sector* = 2. The various plots correspond to different momentum bins. Note that ϕ_{vertex} is shifting down with decreasing momentum.

cuts a slice in θ for a momentum bin turns out to be flat in ϕ as expected (see Figure 3.34 and Figure 3.35). After fiducial cuts one can also notice that some periodic structures in θ disappear. These structures are at the edges of the inner region (see Figure 3.21) and have a period of approximately $1.5°$. Figure 3.36(a) shows this periodicity in θ. The structure can also be seen in Q^2 which depends on θ

in Figure 3.37(a). Figures 3.36(b) and 3.37(b) show the same plots after applying the fiducial cuts which remove these non-physical striations.

The improvement of the fiducial cuts can also be observed in the spectrum of the number of photo-electrons. The distribution before fiducial cuts present an anomalous peak around 2-3 photoelectrons (see Figure 3.9). This peak stems from bad collection of the Čerenkov light, which occurs at particular kinematics. As can be seen in Figure 3.38, the peak disappears after applying fiducial cuts, which are infact meant to remove any effect coming from an inefficiency of the Čerenkov detector.

So far we have described cuts that remove the outer edges in the θ vs ϕ distribution for electron and proton. However some additional depletions were observed in the remaining data, which can be related to bad scintillator paddles. Because they are nearly ϕ independent, they can be studied most efficiently in θ vs p distributions. Sector dependent cuts were included in the cut-function for both electrons and protons to remove these inefficient regions (see Figure 3.39 and 3.40).

A complete description of the fiducial cuts, with all the formulas and tables of the various parameters used can be found in Appendix E.

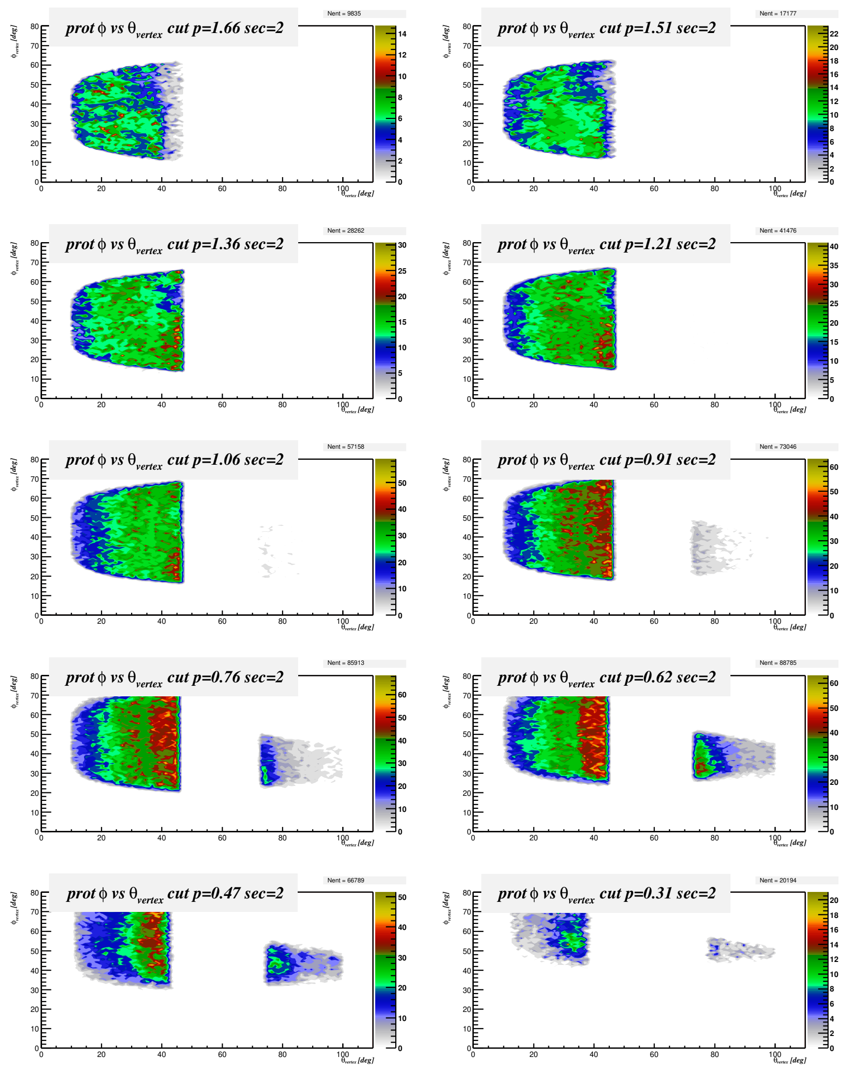

Figure 3.33: ϕ_{vertex} vs θ_{vertex} distributions for protons after loose fiducial cuts for $sector = 2$. The various plots correspond to different momentum bins. Note that ϕ_{vertex} is shifting up with decreasing momentum.

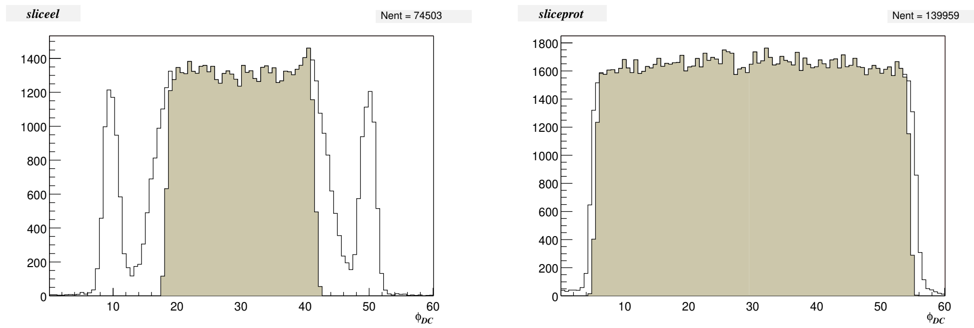

(a) (b)

Figure 3.34: Example of ϕ distributions for electron and proton for a bin in θ_{DC} and momentum. The shaded areas are the events selected by the fiducial cuts and are flat as expected. The fringes on the side of the electron spectrum are removed by the fiducial cuts.

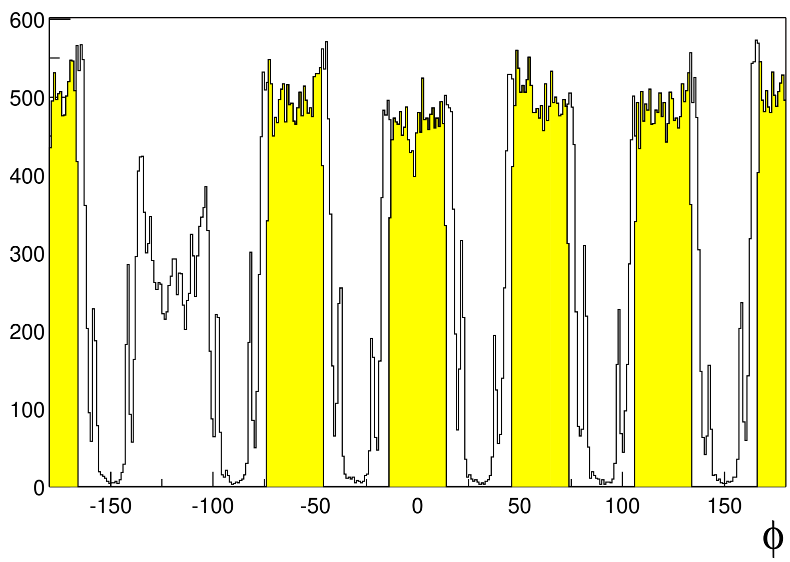

Figure 3.35: Example of the complete ϕ distribution for electrons for a bin in θ_{DC} and momentum. The fiducial cuts select regions where the distribution is flat and with the same efficency for each sector.

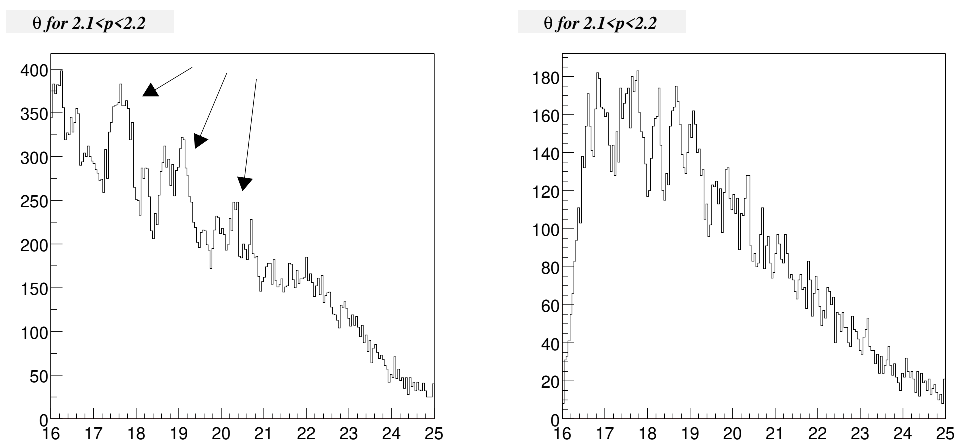

(a) before cut   (b) after cut

Figure 3.36: θ of the electron before and after fiducial cuts for the momentum bin 2.1 GeV/c $< p <$ 2.2 GeV/c in sector 1. The peaks appearing every 1.5° indicated by the arrows in figure (a) disappear after applying fiducial cut. Note that the plot presents small peaks with higher frequency (0.4°) which are not due to the Čerenkov counters and start to appear when the momentum is binned in intervals less than 0.1 GeV/c. Studies were undertaken to investigate the reason for these oscillations however the problem has not been understood [37].

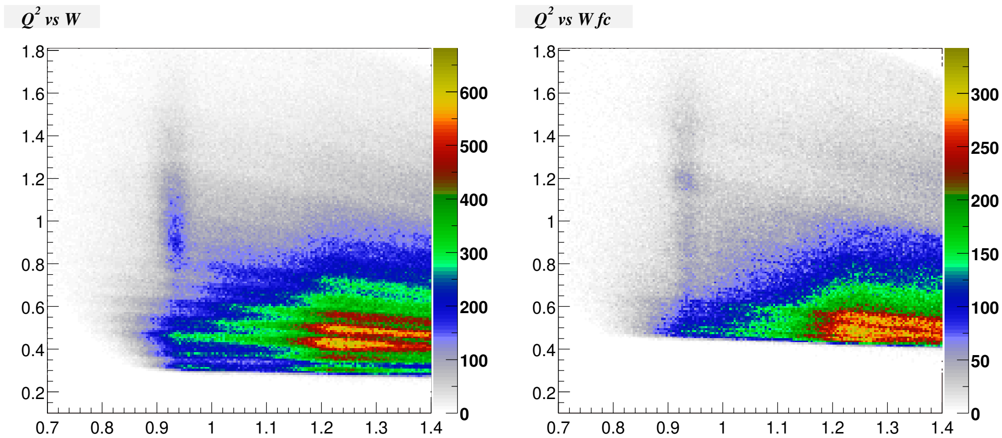

(a) before cuts (b) after cuts

Figure 3.37: Q^2 *vs* W before and after fiducial cuts. The striations in Q^2 are removed achieving the expected smoothness. Note that the fiducial cuts reduce the range in Q^2, and in particular the low Q^2 region is strongly affected, since forward electrons are removed. The band that appears after the cuts is due to an inefficient scintillator in one of the sectors.

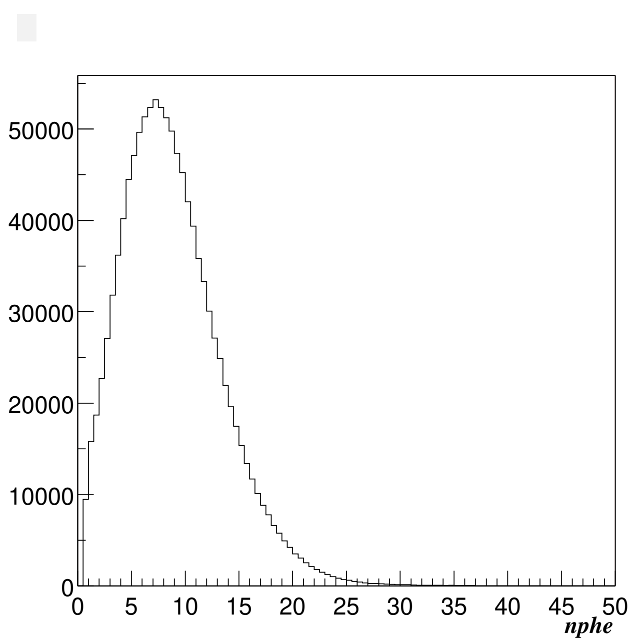

Figure 3.38: Number of photoelectrons detected in the Čerenkov Counter after fiducial cuts. The peak at 1-2 photoelectrons present in Figure 3.9 disappears after applying the fiducial cuts.

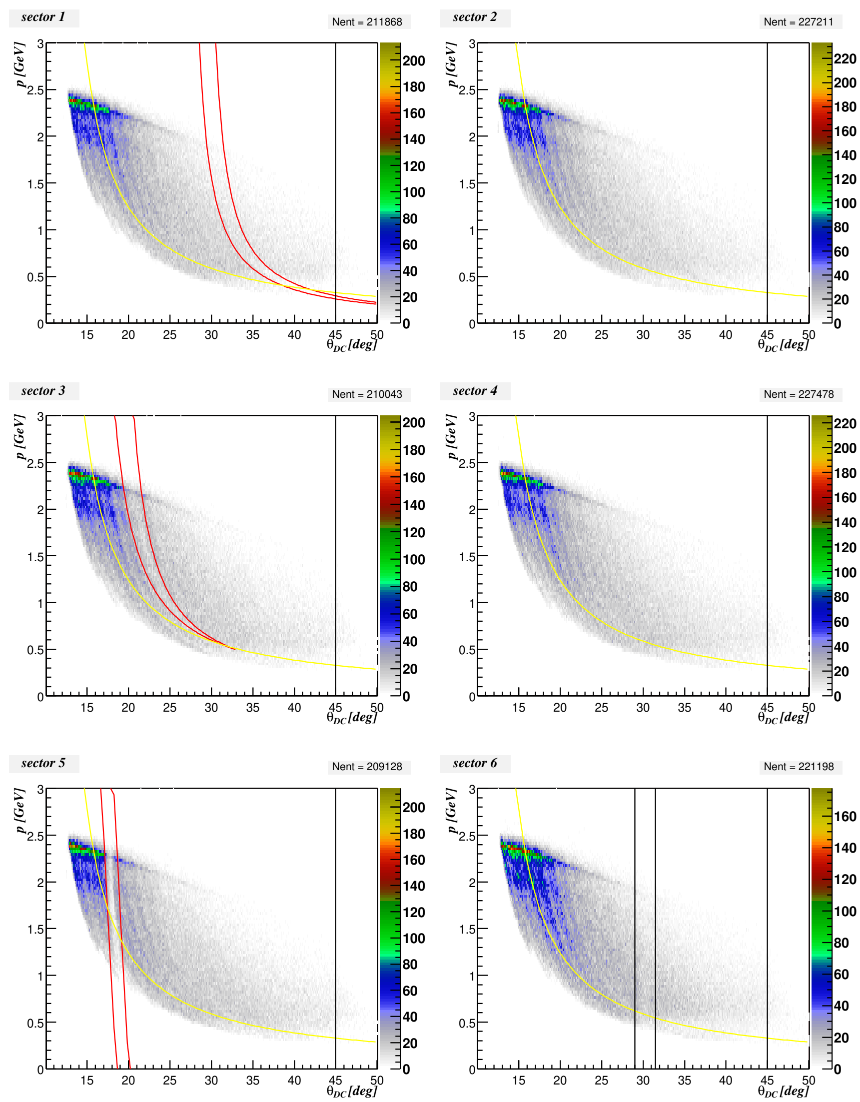

Figure 3.39: p *vs* θ_{DC} **for electron events for the six sectors. Holes were found in sector 1, 3 and 5. The red lines show the cuts applied to remove these inefficiencies. The yellow lines represent θ_{cut} of equation 3.14. The vertical black line at 45° is a cutoff applied to the data to remove very low momentum events.**

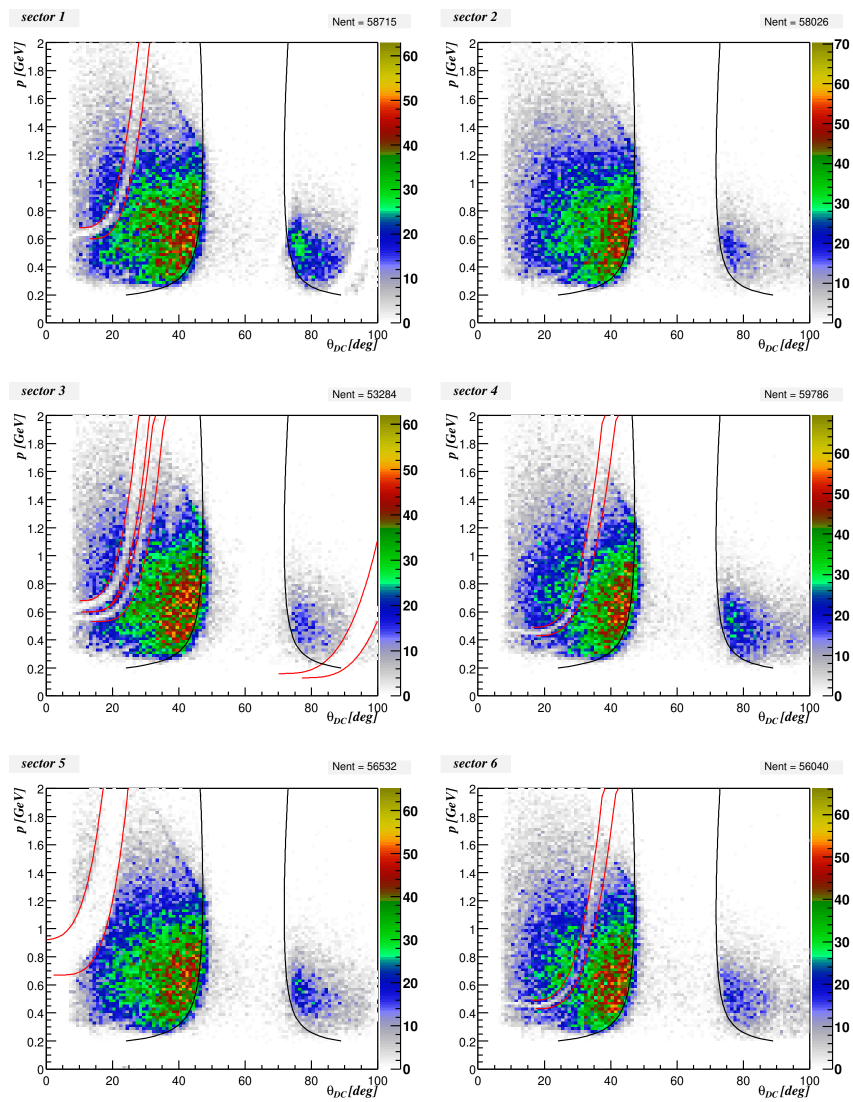

Figure 3.40: p vs θ_{DC} for proton events for the six sectors. Holes were found in sector 1, 3, 4, 5 and 6. The red lines show the cuts applied to remove these inefficiencies. The black lines represent the cut applied to remove events close to the coils.

CHAPTER 4
DATA ANALYSIS

4.1 Definitions of the asymmetries A_e, A_t and A_{et}

The object of the present analysis is the extraction of the asymmetries

$$A_e \equiv \frac{\sigma_e}{\sigma_0} \qquad A_t \equiv \frac{\sigma_t}{\sigma_0} \qquad A_{et} \equiv \frac{\sigma_{et}}{\sigma_0} \tag{4.1}$$

where the terms σ_0, σ_e, σ_t and σ_{et} are the cross sections introduced in the first chapter. The number of events for the various beam and target helicity combinations are related to these cross sections, however they need to be combined in a proper way in order to give a result that depends only on these quantities and not on experimental variables like the value of the beam and target polarizations or the Faraday cup. The definitions of the three asymmetries in terms of the experimental quantities is therefore a crucial point of the analysis.

In general the number of events for scattering with both polarized target and polarized beam can be related to the total cross section by the following formulas

$$N = D(\sigma_0 + P_e\sigma_e + P_t\sigma_t - P_eP_t\sigma_{et}) \tag{4.2}$$

where D is related to the luminosity L by the equation

$$D = \int L(t)dt = \frac{N_0\rho x}{Ae^-}\int I(t)dt = \frac{N_0\rho x}{Ae^-}Q \tag{4.3}$$

in which $I(t)$ is the beam current, e^- the electron charge, N_0 is the Avogadro constant, ρ the target density, x the thickness of the target, A the atomic number, t is the time and $\int I(t)dt = Q$ is the total accumulated charge. For each helicity configuration the number of events can therefore be written as

$$\begin{aligned}
N_{\uparrow\uparrow} &= D_1(\sigma_0 + \sigma_0^N + P_e^a\sigma_e + P_e^a\sigma_e^N + P_t^a\sigma_t - P_e^a P_t^a\sigma_{et}) \\
N_{\downarrow\uparrow} &= D_2(\sigma_0 + \sigma_0^N - P_e^a\sigma_e - P_e^a\sigma_e^N + P_t^a\sigma_t + P_e^a P_t^a\sigma_{et}) \\
N_{\uparrow\downarrow} &= D_3(\sigma_0 + \sigma_0^N + P_e^b\sigma_e + P_e^b\sigma_e^N - P_t^b\sigma_t + P_e^b P_t^b\sigma_{et}) \\
N_{\downarrow\downarrow} &= D_4(\sigma_0 + \sigma_0^N - P_e^b\sigma_e - P_e^b\sigma_e^N - P_t^b\sigma_t - P_e^b P_t^b\sigma_{et})
\end{aligned} \tag{4.4}$$

where the arrows in $N_{\uparrow\uparrow}$ $N_{\uparrow\downarrow}$ $N_{\downarrow\uparrow}$ and $N_{\downarrow\downarrow}$ indicate the beam and the target polarizations, respectively. Since the target was the same for all configurations the parameters D_1 through D_4 differ only by the total accumulated charge Q. P_e^a and P_t^a are the beam and target polarizations for runs with positive polarized target and P_e^b and P_t^b for negative target polarization runs. The beam polarizations for the groups ($N_{\uparrow\uparrow}$,$N_{\downarrow\uparrow}$), and ($N_{\uparrow\downarrow}$,$N_{\downarrow\downarrow}$) are assumed to be equal because for the beam the polarization was actually flipped every half second and therefore each pair was taken at the same time. On the other hand the target polarization was changed on a timescale of several days and therefore the beam polarization could be different during these two run periods. The terms σ_0, σ_e, σ_t and σ_{et} represent the cross sections for scattering of polarized electrons on a polarized proton in the $^{15}NH_3$ target, while the terms σ_0^N and σ_e^N were added to take into account that there are additional contributions coming from the 7 unpolarized protons bound in the nitrogen nucleus. To extract the asymmetries linear combinations of the four terms are needed where the parameters of the combinations are chosen in a way that the quantities related to the experiment, such as the accumulated charge and the polarization, drop out.

Let us define for simplicity:

$$\begin{aligned}
\overline{N_{\uparrow\uparrow}} &\equiv \frac{D_2}{D_1} N_{\uparrow\uparrow} \\
\overline{N_{\downarrow\uparrow}} &\equiv N_{\downarrow\uparrow} \\
\overline{N_{\uparrow\downarrow}} &\equiv N_{\uparrow\downarrow} \\
\overline{N_{\downarrow\downarrow}} &\equiv \frac{D_3}{D_4} N_{\downarrow\downarrow}
\end{aligned} \tag{4.5}$$

It can then be easily proven that

$$
\begin{aligned}
A_e \sim \frac{\sigma_e + \sigma_e^N}{\sigma_0 + \sigma_0^N} &= \frac{1}{P_e^a} \frac{(\overline{N_{\uparrow\uparrow}} - \overline{N_{\downarrow\uparrow}}) + d\alpha_{et}(\overline{N_{\uparrow\downarrow}} - \overline{N_{\downarrow\downarrow}})}{(\overline{N_{\uparrow\uparrow}} + \overline{N_{\downarrow\uparrow}}) + d\alpha_t(\overline{N_{\uparrow\downarrow}} + \overline{N_{\downarrow\downarrow}})} \\
A_t = \frac{\sigma_t}{\sigma_0} &= \frac{1}{P_t^b} \frac{(\overline{N_{\uparrow\uparrow}} + \overline{N_{\downarrow\uparrow}}) - d(\overline{N_{\uparrow\downarrow}} + \overline{N_{\downarrow\downarrow}})}{(\overline{N_{\uparrow\uparrow}} + \overline{N_{\downarrow\uparrow}}) + d\alpha_t(\overline{N_{\uparrow\downarrow}} + \overline{N_{\downarrow\downarrow}}) - D_2\sigma_0^N} \qquad (4.6) \\
A_{et} = \frac{\sigma_{et}}{\sigma_0} &= \frac{1}{P_e^a P_t^b} \frac{-(\overline{N_{\uparrow\uparrow}} - \overline{N_{\downarrow\uparrow}}) + d\alpha_e(\overline{N_{\uparrow\downarrow}} - \overline{N_{\downarrow\downarrow}})}{(\overline{N_{\uparrow\uparrow}} + \overline{N_{\downarrow\uparrow}}) + d\alpha_t(\overline{N_{\uparrow\downarrow}} + \overline{N_{\downarrow\downarrow}}) - D_2\sigma_0^N}
\end{aligned}
$$

where

$$
\begin{aligned}
\alpha_{et} &= \frac{P_e^a P_t^a}{P_e^b P_t^b} \\
\alpha_e &= \frac{P_e^a}{P_e^b} \\
\alpha_t &= \frac{P_t^a}{P_t^b} \qquad (4.7) \\
d &= \frac{D_2}{D_3}
\end{aligned}
$$

In order to use these formulas the quantities α_{et}, α_e, α_t, d, P_e^a, P_t^b, $P_e^a P_t^b$, $\frac{D_2}{D_1}$, $\frac{D_3}{D_4}$ and $D_2\sigma_0^N$ need to be calculated from measured experimental quantities. The beam polarization P_e^a and P_e^b were equal to $70.74 \pm 1.04\%$ constantly throughout the experiment and therefore $\alpha_e = 1 \pm 0.03$. The product of the polarizations $P_e^a P_t^a$ and $P_e^b P_t^b$ can be extracted from the data using a procedure that will be described in section 4.5. This allows one to calculate P_t^a, P_t^b and α_{et} which is equal to α_t since $P_e^a = P_e^b$. The ratios $\frac{D_2}{D_1}$ and $\frac{D_3}{D_4}$ can be determined using the Faraday cup measurement. In particular, the values evaluated by the program "HelP" were used (see section 3.3). The factor d can be found in two alternative ways. The first method is to take just the ratio of the Faraday cup readings. However this method is not accurate, since the Faraday cup determined in "HelP" was not corrected for different dead times in different run periods. The second method uses the inclusive data and will be described in section 4.2. Finally the term $D_2\sigma_0^N$ appearing in A_t and A_{et}, which is included to remove the unpolarized background coming from the nitrogen nucleus from the denominator, was estimated using data on a carbon target. The procedure how to relate $D_2\sigma_0^N$ to the number of events of the carbon target will be described in section 4.3.

4.2 Normalization of positive and negative polarized target data

As mentioned before a method to normalize the two sets of runs with different target polarizations is to use the inclusive data. In the section about the formalism it was shown that each piece of the sum $(\sigma_0 + P_e\sigma_e + P_t\sigma_t - P_eP_t\sigma_{et})$ is actually a differential cross section in the pion center of mass angles θ^* and ϕ^*. If an integration over these angles is performed over all states, the dependence on the pion variables will disappear and the result is the inclusive cross section for "inclusive" electro-production of π^0. Of the four terms in the sum, only σ_0 and σ_{et} survive after the integration since they are the only two which contain even functions of ϕ^* as can be seen in equations 1.17. The number of events in the case of inclusive scattering for pion production is therefore in general given by

$$N = D(\sigma_0 - P_eP_t\sigma_{et}) \tag{4.8}$$

where the notation σ_0 and σ_{et} was used again, although these term now actually stand for the integral of the ones in the previous formulas. This simple relation can actually be shown to be valid in **general** for inclusive lepton scattering off hadrons [38]. For each helicity configuration the number of events can therefore be written as

$$\begin{aligned}
N_{\uparrow\uparrow} &= D_1(\sigma_0 + \sigma_0^N - P_e^aP_t^a\sigma_{et}) \\
N_{\downarrow\uparrow} &= D_2(\sigma_0 + \sigma_0^N + P_e^aP_t^a\sigma_{et}) \\
N_{\uparrow\downarrow} &= D_3(\sigma_0 + \sigma_0^N + P_e^bP_t^b\sigma_{et}) \\
N_{\downarrow\downarrow} &= D_4(\sigma_0 + \sigma_0^N - P_e^bP_t^b\sigma_{et})
\end{aligned} \tag{4.9}$$

It can be easily shown that

$$d = \frac{D_2}{D_3} = \frac{\frac{D_2}{D_1}N_{\uparrow\uparrow} + N_{\downarrow\uparrow}}{N_{\uparrow\downarrow} + \frac{D_3}{D_4}N_{\downarrow\downarrow}} \tag{4.10}$$

and

$$\alpha_{et} = \frac{1}{d}\frac{\frac{D_2}{D_1}N_{\uparrow\uparrow} - N_{\downarrow\uparrow}}{N_{\uparrow\downarrow} - \frac{D_3}{D_4}N_{\downarrow\downarrow}} \tag{4.11}$$

To apply this procedure the inclusive W spectra for the various helicity combinations were considered. According to equation 4.10, the numerator and the denominator were properly calculated using the ratios $\frac{D_2}{D_1}$ and $\frac{D_3}{D_4}$ where the values for D_1 through D_4, as previously mentioned in section 3.3 were determined from the Faraday cup measurements. Finally the ratio of the integrals of the two resulting spectra was calculated.

A problem in this procedure was encountered. The shape of the two spectra was found to be slightly different although it is expected to be the same (see Figure 4.1). A possible explanation of this effect is that the two sets of runs have slightly different set of calibration constants and therefore the width of the two peaks is different. Another possible cause is that there is a small shift in electron momentum between the two sets due to momentum corrections which were optimized using only a few runs. In case both these effects are the cause of this difference, one can expect that the total area of subtraction of the two distributions is zero. The integral of the curve in Figure 4.1(b) is 257 ± 7817 which is compatible with zero.

4.3 Carbon normalization

As can be seen from equation 4.6 in order to extract the asymmetries A_t and A_{et} the nuclear background coming from reaction on ^{15}N nuclei (the term $D_2\sigma_0^N$ in equation 4.6) needs to be removed. The only way to separate the contributions from scattering on H and ^{15}N is to have data taken with a second target that, of course, behaves like ^{15}N. For this reason data on a ^{12}C target were taken, since ^{12}C is fairly similar to ^{15}N and therefore the Fermi motion can be assumed to be almost the same. The advantage of this kind of target compared to a pure ^{15}N target is from a technical point of view. The disadvantage is that the two targets have a different ratio of protons to neutrons and therefore they behave slightly different. In particular, in the case of exclusive reactions where the proton is identified, the problem is that even scaling one of the two spectra in order to adjust

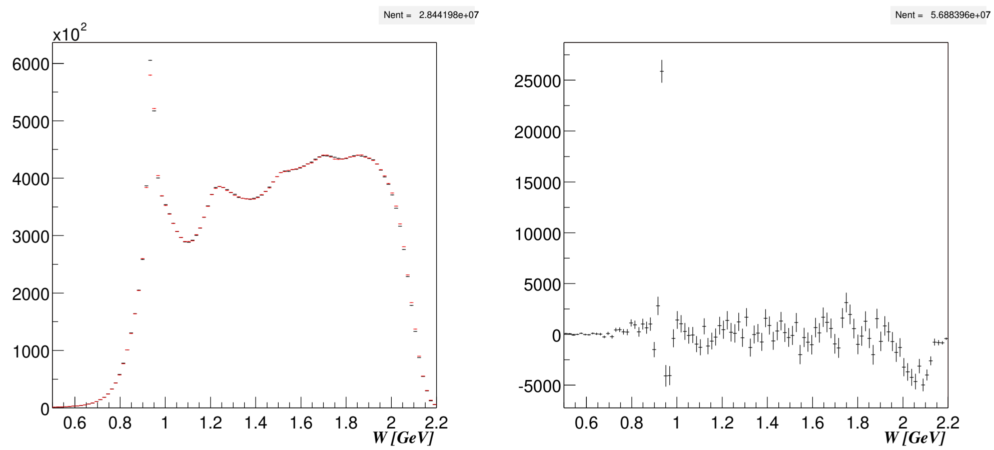

(a) Overlay (b) Difference

Figure 4.1: The left figure shows the overlay of inclusive W spectra for positive (black) and negative (red) target polarization data. The two spectra are normalized to each other using the total number of events of the spectra themselves. The right plot shows the difference of the two W spectra. The shape of the two is expected to be the same, but in the region of the elastic and at very high W the difference is not zero.

for the different number of protons, scattering on neutrons becomes important at higher W. Because the ratio of protons to neutrons is different the scaling factor found in the elastic region, where the only possible reaction is $ep \to e'p'$, is not valid anymore. At higher W, for example, in the $\Delta(1232)$ region, events with a proton in the final state can come from the reaction $e + p \to e' + \Delta^+ \to e' + p + \pi^0$ as well as $e + n \to e' + \Delta^0 \to e' + p + \pi^-$ and from non-resonant background.

In the following two subsections a detailed discussion of how to estimate the term $D_2\sigma_0^N$ using the ^{12}C data in the elastic region and in the $\Delta(1232)$ region will be given. In particular it will be described how to find the normalization factor C where C is such that

$$CN^C = D_2\sigma_0^N \tag{4.12}$$

where N^C is the number of events from scattering on the carbon target.

4.3.1 Elastic region normalization

The normalization in the elastic region was considered for two reason. First because it is possible to find the scaling factor in four different ways, therefore offering the possibility to make consistency checks. Secondly because one the possibilities to calculate the normalization in the $\Delta(1232)$ region is to apply a correction to the constant found in the elastic region.

The four methods to normalize the carbon in the elastic region are using:

- the tail of the W inclusive spectrum (0.6 GeV/$c^2 < W < 0.85$ GeV/c^2)
- the tail of the W exclusive spectrum (0.6 GeV/$c^2 < W < 0.85$ GeV/c^2)
- the tails of $|\phi_e - \phi_p|$
- the M_X^2 tail

The first two methods rely on the fact that there is no scattering off the free protons for $W < 0.85$ GeV/c^2 [9] and therefore all the events found in the W spectrum of the $^{15}NH_3$ target come only from scattering on the ^{15}N nucleons. Therefore one can use the ratio of the integrals of the tails of the ^{15}N and ^{12}C W spectra, $I(^{15}N)$ and $I(^{12}C)$, respectively to find the normalization constant C as

$$C = \frac{I(^{15}N)}{I(^{12}C)} \tag{4.13}$$

The reason the integral uses only $W > 0.6$ GeV/c^2 and not all the tail, is that it was found that at very low W the tails have a slightly different shape due to the fact that in this region one is sensitive for example to differences in the binding energy.

The ratio obtained in the inclusive case need to be corrected if one wants to use the exclusive channel. The correction factor can be determined in the following way. The number of inclusive events on $^{15}NH_3$ (where only ^{15}N is contributing)

[9] Note that scattering off free protons ideally does not occur below $W < 0.938$ GeV/c^2 (mass of the proton), however because of detector resolution tails extend to $W \sim 0.85$ GeV/c^2

and ^{12}C can be written as

$$\begin{aligned} N^N &= D_2(7\sigma_p + 8\sigma_n) \\ N^C &= D_c(6\sigma_p + 6\sigma_n) \end{aligned} \tag{4.14}$$

where σ_p and σ_n are the cross sections on the proton and neutron respectively, and D_c is the "dose" for the carbon. The ratio of the two integrals is therefore

$$C_{inc} = \frac{D_2}{D_c}\frac{7\sigma_p + 8\sigma_n}{6\sigma_p + 6\sigma_n} \sim \frac{1}{0.8}\frac{D_2}{D_c} \tag{4.15}$$

Note that the ratio $\frac{7+8R}{6+6R}$ with $R = \frac{\sigma_n}{\sigma_p}$ is varying slowly as a function of R in the kinematical region under consideration. The value $\frac{1}{0.8}$ which results from the assumption $R = \frac{\sigma_n}{\sigma_p} = 1$, was considered for simplicity. A study of the systematic errors, using small variations in this ratio will be performed at a later stage.

For the exclusive case one has

$$\begin{aligned} N^N &= D_2(7\sigma_p) \\ N^C &= D_c(6\sigma_p) \end{aligned} \tag{4.16}$$

and therefore

$$C_{exc} = \frac{D_2}{D_c}\frac{7}{6} \tag{4.17}$$

The relation between C_{inc} and C_{exc} is then

$$C_{exc} = \frac{7}{6}0.8C_{inc} \tag{4.18}$$

Figures 4.2(a) and 4.2(b) show the inclusive and exclusive W spectra for $^{15}NH_3$ (black) and ^{12}C (red) data after the normalization procedures just described. As can be seen the tails from 0.6 GeV/c^2 to 0.85 GeV/c^2 have the same shape, whereas the higher W region looks very different for both data sets due to the presence of scattering off the free protons.

The third method uses the fact that elastic scattering of electrons off free protons occurs in a plane, meaning all four-momenta are in the same plane. Plotting

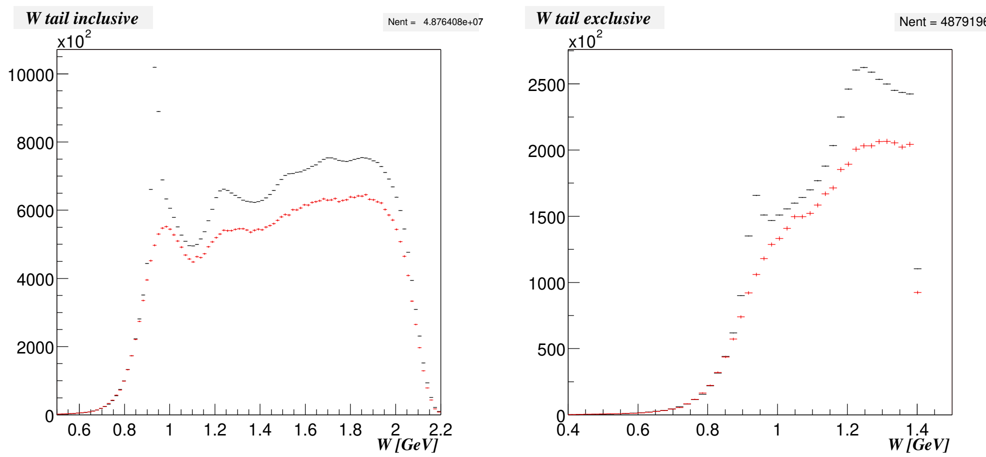

(a) inclusive (b) exclusive

Figure 4.2: Inclusive and exclusive W spectra for $^{15}NH_3$ (black) and ^{12}C (red). The spectra are normalized to each other using the integrals of the W tails in the range 0.6 GeV/c^2 to 0.85 GeV/c^2. Note that the elastic peak in the exclusive W spectrum is much smaller than the peak in the inclusive one due to the presence of the coils of the target magnet which block protons at angles $45° < \theta < 80°$.

the difference $|\phi_e - \phi_p|$ [10] a sharp peak around 180° can be observed for elastic events. On the other hand elastic scattering on bound protons does not have such a high correlation due to the fact that bound nucleons are moving inside the nucleus. It turns out that the plot $|\phi_e - \phi_p|$ for data on ^{15}N presents a sharp peak sitting on a broad Gaussian distribution (see Figure 4.3(a)). The two tails come only from scattering on ^{15}N and, similarly to the case of the W tail, one can calculate the ratio of the integrals of the tails for $^{15}NH_3$ and ^{12}C data to determine C_{exc}. The integrals are the sum of the integrals of the left ($170.° < |\phi_e - \phi_p| < 176°$) and right tail ($184° < |\phi_e - \phi_p| < 190°$).

Finally, the last method uses the M_X^2 spectrum. This spectrum in the elastic region (0.842 GeV/c^2 $< W <$ 1.022 GeV/c^2) presents a peak around zero corresponding to elastic events and a long negative tail corresponding to quasi-

[10] The quantity that was actually considered was $|\phi_e - \phi_p - 1.5°|$. The additional 1.5° are applied to account for a difference in tracking between electrons and protons

elastic events (see Figure 4.3(b)). The reason for the negative tail is that in the M_X^2 calculation the proton is treated always as free and the Fermi motion and binding energy was not taken into account. The tail again comes only from ^{15}N and the constant C_{exc} was found as the ratio of the integrals using the range $-0.6\ \mathrm{GeV}^2/c^4 < M_X^2 < -0.1\ \mathrm{GeV}^2/c^4$.

Figures 4.3 show, similarly to Figures 4.2 the carbon normalized to the $^{15}NH_3$ data using the respective methods. As can be seen the tails where the normalization is done have again the same shape. The four constants are listed in Table 4.1 where

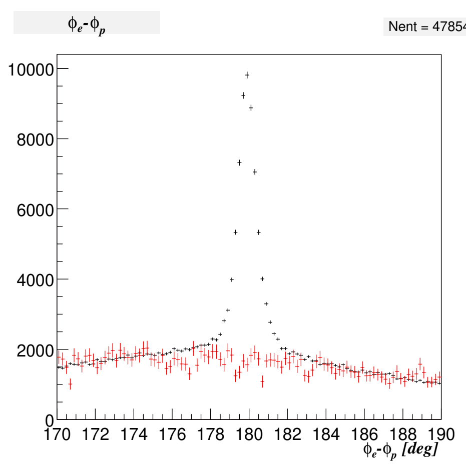

(a) scattering in plane

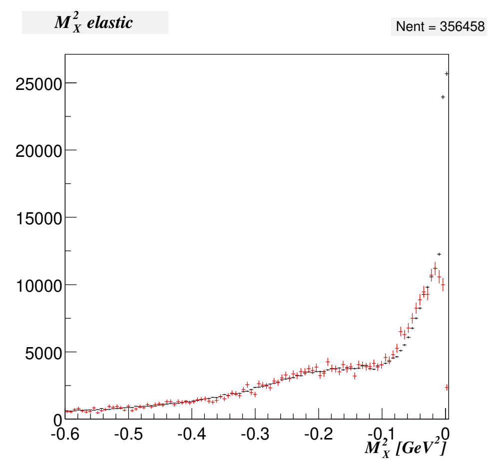

(b) missing mass squared

Figure 4.3: The left plot shows the $^{15}NH_3$ (black) and ^{12}C (red) $|\phi_e - \phi_p|$ spectra normalized to each other using the two tails. The elastic region was selected by applying a cut in the invariant mass W: 0.85 GeV/c^2 $< W <$ 0.95 GeV/c^2. The right plot shows the $^{15}NH_3$ (black) and ^{12}C (red) M_X^2 spectra in the elastic region (0.842 GeV/c^2 $< W <$ 1.022 GeV/c^2) normalized to each other using the negative M_X^2 tail. These two methods are possible since the ^{12}C and $^{15}NH_3$ spectra have the same shape in the tails.

the error is purely statistical. Using equation 4.18 one can calculate the constant C_{exc} for the inclusive method

$$C_{exc} = 0.8\frac{7}{6}(15.63 \pm 0.07) = 14.59 \pm 0.06 \tag{4.19}$$

Inclusive method	C_{inc}	$\Delta(C_{inc})$
W tail inclusive	15.63	0.07
Exclusive methods	C_{exc}	$\Delta(C_{exc})$
W tail exclusive	14.9	0.2
scattering in plane tails	18.0	0.3
M_X^2	17.0	0.2

Table 4.1: Normalization constants for the elastic region calculated with different methods

As can be seen only the two methods using the W tails agree with each other within the statistical error. The difference between the first two and the other methods will be studied later as a systematic effect.

4.3.2 $\Delta(1232)$ region normalization

As discussed at the beginning of this section the normalization in the $\Delta(1232)$ region is a non trivial problem. Above the pion production threshold events with final state $e' + p + X$ can come from either scattering on the proton or the neutron. Since ^{15}N and ^{12}C nuclei have different ratios of protons to neutrons, the shapes of the W spectra can be different depending on the strengths of the cross sections of the various possible reactions on the two nucleons. Two methods were identified as a solution to determine the constant C in the $\Delta(1232)$ region:

- The tail of the M_X^2 distribution in the $\Delta(1232)$ region
- A correction of the constant found in the elastic region

The first method is basically the same as the one described for the elastic region. The $\Delta(1232)$ decays into a pion and a nucleon and therefore the missing mass spectrum shows a peak around the pion mass. Because of the nuclear background, the peak has, as in the case of elastic scattering, a long negative tail, and therefore it is possible to normalize ^{12}C and $^{15}NH_3$ data using the ratio of the integrals of the two tails. Figure 4.4 show the M_X^2 spectrum of the ^{12}C (and $^{15}NH_3$) data after normalization. The second method uses physics arguments to find a correction

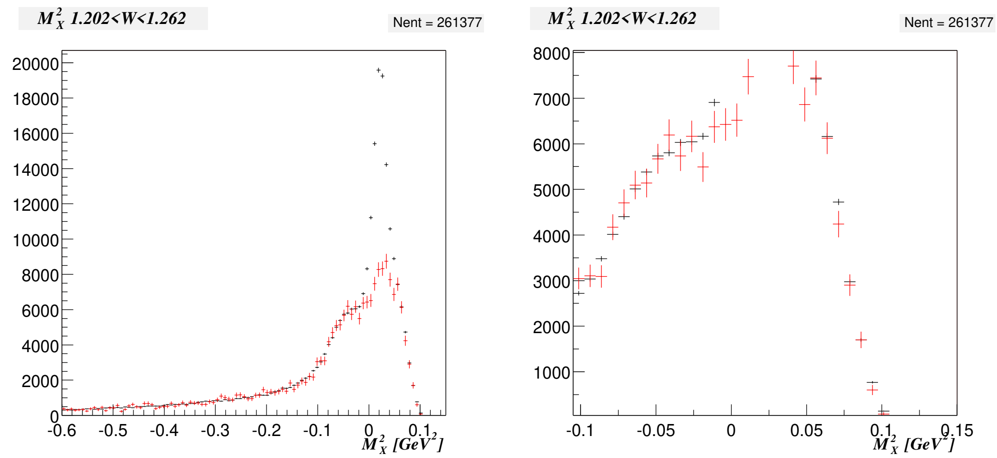

(a) full range (b) zoomed around the peak

Figure 4.4: $^{15}NH_3$ (black) and ^{12}C (red) M_X^2 spectra normalized to each other using the left tail. The right plot is an enlargement of the left one in the region of the pion and quasi-elastic peak. As in the elastic case the two tails have the same shape.

factor to the constant C found in the elastic region. More precisely, this factor is calculated estimating the strengths of the proton and neutron contributions using the fact that the $\Delta(1232)$ has isospin $\frac{3}{2}$ and the Clebsch-Gordan decomposition. For scattering of electrons off protons and neutrons Δ^+ and Δ^0 can be produced which can then decay in the following ways:

$$ep \to e\Delta^+ \to \begin{cases} ep\pi^0 \\ en\pi^+ \end{cases} \tag{4.20}$$

$$en \to e\Delta^0 \to \begin{cases} ep\pi^- \\ en\pi^0 \end{cases} \tag{4.21}$$

The Δ^+ is a $\left|J, J_3\right\rangle = \left|\frac{3}{2}, \frac{1}{2}\right\rangle$ isospin state, while the Δ^0 has $\left|\frac{3}{2}, -\frac{1}{2}\right\rangle$. The strengths of the previous decay channels can be found using the Clebsch-Gordan decomposition

$$
\begin{array}{ccccc}
\Delta^0 & \rightarrow & n\pi^0 & + & p\pi^- \\
\left|\frac{3}{2},-\frac{1}{2}\right\rangle & \rightarrow & \sqrt{\frac{2}{3}}\left|\frac{1}{2},-\frac{1}{2}\right\rangle\left|1,0\right\rangle & + & \sqrt{\frac{1}{3}}\left|\frac{1}{2},\frac{1}{2}\right\rangle\left|1,-1\right\rangle
\end{array}
$$

$$
\begin{array}{ccccc}
\Delta^+ & \rightarrow & p\pi^0 & + & n\pi^+ \\
\left|\frac{3}{2},\frac{1}{2}\right\rangle & \rightarrow & \sqrt{\frac{2}{3}}\left|\frac{1}{2},\frac{1}{2}\right\rangle\left|1,0\right\rangle & + & \sqrt{\frac{1}{3}}\left|\frac{1}{2},-\frac{1}{2}\right\rangle\left|1,1\right\rangle
\end{array}
$$

From the previous formulas it is obvious that

$$
\begin{aligned}
\sigma^{inc}(\Delta^0) &= \sigma(\Delta^0 \rightarrow p\pi^-) + \sigma(\Delta^0 \rightarrow n\pi^0) && (4.22)\\
&= \frac{1}{3}\sigma^{inc}(\Delta^0) \quad + \quad \frac{2}{3}\sigma^{inc}(\Delta^0) && (4.23)
\end{aligned}
$$

and

$$
\begin{aligned}
\sigma^{inc}(\Delta^+) &= \sigma(\Delta^+ \rightarrow p\pi^0) + \sigma(\Delta^+ \rightarrow n\pi^+) && (4.24)\\
&= \frac{2}{3}\sigma^{inc}(\Delta^+) \quad + \frac{1}{3}\sigma^{inc}(\Delta^+) && (4.25)
\end{aligned}
$$

The number of events for ^{15}N and ^{12}C when the proton is detected in the final state is therefore given by

$$
\begin{aligned}
N^N &= D_2\big[7\sigma(\Delta^+ \rightarrow p\pi^0) + 8\sigma(\Delta^0 \rightarrow p\pi^-)\big]\\
N^C &= D_c\big[6\sigma(\Delta^+ \rightarrow p\pi^0) + 6\sigma(\Delta^0 \rightarrow p\pi^-)\big]
\end{aligned} \tag{4.26}
$$

which, according to the equations 4.23 and 4.25 become

$$
\begin{aligned}
N^N &= D_2(7\frac{2}{3}\sigma^{inc}(\Delta^+) + 8\frac{1}{3}\sigma^{inc}(\Delta^0))\\
N^C &= D_c(6\frac{2}{3}\sigma^{inc}(\Delta^+) + 6\frac{1}{3}\sigma^{inc}(\Delta^0))
\end{aligned} \tag{4.27}
$$

It has been experimentally observed [39, 40] that $\sigma^{inc}(\Delta^+) = \sigma^{inc}(\Delta^0) \equiv \sigma^{inc}(\Delta)$ since it was found that the inclusive cross section for the $\Delta(1232)$ scales with the number of nucleons A . It turns out that in the $\Delta(1232)$ region:

$$
\frac{N^N}{N^C} = \frac{D_2}{D_c}\frac{7\frac{2}{3}\sigma^{inc}(\Delta) + 8\frac{1}{3}\sigma^{inc}(\Delta)}{6\frac{2}{3}\sigma^{inc}(\Delta) + 6\frac{1}{3}\sigma^{inc}(\Delta)} = \frac{D_2}{D_c}\frac{22}{18} \tag{4.28}
$$

where the factor $\frac{D_2}{D_c}$ can be determined using the elastic region

$$\frac{D_2}{D_c} = C_{exc}\frac{6}{7} \tag{4.29}$$

or

$$\frac{D_2}{D_c} = 0.8C_{inc} \tag{4.30}$$

(see equation 4.17 and 4.18 in section 4.3.1).
Figure 4.5 (a) shows the normalized M_X^2 spectra of ^{12}C (red) and $^{15}NH_3$ (black) using the exclusive W tail method described earlier. As can be seen the ^{12}C distribution seems to be too low in practically all bins, which is clear indication that a correction is needed. After correcting the normalization constant according to $C_{corr} = \frac{6}{7}\frac{22}{18}C_{exc}$ the result is very similar to the one obtained using the M_X^2 tail method (Figures 4.4(b) and 4.5 (b)) The numerical values of the constants are listed in Table 4.2. These methods neglect the non resonant background which, in

method	C_{exc}	$\Delta(C_{exc})$
W tail inclusive	15.63	0.07
W tail inclusive corr	15.28	0.07
W tail exclusive	14.9	0.2
W tail exclusive corr	15.6	0.2
M_X^2	16.1	0.3

Table 4.2: Normalization constants for the $\Delta(1232)$ region calculated with different methods.

the case of the π^0 channel, is small, but large for the $\pi^{\pm}$ channels.

4.4 Fill factor

The methods described in section 4.3 rely on the fact that the ^{15}N and ^{12}C spectra have the same shape. This would be a reasonable assumption if the scattering was only on $^{15}NH_3$ and ^{12}C, however there is also a significant contribution from the helium of the cooling bath the targets are immersed in. This causes differences in the two spectra, since the two targets, $^{15}NH_3$ and ^{12}C, have different

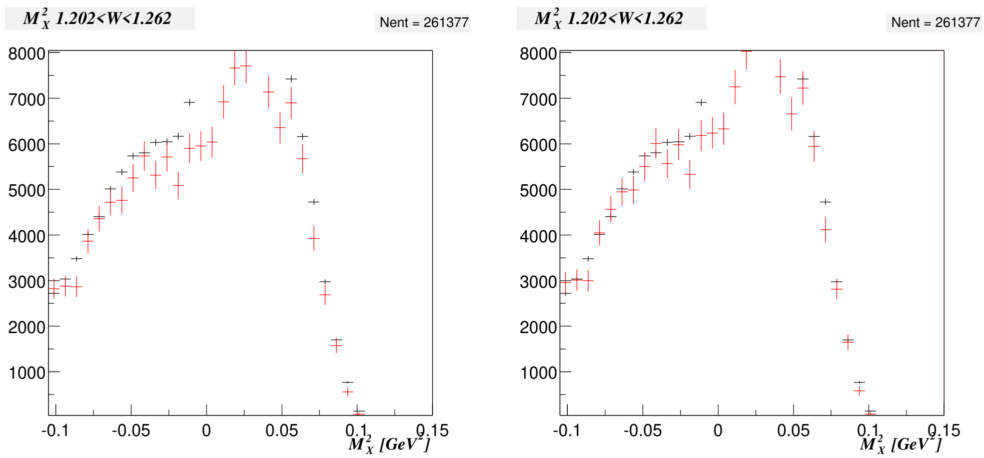

(a) uncorrected

(b) corrected

Figure 4.5: Normalized $^{15}NH_3$ (black) and ^{12}C (red) M_X^2 spectra. The left plot uses the constant found by normalizing the W exclusive tails. Almost all the points of the carbon are below the $^{15}NH_3$ ones, which means that the constant is underestimated. In the right plot the constant was corrected with the factor found by means of the Clebsch Gordan decomposition. After the correction the two shapes match better.

thickness and therefore displace different amounts of ^4He. In addition the shape of the carbon and helium W spectra are not the same (see Figure 4.6). A technique was developed to estimate the amount of helium in the two targets and, using the data on the empty target, the carbon spectrum was adjusted in order to have the same amount of helium as in $^{15}NH_3$ data. The technique is the following. The background spectrum N^{BG} can be constructed as

$$N^{BG} = aN^C + bN^E \tag{4.31}$$

where N^C and N^E stand for number of events from carbon and empty target respectively and a and b are the two values that are sought. These values are calculated imposing the constraint that the total amount of helium events is the same for the background and for the $^{15}NH_3$ data. The number of events can be written in general

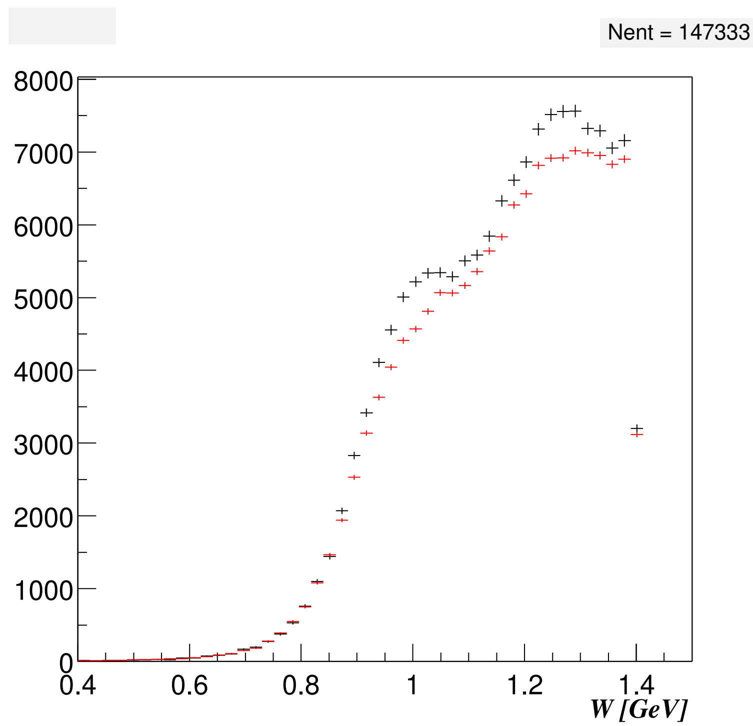

Figure 4.6: Comparison of empty target (black) and ^{12}C (red) W spectra. The two spectra have a different shapes. The empty target spectrum presents more narrow quasi-elastic and quasi-delta peaks.

as the sum of the various contributions

$$N = N^W + N^T + N^{He} \tag{4.32}$$

where N^W, N^T and N^{He} refers to the number of events coming from the scattering off the windows, off the target (either ^{12}C or $^{15}NH_3$ or nothing in case of empty target) and the helium, respectively. In general the number of events can be written as

$$N = \frac{Q}{e}\frac{\rho x}{A} N_A \sigma \tag{4.33}$$

where N_A is the Avogadro number, A the atomic weight, ρ the density of the material, x the thickness of the target, Q the total accumulated charge and e the electron charge. The number of events can therefore be written as

$$N = \frac{Q}{e} N_A \big(\frac{\rho^W x^W}{A^W} \sigma^W + \frac{\rho^T x^T}{A^T} \sigma^T + \frac{\rho^{He} x^{He}}{A^{He}} \sigma^{He} \big) \tag{4.34}$$

In the $\Delta(1232)$ region, as mentioned already in section 4.3.2, it is experimentally found that the total inclusive cross section is proportional to A and therefore one has

$$\sigma^0 \equiv \frac{\sigma^W}{A^W} = \frac{\sigma^T}{A^T} = \frac{\sigma^{He}}{A^{He}} \tag{4.35}$$

and this allows one to simplify equation 4.34

$$N = \frac{Q}{e} N_A \sigma^0 \big(\rho^W x^W + \rho^T x^T + \rho^{He} x^{He} \big) \tag{4.36}$$

in which now the number of events is simply proportional to the density times the thickness.

The densities for the window materials, carbon, helium and nitrogen are known. The thicknesses were experimentally measured. The resulting values are listed in Table 4.3. The value for $\rho^W x^W$ quoted is obtained by combining the values

Target type	x^T	$\rho^W x^W$	$\rho^T x^T$	$\rho^{He} x^{He}$ $x^{He} = L - x^T$
unit	[cm]	[g/cm^2]	[g/cm^2]	[g/cm^2]
empty	N/A	63.95	-	217.5
^{12}C	0.227	63.95	495.0	184.585
$^{15}NH_3$	0.65	63.95	525.958	123.25
$^{15}NH_3$	0.54	63.95	436.950	139.2
$^{15}NH_3$	0.582	63.95	470.935	133.11

Table 4.3: Parameters of the different target types used to determine the fill factor. The three different values for ^{15}N thickness x_T reported were determined with separate methods.

from the Kapton foil and Aluminum window that make up the window of the target cells [30]. For x^T three values are mentioned. The first one was determined fitting the data and the other two were estimated [41]. For the final calculation the first value was chosen because it is directly extracted from the data. Also, for the three values of $\rho^T x^T$ it was taken into account that the target was actually $^{15}NH_3$ and therefore containing three free protons. Each value was multiplied by a factor $\frac{15}{18}$ to correct for this.

Recalling equation 4.31 one can write the background as

$$N^{BG} = a(\rho^W x^W + \rho^C x^C + \rho^{He} x_1^{He}) + b(\rho^W x^W + \rho^{He} x_2^{He}) \qquad (4.37)$$

where x_1 and x_2 are the thicknesses of the ^4He in the ^{12}C and empty target, respectively. The number of events from $^{15}NH_3$ target can be written as

$$N^N = \rho^W x^W + \rho^N x^N + \rho^{He} x_3^{He} \qquad (4.38)$$

where x_3 is the thickness of the ^4He in the $^{15}NH_3$ target. The two conditions to determine a and b are then:

$$\rho^{He} x_3^{He} = a(\rho^{He} x_1^{He}) + b(\rho^{He} x_2^{He}) \qquad (4.39)$$

which corresponds to requiring the same amount of helium in $^{15}NH_3$ and background spectra, and

$$\rho^W x^W + \rho^N x^N = a(\rho^W x^W + \rho^C x^C) + b(\rho^W x^W) \qquad (4.40)$$

which corresponds to imposing that the window and carbon contribution cancel out with the window and nitrogen contribution [11].

Since the background spectrum was adjusted to normalize it to the same number of events it is actually not necessary to calculate the absolute values for a and b in equation 4.31. Instead the ratio $\frac{b}{a}$ is quoted and was determined to be -0.33, leading to a background spectrum as

$$N^{BG} = N^C - 0.33 N^E \qquad (4.41)$$

[11]Note that is assumed that the spectra from events coming from scattering off the windows and off the carbon target have the same shape. This assumption is reasonable considering that they are heavy nuclei.

Assuming a 10% error on the measurement of the thicknesses x^T and x^W the error on the ratio $\frac{b}{a}$ is of the order of 2.5%.

Throughout the analysis the background was constructed using the previous background constructed from the carbon and the empty target data. Figures 4.7 (a) and (b) shows the comparison and the difference between the pure carbon and the background obtained using the method described above.

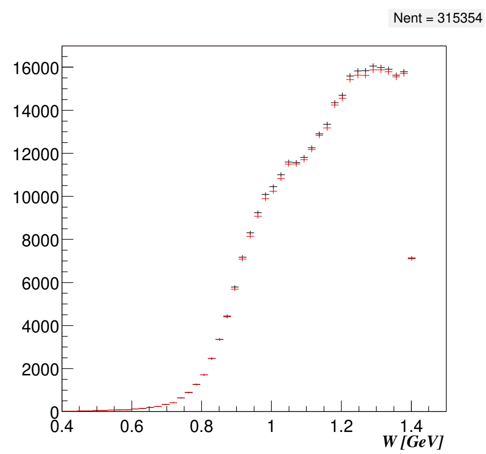

(a) Overlay

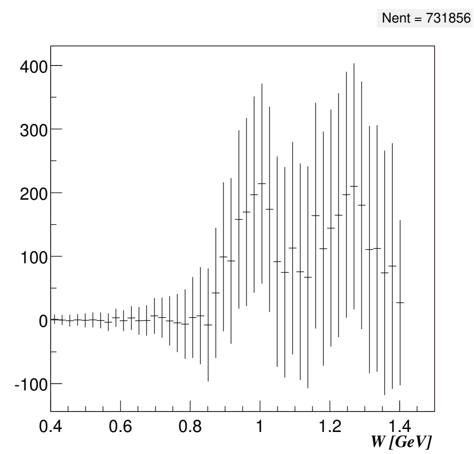

(b) difference

Figure 4.7: The left plot shows the comparison between pure carbon (black) and the background obtained using a combination of carbon and empty target data. The two histogram were normalized to each other using the integral of the tails. The right plot shows the difference between carbon and background spectra. The carbon has a more pronounced elastic and $\Delta(1232)$ peak as compared to the new background.

4.5 P_eP_t calculation

To extract the asymmetries it is necessary to know the product of the polarizations P_eP_t as seen in section 4.1 in equations 4.6 and 4.7. During the run both the beam and target polarizations were measured. However while the measurement of the beam polarization P_e is very accurate, the measurement of the target polarization P_t was unreliable. P_t was determined during the run by means of the Nuclear Magnetic Resonance (NMR). This method had some problems because the coils of the NMR system were placed too far away from the target and therefore the system was mostly sensitive to the external part of the target which was the closest to the coils [30]. For this reason a procedure to extract P_eP_t using data was studied.

A full description of the procedure can be found in CLAS-note 00-001 [42] and therefore in this section the steps that led to the result will be shown only briefly[12].

The procedure to extract the product makes use of the experimentally known single spin asymmetry, where the proton polarization is fixed, as a function of Q^2 in the elastic region (A_{theo}, see Figure 4.8). Data were divided in six Q^2 regions from

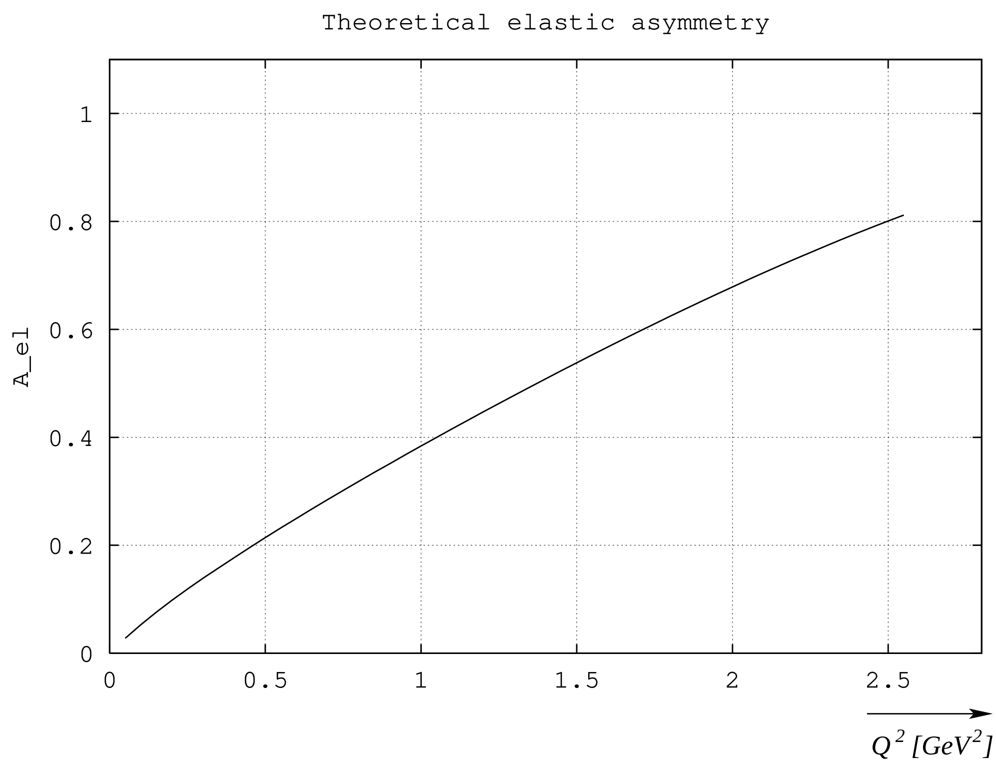

Figure 4.8: Single spin asymmetry A_{theo} with fixed proton polarization as a function of Q^2 in the elastic region.

[12]The value of P_eP_t depends on the runs used for the analysis. In this section the following positive target polarization runs were used:15058, 15059, 15060, 15061, 15063, 15068, 15069, 15070, 15071, 15072, 15073, 15176, 15177, 15178, 15179, 15180, 15182, 15184, 15185, 15186, 15187. For negative target polarization runs 15121, 15123, 15124, 15127, 15128 , 15129, 15135, 15136, 15137, 15138, 15141, 15142, 15143, 15144, 15146, 15148, 15149, 15152, 15153, 15154, 15155, 15156 were used.

0.4 GeV$^2/c^2$ to 1.8 GeV$^2/c^2$ and the experimental asymmetry

$$A_{meas} = \frac{N_{\uparrow\uparrow} - N_{\downarrow\uparrow}}{N_{\uparrow\uparrow} + N_{\downarrow\uparrow}} \tag{4.42}$$

was evaluated for each bin. A_{meas} can be related to A_{theo} using equations 4.9

$$A_{meas} = \frac{P_eP_t\sigma_{et}}{\sigma_0} \equiv P_eP_tA_{theo} \tag{4.43}$$

The final result was calculated as the average of the six values. In order to cover such a big range both inclusive and exclusive channels were used. As can be seen in Figure 4.9(a) the lowest Q^2 accessible in the elastic region ($W \sim 0.938$ GeV$/c^2$) is 0.8 GeV$^2/c^2$. On the other hand Figure 4.9(b) shows that by not requiring the proton (inclusive events) the low Q^2 region can be accessed. Therefore the first

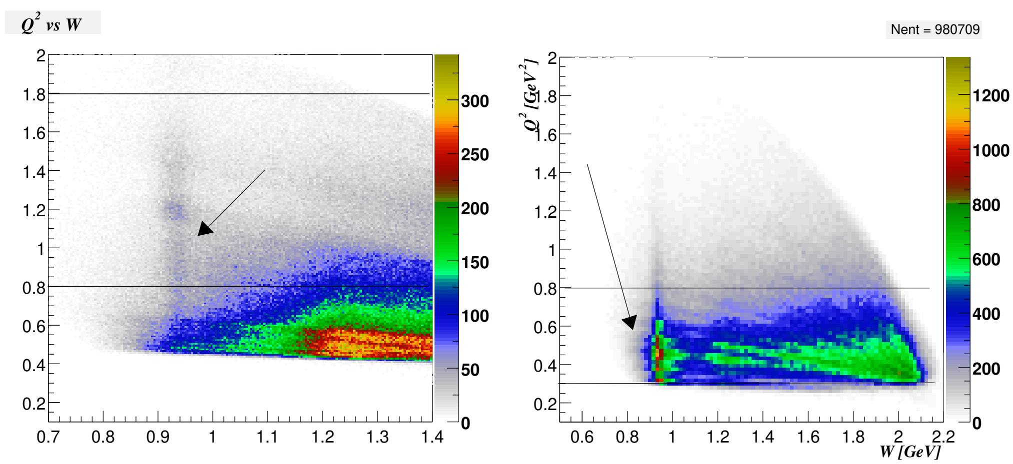

(a) exclusive　　(b) inclusive

Figure 4.9: Q^2 *vs* W for exclusive and inclusive channels. The two plots show the elastic peaks (indicated by the arrows) in respective Q^2 ranges of 0.8 GeV$^2/c^2$ < Q^2 < 1.8 GeV$^2/c^2$ and 0.3 GeV$^2/c^2$ < Q^2 < 0.8 GeV$^2/c^2$. The events in the left plot at low Q^2 (lower than $Q^2 < 0.8$ GeV$^2/c^2$) belong actually to the tail of the quasi-delta peak. The reason that events with low Q^2 can be achieved only without requiring the proton is that low Q^2 elastic events correspond to events with high θ of the proton, which are suppressed by the target coils.

three regions in Q^2 used the inclusive W spectrum to calculate the asymmetry and for the last three the exclusive $|\phi_e - \phi_p|$ spectra were utilized. The Q^2 bins and the corresponding average value at which the theoretical asymmetry was calculated are summarized in Table 4.4. Figures 4.10 and 4.11 show how the asymmetry for each

Q^2[GeV$^2/c^2$] range	$< Q^2 >$	*datasample*	A_{theo}
$0.3 < Q^2 < 0.5$	0.39	inc	-0.154
$0.5 < Q^2 < 0.9$	0.64	inc	-0.266
$0.9 < Q^2 < 1.5$	1.10	inc	-0.410
$1.1 < Q^2 < 1.3$	1.19	exc	-0.439
$1.3 < Q^2 < 1.6$	1.43	exc	-0.512
$1.6 < Q^2 < 2.2$	1.82	exc	-0.626

Table 4.4: Theoretical values for the elastic asymmetry A_{theo} for different Q^2 bins.

bin was calculated. The top plots show the carbon normalization and the bottom three are the result of the ratio A_{meas} in a narrow region around the elastic peak (0.912 GeV/c^2 $< W <$ 0.95 GeV/c^2 for inclusive and $179.0° < |\phi_e - \phi_p| < 180.6°$ for the exclusive). The asymmetry in that small bin is expected to be constant and therefore a fit was performed to evaluate the average value A_{meas}. Figure 4.12 is a graph of the values of P_eP_t obtained from the six asymmetries using the formula

$$P_eP_t = \frac{A_{meas}}{A_{theo}} \tag{4.44}$$

and the fit to calculate the average value for positive target polarization data. Figure 4.13 contains the analogous result for the negative target polarization data.

Further tests were performed in order to understand the systematic uncertainties of the procedure. First, to remove the statistical fluctuations of the carbon data, of which the statistic is poor, a fit of the ^{12}C data was performed and the nuclear background was removed using the fitted curve. Second, for the exclusive data, fiducial cuts and acceptance corrections were applied. This test was done only for the exclusive case, because the acceptance calculation described in the next section

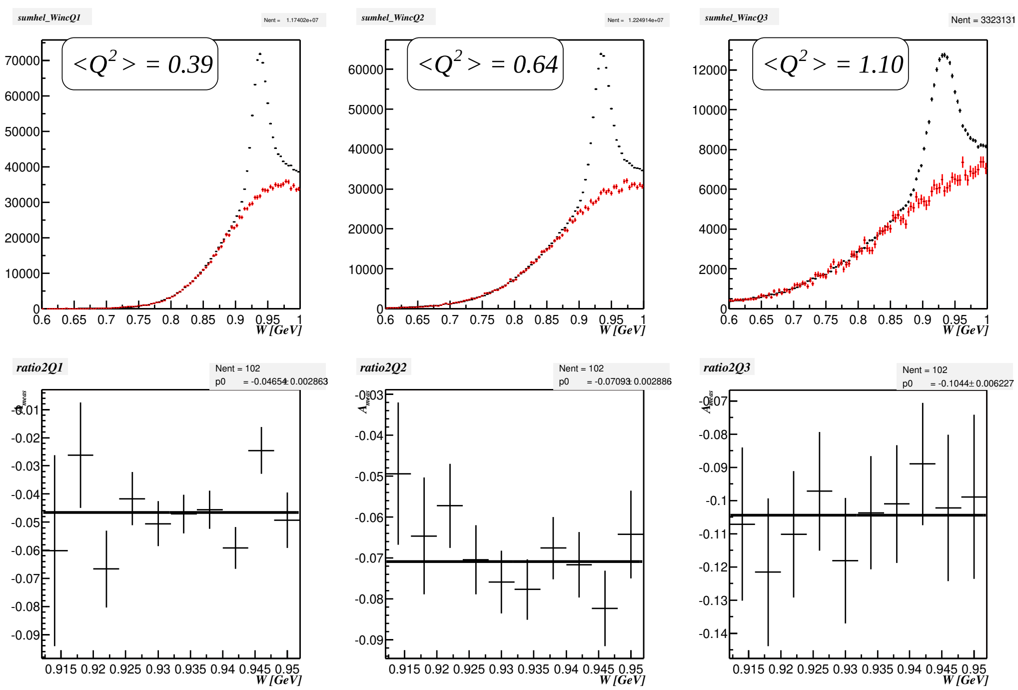

Figure 4.10: Normalization (top) and asymmetry A_{meas} (bottom) for the three low Q^2 bins and positive target polarization runs. The ^{12}C W spectra (red) were normalized to the $^{15}NH_3$ (black) by using the W tail method. The A_{meas} distributions were fitted to a straight line to obtain an average value.

was done only for the case of electron and proton in the final state. The resulting product of polarization turned out to be fairly stable. Figures 4.14 and 4.15 show the results for positive and negative polarized target runs, respectively.

4.6 Acceptance calculation

The object of the present analysis is to extract asymmetries which, as seen in the previous section, are ratios of combinations of $N_{\uparrow\uparrow}$, $N_{\uparrow\downarrow}$, $N_{\downarrow\uparrow}$ and $N_{\downarrow\downarrow}$. Because the acceptance does not depend on the polarization of beam and target one might come to think that the acceptance is a common factor both in numerator and denominator and therefore that it cancels out. However, this is true only if the asymmetries are binned in all the variables they depend on, $X_i = \{Q^2, W, \phi^*, \theta^*\}$, and if these bins are small enough. In this case the acceptance can be considered

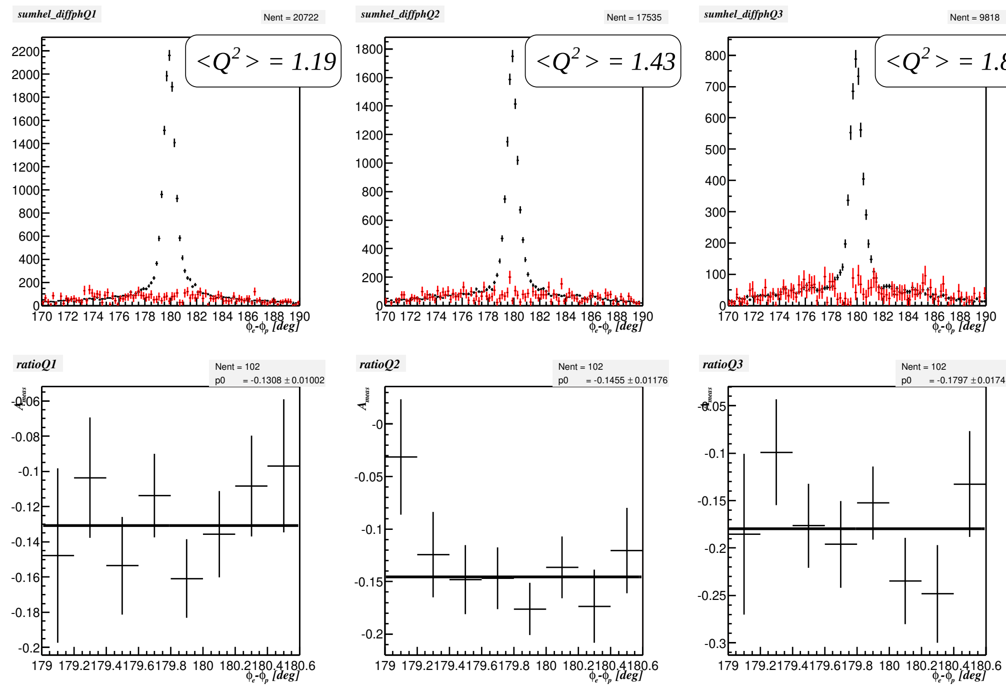

Figure 4.11: Normalization (top) and asymmetry A_{meas} (bottom) for the three high Q^2 bins and positive target polarization runs. The ^{12}C $|\phi_e - \phi_p|$ spectra (red) were normalized to the $^{15}NH_3$ (black) by using the two tails. The A_{meas} distributions were fitted to a straight line to obtain an average value.

a constant in each bin in the variables X_i and therefore be canceled for each bin. As soon as integrations over bigger ranges of the variables X_i are considered the experimentally calculated asymmetry is related to the ratio of the cross sections by an expression of the type

$$\frac{N}{N_0} = \frac{\int \sigma(\theta^*, \phi^*, E_{beam}, W, Q^2) a(p_e, \theta_e, \phi_e, p_p, \theta_p, \phi_p)}{\int \sigma_0(\theta^*, \phi^*, E_{beam}, W, Q^2) a(p_e, \theta_e, \phi_e, p_p, \theta_p, \phi_p)} \tag{4.45}$$

where it is clear that the acceptance does not cancel. Because the asymmetries which are going to be extracted are indeed partially integrated over the various variables in order to reduce the statistical errors, an acceptance correction to the asymmetries is needed. The previous chapter includes a discussion on fiducial cuts, which define a geometrical region within which the efficiency is considered to be 100%. This solves only part of the problem, since a correction for the geometrical

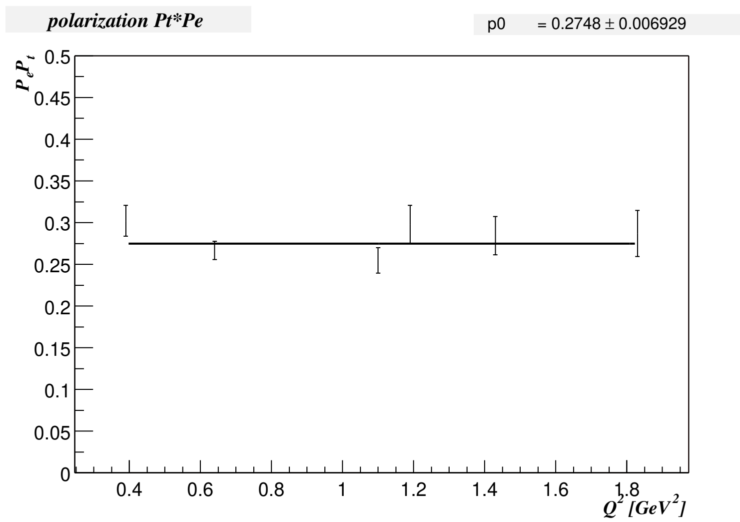

Figure 4.12: P_eP_t as a function of Q^2 for positive target polarization runs. The six values were fitted with a constant in order to obtain the average value.

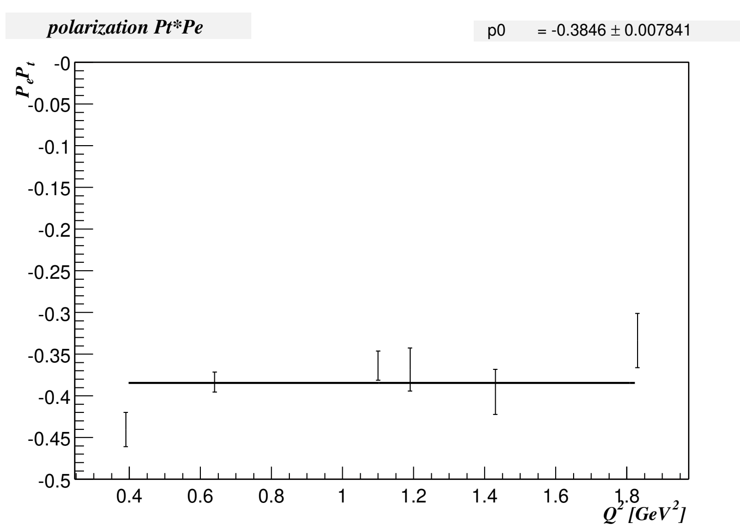

Figure 4.13: P_eP_t as a function of Q^2 for negative target polarization runs. The six values were fitted with a constant in order to obtain the average value.

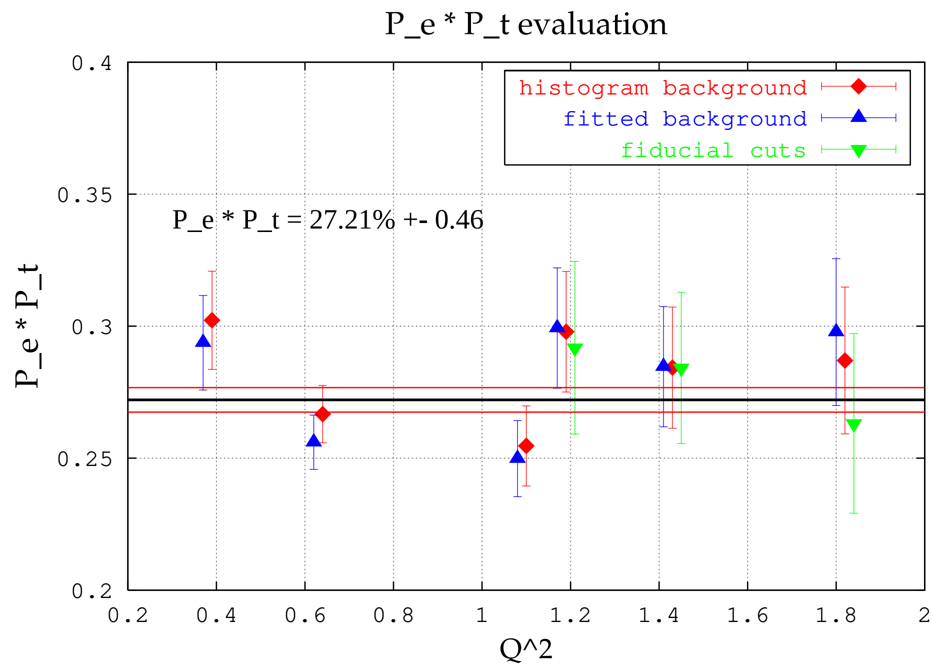

Figure 4.14: P_eP_t as a function of Q^2 for positive target polarization runs. The points were obtained with different methods: normal method, fitting the background and with fiducial cuts. The average value results from a combined fit to all points, and the error from the fit is indicated by the red lines.

acceptance still has to be applied. This is however a much easier task than before.

The idea is the following: the asymmetries are the ratios of cross sections that are independent of the azimuthal angle of the electron in the lab frame ϕ_e (see Figures 3.34 and 3.35). In other words an event identified by the quantities $\theta^*, \phi^*, E_{beam}, W, Q^2$ has the corresponding values in the laboratory frame fixed: $p_e, \theta_e, p_p, \theta_p, \Phi \equiv \phi_p - \phi_e$. ϕ_e on the other hand remains undetermined. It is easy to see that an event with $\theta^*, \phi^*, E_{beam}, W, Q^2$ does not have 100% acceptance because the electron and the proton can have ϕ_e and $\phi_p = \phi_e + \Phi$ corresponding to a hole in the detector. Because electrons and protons can have any ϕ with the same probability, the acceptance will be the combined ϕ coverage divided by 2π. If fiducial cuts were not used, it would not be true that the ϕ dependency is flat and therefore the acceptance would not have this simple form. We can express this idea in a

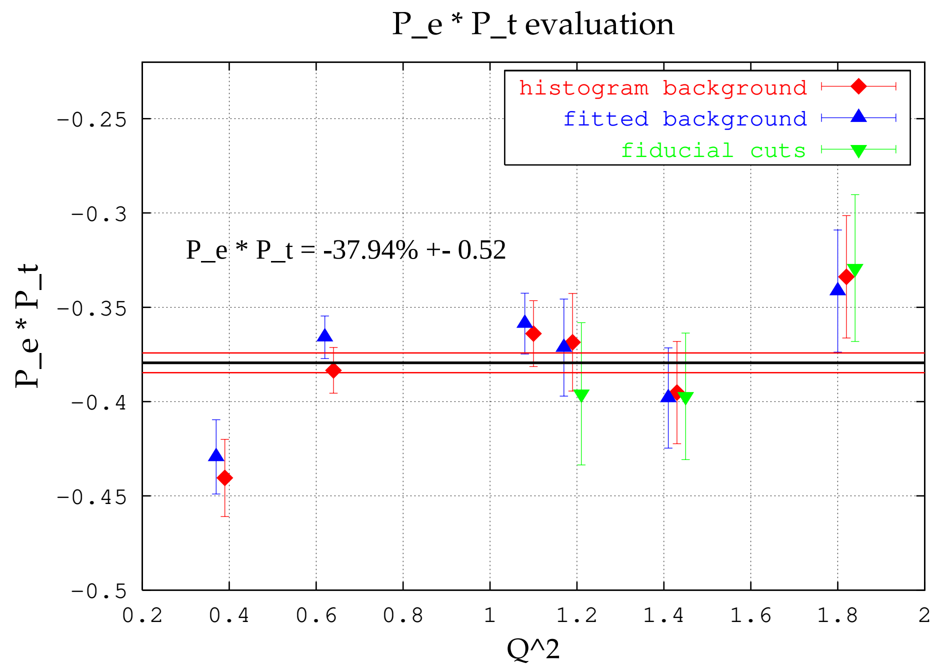

Figure 4.15: P_eP_t as a function of Q^2 for negative target polarization runs. The points were obtained with different methods: normal method, fitting the background and with fiducial cuts. The average value results from a combined fit to all points, and the error from the fit is indicated by the red lines.

mathematical way:

$$\begin{aligned} N(\theta^*, \phi^*, &E_{beam}, W, Q^2) = \\ &= \int \sigma(\theta^*, \phi^*, E_{beam}, W, Q^2) a(p_e, \theta_e, \phi_e, p_p, \theta_p, \phi_p) d\phi_e \\ &= \int \sigma(p_e, \theta_e, p_p, \theta_p, \phi_p - \phi_e) a(p_e, \theta_e, \phi_e, p_p, \theta_p, \phi_p) d\phi_e \\ &= \int \sigma(p_e, \theta_e, p_p, \theta_p, \Phi) a(p_e, \theta_e, \phi_e, p_p, \theta_p, \phi_e + \Phi) d\phi_e \\ &= \sigma(p_e, \theta_e, p_p, \theta_p, \Phi) \int a(p_e, \theta_e, \phi_e, p_p, \theta_p, \phi_e + \Phi) d\phi_e \\ &= \sigma(\theta^*, \phi^*, E_{beam}, W, Q^2) \int a(p_e, \theta_e, \phi_e, p_p, \theta_p, \phi_e + \Phi) d\phi_e \end{aligned} \tag{4.46}$$

where the integral can be expressed as the convolution of the two step function for proton and electron(see Figure 4.16)

$$
\begin{aligned}
A_{tot}(p_e, \theta_e, p_p, \theta_p, \Phi) &= \int a(p_e, \theta_e, \phi_e, p_p, \theta_p, \phi_e + \Phi) d\phi_e \\
&= \int A_e(p_e, \theta_e, \phi_e) A_p(p_p, \theta_p, \phi_e + \Phi) d\phi_e
\end{aligned}
\tag{4.47}
$$

This last integral is therefore the correction factor we were looking for: every event

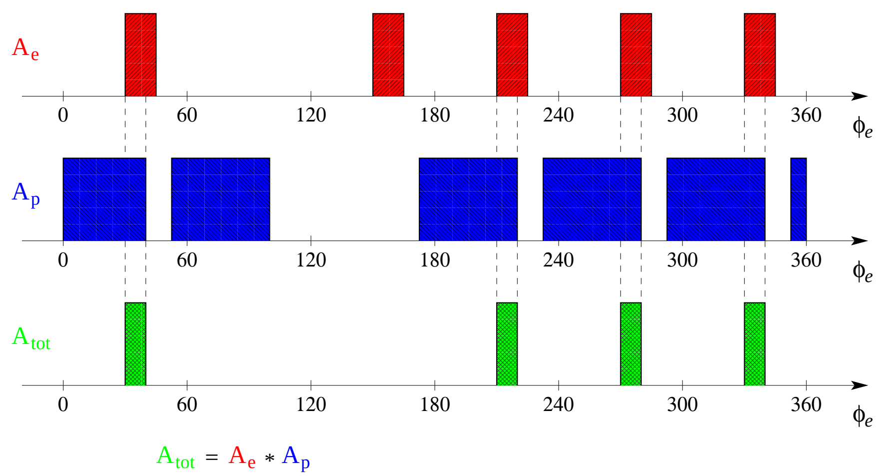

Figure 4.16: Analytical calculation of the acceptance as a function of ϕ_e. A_e and A_p are respectively the electron and proton acceptances for fixed values of Q^2, W, θ^* and ϕ^*. They are normally six part step functions, unless a sector is missing due to a hole. The holes are due to the fact that fiducial cuts remove regions of the detector with inefficiencies for examples caused by a bad scintillator paddle. Note that A_p has to be translated by an angle Φ to get it as a function of ϕ_e. A_{tot} is the product $A_e A_p$ and the integral of A_{tot} is the acceptance for this event.

can be corrected with the factor $\frac{1}{A_{tot}}$.

An alternative method to correct for the acceptance is to use a Monte Carlo event generator. In this method events are generated with a flat distribution in ϕ^* and θ^* for a certain Q^2, E_{beam} and W, fiducial cuts are applied and the result is divided by the original distribution. Later on in the analysis the real data for the same Q^2, E_{beam} and W combination is divided by the so obtained acceptance. It is clear that the analytical method is more convenient because it is more accurate and faster. To obtain a small error with the Monte Carlo method, one needs to generate many events for many combinations of ϕ^*, θ^*, Q^2, E_{beam} and W. The analytical method is also convenient because this kind of correction can be done on a event by event basis.

The Monte Carlo event generator was however used to test if the analytical calculation is correct and Figure 4.17 shows the comparison between the ϕ^* acceptance distributions obtained with the Monte Carlo fixing different kinematics conditions and the equivalent curve calculated with the analytical method. For the Monte Carlo method 500,000 events were generated for each plot. All the plots have a fixed $W = 1.232$ GeV$/c^2$ two different θ^* angles equal to 30° and 100° and three different Q^2 values equal to 0.4, 0.7 and 1.2 GeV$^2/c^2$. Figure 4.18 shows the acceptance in θ^* vs ϕ^* for different W and Q^2 values. The plots show that while the acceptance changes rapidly with Q^2, it is fairly independent on the value of W, within the $\Delta(1232)$ region. This is important because it allows one to identify for the $\Delta(1232)$ three regions in Q^2 with approximately the same acceptance within each Q^2 region itself. A full set of pictures can be found in Appendix F. Using the analytical method the statistical errors have to be dealt with properly. A bin of a histogram with N events has an error that is simply $\sqrt{N}$, if it is multiplied by a factor $\frac{1}{A_{tot}}$ the error will be $\frac{\sqrt{N}}{A_{tot}}$.

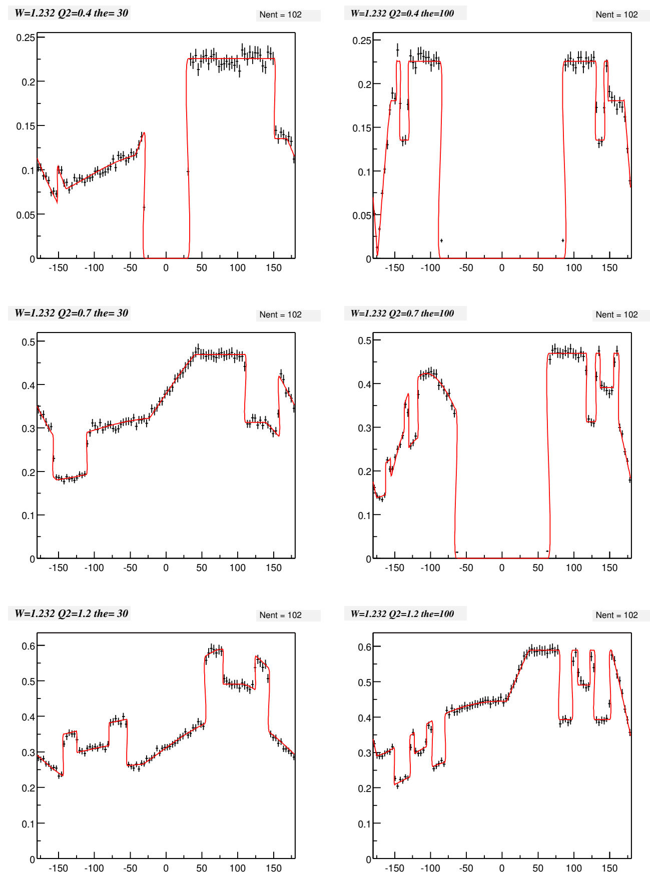

Figure 4.17: Comparison between Monte Carlo and analytical calculation. The red line is the calculation of the acceptance as a function of ϕ^* for fixed values of E_{beam}, θ^*, Q^2 and W. The histogram is obtained generating a flat distribution in ϕ^* and applying fiducial cuts. The plots show full agreement between the two methods. The different plots correspond to different values of θ^*, Q^2 and W. The discontinuous structures in these plots are due to the fact that they are calculated for precise kinematic values. An integration over these variables will smear the discontinuities out.

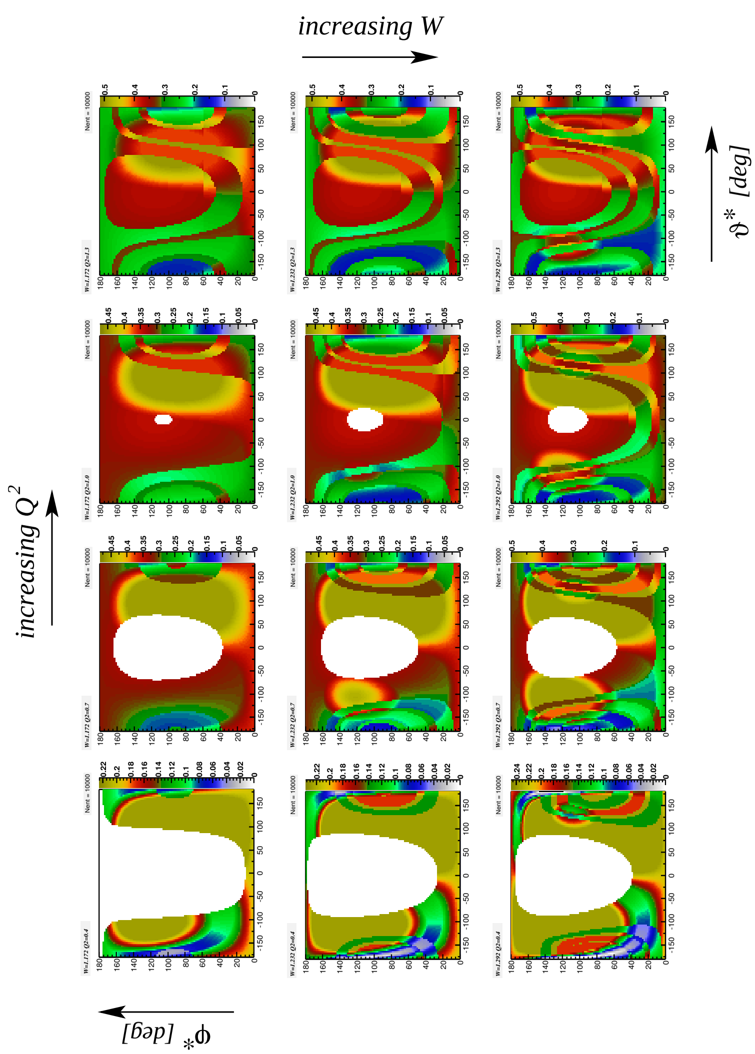

Figure 4.18: Calculation of the acceptance as a function of θ^* *vs* ϕ^*, the pion angles in the center of mass system for different values of Q^2 and W in the $\Delta(1232)$ region. The plot shows that the acceptance does not change significantly with W but does so with Q^2. The hole at low Q^2 makes the use of data in this region impossible.

CHAPTER 5
RESULTS AND DISCUSSION

The object of this analysis is the extraction of the asymmetries A_e, A_t and A_{et} in the $\Delta(1232)$ region. In the previous two chapters the preliminary steps needed to achieve the final result were described. In particular section 3 described selection of and corrections to the data set. Section 4 illustrated how to extract all the relevant quantities that enter in the equations for the asymmetries such as the product of beam and target polarization, $P_e P_t$, and the method of subtracting the nuclear background.

In this chapter the three asymmetries will be shown as functions of ϕ^* and $\cos\theta^*$, the angles of the pion in the center of mass frame of the $\Delta(1232)$ ($1.1\ \mathrm{GeV}/c^2 < W < 1.3\ \mathrm{GeV}/c^2$), in Q^2 ranges from $0.5\ \mathrm{GeV}^2/c^2$ to $0.9\ \mathrm{GeV}^2/c^2$ and $0.9\ \mathrm{GeV}^2/c^2$ to $1.5\ \mathrm{GeV}^2/c^2$. The ϕ^* distributions of the asymmetries is fairly well understood, since it originates from the purely kinematic dependence of the cross section on ϕ^*. The dependence on $\cos\theta^*$, on the other hand, is contained in the response functions, whose behavior is predicted by models.

The Q^2 dependence integrated over ϕ^* and $\cos\theta^*$ will be presented as well.

All the results will be compared to theoretical models. In particular three models were considered: MAID2000, MAID98 [13] an Effective Lagrangian model developed by Rick Davidson and Nimai Mukhopadhyay [10] and the dynamic model by Sato and Lee [14].

5.1 Acceptance in the models

As seen in chapter 4.6 a region with zero acceptance centered around $\phi^* = 0°$ is present in the lower Q^2 region ($0.5\ \mathrm{GeV}^2/c^2 < Q^2 < 0.9\ \mathrm{GeV}^2/c^2$). Since it is not possible to correct the data, this region has to be taken into account in the models. In particular the fiducial cuts described in section 3.7 were applied to the models in order to remove the region where CLAS was unable to detect events.

Some studies were performed to demonstrate the effects of the fiducial cuts on the asymmetries. It was found that, while the inefficient region affects the numerator and the denominator of A_e and A_t rather strongly, the asymmetries themselves are almost unchanged. This is somewhat surprising since the acceptance is not expected to cancel out if the ranges of integration are large (see section 4.6). Figure 5.1 shows the prediction from MAID2000 of the denominator of the asymmetries for the low Q^2 region[13]. The black curve is the result without accounting for the acceptance and the red excludes integration over ineffective regions. The same comparison is

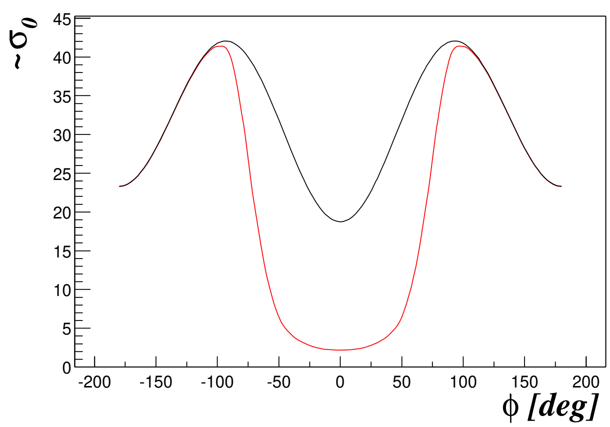

Figure 5.1: Denominator of the asymmetries ($\propto \sigma_0$) as predicted by MAID2000 for $0.5\ \mathrm{GeV}^2/c^2 < Q^2 < 0.9\ \mathrm{GeV}^2/c^2$ and $-1 < \cos\theta^* < 1$ without (black) and with (red) taking into account the acceptance.

done for the numerator of A_e (Figure 5.2(a)) and for A_e (Figure 5.2(b)). As already mentioned above, the effect of the region with zero acceptance on the asymmetry is small even though the pieces show large variations. A similar comparison was performed for the asymmetry A_t and the results are shown in Figures 5.3. Again, the effect on the final result is very small despite the large variations on the numerator and denominator. However, a significant effect was observed for the double spin asymmetry A_{et}, as shown in Figure 5.4. A_{et} changes by an amount of the order of 50%. For the higher Q^2 region ($0.9\ \mathrm{GeV}^2/c^2 < Q^2 < 1.5\ \mathrm{GeV}^2/c^2$) the effect of the acceptance is expected to be negligible because there are only small zero acceptance regions in this range. Figures 5.5, 5.6, 5.7 show that this is in fact the case.

[13]Note that this term is common to all three asymmetries.

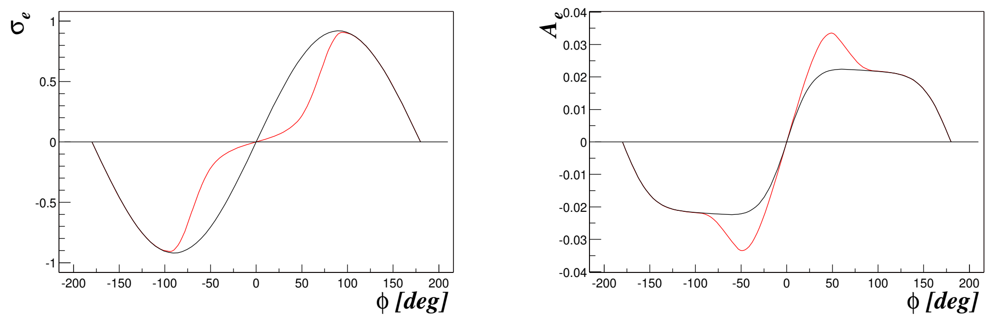

(a) Numerator of A_e (b) Asymmetry A_e

Figure 5.2: Effect of the acceptance on the numerator of A_e and the asymmetry A_e itself for $0.5\mathrm{GeV}^2/c^2 < Q^2 < 0.9\ \mathrm{GeV}^2/c^2$ and $-1 < \cos\theta^* < 1$. The red and black curves represent the predictions from MAID2000 with and without taking into account the acceptance, respectively.

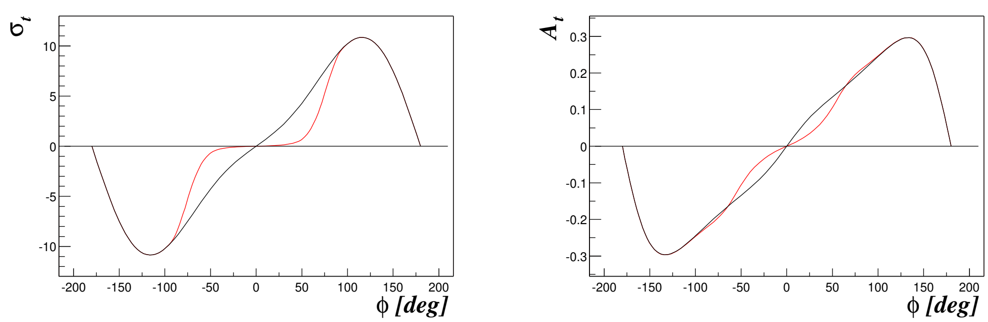

(a) Numerator of A_t (b) Asymmetry A_t

Figure 5.3: Effect of the acceptance on the numerator of A_t and the asymmetry A_t itself for $0.5\ \mathrm{GeV}^2/c^2 < Q^2 < 0.9\ \mathrm{GeV}^2/c^2$ and $-1 < \cos\theta^* < 1$. The red and black curves represent the predictions from MAID2000 with and without taking into account the acceptance, respectively.

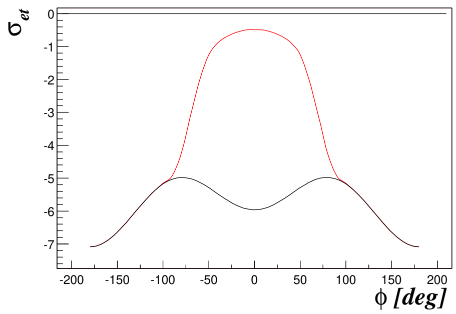

(a) Numerator of A_{et}

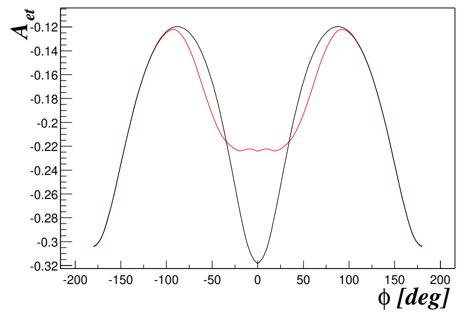

(b) Asymmetry A_{et}

Figure 5.4: Effect of the acceptance on the numerator of A_{et} and the asymmetry A_{et} itself for $0.5 \text{ GeV}^2/c^2 < Q^2 < 0.9 \text{ GeV}^2/c^2$ and $-1 < \cos\theta^* < 1$. The red and black curves represent the predictions from MAID2000 with and without taking into account the acceptance, respectively.

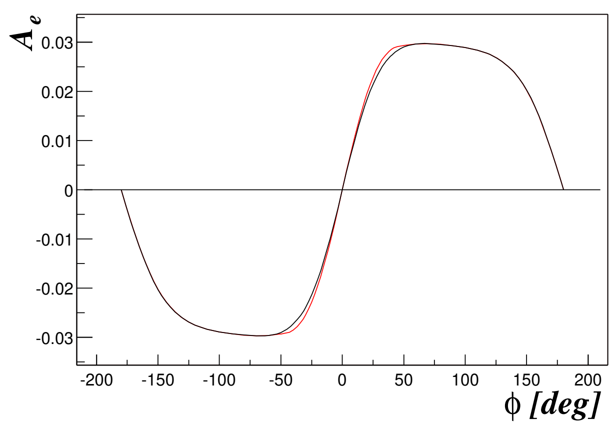

Figure 5.5: Effect of the acceptance on the asymmetry A_e for $0.9 \text{ GeV}^2/c^2 < Q^2 < 1.5 \text{ GeV}^2/c^2$ and $-1 < \cos\theta^* < 1$. The red and black curves represent the predictions from MAID2000 with and without taking into account the acceptance, respectively. The curves overlap almost perfectly.

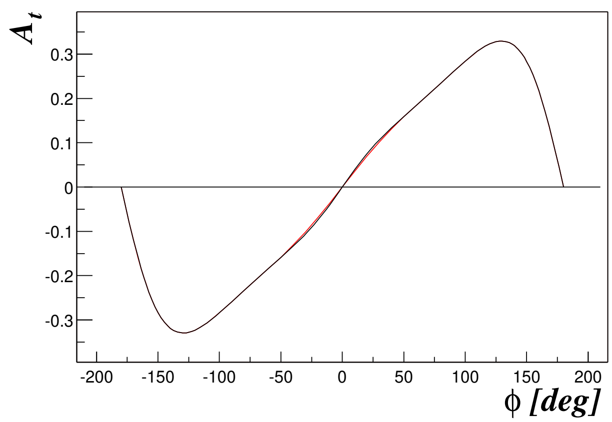

Figure 5.6: Effect of the acceptance on the asymmetry A_t for $0.9\ \mathrm{GeV}^2/c^2 < Q^2 < 1.5\ \mathrm{GeV}^2/c^2$ and $-1 < \cos\theta^* < 1$. The red and black curves represent the predictions from MAID2000 with and without taking into account the acceptance, respectively. The curves overlap perfectly.

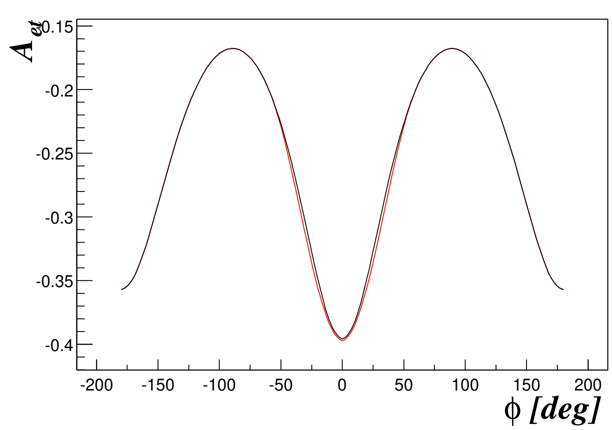

Figure 5.7: Effect of the acceptance on the asymmetry A_{et} for $0.9\ \mathrm{GeV}^2/c^2 < Q^2 < 1.5\ \mathrm{GeV}^2/c^2$ and $-1 < \cos\theta^* < 1$. The red and black curves represent the predictions from MAID2000 with and without taking into account the acceptance, respectively.

The results presented in the following sections are always compared to the predictions from different models. Since the effect of the acceptance in lower Q^2 region (0.5 GeV$^2/c^2$ $< Q^2 <$ 0.9 GeV$^2/c^2$) is clearly visible the models always take the zero acceptance region into account.

5.2 Beam asymmetry A_e

The electron spin asymmetry A_e is not the main goal of the present analysis since other experiments, with polarized beam and unpolarized target [43] already measured this quantity. However, since σ_e is simply proportional to $sin(\phi^*)$ it was initially considered to verify that the data were obeying the expected behavior.

To verify the $sin(\phi^*)$ dependence of σ_e, the numerator of the definition of A_e was considered (see equation 4.6)

$$\sigma_e + \sigma_e^N \propto (\overline{N_{\uparrow\uparrow}} - \overline{N_{\downarrow\uparrow}}) + d\alpha_{et}(\overline{N_{\uparrow\downarrow}} - \overline{N_{\downarrow\downarrow}}) \tag{5.1}$$

Figure 5.8 shows the result for 0.9 GeV$^2/c^2$ $< Q^2 <$ 1.5 GeV$^2/c^2$ and the result of a fit to the function $p0sin(\phi^*)$.

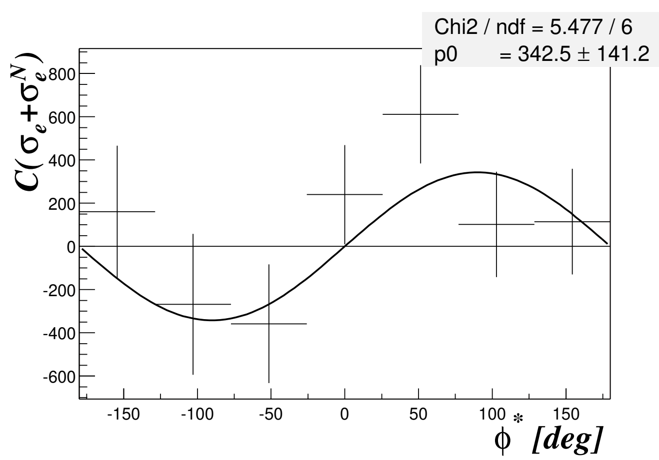

Figure 5.8: $(\overline{N_{\uparrow\uparrow}} - \overline{N_{\downarrow\uparrow}}) + d\alpha_{et}(\overline{N_{\uparrow\downarrow}} - \overline{N_{\downarrow\downarrow}})$ for 0.9 GeV$^2/c^2$ $< Q^2 <$ 1.5 GeV$^2/c^2$ and $-1 < \cos\theta^* < 1$. The data follow the expected $sin(\phi^*)$ behavior.

Finally, the extraction of the asymmetry A_e was performed according to equation 4.6, and Figure 5.9 shows the results together with a comparison to the predictions from MAID2000, MAID98, Sato-Lee and the Effective Lagrangian model. In principle a fit of $A_e(\phi^*)$ to the function $F(\phi^*) = \frac{p0\sin(\phi^*)}{p1+p2\cos(\phi^*)+p3\cos(2\phi^*)}$ (see eq 1.17) would allow one to extract the response functions. However the poor statistics combined with the fact that A_e is very small in the $\Delta(1232)$ region (see section 1.3.1) makes a fit with four parameters difficult. Since MAID2000 was found to be in very good agreement with the data for unpolarized scattering, the parameters $p1$, $p2$ and $p3$ of the function $F(\phi^*)$ were fixed using the results from MAID2000. Figure 5.10(a) shows the result of a fit to the MAID2000 prediction with the function $F(\phi^*) = \frac{p0\sin(\phi^*)}{p1+p2\cos(\phi^*)+p3\cos(2\phi^*)}$ in order to extract the "theoretical" values of $p0$, $p1$ $p2$ and $p3$. The parameters $p1$, $p2$ and $p3$ were then fixed in a fit to the data with the same function F. The result for 0.9 GeV$^2/c^2 < Q^2 <$ 1.5 GeV$^2/c^2$ is shown in Figures 5.10(b).

The dependence of the asymmetries on $\cos\theta^*$ is more interesting than the ϕ^* dependence, since it is not well known and can only be predicted by means of models. This offers a way to test the different models and their predictions. Due the limited statistics it would be preferable to study the $\cos\theta^*$ dependence integrating over the whole range in ϕ^*. However in the case of A_e this integral is expected to be zero because the ϕ^* dependence is an odd function of ϕ^* ($A_e \propto \frac{p0\sin(\phi^*)}{p1+p2\cos(\phi^*)+p3\cos(2\phi^*)}$). Figures 5.11(a) and (b) show this behavior and a χ^2 and a z-test comparison gives the values listed in Table 5.1.

Q^2 *range* [GeV$^2/c^2$]	χ^2/ndf	*z-test*
0.5 to 0.9	1.73	0.78±1.06
0.9 to 1.5	0.66	0.36±0.73

Table 5.1: Values of the χ^2 and z-test comparisons between A_e *vs* $\cos\theta^*$ integrated over the whole range in ϕ^* and the expected value $A_e \equiv 0$.

Instead the $\cos\theta^*$ distributions were compared in partial integrations over half ranges of ϕ^*: $-180° < \phi^* < 0°$ and $0° < \phi^* < 180°$. The results are shown in Figures 5.12 and 5.13.

Finally, in order to reduce the size of error bars, the fact that $\sigma_e(\phi^*) =$

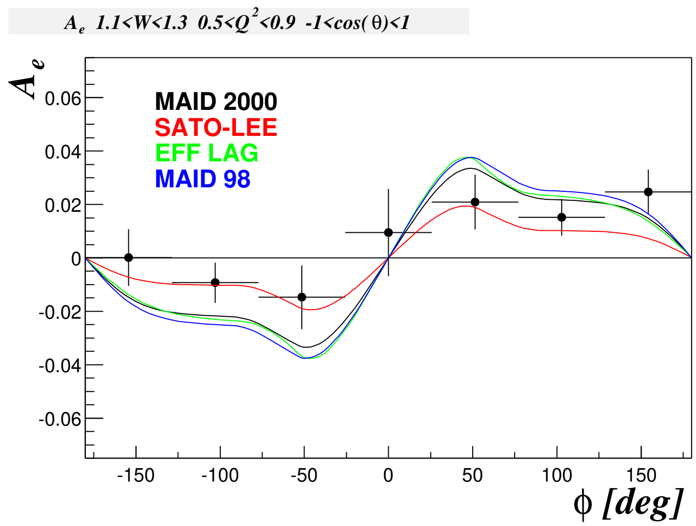

(a) $0.5\ \mathrm{GeV}^2/c^2 < Q^2 < 0.9\ \mathrm{GeV}^2/c^2$

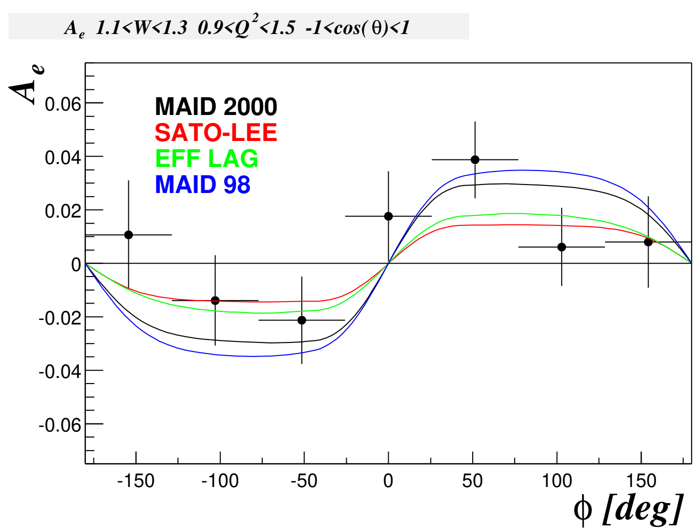

(b) $0.9\ \mathrm{GeV}^2/c^2 < Q^2 < 1.5\ \mathrm{GeV}^2/c^2$

Figure 5.9: A_e *vs* ϕ^* for two Q^2 regions and $-1 < \cos\theta^* < 1$ compared to MAID2000 (black), MAID98 (blue), Sato-Lee (red) and the Effective Lagrangian model (green).

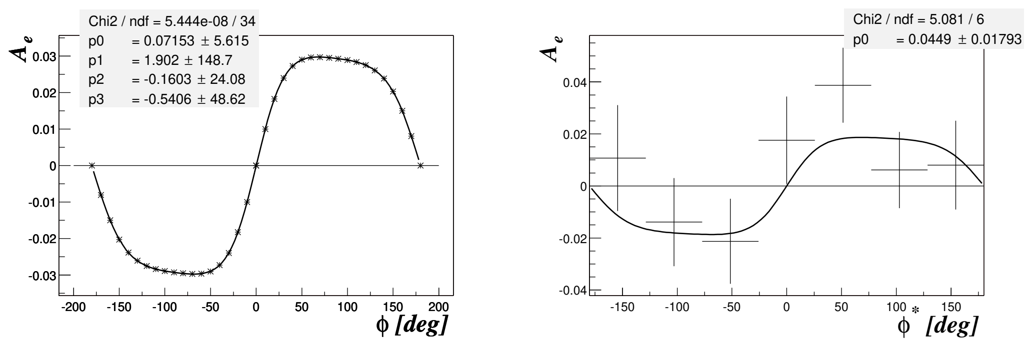

(a) MAID2000

(b) data

Figure 5.10: A_e *vs* ϕ^* for 0.9 GeV$^2/c^2 < Q^2 <$ 1.5 GeV$^2/c^2$ and $-1 < \cos\theta^* < 1$.

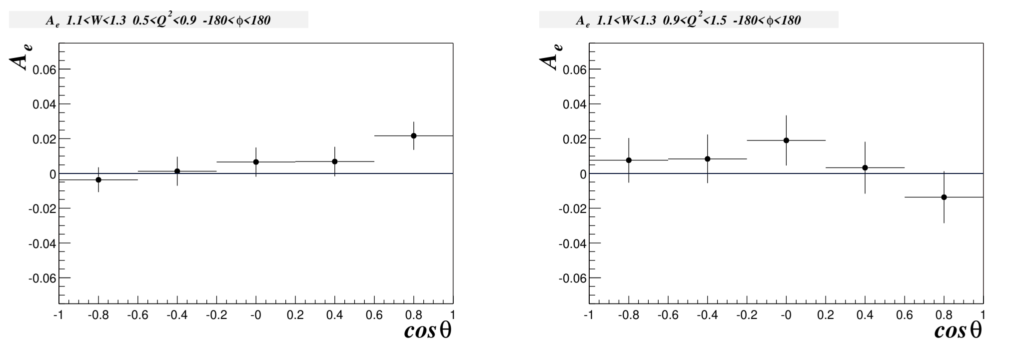

(a) 0.5 GeV$^2/c^2 < Q^2 <$ 0.9 GeV$^2/c^2$

(b) 0.9 GeV$^2/c^2 < Q^2 <$ 1.5 GeV$^2/c^2$

Figure 5.11: A_e *vs* $\cos\theta^*$ for two Q^2 regions integrated over the whole range in ϕ^*.

$-\sigma_e(-\phi^*)$ was used and the asymmetry was redefined as

$$A'_e = \frac{\sigma_e(\cos(\theta^*), \phi^* > 0°) - \sigma_e(\cos(\theta^*), \phi^* < 0°)}{\sigma_0(\cos(\theta^*), 180° < \phi^* < 180°)} \tag{5.2}$$

Defining the asymmetry in this way, it is possible to use the whole range in ϕ^* without obtaining a zero result. This asymmetry is theoretically equal to A_e integrated over positive ϕ^* angles and the results compared to the models are shown in Figures 5.14.

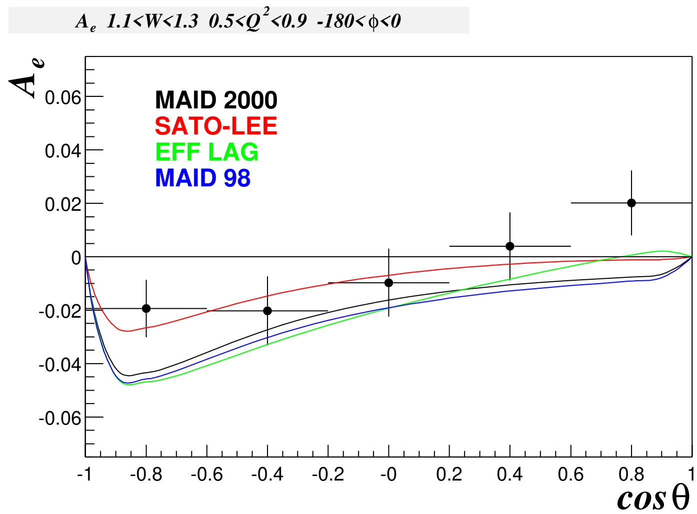

(a) $-180° < \phi^* < 0°$

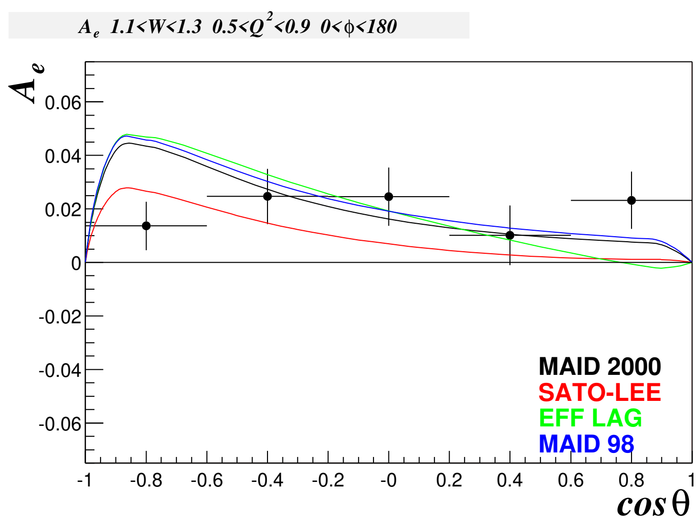

(b) $0° < \phi^* < 180°$

Figure 5.12: A_e *vs* $\cos\theta^*$ for 0.5 GeV$^2/c^2 < Q^2 <$ 0.9 GeV$^2/c^2$ and two different ϕ^* bins compared to MAID2000 (black), MAID98 (blue), Sato-Lee (red) and the Effective Lagrangian model (green).

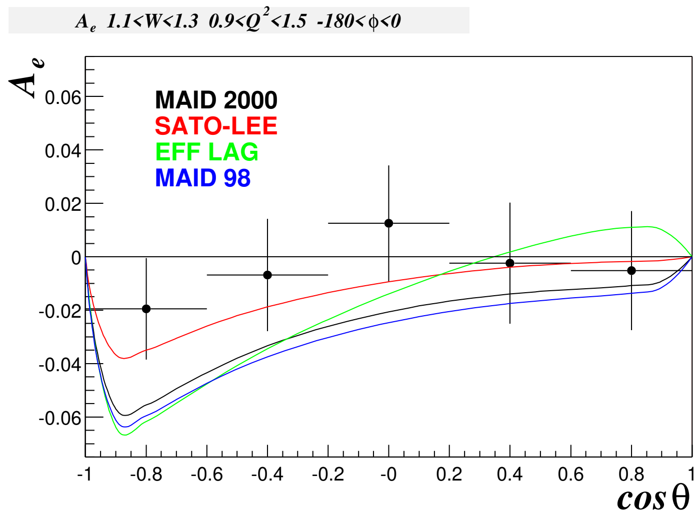

(a) $-180° < \phi^* < 0°$

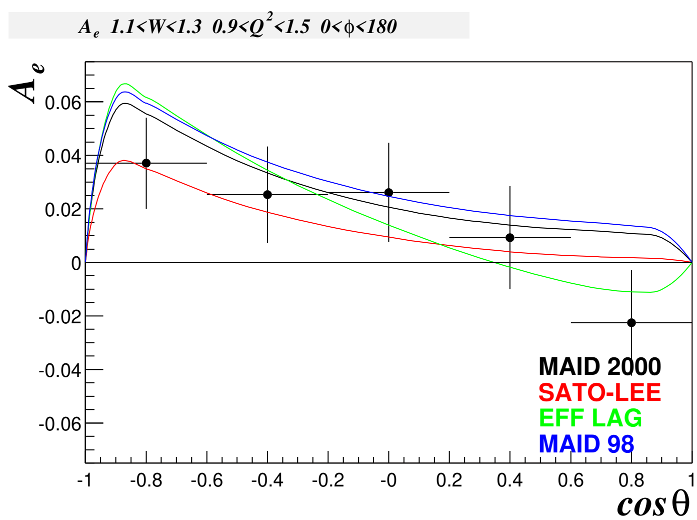

(b) $0° < \phi^* < 180°$

Figure 5.13: A_e *vs* $\cos\theta^*$ for 0.9 GeV$^2/c^2 < Q^2 <$ 1.5 GeV$^2/c^2$ and two different ϕ^* bins compared to MAID2000 (black), MAID98 (blue), Sato-Lee (red) and the Effective Lagrangian model (green).

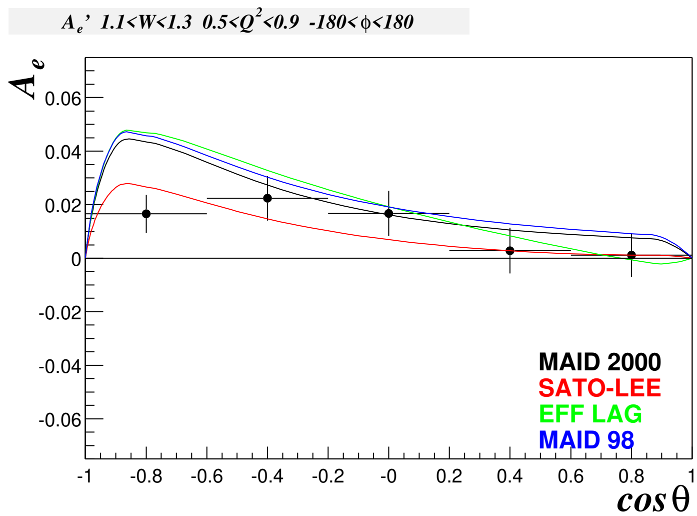

(a) $0.5\ \mathrm{GeV}^2/c^2 < Q^2 < 0.9\ \mathrm{GeV}^2/c^2$

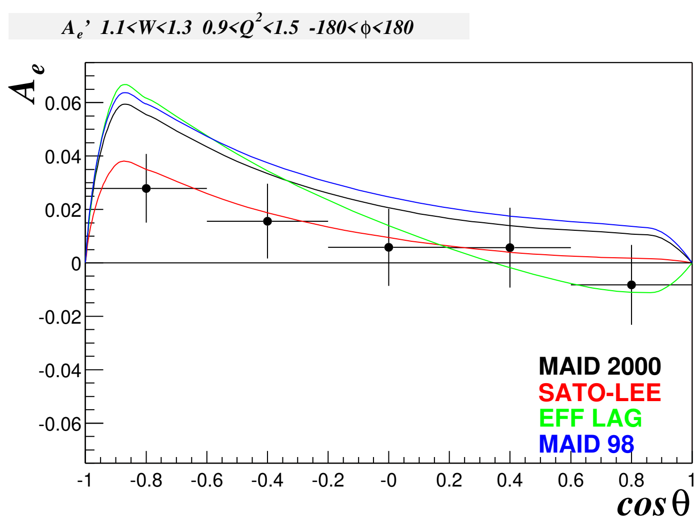

(b) $0.9\ \mathrm{GeV}^2/c^2 < Q^2 < 1.5\ \mathrm{GeV}^2/c^2$

Figure 5.14: A'_e *vs* $\cos\theta^*$ for two Q^2 regions integrated over the whole range in ϕ^* compared to MAID2000 (black), MAID98 (blue), Sato-Lee (red) and the Effective Lagrangian model (green).

5.3 Target asymmetry A_t

The target asymmetry A_t is the asymmetry involving the cross section for scattering of unpolarized electrons off of a polarized target. EG1 used both a polarized beam and polarized target, however combining the data with different beam helicities, it is possible to extract A_t. As in the case of A_e, the ϕ^* and $\cos\theta^*$ dependence were studied.

Before extracting the asymmetries, a test on the ϕ^* dependence of its denominator was done. According to equation 4.6 the denominator of A_t is proportional to σ_0 and is defined as

$$\sigma_0 \propto (\overline{N_{\uparrow\uparrow}} + \overline{N_{\downarrow\uparrow}}) + d\alpha_t(\overline{N_{\uparrow\downarrow}} + \overline{N_{\downarrow\downarrow}}) - D_2\sigma_0^N \tag{5.3}$$

The ϕ^* dependency of the unpolarized cross section σ_0 is of the type $p1+p2\cos(\phi^*)+p3\cos(2\phi^*)$. A fit to the expected ϕ^* distribution was performed for the $0.9\ \mathrm{GeV}^2/c^2 < Q^2 < 1.5\ \mathrm{GeV}^2/c^2$ region and the result is shown in Figure 5.15. As can be seen

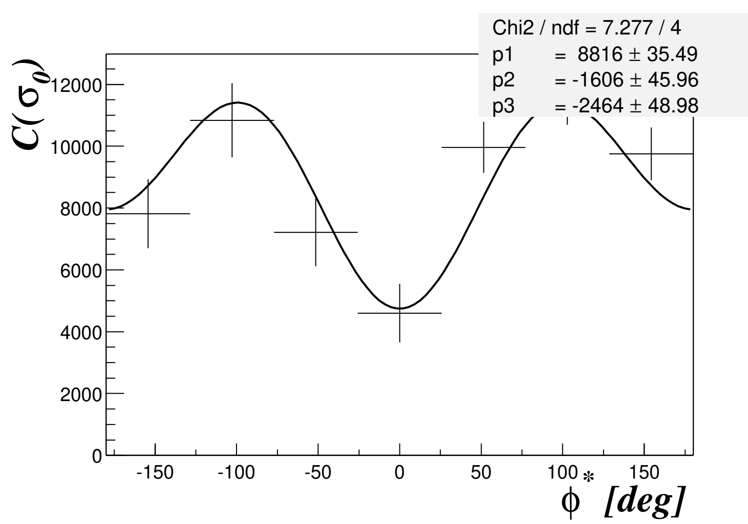

Figure 5.15: $(\overline{N_{\uparrow\uparrow}} + \overline{N_{\downarrow\uparrow}}) + d\alpha_t(\overline{N_{\uparrow\downarrow}} + \overline{N_{\downarrow\downarrow}})$ for $0.9\ \mathrm{GeV}^2/c^2 < Q^2 < 1.5\ \mathrm{GeV}^2/c^2$ and $-1 < \cos\theta^* < 1$. The data follow the expected behavior $p1 + p2\cos(\phi^*) + p3\cos(2\phi^*)$.

from the value of $\chi^2/ndf = 7.277/4 = 1.82$ the data follow the expected behavior rather well. For the low Q^2 region ($0.5\ \mathrm{GeV}^2/c^2 < Q^2 < 0.9\ \mathrm{GeV}^2/c^2$) a fit to the expected behavior reveals a large discrepancy, as shown in Figure 5.16(a), indicated by the high value of $\chi^2/ndf = 79/4$ from the fit. This is to be expected, since, as seen in section 5.1, the hole of the acceptance changes the shape of the ϕ^* distribution. Because the resulting distribution is unknown the fit cannot be performed in this region. However, an overlay of the data to the expected behavior predicted by MAID2000 including the hole in the acceptance shows once again very good agreement. This can be seen in Figure 5.16(b), where the data were normalized, so that the total integral of the histogram is the same of the integral of the curve. The ϕ^*

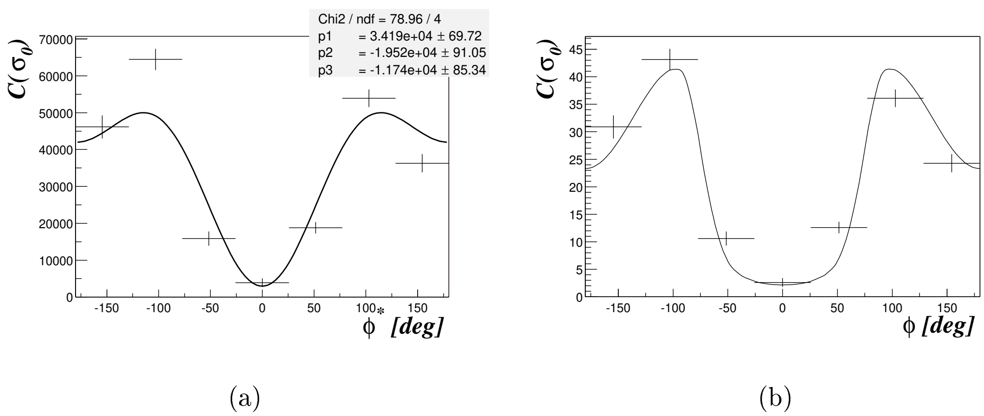

Figure 5.16: $(\overline{N_{\uparrow\uparrow}} + \overline{N_{\downarrow\uparrow}}) + d\alpha_t(\overline{N_{\uparrow\downarrow}} + \overline{N_{\downarrow\downarrow}})$ for 0.5 GeV$^2/c^2 < Q^2 <$ 0.9 GeV$^2/c^2$ and $-1 < \cos\theta^* < 1$. Figure (a) shows a fit to $p1 + p2\cos(\phi^*) + p3\cos(2\phi^*)$ and Figure (b) is an overlay of the data and the acceptance corrected model, normalized so that both, histogram and curve, have the same integral.

dependence of A_t is more complicated than the one of A_e but it is still expected to be an odd function in ϕ^*. Figures 5.17(a) and (b) show the asymmetry A_t as a function of ϕ^* for the two different Q^2 bins. Figures 5.18(a) and (b) show the asymmetry as a function of $\cos\theta^*$ integrated over the whole range in ϕ^*. Since the ϕ^* dependence is again an odd function in ϕ^*, this asymmetry is expected to be zero, as the data show. The χ^2 and z-test values in these cases are listed in Table 5.2.

Figures 5.19 and 5.20 show A_t as a function of $\cos\theta^*$ for the two different Q^2 bins with the integration over ϕ^* only from $-180° < \phi^* < 0°$ and $0° < \phi^* < 180°$, respectively, in order to avoid the result to be zero.

Similar to the beam asymmetry A'_e, A_t was redefined in order to use the whole

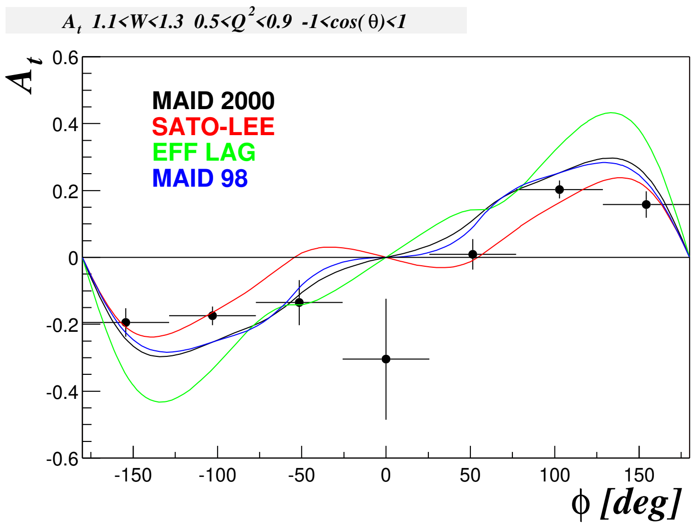

(a) $0.5\ \mathrm{GeV}^2/c^2 < Q^2 < 0.9\ \mathrm{GeV}^2/c^2$

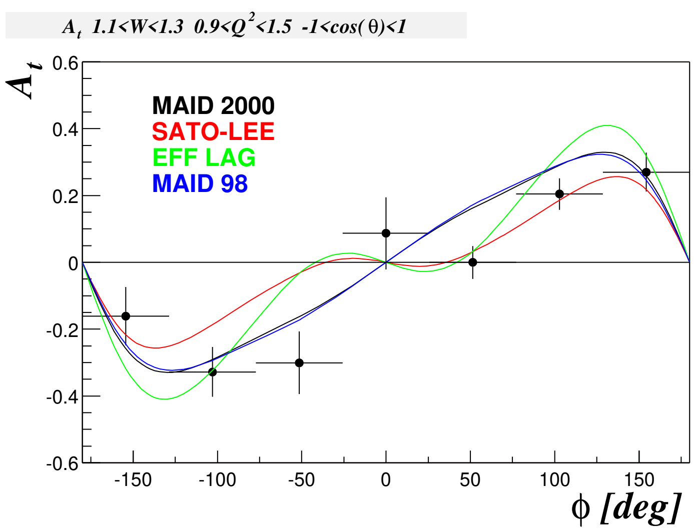

(b) $0.9\ \mathrm{GeV}^2/c^2 < Q^2 < 1.5\ \mathrm{GeV}^2/c^2$

Figure 5.17: A_t *vs* ϕ^* for two Q^2 regions and $-1 < \cos\theta^* < 1$ compared to MAID2000 (black), MAID98 (blue), Sato-Lee (red) and the Effective Lagrangian model (green).

Q^2 [GeV$^2/c^2$]	χ^2/ndf	*z-test*
0.5 to 0.9	1.77	0.80±1.1
0.9 to 1.5	1.41	0.46±1.1

Table 5.2: Values of the χ^2 and z-test comparisons between A_t *vs* $\cos\theta^*$ integrated over the whole range in ϕ^* and the expected value $A_t \equiv 0$.

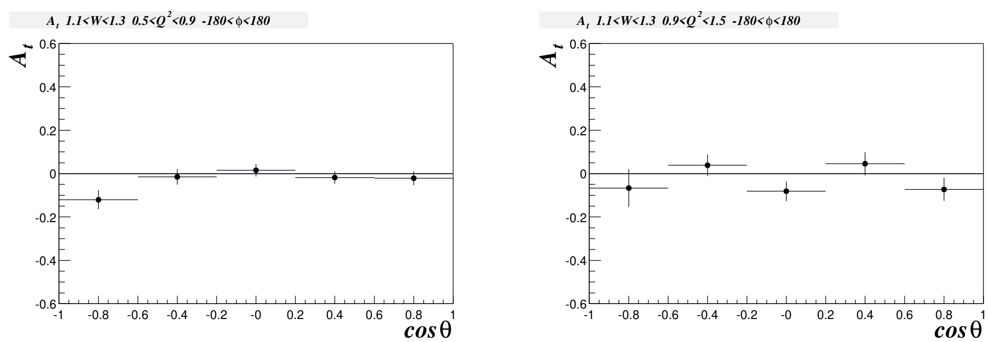

(a) 0.5 GeV$^2/c^2$ < Q^2 < 0.9 GeV$^2/c^2$ (b) 0.9 GeV$^2/c^2$ < Q^2 < 1.5 GeV$^2/c^2$

Figure 5.18: A_t *vs* $\cos\theta^*$ for two Q^2 regions integrated over the whole range in ϕ^*.

data set without obtaining a zero result

$$A'_t = \frac{\sigma_t(\cos(\theta^*), \phi^* > 0^\circ) - \sigma_t(\cos(\theta^*), \phi^* < 0^\circ)}{\sigma_0(\cos(\theta^*), 180 <^\circ \phi^* < 180^\circ)} \tag{5.4}$$

The results compared to the models are shown in Figures 5.21

5.4 Double spin asymmetry A_{et}

The double spin asymmetry A_{et} is the most interesting quantity which can be extracted from EG1 data, since its measurement requires having both polarized beam and polarized target. This asymmetry is expected to be an even function in ϕ^*, as opposed to A_e and A_t. Figures 5.22(a) and (b) show the asymmetry A_{et} for the two different Q^2 bins as a function of ϕ^*. Since the model calculations predict the asymmetry as a function of ϕ^* may vary strongly with $\cos\theta^*$, partial integrations

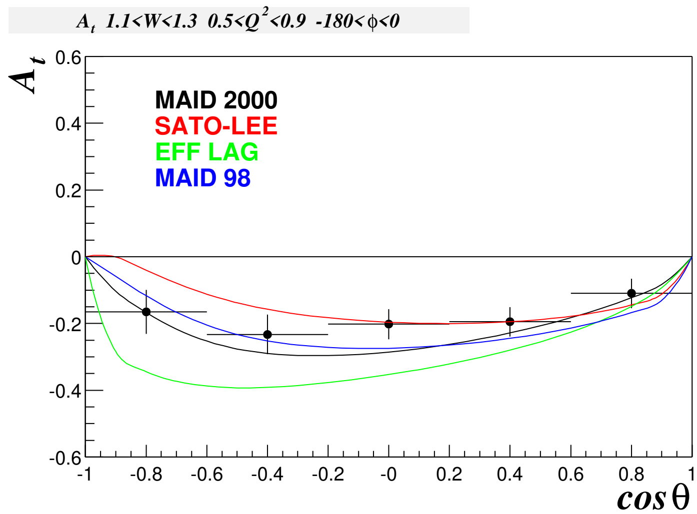

(a) $-180° < \phi^* < 0°$

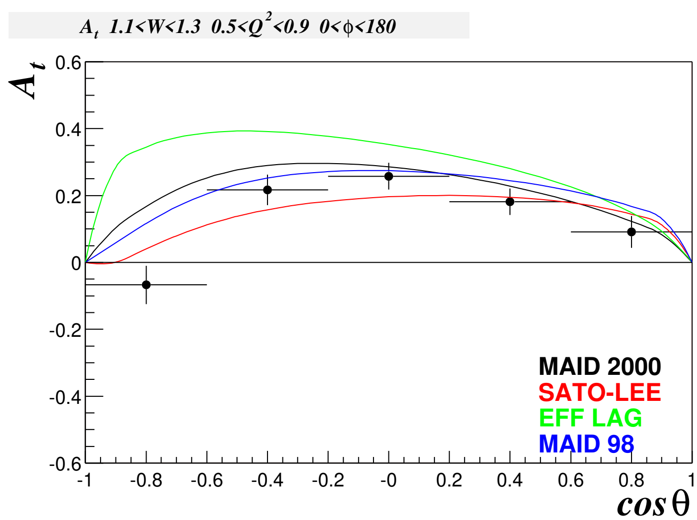

(b) $0° < \phi^* < 180°$

Figure 5.19: A_t *vs* $\cos\theta^*$ for $0.5\ \mathrm{GeV}^2/c^2 < Q^2 < 0.9\ \mathrm{GeV}^2/c^2$ and two different ϕ^* bins compared to MAID2000 (black), MAID98 (blue), Sato-Lee (red) and the Effective Lagrangian model (green).

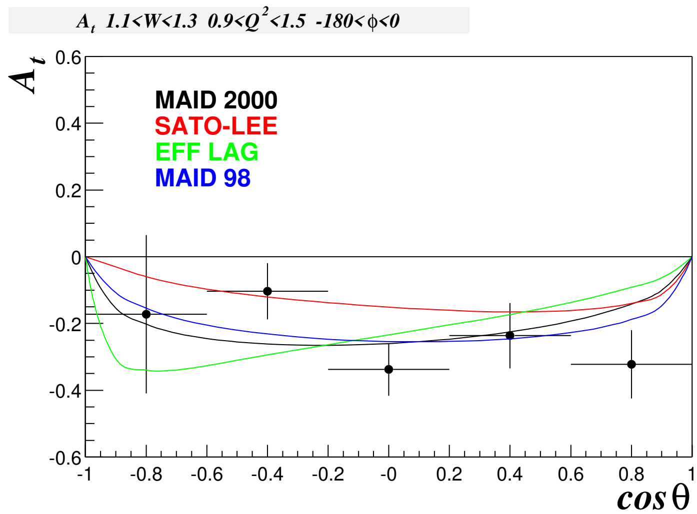

(a) $-180° < \phi^* < 0°$

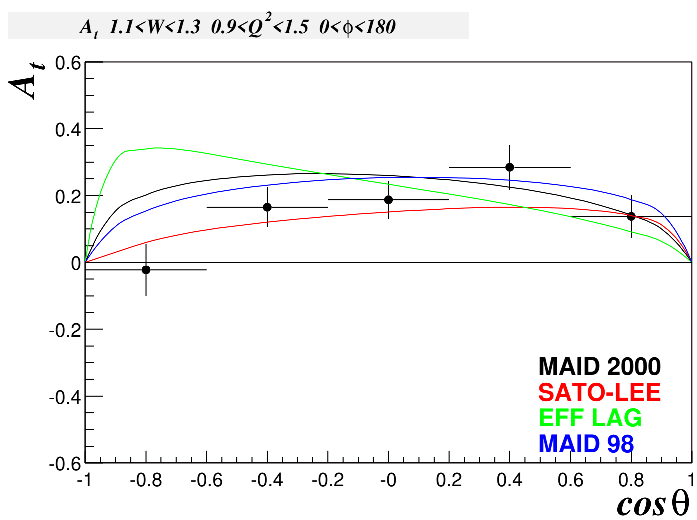

(b) $0° < \phi^* < 180°$

Figure 5.20: A_t *vs* $\cos\theta^*$ **for 0.9 GeV$^2/c^2 < Q^2 <$ 1.5 GeV$^2/c^2$ and two different ϕ^* bins compared to MAID2000 (black), MAID98 (blue), Sato-Lee (red) and the Effective Lagrangian model (green).**

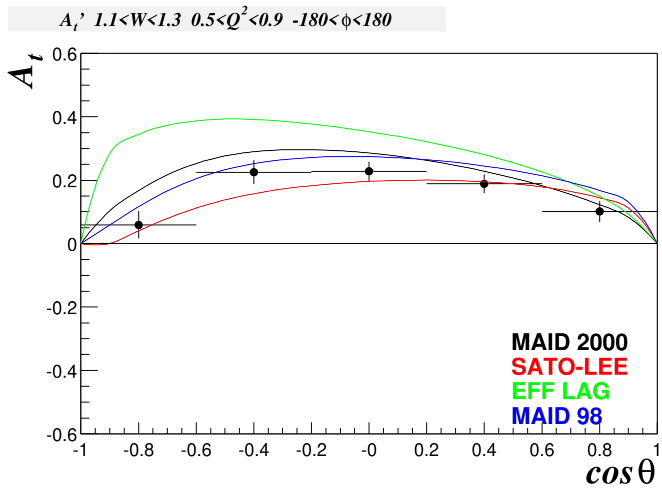

(a) 0.5 GeV$^2/c^2 < Q^2 <$ 0.9 GeV$^2/c^2$

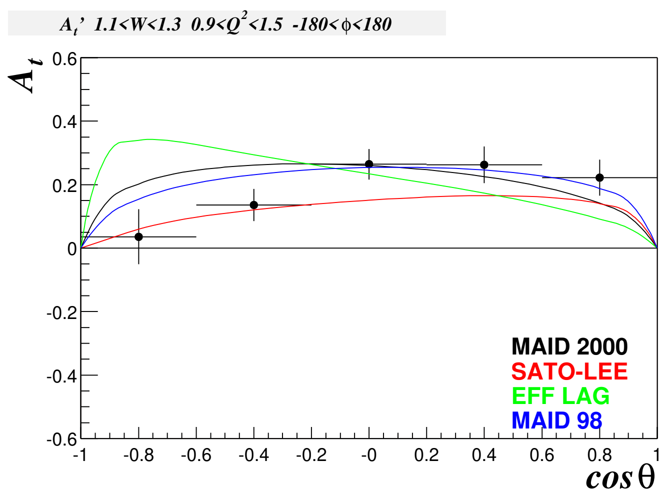

(b) 0.9 GeV$^2/c^2 < Q^2 <$ 1.5 GeV$^2/c^2$

Figure 5.21: A'_t *vs* $\cos\theta^*$ for two Q^2 regions integrated over the whole range in ϕ^*. the data are compared to MAID2000 (black), MAID98 (blue), Sato-Lee (red) and the Effective Lagrangian model (green).

were considered as well. Figures 5.23 and 5.24 show A_{et} as a function of ϕ^* for the two different Q^2 regions, where the integration over $\cos\theta^*$ was only carried over half ranges: $-1 < \cos\theta^* < 0$ and $0 < \cos\theta^* < 1$.

Figure 5.25 shows the asymmetry as a function of $\cos\theta^*$ integrated over the whole range of ϕ^* and in Figures 5.26 and 5.27 partial integrations over half ranges in ϕ^* were performed.

5.5 Q^2 dependence of A_e, A_t and A_{et}

So far the asymmetries were presented as a function of the center of mass angles, $\cos\theta^*$ and ϕ^*, for a specific range in Q^2. One can actually study a third kind of dependence i.e. the Q^2 dependence. From the result presented so far, one can see that the asymmetries do not significantly change neither in shape nor intensity for different Q^2 bins. However the models still predict a slight change and it is interesting to test the data against these predictions. Again, for the asymmetries that are an odd function in ϕ^*, partial integrations over ϕ^* were considered. It was also verified that the results were consistent with zero when the integration was carried out over the whole range in ϕ^*. Figures 5.28(a) and (b) show A_e and A_t integrated over the all range of ϕ^* and the χ^2 and the z-test values in these cases are listed in Table 5.3. Figure 5.29 shows A_{et} integrated over the whole range in ϕ^*.

Asymmetry	χ^2/*ndf*	*z-test*
A_e	0.74	0.75±0.42
A_t	2.4	-0.77±1.3

Table 5.3: Values of the χ^2 and z-test comparisons between A_e and A_t *vs* Q^2 integrated over the whole range in ϕ^* and the expected values $A_e = A_t \equiv 0$.

Figures 5.30, 5.31 and 5.32 show the results for the partial integrations for the three asymmetries.

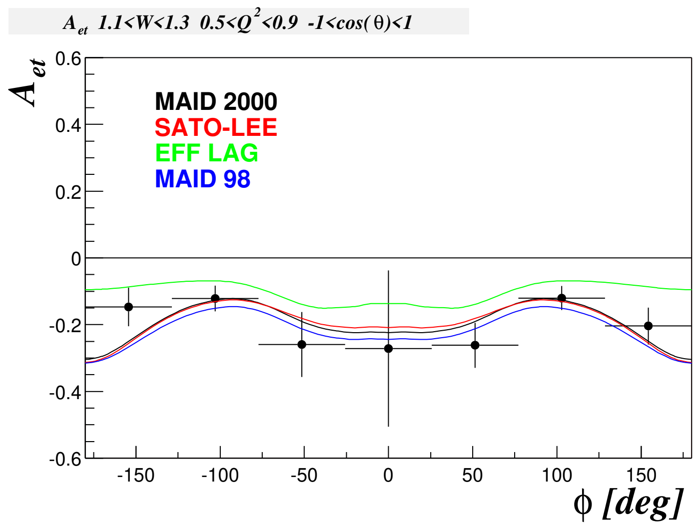

(a) $0.5\ \mathrm{GeV}^2/c^2 < Q^2 < 0.9\ \mathrm{GeV}^2/c^2$

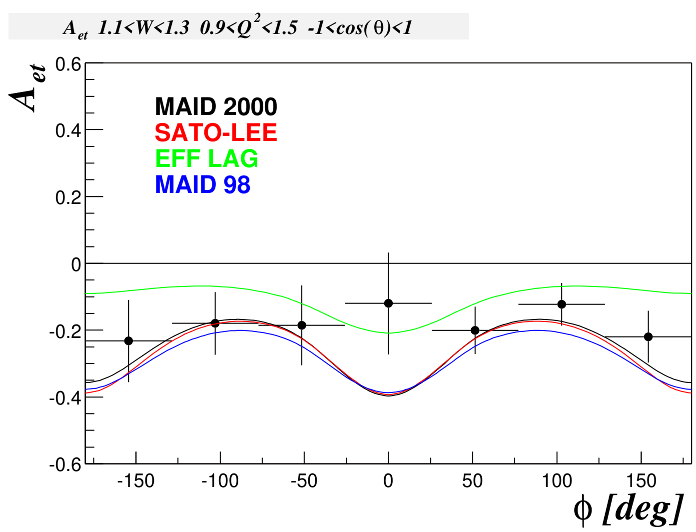

(b) $0.9\ \mathrm{GeV}^2/c^2 < Q^2 < 1.5\ \mathrm{GeV}^2/c^2$

Figure 5.22: A_{et} *vs* ϕ^* for two Q^2 and $-1 < \cos\theta^* < 1$ regions compared to MAID2000 (black), MAID98 (blue), Sato-Lee (red) and the Effective Lagrangian model (green).

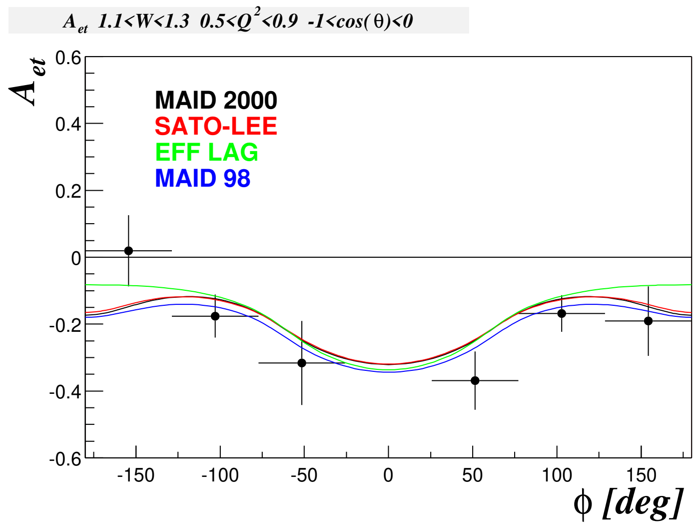

(a) $-1 < \cos\theta^* < 0$

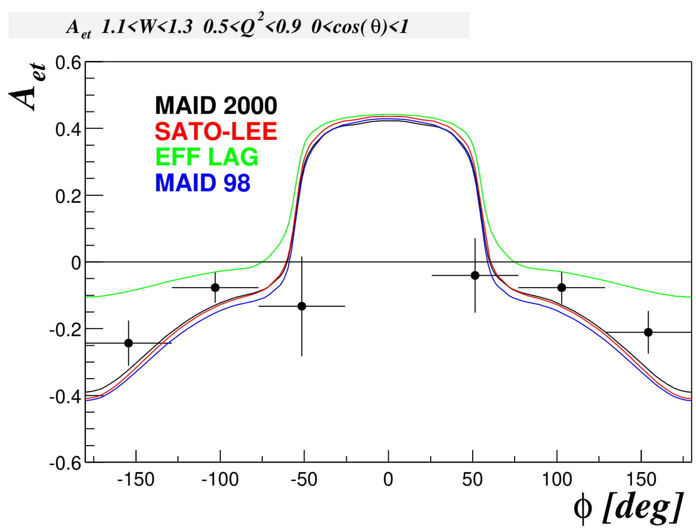

(b) $0 < \cos\theta^* < 1$

Figure 5.23: A_{et} *vs* ϕ^* for 0.5 GeV$^2/c^2 < Q^2 <$ 0.9 GeV$^2/c^2$ and two different $\cos\theta^*$ bins compared to MAID2000 (black), MAID98 (blue), Sato-Lee (red) and the Effective Lagrangian model (green).

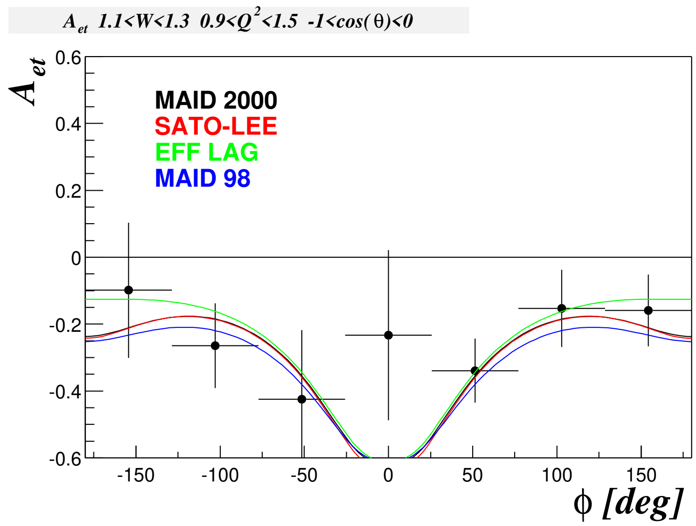

(a) $-1 < \cos\theta^* < 0$

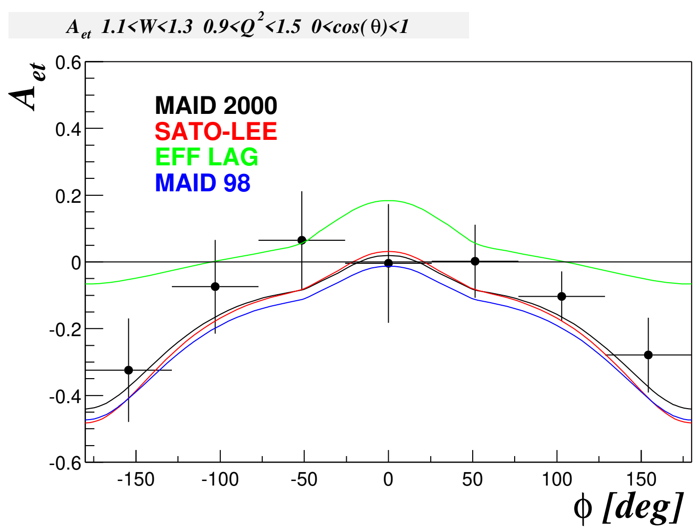

(b) $0 < \cos\theta^* < 1$

Figure 5.24: A_{et} *vs* ϕ^* for 0.9 GeV$^2/c^2 < Q^2 <$ 1.5 GeV$^2/c^2$ and two different $\cos\theta^*$ bins compared to MAID2000 (black), MAID98 (blue), Sato-Lee (red) and the Effective Lagrangian model (green).

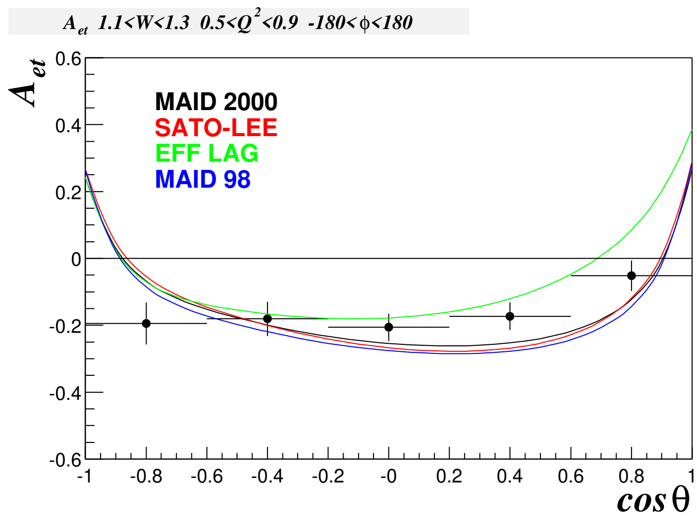

(a) $0.5\ \mathrm{GeV}^2/c^2 < Q^2 < 0.9\ \mathrm{GeV}^2/c^2$

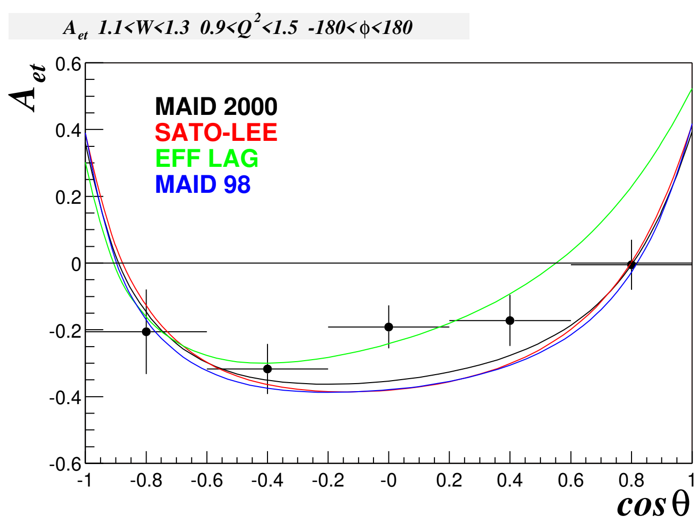

(b) $0.9\ \mathrm{GeV}^2/c^2 < Q^2 < 1.5\ \mathrm{GeV}^2/c^2$

Figure 5.25: A_{et} *vs* $\cos\theta^*$ for two Q^2 regions compared to MAID2000 (black), MAID98 (blue), Sato-Lee (red) and the Effective Lagrangian model (green).

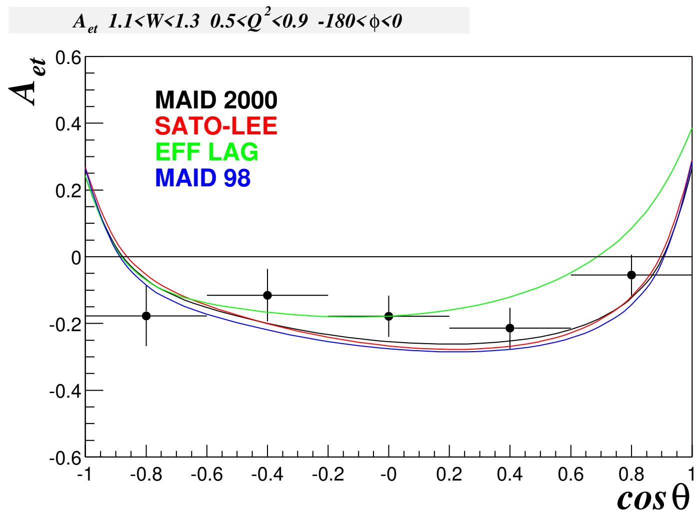

(a) $-180° < \phi^* < 0°$

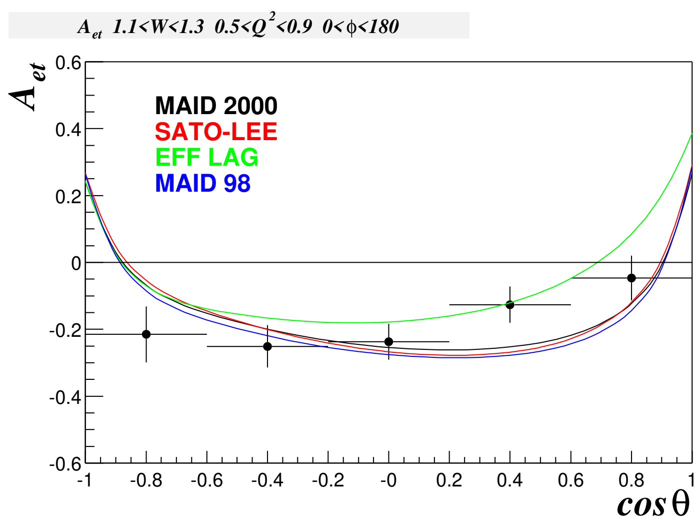

(b) $0° < \phi^* < 180°$

Figure 5.26: A_{et} *vs* $\cos\theta^*$ for $0.5\ \mathrm{GeV}^2/c^2 < Q^2 < 0.9\ \mathrm{GeV}^2/c^2$ and two different ϕ^* bins compared to MAID2000 (black), MAID98 (blue), Sato-Lee (red) and the Effective Lagrangian model (green).

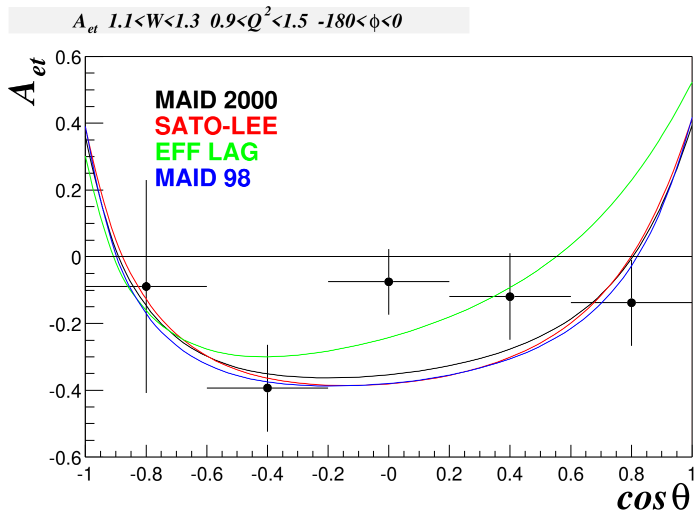

(a) $-180° < \phi^* < 0°$

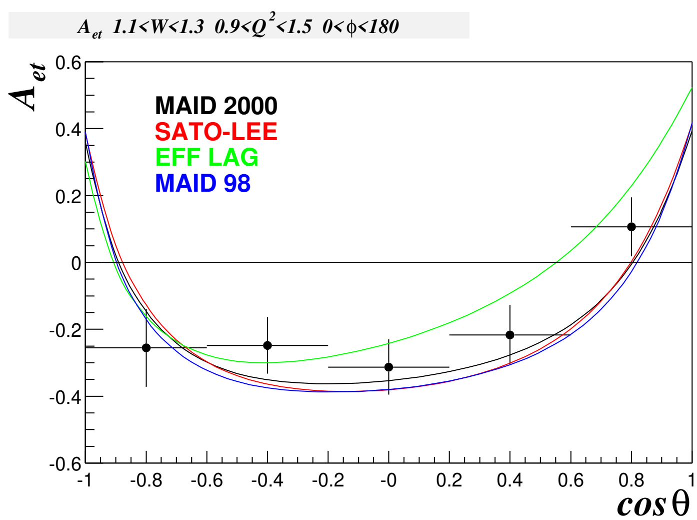

(b) $0° < \phi^* < 180°$

Figure 5.27: A_{et} *vs* $\cos\theta^*$ for $0.9\ \mathrm{GeV}^2/c^2 < Q^2 < 1.5\ \mathrm{GeV}^2/c^2$ and two different ϕ^* bins compared to MAID2000 (black), MAID98 (blue), Sato-Lee (red) and the Effective Lagrangian model (green).

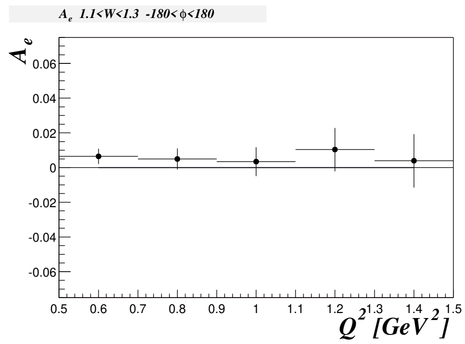

(a) A_e

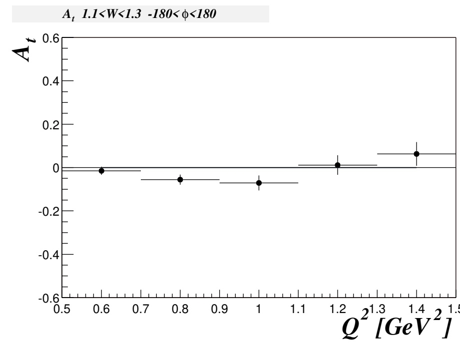

(b) A_t

Figure 5.28: A_e and A_t *vs* Q^2 integrated over the whole range in ϕ^* and $\cos\theta^*$. The result for A_e is consistent with zero but not for A_t.

Again the symmetry on ϕ^* of σ_e and σ_t was used

$$\sigma_e(\phi^*) = -\sigma_e(-\phi^*) \tag{5.5}$$

$$\sigma_t(\phi^*) = -\sigma_t(-\phi^*) \tag{5.6}$$

and the asymmetry was integrated over the whole range in ϕ^* as shown in Figure 5.33.

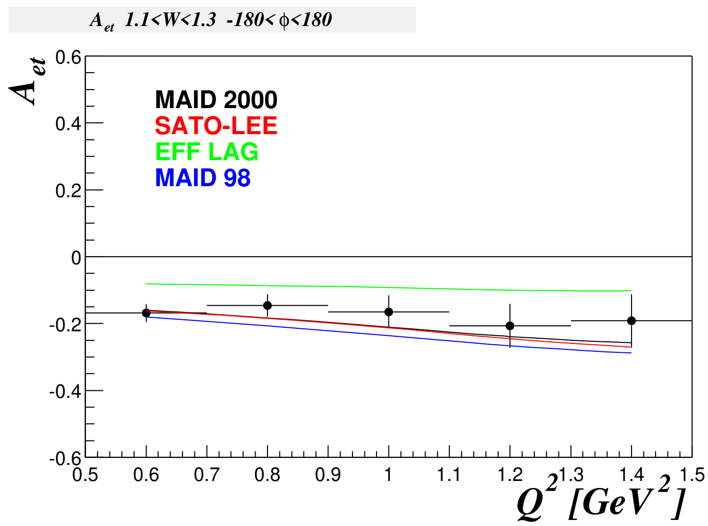

Figure 5.29: A_{et} *vs* Q^2 integrated over the whole range in ϕ^* and $\cos\theta^*$ compared to MAID2000 (black), MAID98 (blue), Sato-Lee (red) and the Effective Lagrangian model (green).

5.6 Systematic errors

All the results shown in the previous sections present error bars which are purely statistical. Throughout the analysis many intermediate steps were taken to achieve the result. These steps might be sources of systematic errors. This section will describe the studies which were done in order to understand the importance of these possible errors.

The following items were identified as possible sources for systematic errors:

- Carbon normalization
- Calculation of P_eP_t
- P_e value
- Polarization of the unpaired nucleon in ^{15}N
- Target fill factor
- Determination of the normalization constant d
- Fiducial cuts

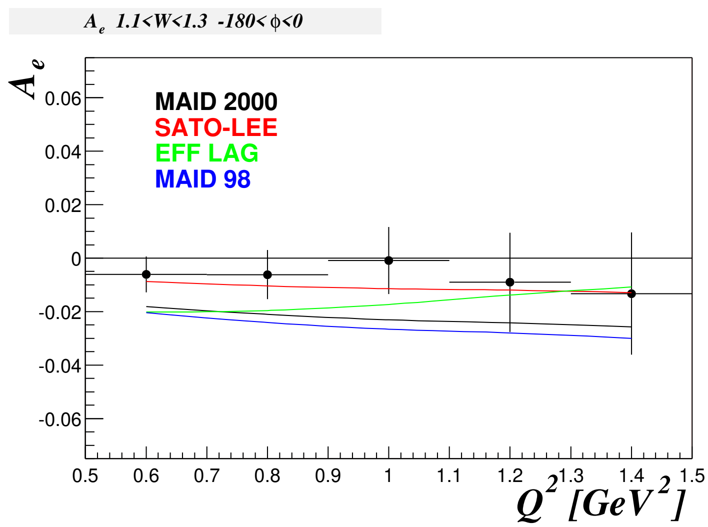

(a) $-180° < \phi^* < 0°$

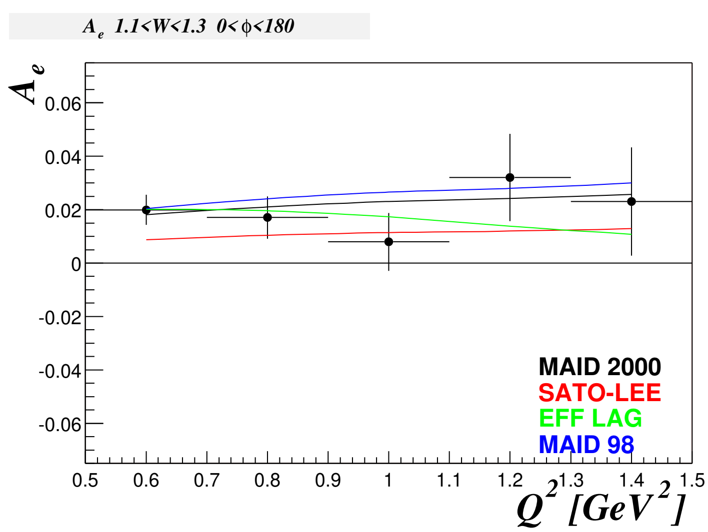

(b) $0° < \phi^* < 180°$

Figure 5.30: A_e *vs* Q^2 integrated over two different ϕ^* ranges and $-1 < \cos\theta^* < 1$ compared to MAID2000 (black), MAID98 (blue), Sato-Lee (red) and the Effective Lagrangian model (green).

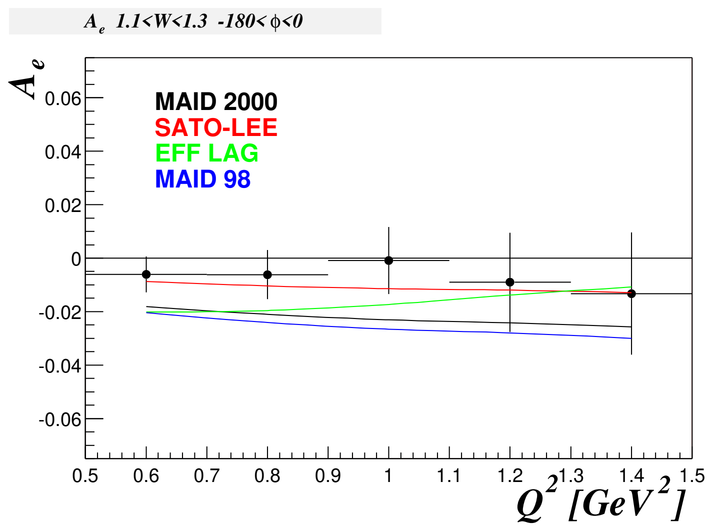

(a) $-180° < \phi^* < 0°$

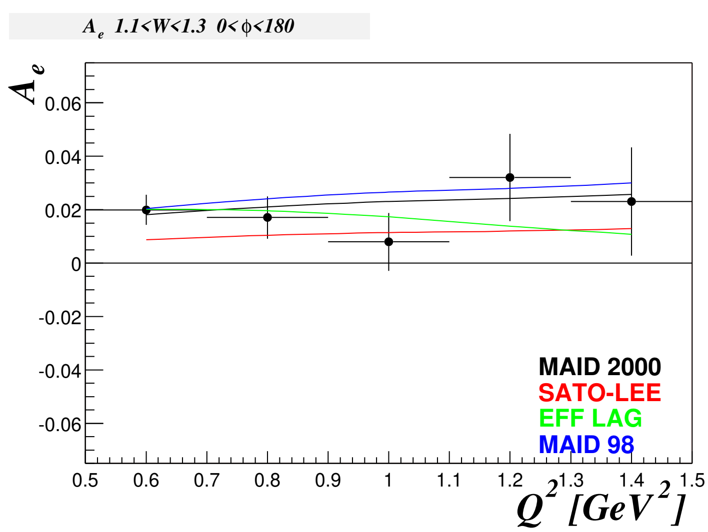

(b) $0° < \phi^* < 180°$

Figure 5.31: A_t *vs* Q^2 integrated over two different ϕ^* bins and $-1 < \cos\theta^* < 1$ compared to MAID2000 (black), MAID98 (blue), Sato-Lee (red) and the Effective Lagrangian model (green).

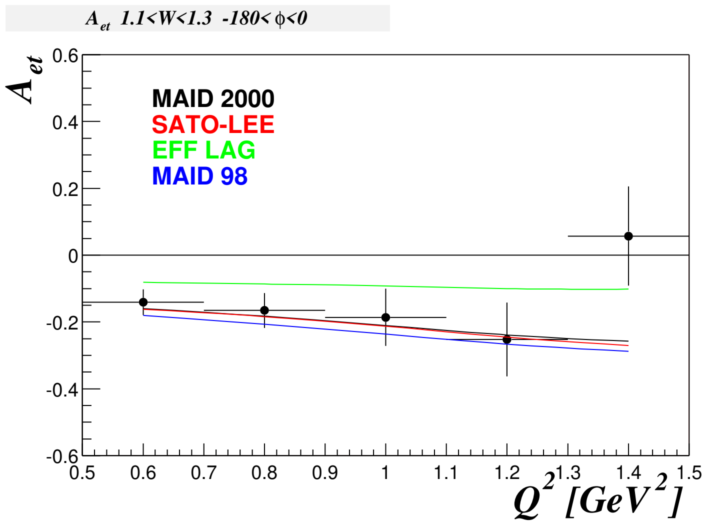

(a) $-180° < \phi^* < 0°$

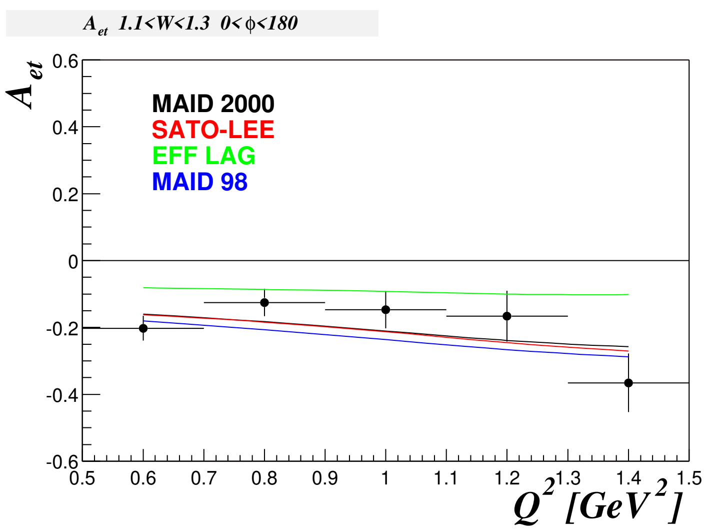

(b) $0° < \phi^* < 180°$

Figure 5.32: A_{et} *vs* Q^2 integrated over two different ϕ^* bins and $-1 < \cos\theta^* < 1$ compared to MAID2000 (black), MAID98 (blue), Sato-Lee (red) and the Effective Lagrangian model (green).

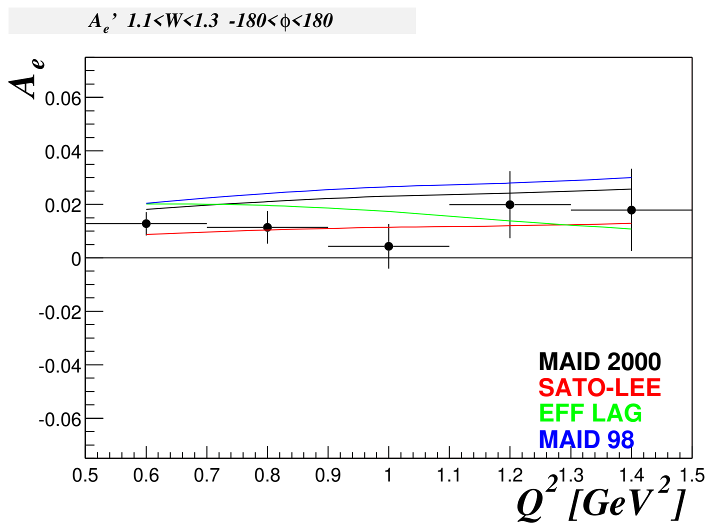

(a) A'_e

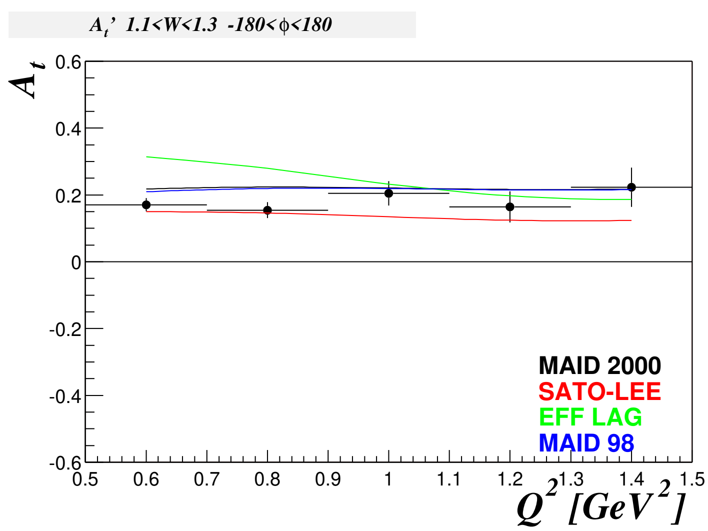

(b) A'_t

Figure 5.33: A'_e and A'_t *vs* Q^2 integrated over the whole range in ϕ^* and θ^*. The data are compared to MAID2000 (black), MAID98 (blue), Sato-Lee (red) and the Effective Lagrangian model (green).

- Cuts for the electron identification
- Cuts for the π^0 identification
- Acceptance calculation

To estimate the size of the systematic error for each of these items, just one of the parameters was changed, the asymmetries recalculated and then compared to the original asymmetry. For some cases the difference of the two asymmetries is the systematic error. For other cases, since changing the cut means changing the statistical sample as well, the difference is not just the systematic error, but a combination of a systematic and a statistical effect. However the difference is still an indication of how big the effect is and in particular, it can be considered an upper limit for the systematic effect. The various asymmetries and angular distributions can be sensitive in different ways to these effects. In the following subsections a particular asymmetry, A_{et} as a function of ϕ^* integrated over the whole range in $\cos\theta^*$ will be considered.

5.6.1 Carbon normalization

As seen in section 4.3 the carbon subtraction can be done in several different ways: normalization on the tail of the missing mass distribution or on the tail of the W distribution. These methods give fairly similar constants which are however not compatible with each other within the statistical error. For the analysis the method of normalization was chosen to be the one that uses the tail of the exclusive W spectrum. To understand what the magnitude of the effect is if another method is used, the asymmetry was extracted normalizing on the tails of the missing mass tail and the inclusive W spectra. Figures 5.34 (a) and (b) show the comparison of the original asymmetry (black triangles) with the one where a different method was used (red squares). The different normalization constants give a systematic shift in one direction depending on the constant being greater (negative shift) or smaller (positive shift). In particular it was found that the inclusive W tail and the missing mass methods give a +2.7% and -4.2% shift, respectively. These values and therefore the systematic error associated with the carbon normalization is very small compared to the statistical error.

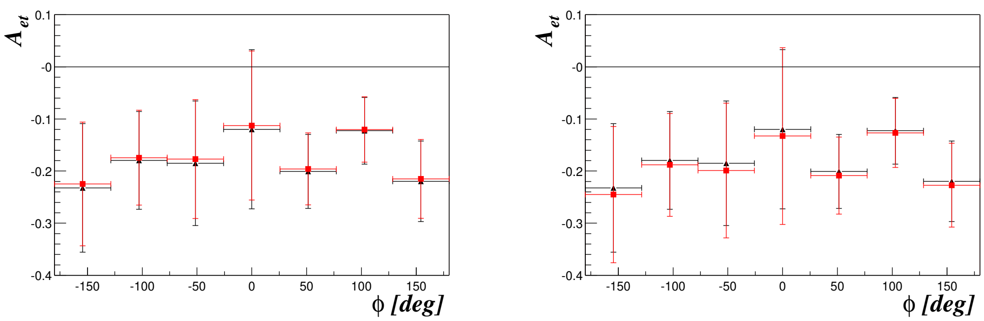

(a) inclusive W tail

(b) missing mass

Figure 5.34: Comparison of A_{et} *vs* ϕ^* for 0.9 GeV$^2/c^2$ $<$ Q^2 $<$ 1.5 GeV$^2/c^2$. The black triangles use the exclusive W tail method, whereas the red squares use the indicated method.

5.6.2 Calculation of P_eP_t

The asymmetries contain the factors α_{et} and α_t, which depend on the value of the polarization P_e and P_t (see eq 4.6). This value is determined using the known value of P_e (measured during the Møller runs) and the product P_eP_t determined with the procedure described in section 4.5. As mentioned in that section, it is possible to use slightly different methods, like for example utilizing the fitted carbon distribution instead of the carbon spectrum directly. The results of the two methods are slightly different (see Figures 4.14 and 4.15) and therefore the impact of this effect on the final result has to be taken into account for the systematic error evaluation. Figure 5.35 shows the comparison between the original asymmetry (black triangles), where $P_e^aP_t^a = 0.275\pm0.007$ and $P_e^bP_t^b = 0.385\pm0.008$, and the resulting asymmetry using the values obtained with the fit method (red squares), where $P_e^aP_t^a$ and $P_e^bP_t^b$ were determined to be 0.269 ± 0.007 and 0.376 ± 0.007, respectively. The slightly lower values cause a negative shift of the order of -2.3% but, like in the case before, it is very small compared to statistical error.

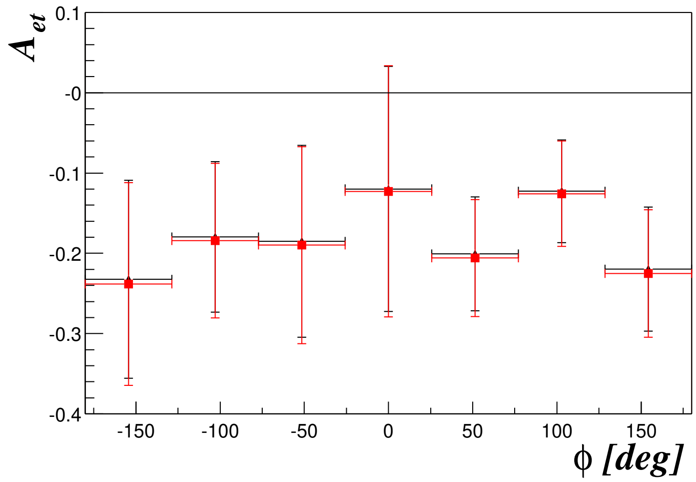

Figure 5.35: Comparison of A_{et} *vs* ϕ^* for 0.9 GeV$^2/c^2$ $<$ Q^2 $<$ 1.5 GeV$^2/c^2$. The black triangles use P_eP_t determined with the carbon spectrum directly, whereas the red squares use a fitted carbon distribution.

5.6.3 P_e value

The beam polarization was measured several times during the whole EG1 experiment, using a Møller polarimeter. During the acquisition of the 2 GeV data, only one measurement was performed and the result obtained was $P_e = 70.74 \pm 1.04\%$. The polarization was considered to be constant for this analysis. However a possible difference of the value of the polarization for runs with positive target polarization with respect to the value for runs with negative target polarization, or a variation of just one of the two values can affect the final result. To study this possible systematic effect, the case in which the beam polarization for positive target polarization runs is $P_e^a = 70.74 + 1.04\% = 71.78\%$ and the beam polarization for negative target polarization runs is $P_e^b = 70.74 - 1.04\% = 69.7\%$ was considered . The asymmetry was then recalculated and Figure 5.36 shows the difference between the original asymmetry and the one where the new values of the beam polarization were used. The effect is very small (a shift of +1.3%) compared to the statistical error. The error considered for this test is actually over-estimated. The polarization was monitored during the entire run and the average value was $P_e = 69.78 \pm 0.35\%$ as can be seen in Figure G.1 in Appendix G. Using this fluctuation instead of the

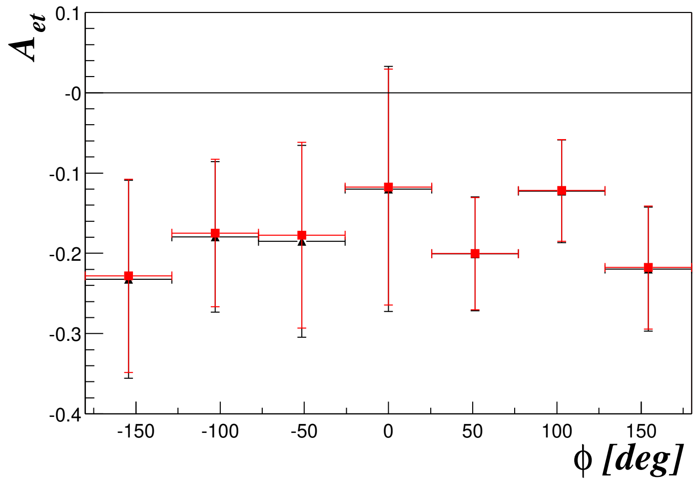

Figure 5.36: A_{et} *vs* ϕ^* for 0.9 GeV$^2/c^2 < Q^2 <$ 1.5 GeV$^2/c^2$. Comparison between the asymmetries found using the $P_e^a = P_e^b = 70.74$ (black triangles) and using $P_e^a = 71.78\%$ and $P_e^b = 69.7\%$ (red squares).

error of the Møller measurement, the variation of the asymmetry and therefore the systematic error is even smaller.

5.6.4 Polarization of the unpaired nucleon in ^{15}N

As mentioned in section 2.3.2 the unpaired proton of the ^{15}N is actually slightly polarized and therefore there is a contribution to the asymmetry. To understand the magnitude of such contributions an estimate of the polarization of the proton of the ^{15}N was done.

^{15}N and H nuclei were found to follow the Equal Spin Temperature (EST) prediction [44, 45]. This regime is established when two polarizable systems are connected by spin-spin interactions. In this case, at equilibrium, the polarizations of ^{15}N, $P(^{15}N)$, and H, $P(H)$, are related by:

$$P(^{15}N) = \tanh\left[\frac{\mu_{^{15}N} B}{\mu_p B} \tanh^{-1} P(H)\right] \tag{5.7}$$

where $\mu_p = 2.79\mu_N$ and $\mu_{^{15}N} \sim -0.28\mu_N$ are the magnetic magnetons for the proton and the ^{15}N, respectively. For $P(H) \sim 60\%$, one gets $P(^{15}N) = -7\%$. Under the assumption that the ^{15}N with total angular momentum $J = 1/2$ can be simply seen as a system of nucleons with total orbital momentum $L = 1$ and an unpaired proton with spin $S = 1/2$, this value can be related to the proton polarization using Clebsh-Gordan decomposition. The result is

$$P(p) = -\frac{1}{3}P(^{15}N) \tag{5.8}$$

The polarization is therefore on the order of 2%. As seen in section 5.6.2 a 2% difference in the proton polarization does not have any effect in the asymmetry and therefore the contribution of the ^{15}N asymmetry is completely negligible. This contribution is actually even smaller considering that the ^{15}N events are reduced by the missing mass cut.

5.6.5 Target fill factor

The method to evaluate the target fill factor was described in great detail in section 4.4. The procedure involves several parameters, which need to be determined in order to get the final result. Some of these parameters are well known, for example the thickness of the target windows. Others, like the target thickness, are known with only a limited precision. The choice of the values of the parameters was based on an independent analysis of the data [41]. However it is still necessary to see how much the asymmetry changes if other possibilities for the parameter are selected. For this systematic error evaluation, the values of the parameters that give the most different result were chosen. In particular $x^T = 0.54\ cm$ for the target thickness and $L = 1.6\ cm$ for the total length of the cell were selected. With this choice the fill factor is $\frac{b}{a} = -0.13$. Figure 5.37 shows the asymmetry A_{et} calculated with this value (red squares) compared to A_{et} with the original value of $\frac{b}{a} = -0.33$ (black triangles). The resulting shift is of the order of -3.3%.

5.6.6 Determination of the normalization constant *d*

Another parameter needed to calculate the asymmetries is the factor d to normalize negative target polarization runs with respect to positive target polarization runs. This parameter, as seen in section 4.2 is determined using the integral of the

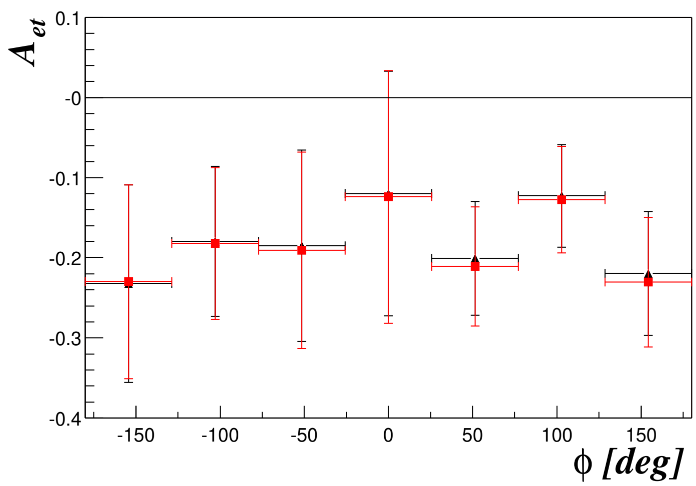

Figure 5.37: Comparison of A_{et} *vs* ϕ^* for 0.9 GeV$^2/c^2$ < Q^2 < 1.5 GeV$^2/c^2$. The black triangles and the red squares were determined using the ratio $\frac{b}{a} = -0.33$ and $\frac{b}{a} = -0.13$, respectively.

inclusive W spectrum. This method results in a statistical error on d on the order of $\Delta d/d$ =0.03%. A variation in d of this magnitude does not cause any changes in the asymmetry. However, the normalization procedure can still have a systematic error and in order to understand the impact on the asymmetry the case was considered where $d' = d + \Delta d * 100$. Figure 5.38 shows the comparison between the asymmetries calculated using d and d'. As can be seen the effect is very small (< -0.1%) compared to the statistical error.

5.6.7 Fiducial cuts

In order to take into account the acceptance, data was selected in a fiducial region by means of momentum dependent cuts in ϕ *vs* θ. Two sets of cuts were studied, a tight one, which cuts in a safe region and a loose one, which selected events in order to maximize statistics. The choice of using the latter in this analysis is reasonable, since we want to study asymmetries and not absolute cross sections, where understanding the acceptance becomes a crucial point. Nevertheless a study of how much the resulting asymmetries change in case one uses the tight cuts was done. Figure 5.39 shows the comparison between the asymmetry A_{et} obtained using

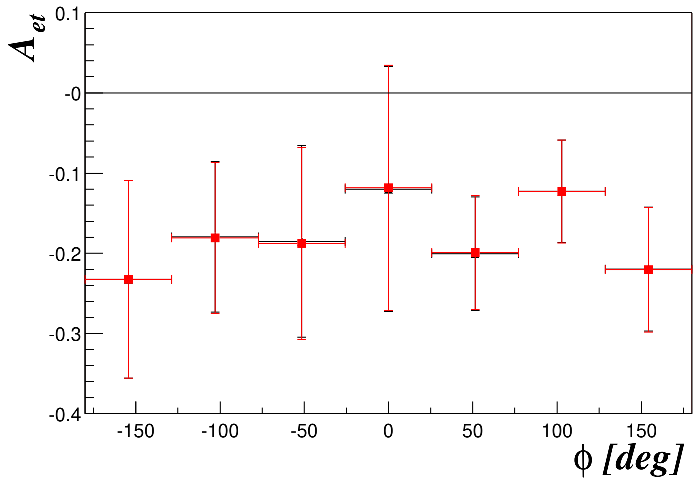

Figure 5.38: Comparison of A_{et} *vs* ϕ^* for 0.9 $\mathrm{GeV}^2/c^2 < Q^2 <$ 1.5 GeV^2/c^2. The black triangles and the red squares were determined using the normalization constant d and $d' = d + \Delta d * 100$, respectively.

loose (black squares) and tight (red triangles) cuts. The variations in this case are much bigger that in the previous cases, however in this study the statistical sample is changing and therefore the differences between the two asymmetries are a combination of a statistical and a systematic effect. These variations, which in any case are fairly small for most of the points, can therefore only be considered an upper limit of the systematic error.

5.6.8 Electron identification

Several cuts where applied to improve the identification of the electron in each event (see section 3.4). In particular the distribution of the number of photoelectrons detected in the Čerenkov counters has a peak at ~ 2.5 photoelectrons which stems from an artifact of the Čerenkov counters (see Figure 3.9). It was already shown in section 3.7 that fiducial cuts remove this peak, but a study was undertaken to estimate the systematic error due to contamination from negative pions. The asymmetry was recalculated using a stricter cut by requiring the number of photoelectrons to be greater than 2.5 instead of 0.5, and Figure 5.40 shows the comparison between the two. Again the statistical sample is changing and therefore

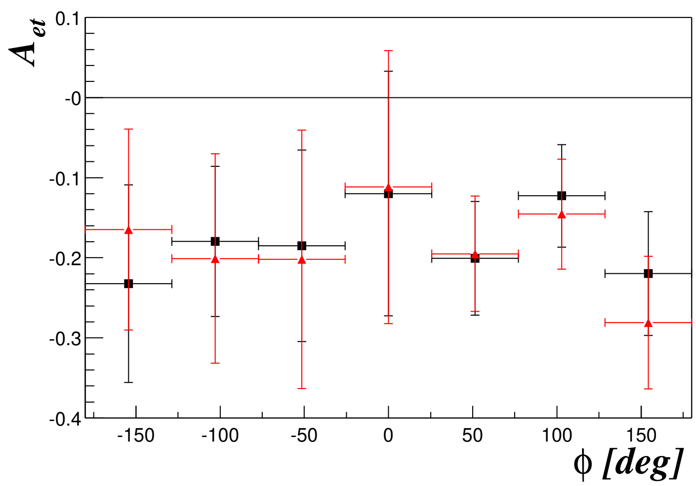

Figure 5.39: Comparison of A_{et} *vs* ϕ^* for 0.9 GeV$^2/c^2$ $<$ Q^2 $<$ 1.5 GeV$^2/c^2$. The black squares and the red triangles were determined using loose and tight fiducial cuts, respectively.

some of the differences are also due to statistical fluctuations, but, as before the changes are very small compared to the statistical error.

5.6.9 π^0 identification

As seen in section 3.6 a missing mass cut was applied in order to select the π^0 channel. The cut chosen in the analysis selects the peak remaining after the subtraction of the nuclear background: -0.01 GeV$^2/c^4 < M_X^2 < 0.06$ GeV$^2/c^4$. The asymmetry was recalculated with a looser cut -0.02 GeV$^2/c^4 < M_X^2 < 0.07$ GeV$^2/c^4$ in order to understand whether the events in the side bands are really unpolarized background (see Figure 5.41). Again, the sample is changing and therefore the fluctuations include also statistical effects. Figure 5.42 shows the comparison of the two asymmetries and again the changes are small compared to the statistical error, although there may appear to be a small systematic shift.

5.6.10 Acceptance calculation

The method to correct for the acceptance relies on the fact that fiducial cuts select regions of 100% efficiency. As described in section 4.6, under this assumption the only effect one has to correct for is the geometrical acceptance,which can be

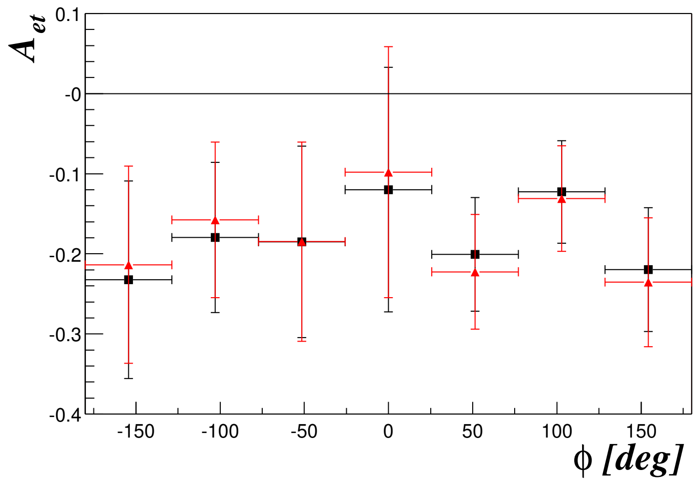

Figure 5.40: Comparison of A_{et} *vs* ϕ^* for $0.9\ \text{GeV}^2/c^2 < Q^2 < 1.5\ \text{GeV}^2/c^2$. The black squares and the red triangles were determined requiring the number of photoelectrons detected in the Čerenkov counter to be greater than 0.5 and greater than 2.5, respectively.

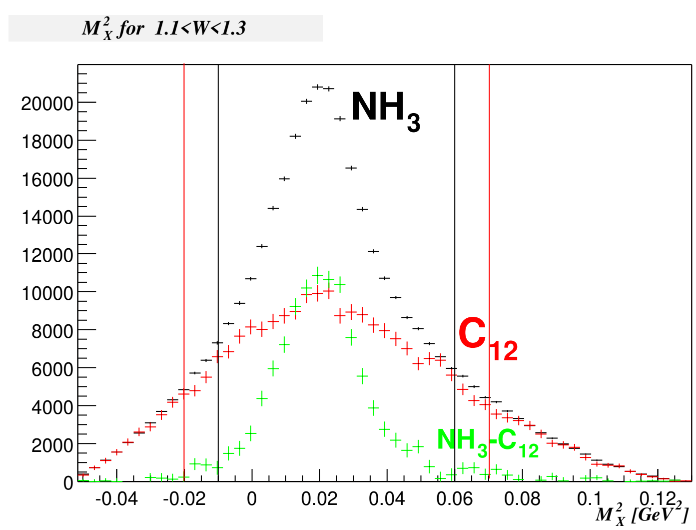

Figure 5.41: M_x^2 spectrum for $^{15}NH_3$, ^{12}C data and the subtraction $^{15}NH_3$-^{12}C. The black and the red lines indicates the cuts $-0.01\ \text{GeV}^2/c^4 < M_X^2 < 0.06\ \text{GeV}^2/c^4$ and $-0.02\ \text{GeV}^2/c^4 < M_X^2 < 0.07\ \text{GeV}^2/c^4$ respectively.

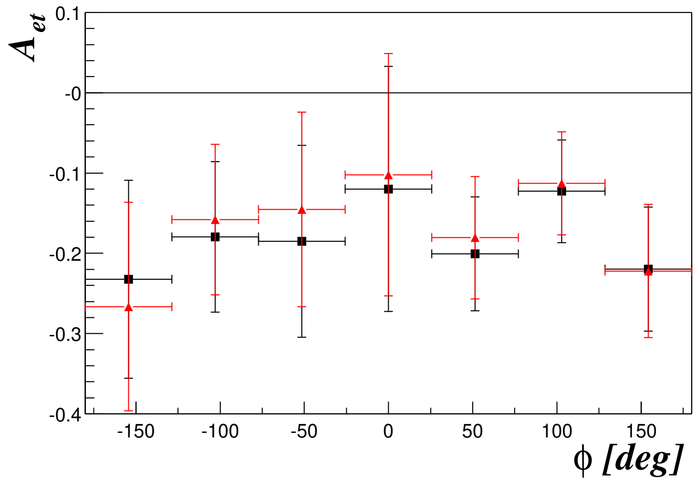

Figure 5.42: Comparison of A_{et} *vs* ϕ^* for $0.9\ \mathrm{GeV}^2/c^2 < Q^2 < 1.5\ \mathrm{GeV}^2/c^2$. The black squares and the red triangles were determined using the cuts $-0.01\ \mathrm{GeV}^2/c^4 < M_X^2 < 0.06\ \mathrm{GeV}^2/c^4$ and $-0.02\ \mathrm{GeV}^2/c^4 < M_X^2 < 0.07\ \mathrm{GeV}^2/c^4$, respectively, in order to select the π^0 events.

done analytically. In this case there are two possible sources of systematic errors: firstly the efficiency is not 100% and secondly it could be that it is not equally efficient from one sector to another. The first point does not cause an error since an overall multiplicative factor to correct for the actual lower efficiency would drop out when asymmetries are considered. The second effect is estimated to be very small. Infact, as shown for example in Figure 3.35, the six sectors after fiducial cuts have the same average counts and any inefficiency due to scintillators or drift chambers are removed by the fiducial cuts.

5.6.11 Summary

Several sources for systematic errors were studied in the previous subsections. Some of these errors such as the one related to the normalization of the carbon or the target fill factor were evaluated by varying some parameters in the analysis. In these cases the asymmetries obtained with different values for these quantities in different conditions present a defined shift in one direction as compared to the original asymmetry which is fairly uniform for all the points. Table 5.4 summarizes the systematic errors for A_{et} as a function of ϕ^* for 0.9 GeV$^2/c^2 < Q^2 <$ 1.5 GeV$^2/c^2$.

Systematic error source	Systematic error (%)
Carbon norm	+2.7,-4.2
P_eP_t	-2.3
P_e	+1.3
Fill factor	-3.3
Norm const d	<-0.1

Table 5.4: Summary of the systematic errors for the asymmetry A_{et} as a function of ϕ^* for 0.9 GeV$^2/c^2 < Q^2 <$ 1.5 GeV$^2/c^2$

Combining these quadratically, would result in a systematic error of $\sim$ 5% which is considerably smaller than the statistical error which is on the order of 60%.

Other sources related the choice of cuts were investigated. The variation of the cuts applied to the data gives a final result which is sometime very different from the original. For example, applying tight instead of the loose fiducial cuts, some points have a variation up to 30%. These variations are very different for each point of the asymmetries and they don't have a systematic shift in one direction. As it was already pointed out, in these cases the statistical sample is changing and therefore the variation can be due to statistical effects. To verify this point the following test was made. The statistical sample was reduced randomly by 10% and the asymmetry was recalculated and compared with the asymmetry from the full sample. Since in this case the effect is purely statistical, the variations found are purely statistical as well. It was found that the variations are of the same magnitude as the ones found when systematic effects were studied, proving that the fluctuations have a large statistical component. Figure 5.43 shows the comparison between the asymmetry with full statistic (red triangles) and with 10% less events (black squares), both with a loose missing mass cut (-0.02 GeV$^2/c^4 < M_X^2 <$ 0.07 GeV$^2/c^4$). This plot has to be compared with Figure 5.42 were the asymmetry with loose missing mass cut (red triangles) is compared with the asymmetry with tight cut (black squares) which corresponds to a loss in events of roughly a 10%. The two figures present similar sizes of fluctuations.

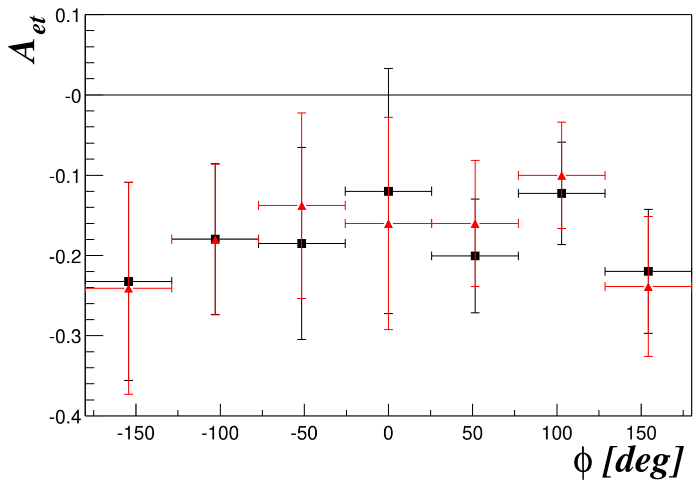

Figure 5.43: Comparison of A_{et} *vs* ϕ^* for 0.9 GeV$^2/c^2$ $< Q^2 <$ 1.5 GeV$^2/c^2$. The red triangles use the full statistics and the black squares a sample with a random loss of 10%. A loose missing mass cut -0.02 GeV$^2/c^4$ $< M_X^2 <$ 0.07 GeV$^2/c^4$ was applied to both.

5.7 Radiative corrections

The object of the thesis is the measurement of asymmetries for the channel $\vec{e}\vec{p} \to e'p\pi^0$. The detection of the final state containing e' and p and the missing mass cut to select the π^0 events is not enough to select this channel exclusively. Higher order processes which involve emission of real photons, internal exchange of virtual photons and vacuum polarization are characterized by the same final state and therefore contribute to the experimental cross section. Figure 5.44 shows the Feynman diagrams contributing to the cross section up to order α^4. The diagram in (a) is the lowest order for the $\Delta(1232)$ production, which is the object of this study. To order α^4 the five diagrams in (b) contribute to the cross section, one is the production of an e^+e^- pair and the other four are diagrams where a second virtual photon is exchanged. To order α^3 there are two kind of processes: in the first, also known as internal Bremsstrahlung, the incoming or outgoing particle radiates one real photon in the field of the nucleon involved in the scattering (the four diagrams in (c)), in the second, the so called external Bremsstrahlung, the incoming or outgoing particle radiates one real photon in the field of a nucleon other than the one which undergoes the scattering (the diagrams in (d))[14]. The qualitative consequence of these processes is that the actual value of the energy at which the reaction takes place, is different from the measured one. For example, if the electron emits a photon before the scattering, its energy at the moment of the interaction will be $\epsilon_i - \epsilon_\gamma$ where ϵ_γ is the energy of the emitted real photon. This means that the actual invariant mass $W_{real} = |e - \gamma_{real} + M - e'|$, where γ_{real} is the 4-vector of the real photon. It is easy to see that $W_{real} < W = |e + M - e'|$. Therefore an event measured at a certain apparent W can actually come from a reaction that took place at lower $W = W_{real}$. An example of this effect is the big radiative tail, present in the inclusive spectrum rising with W, which comes mostly from elastic scattering.

Similarly to W, the square of the missing mass, M_X^2, is miscalculated as well in case of the presence of radiative background resulting in a long tail towards higher M_X^2. This affects the measurement of the exclusive cross section since the missing mass cut around the peak of the missing particle cuts away radiative events and, at the same time, the peak can also be contaminated by the M_X^2 tail of a particle with lower mass. There are several theoretical formulations that describe, at least partially, these processes. For this analysis the Mo-Tsai formulation was used, which takes into account all the possible effects described above [47]. Mo and Tsai provides the equations for calculating the radiative cross section for elastic and inelastic inclusive electron-proton scattering. To deal with the exclusive channel $\vec{e}\vec{p} \rightarrow e'p\pi^0$ a generalization was done, by replacing the inclusive cross section with the one given by the MAID98 model for pion electro-production [48]. This generalization is an approximation [43], however for this present work it is believed to give a reasonable estimate of the effect. The reasons are twofold: firstly, the corrections for this channel are expected to be small and secondly the final results sought are asymmetries

[14]There are no diagrams for external Bremsstrahlung for the proton or $\Delta(1232)$ since they are negligible. These contributions are much smaller than the ones of the electrons because the energy loss by Bremsstrahlung is proportional to E/m^2, where E and m are the energy and the mass of the incident particle [46].

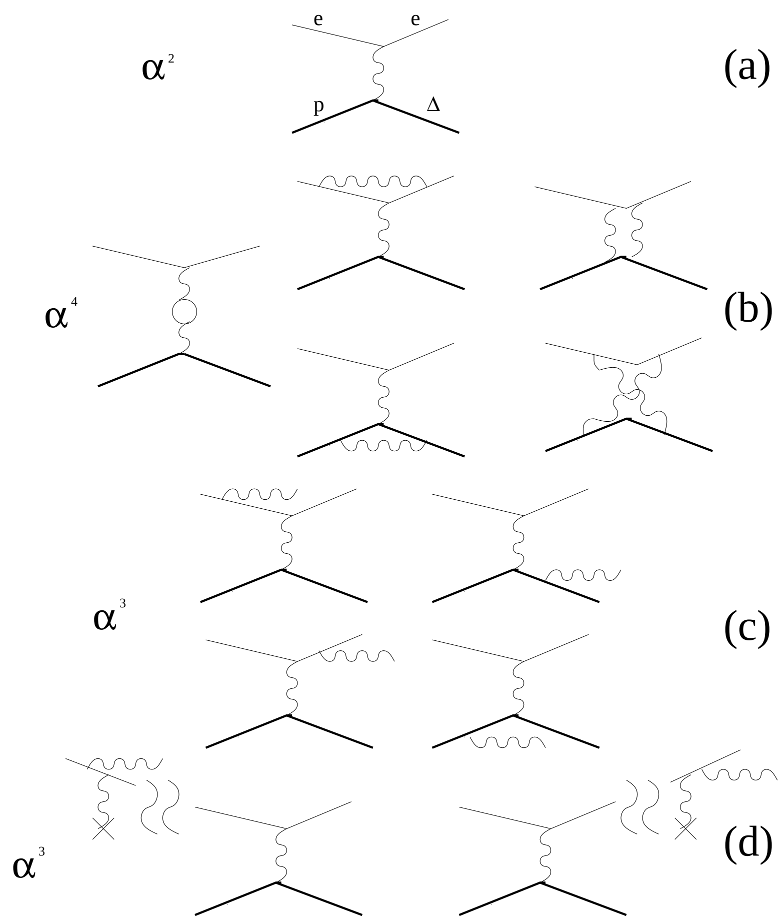

Figure 5.44: Feynman diagrams contributing to the cross section of $ep \rightarrow e'\Delta$ up to order α^4.

in which some effects cancel out. These two points can be intuitively understood as follows: radiative corrections for pion electro-production of the $\Delta(1232)$ channel are expected to be small since the $\Delta(1232)$ is the lowest lying resonance and there is nothing at lower W that can "leak" into the $\Delta(1232)$ cross section[15]. Events that instead "leak" out of the $\Delta(1232)$ will change the total cross section but not the asymmetry since they will be lost after the missing mass cut, both in the numerator and denominator of the asymmetries. Finally, the last important point is that there

[15] Experimentally, since the π^0 can be detected only indirectly through a missing mass cut, there is the possibility that the elastic radiative tail contaminates the $\Delta(1232)$ cross section. This effect cannot be accounted for by the theory which ideally describes only events with the pion in the final state. However the cut described in section 3.6.2 removes almost completely these radiative tail events.

is still the non-resonant background, which can give a sizeable correction. For the π^0 channel this background from the Born terms is small (as compared to the π^+).

To obtain the cross section and therefore the asymmetries coming from only the lowest order process (see Figure 5.44(a)) one can apply the so called *radiative corrections*. Radiative corrections are evaluated using a Monte Carlo simulation. Radiative events are generated according to theories that describe the higher order processes and the comparison with generated non-radiative events gives the corrections. The acceptance holes existing in the data were reproduced in the Monte Carlo events as well in order to have the model as close to the data as possible. The difference between the asymmetries calculated with radiative and non-radiative events gives the radiative correction on a bin-by-bin basis. Figures 5.45, 5.46 and 5.47 show the comparison of non-radiative with radiative events for the asymmetries A_e, A_t and A_{et}, respectively. The magnitude of the corrections for A_t and A_{et} is very small (typically a few percent at most) and therefore negligible compared to the error bars of the data. The corrections for A_e seem bigger than the ones for the other two asymmetries, however considering that the statistical error bars of the Monte Carlo events are much bigger as well, these correction were also neglected.

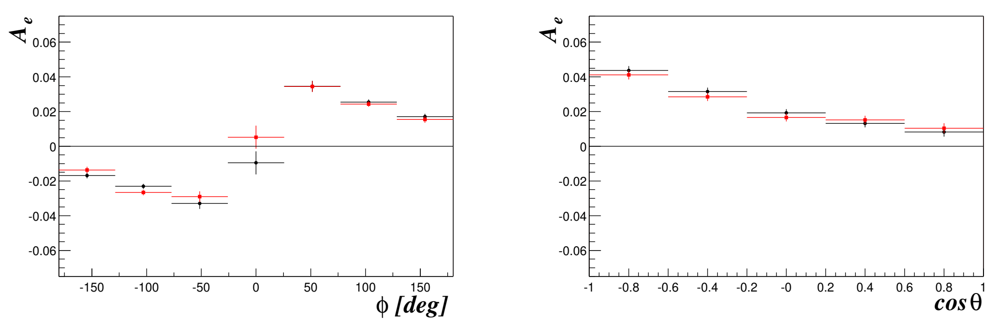

(a) A_e *vs* ϕ^*

(b) A_e *vs* $\cos\theta^*$

Figure 5.45: Comparison between A_e for $0.9\ \mathrm{GeV}^2/c^2 < Q^2 < 1.5\ \mathrm{GeV}^2/c^2$ with non-radiative (black) and radiative Monte Carlo events (red). The left plot is integrated over the whole range in $\cos\theta^*$, the right one is integrated over $0° < \phi^* < 180°$.

Even though the corrections are small, for completeness the asymmetries from

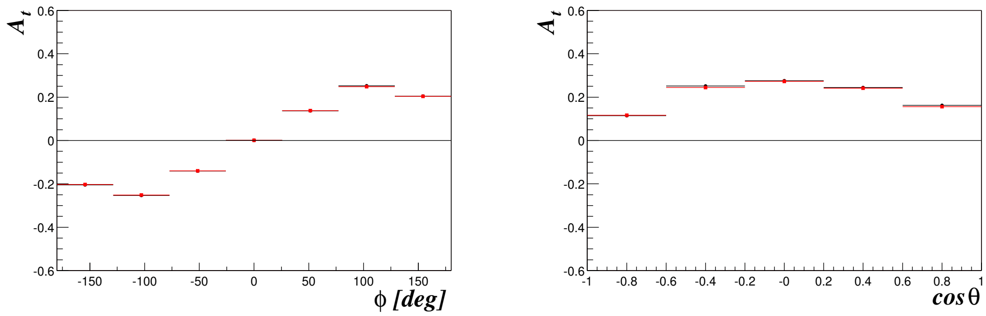

(a) A_t *vs* ϕ^* (b) A_t *vs* $\cos\theta^*$

Figure 5.46: Comparison between A_t for $0.9\ \mathrm{GeV}^2/c^2 < Q^2 < 1.5\ \mathrm{GeV}^2/c^2$ with non-radiative (black) and radiative Monte Carlo events (red). The left plot is integrated over the whole range in $\cos\theta^*$, the right one is integrated over $0° < \phi^* < 180°$.

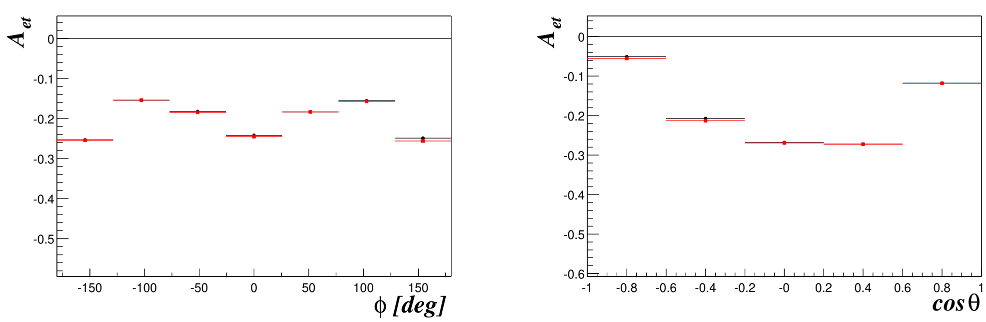

(a) A_{et} *vs* ϕ^* (b) A_{et} *vs* $\cos\theta^*$

Figure 5.47: Comparison between A_{et} for $0.9\ \mathrm{GeV}^2/c^2 < Q^2 < 1.5\ \mathrm{GeV}^2/c^2$ with non-radiative (black) and radiative Monte Carlo events (red). The left plot is integrated over the whole range in $\cos\theta^*$, the right one is integrated over $-180° < \phi^* < 180°$.

the data were corrected. An example can be found in Figures 5.48, 5.49 and 5.50 which show the uncorrected (black) and corrected (red) data. These plots show one more time that the corrections are negligible compared to the statistical errors.

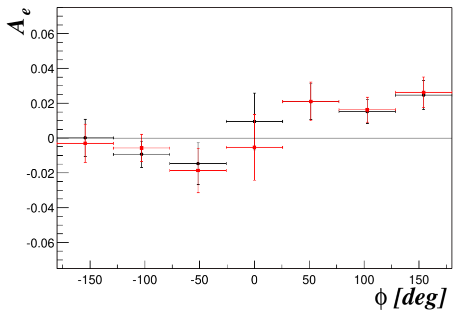

(a) A_e *vs* ϕ^*

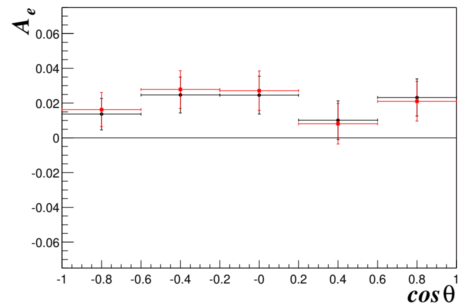

(b) A_e *vs* $\cos\theta^*$

Figure 5.48: Comparison between A_e for $0.9\ \mathrm{GeV}^2/c^2 < Q^2 < 1.5\ \mathrm{GeV}^2/c^2$ without (black) and with (red) radiative corrections. The left plot is integrated over the whole range in $\cos\theta^*$, the right one is integrated over $0° < \phi^* < 180°$.

5.8 χ^2 comparison

The four models the data were compared with are fairly similar in many cases, and it is therefore impossible to establish if one model is better than another. For this reason a simultaneous χ^2 comparison of all angular, as well as the Q^2 distributions was made.

The χ^2 was defined as

$$\chi^2 = \sum_i \frac{(x_i^{\mathrm{data}} - x_i^{\mathrm{model}})^2}{(\sigma_i^{\mathrm{data}})^2}$$

where x_i^{data} is the value of each experimental point for all the asymmetries and x_i^{model} is the corresponding value of the theoretical prediction. Since the model is given without errors, only the experimental errors σ_i^{data} were used in the denominator.

All the curves shown in this chapter so far represent the exact point by point model prediction. In order to compare the model to the data, it is necessary to

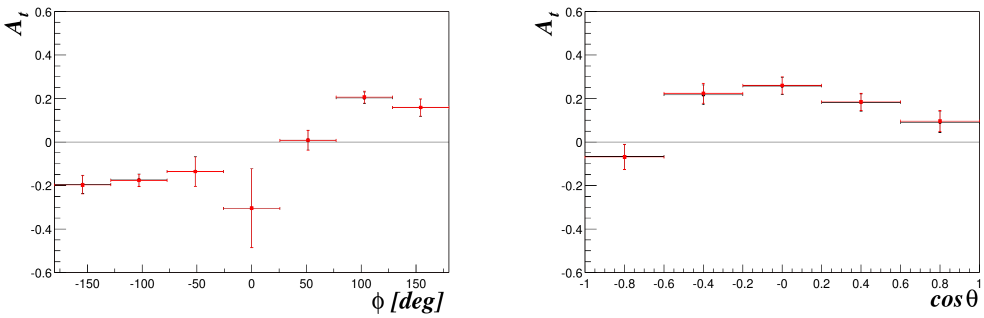

(a) A_t *vs* ϕ^*

(b) A_t *vs* $\cos\theta^*$

Figure 5.49: Comparison between A_t for $0.9\ \mathrm{GeV}^2/c^2 < Q^2 < 1.5\ \mathrm{GeV}^2/c^2$ without (black) and with (red) radiative corrections. The left plot is integrated over the whole range in $\cos\theta^*$, the right one is integrated over $0° < \phi^* < 180°$.

integrate over the bin size in order to get an average value equivalent to the one for the data. All the models were therefore recalculated.

Each experimental point is a degree of freedom and therefore each asymmetry as a function of $\cos\theta^*$ or Q^2 contributes 5 and each asymmetry as a function of ϕ^* 7 degrees of freedom. Therefore the three asymmetries as a function of ϕ^* and $\cos\theta^*$ integrated over the two possible Q^2 regions plus the asymmetries as a function of Q^2, give a total *number of degrees of freedom*, $ndf = 117$.

The comparison gave the results listed in Table 5.5 From this calculation one

Model	χ^2	χ^2/ndf
MAID2000	217.3	1.86
MAID98	238.0	2.03
Sato-Lee	150.2	1.28
Eff Lag	473.3	4.05

Table 5.5: χ^2 comparison between the data and the four models

can conclude that the model that describes the data best is the dynamic model by Sato and Lee. MAID2000 and MAID98 are very similar to each other and they are a slightly worse description of the data and the Effective Lagrangian is just in

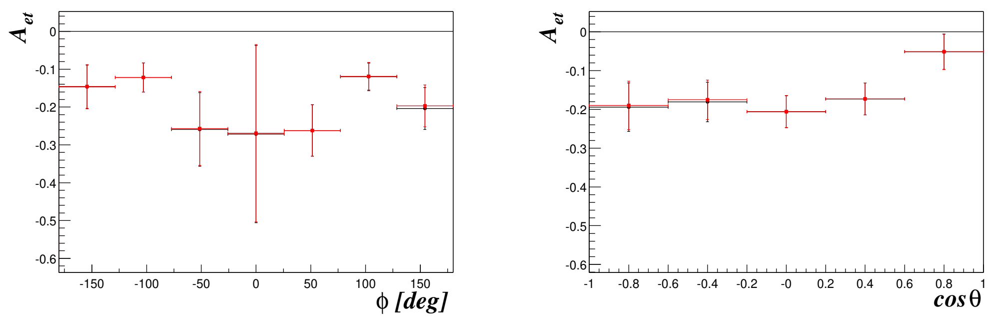

(a) A_{et} *vs* ϕ^* (b) A_{et} *vs* $\cos\theta^*$

Figure 5.50: Comparison between A_{et} for $0.9\ \mathrm{GeV}^2/c^2 < Q^2 < 1.5\ \mathrm{GeV}^2/c^2$ without (black) and with (red) radiative corrections. The left plot is integrated over the whole range in $\cos\theta^*$, the right one is integrated over $-180° < \phi^* < 180°$.

qualitative agreement.

The χ^2 comparison was also used to judge if a narrower W cut around the $\Delta(1232)$ gives a significant change in the final result. The asymmetries and the model were recalculated for the bin $1.164\ \mathrm{GeV}/c^2 < W < 1.3\ \mathrm{GeV}/c^2$, just slightly bigger than the width of the $\Delta(1232)$. The result is given in Table 5.6

Model	χ^2	χ^2/ndf
MAID2000	198.7	1.70
MAID98	220.3	1.88
Sato-Lee	156.8	1.34
Eff Lag	383.7	3.28

Table 5.6: χ^2 comparison between the data and the four models for $1.164\ \mathrm{GeV}/c^2 < W < 1.3\ \mathrm{GeV}/c^2$.

The χ^2 values are basically unchanged as compared to the wide W cut.

Finally, even though the radiative corrections are very small, the χ^2 comparison was done with the asymmetries with the radiative corrections. The final result in table 5.7 shows that the χ^2 is unchanged.

Model	χ^2	χ^2/ndf
MAID2000	204.5	1.75
MAID98	222.8	1.90
Sato-Lee	148.0	1.26
Eff Lag	457.8	3.91

Table 5.7: χ^2 comparison between the data with radiative corrections and the four models.

5.9 Conclusions

Single and double asymmetries for the exclusive channel $\vec{p}(\vec{e}, e'p)\pi^0$ in the $\Delta(1232)$ region were extracted. The dependencies of the asymmetries on the center of mass angles, θ^* and ϕ^*, and the momentum transfer Q^2 were studied and compared with electro-production models. In this work the Effective Lagrangian by R. Davidson and N. Mukhopadhyay, the MAID and the Sato-Lee models were considered. The limited statistics combined with the fact that asymmetries are extremely small quantities, resulted in a fairly big statistical error, which does not allow one to rule out one model as compared to the others. The data were generally found to follow the predictions. In order to have a quantitative way to judge the models a χ^2 comparison was performed. The preferred model was the one by Sato and Lee. MAID2000 and MAID98 were found very similar to each other and they were a slightly worse description of the data, and the Effective Lagrangian was just in qualitative agreement.

Sources for systematic errors were studied and it was found that the overall error does not exceed 5%, which is small compared to the statistical error.

Polarized measurements are very important because they offer the possibility to test in an independent way the existing phenomenological theories which are based on fits of unpolarized data. The agreement of the data with the models in this work is therefore a positive sign of the progress that the theory did in the past 40 years in describing electro-production processes in the resonance region.

The results of this work will be used by theory groups to constrain the free parameters of their models even further. These parameters are often related to more fundamental quantities, such as the multipoles E_{1+} and M_{1+}, which help to better understand the hadronic structure.

In 2000-2001 the second part of the EG1 run was completed and a factor 10 of additional statistics was taken. The new data offer the possibility to extract asymmetries with error $\sim \frac{1}{3}$ in size compared to the ones presented here. In addition, data at higher beam energies (up to 5.7 GeV) will allow one to explore higher Q^2 regions. The procedures described in this pioneering thesis will be the basis for the analysis of a higher statistics sample.

LITERATURE CITED

[1] G. F. Chew, M. L. Goldberger, F. E. Low and Y. Nambu, "Relativistic Dispersion Relation Approach To Photomeson Production," Phys. Rev. **106** (1957) 1345.

[2] G. Knochlein, D. Drechsel and L. Tiator, "Photoproduction and electroproduction of eta mesons," Z. Phys. A **352**, 327 (1995)

[3] R. Davidson, Private Communication.

[4] S. Capstick in Excited Baryons 1998, G Adams et al (editors) Word Scientific.

[5] N. Isgur and G. Karl, "P Wave Baryons In The Quark Model," Phys. Rev. D **18**, 4187 (1978).

[6] N. Isgur and G. Karl, "Positive Parity Excited Baryons In A Quark Model With Hyperfine Interactions," Phys. Rev. D **19**, 2653 (1979)

[7] C. E. Carlson, "Electromagnetic N - Delta Transition At High Q**2," Phys. Rev. D **34**, 2704 (1986).

[8] V. V. Frolov *et al.*, "Electroproduction of the Delta(1232) resonance at high momentum transfer," Phys. Rev. Lett. **82**, 45 (1999)

[9] R. Beck *et al.*, "Measurement of the E2/M1 ratio in the N $\rightarrow$ Delta transition using the reaction p(gamma(pol.),p)pi0," Phys. Rev. Lett. **78**, 606 (1997).

[10] R. M. Davidson, N. C. Mukhopadhyay and R. S. Wittman, "Effective Lagrangian approach to the theory of pion photoproduction in the Delta (1232) region," Phys. Rev. D **43**, 71 (1991).

[11] N. Mathur, Nucleon spin structure and electromagnetic excitation of nucleon resonance, Ph.D. Thesis, Rensselaer Polytechnic Institute (2000)

[12] R. M. Davidson, N. Mathur and N. C. Mukhopadhyay, "The role of the D13(1520) resonance in eta electroproduction," Phys. Rev. C **62**, 058201 (2000)

[13] D. Drechsel, O. Hanstein, S. S. Kamalov and L. Tiator, "A unitary isobar model for pion photo- and electroproduction on the proton up to 1-GeV," Nucl. Phys. A **645**, 145 (1999)

[14] T. Sato and T. S. Lee, "Dynamical study of the Delta excitation in N(e,e' pi) reactions," Phys. Rev. C **63**, 055201 (2001)

[15] T. Sato and T. S. Lee, "Meson-exchange model for pi N scattering and gamma N → pi N reaction," Phys. Rev. C **54**, 2660 (1996)

[16] T. S. Lee, "Study of hadron quark-substructure with gev electrons and photons"

[17] C. W. Leemann, D. R. Douglas, and G. A. Krafft, "THE CONTINUOUS ELECTRON BEAM ACCELERATOR FACILITY: CEBAF at the Jefferson Laboratory," Annu. Rev. Nucl. Part. Sci. 2001. 51:413-450.

[18] C. K. Sinclair, "Report On Polarized Electron Source And Electron Polarimetry Workshop," CEBAF-PR-89-002.

[19] CEBAF Conceptual Design Report for Experimental Equipment, (1990)

[20] M. D. Mestayer *et al.*, "The Clas Drift Chamber System," Nucl. Instrum. Meth. A **449**, 81 (2000).

[21] G. Adams *et al.*, "The Clas Cherenkov Detector," Nucl. Instrum. Meth. A **465**, 414 (2001).

[22] E. S. Smith *et al.*, "The Time-Of-Flight System For Clas," Nucl. Instrum. Meth. A **432**, 265 (1999).

[23] M. Amarian *et al.*, "The Clas Forward Electromagnetic Calorimeter," Nucl. Instrum. Meth. A **460**, 239 (2001).

[24] M. Anghinolfi *et al.*, "Response To Cosmic Rays Of The Large-Angle Electromagnetic Shower Calorimeter Of The Clas Detector," Nucl. Instrum. Meth. A **447**, 424 (2000).

[25] T.O. Niinikoski, Nucl. Instr. Meth. 116 (1974) 269

[26] R. Devita, Realizzazione di un bersaglio di protoni polarizzato per esperimenti di scattering di elettroni, Bachelor Thesis, University of Genoa, Italy (1997)

[27] M. Borghini, Proton spin orientation, CERN Yellow report 1968, CERN-68-32

[28] A. Abragam, The principle of nuclear magnetism, Oxford Claredon Press (1961)

[29] D. S. Carman *et al.*, "The Region One Drift Chamber For The Clas Spectrometer," Nucl. Instrum. Meth. A **419**, 315 (1998).

[30] R. Devita, Measurement of the double spin asymmetry in π^+ electroproduction with CLAS, PhD thesis, University of Genoa, Italy (2000)

[31] A. Skabelin, Spin structure of the proton and the Q^2 evolution of the Gerasimov-Drell-Hearn integral, Ph.D thesis, Massachusetts Institute of Technology (2002)

[32] T. Forest, http://www.jlab.org/ claseg1/analysis/HelP/Beta/

[33] R. Devita, http://www.jlab.org/Hall-B/secure/eg1/AnalysisEG1_RDV.html

[34] K. Joo, CLAS-ANALYSIS note 01-008

[35] L. W. Mo and Y. Tsai, "Radiative Corrections To Elastic And Inelastic E P And Mu P Scattering," Rev. Mod. Phys. **41**, 205 (1969).

[36] V. Burkert, private communication.

[37] http://www.jlab.org/Hall-B/secure/eg1/tforest/Wiggle/Wiggle.html

[38] A. Thomas, W. Weise The Structure of the nucleon (editors) Wiley-vch

[39] N. Bianchi *et al.*, "Total hadronic photo-absorption cross-section on nuclei in the nucleon resonance region," Phys. Rev. C **54**, 1688 (1996).

[40] J. Ahrens, "The Total Absorption Of Photons By Nuclei," Nucl. Phys. A **446**, 229C (1985).

[41] R. Fatemi, The spin structure of the proton in the resonance region, PhD thesis, Charlottesville, Virginia (2001)

[42] R. Devita, CLAS note 00-001

[43] K. Joo, CLAS-ANALYSIS note 01-009

[44] D. G. Crabb and D. B. Day, "The Virginia/Basel/SLAC Polarized Target: Operation And Performance During Experiment E143 At SLAC," Nucl. Instrum. Meth. A **356**, 9 (1995).

[45] M. Goldman, Spin temperature and nuclear magnetic resonance in solids, Clarendon Press (1970)

[46] C. Grupen, "Particle detectors",Cambrige University Press (1996)

[47] L. W. Mo and Y. S. Tsai, "Radiative Corrections To Elastic And Inelastic E P And Mu P Scattering," Rev. Mod. Phys. **41**, 205 (1969).

[48] R. Minehart, Private Communication

[49] R. L. Walker, "Phenomenological Analysis Of Single Pion Photoproduction," Phys. Rev. **182**, 1729 (1969).

[50] A. Bartl and W. Majerotto, "Electroproduction Of Pions With Polarized Beams And Polarized Targets," Nucl. Phys. B **62**, 267 (1973).

APPENDIX A
Helicity amplitudes formalism

A.1 Formalism

The cross section of the $\Delta(1232)$ can be expressed as a function of helicity amplitudes. The helicity amplitudes are related to the amplitudes for the reaction $\gamma_v + N \to N' + \pi$ in the helicity basis, i.e. the probability to go from an initial state $|\lambda_\gamma \lambda_N>$ to a final state $|\lambda_{N'}, \lambda_\pi >= |\lambda_{N'}, 0 >\equiv |\lambda_{N'}>$. The helicity amplitudes are defined as [2, 49, 50]

$$< \lambda_\gamma \lambda_N | T | \lambda_{N'} >= H_i \tag{A.1}$$

where T is the transition operator, that takes the initial state γN to the final state $N'\pi$. There are three possible polarizations for the virtual photon $\lambda_\gamma = \pm 1, 0$, two for the initial and two for the final state nucleon $\lambda_{N,N'} = \pm\frac{1}{2}$. Therefore overall we have $2\times 3\times 2 = 12$ amplitudes, but because of parity symmetry only six are independent. Adopting the conventional notation[49], H_1 through H_4 correspond to the transition with $\lambda_\gamma = 1$ and $(\lambda_{N'}, \lambda_N) = (-\frac{1}{2}, -\frac{1}{2}), (-\frac{1}{2}, \frac{1}{2}), (\frac{1}{2}, -\frac{1}{2}), (\frac{1}{2}, \frac{1}{2})$, respectively, and $H_{5,6}$ correspond to $\lambda_\gamma = 0$ and $(\lambda_{N'}, \lambda_N) = (\frac{1}{2}, \frac{1}{2}), (\frac{1}{2}, -\frac{1}{2})$. The amplitudes $H_{2,3}$ involve a baryon helicity flip, for $H_{1,4}$ the helicity remains unchanged.

The helicity amplitudes can be expanded in terms of Legendre polynomials as follows

$$
\begin{aligned}
H_1 &= \frac{1}{2}\sqrt{2}\sin\theta\cos\frac{\theta}{2}\sum_{l=1}^{\infty}(B_{l+} - B_{(l+1)-})(P_l'' - P_{l+1}'') \\
H_2 &= \sqrt{2}\cos\frac{\theta}{2}\sum_{l=0}^{\infty}(A_{l+} - A_{(l+1)-})(P_l' - P_{l+1}') \\
H_3 &= \frac{1}{2}\sqrt{2}\sin\theta\sin\frac{\theta}{2}\sum_{l=1}^{\infty}(B_{l+} + B_{(l+1)-})(P_l'' + P_{l+1}'') \\
H_4 &= \sqrt{2}\sin\theta\sum_{l=0}^{\infty}(A_{l+} + A_{(l+1)-})(P_l' + P_{l+1}') \\
H_5 &= \sqrt{2}\cos\frac{\theta}{2}\sum_{l=0}^{\infty}(C_{l+} - C_{(l+1)-})(P_l' - P_{l+1}') \\
H_6 &= \sqrt{2}\sin\frac{\theta}{2}\sum_{l=0}^{\infty}(C_{l+} + C_{(l+1)-})(P_l' + P_{l+1}')
\end{aligned}
\tag{A.2}
$$

where the coefficients $A_{l\pm}, B_{l\pm}$, and $C_{l\pm}$ are **helicity elements**, which are the contributions to the helicity amplitudes from the various angular momentum states l, $j = l \pm \frac{1}{2}$.

In the case of polarized scattering usually a slightly different notation is adopted, where $h^N_\pm$, $h^F_\pm$, h^N_0, h^F_0 are used instead of the H_i. The relation between the two notation is given by [50]

$$
\begin{aligned}
h^N_\pm &= (H_4 \pm H_1)/\sqrt{2} \\
h^F_\pm &= (H_3 \mp H_2)/\sqrt{2} \\
h^N_0 &= H_5 \\
h^F_0 &= H_6
\end{aligned}
\tag{A.3}
$$

The helicities $h^{F,N}_+$ correspond to the physical situations where the incident photon, polarized perpendicular to the scattering plane, flips the baryon helicity (F) or not (N). The helicities $h^{F,N}_-$ correspond to case of photons polarized parallel to the scattering plane[1].

[1]The relation between $h^{F,N}_\pm$ and the $H_i(1\ to\ 4)$ are basically a change from a spherical to a Cartesian basis $\epsilon_\pm = \mp(1/\sqrt{2})(\hat{e}_x \pm i\hat{e}_y)$

A.2 Cross sections

The unpolarized cross section as a function of these helicity amplitudes is given by

$$\frac{d\sigma_0}{d\Omega^*} = \sigma_T + \epsilon\sigma_L + \epsilon\sigma_{TT}\cos 2\phi^* + \sqrt{\frac{\epsilon(1+\epsilon)}{2}}\sigma_{LT}\cos\phi^* \tag{A.4}$$

where

$$\begin{aligned}
\sigma_T &= \frac{|\vec{k}^*|}{2K_\gamma^{cm}}(|h_+^N|^2 + |h_+^F|^2 + |h_-^N|^2 + |h_-^F|^2) \\
\sigma_L &= \frac{|\vec{k}^*|}{2K_\gamma^{cm}}(|h_-^N|^2 + |h_-^F|^2 - |h_+^N|^2 - |h_+^F|^2) \\
\sigma_{TT} &= \frac{|\vec{k}^*|}{K_\gamma^{cm}}(|h_0^N|^2 + |h_0^F|^2) \\
\sigma_{TL} &= \frac{2|\vec{k}^*|}{K_\gamma^{cm}}\mathrm{Re}(h_0^N h_-^{*N} + h_0^F h_-^{*F})
\end{aligned} \tag{A.5}$$

and the polarized terms are given by

$$\begin{aligned}
\frac{d\sigma_e}{d\Omega^*} &= h\frac{|\vec{q}^*|}{K_\gamma^{cm}}\sqrt{2\epsilon(1-\epsilon)}\sin\phi\,\mathrm{Im}(h_0^N h_-^{*N} + h_0^F h_-^{*F}) = hf_e \\
\frac{d\sigma_t}{d\Omega^*} &= \frac{|\vec{q}^*|}{K_\gamma^{cm}}[P_x(\sqrt{2\epsilon(1+\epsilon)}\sin\phi\,\mathrm{Im}X_1 + \epsilon\sin 2\phi\,\mathrm{Im}X_2) \\
&- P_y(\mathrm{Im}Y_1 + \epsilon\cos 2\phi\,\mathrm{Im}Y_2 + 2\epsilon\,\mathrm{Im}Y_3 + \sqrt{2\epsilon(1+\epsilon)}\cos\phi\,\mathrm{Im}Y_4) \\
&- P_z(\epsilon\sin 2\phi\,\mathrm{Im}Z_2 + \sqrt{2\epsilon(1+\epsilon)}\sin\phi\,\mathrm{Im}Z_1)] \\
&= P_x f_{tx} - P_y f_{tz} - P_z f_{tz} = \vec{P}\cdot\vec{f}_t \\
\frac{d\sigma_{et}}{d\Omega^*} &= h\frac{|\vec{q}^*|}{K_\gamma^{cm}}[P_x(\sqrt{2\epsilon(1-\epsilon)}\cos\phi\,\mathrm{Re}X_1 + \sqrt{1-\epsilon^2}\mathrm{Re}X_2) \\
&+ P_y(\sqrt{2\epsilon(1-\epsilon)}\sin\phi\,\mathrm{Re}Y_4) \\
&- P_z(\sqrt{1-\epsilon^2}\mathrm{Re}Z_2 + \sqrt{2\epsilon(1-\epsilon)}\cos\phi\,\mathrm{Re}Z_1)] \\
&= h(P_x f_{etx} + P_y f_{etz} - P_z f_{etz}) = h\vec{P}\cdot\vec{f}_{et}
\end{aligned} \tag{A.6}$$

with

$$X_1 = (h_0^F h_+^{*N} + h_0^N h_+^{*F}) \quad X_2 = (h_-^F h_+^{*N} + h_-^N h_+^{*F}) \tag{A.7}$$

$$Y_1 = (h_+^N h_+^{*F} + h_-^N h_-^{*F}) \quad Y_2 = (h_-^N h_-^{*F} - h_+^N h_+^{*F}) \tag{A.8}$$

$$Y_3 = (h_0^N h_0^{*F}) \qquad Y_4 = (h_0^N h_-^{*F} - h_0^F h_-^{*N}) \tag{A.9}$$

$$Z_1 = (h_0^N h_+^{*N} - h_0^F h_+^{*F}) \quad Z_2 = (h_-^N h_+^{*N} - h_-^F h_+^{*F}) \tag{A.10}$$

and

$$\vec{f_t} \equiv (f_{tx}, -f_{ty}, -f_{tz}) \tag{A.11}$$

$$\vec{f_{et}} \equiv (f_{etx}, f_{ety}, -f_{etz}). \tag{A.12}$$

A.3 Multipoles

The connection between the response functions and the multipoles can be found using equations 1.21 together with the ones in Appendix B. The helicity amplitudes (see equations A.2) can also be related to multipoles using the formulas

$$\begin{aligned}
A_{l+} &= \frac{1}{2} l M_{l+} + \frac{1}{2}(l+2) E_{l+} \\
B_{l+} &= -M_{l+} + E_{l+} \\
A_{(l+1)-} &= \frac{1}{2}(l+2) M_{l+1-} - \frac{1}{2} l E_{l+1-} \\
B_{(l+1)-} &= M_{l+1-} + E_{l+1-} \\
C_{l+} &= -\sqrt{\frac{Q^2}{2|\vec{q}^2|}}(l+1) S_{l+} \\
C_{(l+1)-} &= \sqrt{\frac{Q^2}{2|\vec{q}^2|}}(l+1) S_{l+1-}
\end{aligned} \tag{A.13}$$

As was seen in section 1.2, the $\Delta(1232)$ excitation is characterized by 3 multipoles M_{1+}, E_{1+}, S_{1+}. For this special case, neglecting the contribution from background which can contain other multipoles than the three listed above, the helicity amplitudes take the following form

$$
\begin{aligned}
H_1 &= -\frac{3}{\sqrt{2}} \sin\theta^* \cos\frac{\theta^*}{2}(E_{1+} - M_{1+}) \\
H_2 &= \frac{\sqrt{2}}{2} \cos\frac{\theta^*}{2}(3E_{1+} + M_{1+})(1 - 3\cos\theta^*) \\
H_3 &= \frac{3}{\sqrt{2}} \sin\theta^* \sin\frac{\theta^*}{2}(E_{1+} - M_{1+}) \\
H_4 &= \frac{\sqrt{2}}{2} \sin\frac{\theta^*}{2}(3E_{1+} + M_{1+})(1 + 3\cos\theta^*) \\
H_5 &= 2\sqrt{\frac{Q^2}{|\vec{q}^2|}} \cos\frac{\theta^*}{2} S_{1+}(-1 + 3\cos\theta^*) \\
H_6 &= 2\sqrt{\frac{Q^2}{|\vec{q}^2|}} \sin\frac{\theta^*}{2} S_{1+}(1 + 3\cos\theta^*)
\end{aligned}
\tag{A.14}
$$

APPENDIX B
Response functions and CGLN amplitudes

The response functions can be written as a function of real or imaginary parts of the 6 complex CGLN amplitudes as follows:

$$
\begin{aligned}
R_T^0 =& |F_1|^2 + |F_2|^2 + \frac{\sin^2\theta^*}{2}(|F_3|^2 + |F_4|^2) \\
& + \mathrm{Re}\{\sin^2\theta^*(F_2^* F_3 + F_1^* F_4 + \cos\theta^* F_3^* F_4) \\
& - 2\cos\theta^* F_1^* F_2\} \\
R_T^y =& \mathrm{Im}\{\sin\theta^*(F_1^* F_3 - F_2^* F_4 + \cos\theta^*(F_1^* F_4 - F_2^* F_3) \\
& - \sin^2\theta^* F_3^* F_4)\} \\
R_L^0 =& \mathrm{Re}\{|F_5|^2 + |F_6|^2 + 2\cos\theta^* F_5^* F_6\} \\
R_L^y =& -2\sin\theta^* \mathrm{Im}\{F_5^* F_6\} \\
R_{TL}^0 =& \sin\theta^* \mathrm{Re}\{F_2^* F_5 - F_3^* F_5 - F_1^* F_6 - F_4^* F_6 \\
& - \cos\theta^*(F_4^* F_5 + F_3^* F_6) \\
R_{TL}^x =& \mathrm{Im}\{-F_1^* F_5 + F_2^* F_6 + \cos\theta^*(F_2^* F_5 - F_1^* F_6)\} \\
R_{TL}^y =& \mathrm{Im}\{-F_1^* F_5 + F_2^* F_6 + \cos\theta^*(F_2^* F_5 - F_1^* F_6) \\
& + \sin^2\theta^*(F_3^* F_6 - F_4^* F_5)\} \\
R_{TL}^z =& \sin\theta^* \mathrm{Im}(F_2^* F_5 + F_1^* F_6) \\
R_{TT}^0 =& \frac{1}{2}\sin^2\theta^*(|F_3|^2 + |F_4|^2) \\
& + \sin^2\theta^* \mathrm{Re}\{F_2^* F_3 + F_1^* F_4 + \cos\theta^* F_3^* F_4\} \\
R_{TT}^x =& \sin\theta^* \mathrm{Im}\{2F_1^* F_2 + F_1^* F_3 - F_2^* F_4 \\
& + \cos\theta^*(F_1^* F_4 - F_2^* F_3)\}
\end{aligned}
\tag{B.1}
$$

$$
\begin{aligned}
R^{z}_{TT} =& -\sin^2\theta^*\mathrm{Im}\{F_2^*F_3 + F_1^*F_4\}\\
R^{0}_{TL'} =& -\sin\theta^*\mathrm{Im}\{F_2^*F_5 + F_3^*F_5 + F_1^*F_6 + F_4^*F_6\\
& + \cos\theta^*(F_4^*F_5 + F_3^*F_6)\}\\
R^{x}_{TL'} =& \mathrm{Re}\{-F_1^*F_5 + F_2^*F_6 + \cos\theta^*(F_2^*F_5 - F_1^*F_6)\}\\
R^{y}_{TL'} =& \mathrm{Re}\{F_1^*F_5 - F_2^*F_6 + \cos\theta^*(F_1^*F_6 - F_2^*F_5)\\
& + \sin^2\theta^*(F_4^*F_5 - F_3^*F_6)\}\\
R^{z}_{TL'} =& \sin\theta^*\mathrm{Re}\{F_2^*F_5 + F_1^*F_6\}\\
R^{0}_{TT'} =& \sin\theta^*\mathrm{Re}\{F_1^*F_3 - F_2^*F_4 + \cos\theta^*(-F_2^*F_3 + F_1^*F_4)\}\\
R^{z}_{TT'} =& -|F_1|^2 - |F_2|^2\\
& + \mathrm{Re}\{2\cos\theta^*F_1^*F_2 - \sin^2\theta^*(F_2^*F_3 + F_1^*F_4)\}
\end{aligned}
$$

APPENDIX C
Momentum corrections

The general form for the momentum corrections is

$$p_{corr} = p_{meas} \cdot \gamma(a + b\phi + c\phi^2)\frac{d\theta - f}{g\theta - h} \quad if\ \theta \geq \bar{\theta} \tag{C.1}$$

$$p_{corr} = p_{meas}(a + b\phi + c\phi^2)\frac{d\bar{\theta} - f}{g\bar{\theta} - h} \quad if\ \theta < \bar{\theta} \tag{C.2}$$

The parameters $a, b, c, d, f, g, h, \gamma$ and $\bar{\theta}$ depend on the running conditions (beam energy and torus current) and the parameters a, b and c depend on the sector. Tables C.1 and C.2 contains the values of the parameters for 2 GeV data and torus current 2250 A.

Parameter	*sector 1*	*sector 2*	*sector 3*
a	1.019768	1.005781	0.9975991
b	$-0.1373857\ 10^{-2}$	$-0.1199087\ 10^{-2}$	$-0.4010052\ 10^{-3}$
c	$0.1460063\ 10^{-4}$	$0.1363575\ 10^{-4}$	$0.1126817\ 10^{-4}$
Parameter	*sector 4*	*sector 5*	*sector 6*
a	0.9973906	1.010131	1.002511
b	$-0.5077311\ 10^{-3}$	$-0.1051511\ 10^{-2}$	$-0.4971963\ 10^{-3}$
c	$0.1009247\ 10^{-4}$	$0.1526132\ 10^{-4}$	$0.8896011\ 10^{-5}$

Table C.1: Momentum corrections parameters for E_{beam} = 2.565 GeV and I_{torus} = 2250 A.

Parameter	*Value*
d	1.002511
f	12.51147
g	1.007811
h	12.57416
$\bar{\theta}$	12.5
γ	0.9930184

Table C.2: Momentum corrections parameters for $\boldsymbol{E_{beam}} = 2.565$ GeV and $\boldsymbol{I_{torus}} = 2250$ $\boldsymbol{A}$.

APPENDIX D
Particle Trajectories in an Axial Magnetic Field (by S.E. Kuhn, Old Dominion University)

This short document lists a few general properties one can derive about trajectories of charged particles in a magnetic field that is both symmetric around the z–axis (axially symmetric) and that does not contain any ϕ–component (circling the z–axis). Examples include a solenoidal field or the field generated by a Helmholtz–type arrangement of coils, as in the case of the polarized target magnet. We are especially interested in the case where a charge particle originates from the center of the magnetic field, *i.e.* the z–axis.

With the field only in z– and r– direction, we can always describe it by a vector potential $\mathbf{A}$ which points in the ϕ–direction only and depends on z and r: $\mathbf{A} = A_\phi(r, z)\hat{\phi}$. Using cylindrical coordinates, the Hamiltonian for a charge particle of mass m moving in this field is

$$\mathcal{H} = \sqrt{m^2c^4 + \left(\frac{P_\phi}{r} - qA_\phi\right)^2 c^2 + {P_r}^2c^2 + {P_z}^2c^2}, \tag{D.1}$$

where the generalized momentum $P_\phi = \frac{E}{c^2} \cdot r^2\dot{\phi} + q \cdot rA_\phi$ and the other two components are the usual ("ordinary") linear momenta. At this point, we can make some general observations:

1. The Hamiltonian does not depend on ϕ, which means that the generalized momentum P_ϕ is absolutely conserved throughout the trajectory. If in addition we assume that the particle originated on the z–axis, we have $P_\phi = 0$ at all times (since $r = 0$ initially). If the particle in question travels all the way outside the region of the magnetic field (to a region where $A_\phi = 0$), we will have $\dot{\phi} = 0$ in that region (assuming $r \neq 0$). This means that the particle will have no "sideways" motion, or, in other words, its trajectory will point back to the z-axis. However, they do *not* necessarily point back to the z–position of the target.

2. The other two momenta fulfill the following equations:

$$\frac{d}{dt}P_r = \frac{c^2}{E}\left(\frac{P_\phi}{r} - qA_\phi\right)\left(\frac{P_\phi}{r^2} + q\frac{\partial A_\phi}{\partial r}\right) \tag{D.2}$$

and

$$\frac{d}{dt}P_z = \frac{c^2}{E}\left(\frac{P_\phi}{r} - qA_\phi\right)q\frac{\partial A_\phi}{\partial z} \tag{D.3}$$

(these are the Hamilton equations $\dot{P_i} = -\partial\mathcal{H}/\partial q_i$). If in doubt, one can check these equations by exploiting the relationships $\mathbf{B} = \nabla \times \mathbf{A}$ and $(P_\phi/r - qA_\phi)c^2/E = r\dot{\phi} = v_\phi$ to rewrite them as follows:

$$\frac{d}{dt}P_r = v_\phi\left(\frac{E}{c^2}\dot{\phi} + q\frac{1}{r}A_\phi + q\frac{\partial A_\phi}{\partial r}\right) = \frac{Er}{c^2}\dot{\phi}^2 + v_\phi qB_z \tag{D.4}$$

and

$$\frac{d}{dt}P_z = -v_\phi qB_r, \tag{D.5}$$

which is "obviously" true.

3. For a particle originating on the z–axis we can simplify Eqs. D.2, D.3 to

$$\frac{d}{dt}P_r = -\frac{q^2c^2}{E}A_\phi\frac{\partial A_\phi}{\partial r} \tag{D.6}$$

and

$$\frac{d}{dt}P_z = -\frac{q^2c^2}{E}A_\phi\frac{\partial A_\phi}{\partial z}, \tag{D.7}$$

again using the fact that $P_\phi = 0$ at all times. If we now concentrate on particle trajectories that stay relatively close to the z–axis, we can represent A_ϕ by the first order term in a Taylor-expansion:
$A_\phi(r,z) = \frac{r}{2}B_z(r=0,z)$. (The exact expression requires only that $B_z(r=0,z)$ be replaced by the *average* field in z–direction, averaged over the circle of radius r.) The approximation is sufficiently good as long as r stays small compared to the radius of the magnet coils in the case of a Helmholtz arrangement. This is obviously true for particles starting out with an angle θ relative to the z–axis

of less than, say, 10°, throughout the target chamber. In this case, we get

$$\frac{d}{dt}P_r = -\frac{q^2c^2}{E}\frac{r}{4}{B_z}^2 \tag{D.8}$$

and

$$\frac{d}{dt}P_z = \frac{q^2c^2}{E}\frac{r^2}{4}B_z\left(-\frac{\partial B_z}{\partial z}\right). \tag{D.9}$$

If the particle starts out in the center of the target, we can conclude that the time–derivative of P_r is *always* less or equal to zero, and the time–derivative of P_z is always greater or equal to zero along the path length, at least throughout the region of the target chamber. (The second statement follows since the field strength can only *decrease* along z.) These two results mean that the angle $\theta = \arctan(P_r/P_z)$ can only *decrease* with time, *never* increase. In other words, the particle trajectory must be contained within a cone with apex at the target center and opening angle given by the initial angle $\theta(t = 0)$.

APPENDIX E
Fiducial cuts

The general form of the cuts of proton or electron is:

$$30^\circ - \Delta\phi < \phi_{sec} < 30^\circ + \Delta\phi \tag{E.1}$$

$$\theta_{DC} > \theta_{cut} \tag{E.2}$$

where $\Delta\phi$ and θ_{cut} are given by

$$\Delta\phi = A\big[\sin(\theta_{DC} - \theta_{cut})\big]^{expon} \tag{E.3}$$

$$expon = B(p_{scaled})^C$$

$$\theta_{cut} = \begin{cases} D + \frac{E}{(p_{scaled})} \text{ for the electron} \\ D - E(1. - p_{scaled}/5)^F \text{ for the proton} \end{cases} \tag{E.4}$$

Here $p_{scaled} = p\frac{3375}{torcur}$ is the electron or proton momentum in GeV/c scaled to a torus current of 3375 A and the angles are in degrees. The parameters for the electron and the proton are listed in table E.1 and E.2, respectively[1].

Parameter	*loose cut*	*tight cut*
A	23.5	25
B	0.2	0.272
C	0.28	
D	11	
E	16.72	

Table E.1: Parameters of the electron fiducial cuts.

Additional cuts where applied to remove events that occur at the edges of the

[1]The units of the parameters are such that the final result for $\Delta\phi$ or θ_{cut} is in units of degrees.

Parameter	*loose cut*	*tight cut*
A	28.5	26
B	0.15	
C	0.33	
D	10	
E	25	
F	24	

Table E.2: Parameters of the proton fiducial cuts.

coils of the target magnet which shadows events with $45^\circ < \theta_{DC} < 75^\circ$.

The cut for the electrons, which do not reach $\theta_{DC} > 75^\circ$ is simply a cutoff corresponding to the lower edge of the magnet:

$$\theta_{DC} < 45^\circ \tag{E.5}$$

The cuts to remove protons which scatter close to the coils are given by[2]

$$\theta_{DC} > 49 - \frac{1.67\frac{3375}{torcur}}{p_{scaled} - 0.2} + 0.5p_{scaled} - 0.35p_{scaled}^2 \tag{E.6}$$

$$\theta_{DC} < 70 + \frac{1.27\frac{3375}{torcur}}{p_{scaled} - 0.2} - 0.3p_{scaled} + 0.35p_{scaled}^2 \tag{E.7}$$

$$p_{scaled} > 0.3 \tag{E.8}$$

For protons with angles $75^\circ < \theta_{DC} < 100^\circ$ the acceptance is no longer symmetric around 30° and therefore the $\Delta\phi$ in equation E.3 needs to be corrected. The cut becomes

$$30^\circ - \Delta\phi_{inf} < \phi_{sec} < 30^\circ + \Delta\phi_{sup} \tag{E.9}$$

$$\Delta\phi_{inf} = \Delta\phi - a + \frac{b}{p} - c(\theta_{DC} - 75) \tag{E.10}$$

$$\Delta\phi_{inf} = \Delta\phi - d - \frac{e}{p} - f(\theta_{DC} - 75) \tag{E.11}$$

[2] The third cut ($p_{scaled} > 0.3$) is applied since the CLAS spectrometer is not designed to measure particles with momentum less that 0.2 GeV/c.

where p is the proton momentum and a, b, c, d, e and f are parameters that depend on the sector and can be found in Table E.3.

Further cuts where applied to remove inefficiencies due to bad paddles. For the

Parameter	*sector 1*	*sector 2*	*sector 3*	*sector 4*	*sector 5*	*sector 6*
a	2	2	18.75	2	2	15.73
b	0	0	2.09	0	0	1.05
c	0.1	0.1	0.1	0.1	0.1	0.13
d	1.04	18.04	3.04	2.04	17.04	1.04
e	6.8	6.8	6.8	6.8	6.8	6.8
f	0.1	0.27	0.13	0.2	0.1	0.1

Table E.3: Parameters for large θ_{DC} cuts.

electron the following cuts were applied:

- sector 5
$$\theta_{DC} < 18.5^\circ - 0.4 \cdot p_{scaled} \quad \theta_{DC} > 20^\circ - 0.4 \cdot p_{scaled} \tag{E.12}$$

- sector 6
$$\theta_{DC} < 29^\circ \quad \theta_{DC} > 31.5^\circ \tag{E.13}$$

- sector 1,3 and 5
$$\theta_{DC} < G + \frac{H}{(p_{scaled} + I)} \tag{E.14}$$
$$\theta_{DC} > J + \frac{K}{(p_{scaled} + L)} \tag{E.15}$$

  where the parameters G, H, I, J, K and L are listed in table E.4.

For the proton several cuts of the form

$$p < M + N(\theta_{DC} - O)^P \tag{E.16}$$
$$p > Q + R(\theta_{DC} - S)^T \tag{E.17}$$

Parameter	*sector 1*	*sector 3*	*sector 5*
G	23.5	16	20
H	12	10.5	10.5
I	0.225	0.	0.3
J	27.8	18.5	23
K	12	13.5	10.5
L	0.15	0.12	0.225

Table E.4: Parameters for the cuts to remove bad paddles for the electron.

were applied, where the values of the parameters M, N, O, P, Q, R, S and T are listed in table E.5.

Param.	*sector 1,3*	*sector 1,3*	*sector 4,6*	*sector 5*	*sector 3*
	paddle 16	paddle 43	paddle 21	paddle 11,12,13	paddle 18
M	0.6	0.13	0.43	0.67	0.53
N	$1.3\ 10^{-4}$	$1.8\ 10^{-5}$	$5.5\ 10^{-5}$	$4\ 10^{-6}$	$5.6\ 10^{-6}$
O	13	77	17	2	13
P	3.2	3.2	3.2	4	4
Q	0.68	0.16	0.49	0.92	0.6
R	$1.3\ 10^{-4}$	$1.8\ 10^{-5}$	$8\ 10^{-5}$	$5\ 10^{-6}$	$5.6\ 10^{-6}$
S	10	70	16	-4	10
T	3.2	3.2	3.2	4	4

Table E.5: Parameters for the cuts to remove bad paddles for the proton.

APPENDIX F

Acceptance calculation plot

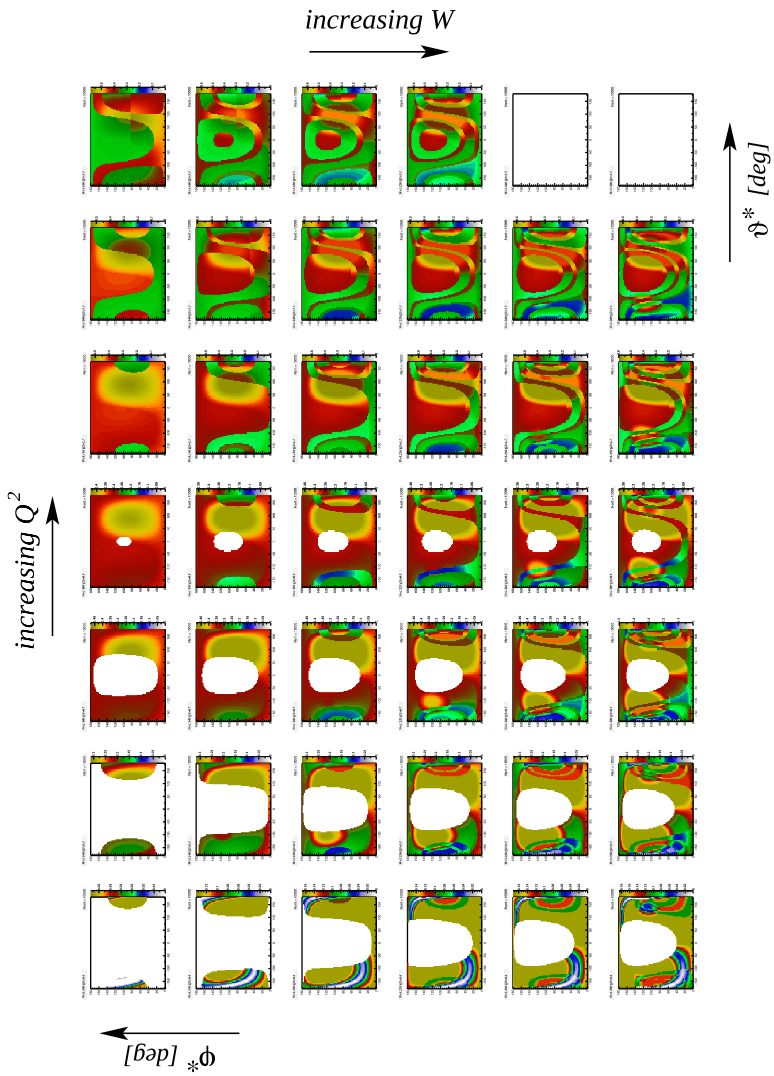

Figure F.1: Calculation of the acceptance as a function of θ^* *vs* ϕ^*, the pion angles in the center of mass system for different values of Q^2 (from 0.3 to 1.5 GeV$^2/c^2$ in steps of 0.2 GeV$^2/c^2$) and W (from 1.1 to 1.3 GeV$/c^2$ in steps of 0.04 GeV$/c^2$).

APPENDIX G
Beam polarization

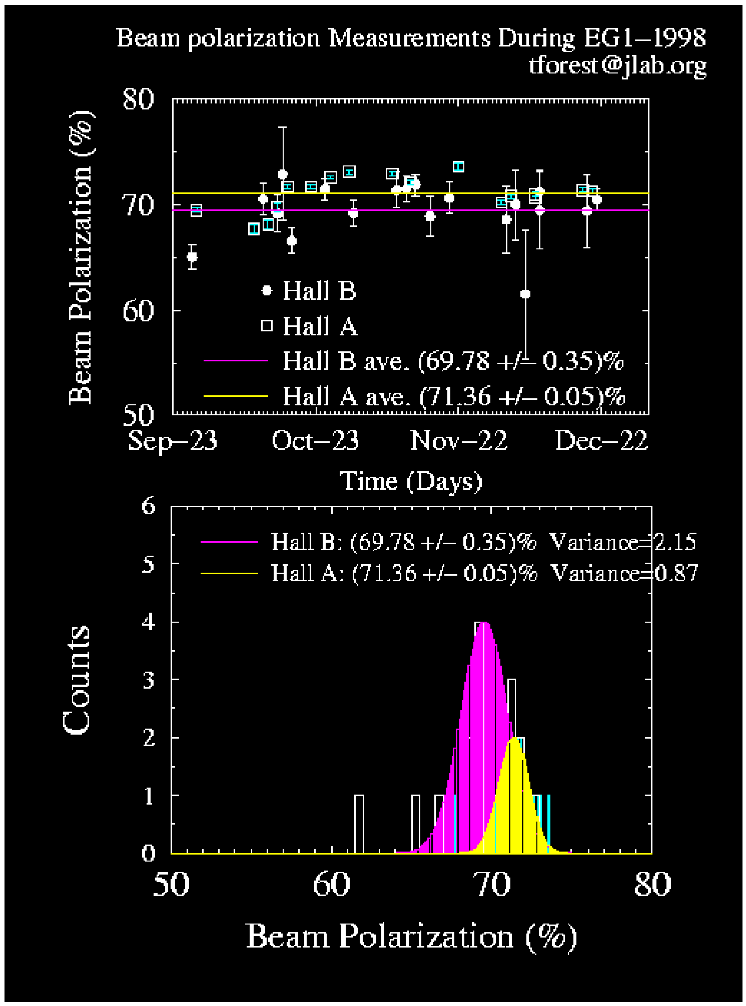

Figure G.1: Beam polarization measurements during EG1 run in 1998 for Hall A and B. The top picture shows the results of the Møller run measurements as a function of time. The bottom plot shows the fit to a Gaussian of all the measurements to extract the average value and the variance.

APPENDIX H

Definition of the asymmetries taking into account the ^{15}N polarization

In section 4.1 the relation between the experimental quantities, such as the number of events, and the cross section terms $\sigma_0,\ \sigma_e,\ \sigma_t$ and σ_{et} was discussed. Equation 4.6 are the exact result if the ^{15}N is not polarized. Since, as discussed in section 5.6.4, the unpaired proton of the ^{15}N carries a small polarization, in this appendix the *real* relation between cross section and experimental quantities will be shown.

The number of events can be written in general as

$$N = D(\sigma_0 + P_e\sigma_e + P_t\sigma_t - P_eP_t\sigma_{et}) \tag{H.1}$$

where D is related to the luminosity (see section 4.1).

For each helicity configuration the number of events can therefore be expressed as

$$\begin{aligned}
N_{\uparrow\uparrow} =& D_1(3\sigma_0 + 15\sigma_0^N + 3P_e^a\sigma_e + 15P_e^a\sigma_e^N + \\
&+ 3P_t^a\sigma_t + P_t^{aN}\sigma_t^N - 3P_e^aP_t^a\sigma_{et} - P_e^aP_t^{aN}\sigma_{et}^N) \\
N_{\downarrow\uparrow} =& D_2(3\sigma_0 + 15\sigma_0^N - 3P_e^a\sigma_e - 15P_e^a\sigma_e^N + \\
&+ 3P_t^a\sigma_t + P_t^{aN}\sigma_t^N + 3P_e^aP_t^a\sigma_{et} + P_e^aP_t^{aN}\sigma_{et}^N) \\
N_{\uparrow\downarrow} =& D_3(3\sigma_0 + 15\sigma_0^N + 3P_e^b\sigma_e + 15P_e^b\sigma_e^N + \\
&- 3P_t^b\sigma_t - P_t^{bN}\sigma_t^N + 3P_e^bP_t^b\sigma_{et} + P_e^bP_t^{bN}\sigma_{et}^N) \\
N_{\downarrow\downarrow} =& D_4(3\sigma_0 + 15\sigma_0^N - 3P_e^b\sigma_e - 15P_e^b\sigma_e^N + \\
&- 3P_t^b\sigma_t - P_t^{bN}\sigma_t^N - 3P_e^bP_t^b\sigma_{et} - P_e^bP_t^{bN}\sigma_{et}^N)
\end{aligned} \tag{H.2}$$

where P_t^{aN}, P_t^{bN} are the polarizations of the unpaired proton in the ^{15}N, and σ_0^N, σ_t^N and σ_{et}^N are the cross section terms for the scattering off the ^{15}N. The number 3 indicates the number of free protons of $^{15}NH_3$ contributing to the cross section, 15 is the number of nucleons in ^{15}N that contribute to the terms σ_0^N and σ_e^N and finally there is only one polarized proton in the ^{15}N that contribute to the terms

σ_t^N and σ_{et}^N. As seen in section 5.6.4 the polarizations of the unpaired proton $P_t^{a,bN}$ can be related to the polarizations of the free proton $P_t^{a,b}$. One can therefore write

$$\begin{aligned} P_t^{aN} &= \alpha^a P_t^a \\ P_t^{bN} &= \alpha^b P_t^b \end{aligned} \tag{H.3}$$

where $P_t^a = 38\%$, $\alpha^a = 0.035$, $P_t^b = -54\%$ and $\alpha^b = 0.037$. The two constants α^a and α^b are almost the same, we will therefore assume $\alpha^a = \alpha^b \equiv \alpha$. Substituting equations H.3 in H.2 one obtains

$$\begin{aligned} N_{\uparrow\uparrow} =& D_1(3\sigma_0 + 15\sigma_0^N + 3P_e^a\sigma_e + 15P_e^a\sigma_e^N + \\ & + P_t^a(3\sigma_t + \alpha\sigma_t^N) - P_e^aP_t^a(3\sigma_{et} + \alpha\sigma_{et}^N)) \\ N_{\downarrow\uparrow} =& D_2(3\sigma_0 + 15\sigma_0^N - 3P_e^a\sigma_e - 15P_e^a\sigma_e^N + \\ & + P_t^a(3\sigma_t + \alpha\sigma_t^N) + P_e^aP_t^a(3\sigma_{et} + \alpha\sigma_{et}^N)) \\ N_{\uparrow\downarrow} =& D_3(3\sigma_0 + 15\sigma_0^N + 3P_e^b\sigma_e + 15P_e^b\sigma_e^N = \\ & - P_t^b(3\sigma_t + \alpha\sigma_t^N) + P_e^bP_t^b(3\sigma_{et} + \alpha\sigma_{et}^N)) \\ N_{\downarrow\downarrow} =& D_4(3\sigma_0 + 15\sigma_0^N - 3P_e^b\sigma_e - 15P_e^b\sigma_e^N + \\ & - P_t^b(3\sigma_t + \alpha\sigma_t^N) - P_e^bP_t^b(3\sigma_{et} + \alpha\sigma_{et}^N)) \end{aligned} \tag{H.4}$$

Combining the number of events for different helicity configuration in the same way of section 4.1 it can be proven that

$$\begin{aligned} A_e \sim \frac{3\sigma_e + 15\sigma_e^N}{3\sigma_0 + 15\sigma_0^N} &= \frac{1}{P_e^a}\frac{(\overline{N_{\uparrow\uparrow}} - \overline{N_{\downarrow\uparrow}}) + d\alpha_{et}(\overline{N_{\uparrow\downarrow}} - \overline{N_{\downarrow\downarrow}})}{(\overline{N_{\uparrow\uparrow}} + \overline{N_{\downarrow\uparrow}}) + d\alpha_t(\overline{N_{\uparrow\downarrow}} + \overline{N_{\downarrow\downarrow}})} \\ A_t + \frac{\alpha\sigma_t^N}{3\sigma_0} = \frac{3\sigma_t + \alpha\sigma_t^N}{3\sigma_0} &= \frac{1}{P_t^b}\frac{(\overline{N_{\uparrow\uparrow}} + \overline{N_{\downarrow\uparrow}}) - d(\overline{N_{\uparrow\downarrow}} + \overline{N_{\downarrow\downarrow}})}{(\overline{N_{\uparrow\uparrow}} + \overline{N_{\downarrow\uparrow}}) + d\alpha_t(\overline{N_{\uparrow\downarrow}} + \overline{N_{\downarrow\downarrow}}) - D_2\sigma_0^N} \\ A_{et} + \frac{\alpha\sigma_{et}^N}{3\sigma_0} = \frac{3\sigma_{et} + \alpha\sigma_{et}^N}{3\sigma_0} &= \frac{1}{P_e^aP_t^b}\frac{-(\overline{N_{\uparrow\uparrow}} - \overline{N_{\downarrow\uparrow}}) + d\alpha_e(\overline{N_{\uparrow\downarrow}} - \overline{N_{\downarrow\downarrow}})}{(\overline{N_{\uparrow\uparrow}} + \overline{N_{\downarrow\uparrow}}) + d\alpha_t(\overline{N_{\uparrow\downarrow}} + \overline{N_{\downarrow\downarrow}}) - D_2\sigma_0^N} \end{aligned} \tag{H.5}$$

These equations show that the quantities extracted experimentally are A_t and A_{et} plus a contribution from the ^{15}N. This contribution is however very small for the following reason. The ^{15}N missing mass spectrum is much broader than the one of the free proton due to the Fermi motion inside the nucleus. To select the π^0

a missing mass cut around the free proton peak is applied, removing most of the events of the ^{15}N tails. The remaining events of the ^{15}N under the peak, correspond to scattering off protons in the nucleus that have almost zero Fermi motion. In this condition it is reasonable to approximate $\sigma^N = \beta\sigma$ where β is a constant that can be estimated to be 1/3. The previous expressions for A_t and A_{et} then become

$$\begin{aligned} A_t + \frac{\alpha\sigma_t^N}{3\sigma_0} = A_t + \frac{\alpha\beta\sigma_t}{3\sigma_0} = A_t(1 + \frac{\alpha\beta}{3}) \\ A_{et} + \frac{\alpha\sigma_{et}^N}{3\sigma_0} = A_{et} + \frac{\alpha\beta\sigma_{et}}{3\sigma_0} = A_{et}(1 + \frac{\alpha\beta}{3}) \end{aligned} \quad \text{(H.6)}$$

It is clear that the contribution from the term $\frac{\alpha\beta}{3} \sim 0.004$ is negligible.

Using these observations it is then possible to see why $A_e \sim \frac{3\sigma_e + 15\sigma_e^N}{3\sigma_0 + 15\sigma_0^N}$ in equation H.5. Using the approximation $\sigma^N = \beta\sigma$ one can write

$$\frac{3\sigma_e + 15\sigma_e^N}{3\sigma_0 + 15\sigma_0^N} = \frac{3\sigma_e + 15\beta\sigma_e}{3\sigma_0 + 15\beta\sigma_0} = \frac{(3 + 15\beta)\sigma_e}{(3 + 15\beta)\sigma_0} = A_e \quad \text{(H.7)}$$